DESIGN AND AERODYNAMIC ANALYSIS OF A NOVEL MEDIUM BYPASS TURBOFAN ENGINE EXHAUST SYSTEM

by

Alexander Wright

Submitted in partial fulfillment of the requirements
for the degree of Doctor of Philosophy

at

Dalhousie University
Halifax, Nova Scotia
December 2019

For my mother, I truly could not have done this without your support.

Table of Contents

List of Tables

List of Figures

Abstract

This thesis presents computational simulations of lobed mixers used in medium bypass turbofan engine exhaust systems. The aim was to investigate performance and redesign the system to reduce overall mass. The computational domain consisted of one 30° sector of a model exhaust system which encapsulated one lobe wavelength of the lobed mixer and three swirling vanes used to model the flow downstream of a low-pressure turbine stage.

An examination of lobed mixer performance at incompressible and compressible boundary conditions found that the low-speed compressible experiments that were used previously to simulate the aft-end ducting of the engine could not accurately model the true flow features produced during actual engine operating conditions. Further investigation was conducted on scalloping of the baseline mixer geometry and concluded that a moderate scallop produced the best mixing of the core and bypass flow within the common nozzle. The lobed mixer was also shown to be tolerant of core flow swirl up to and including 10° before incurring penalties. The tests on swirl tolerance were performed in service of determining the necessity of Turbine Exhaust Casing struts which, until now, have necessitated a large portion of aft-end ducting axial length to accommodate their aerodynamic effects. Low-pressure turbines are most effective when turning the core flow to 30° swirl, and so the TEC struts are still required for optimal lobed mixer and common nozzle performance. However, it has been shown that the TEC struts and lobed mixer can be fully integrated without penalty to performance and with great impact on total aft-end duct length and therefore engine mass.

Simulations were also performed to investigate the relative mixing rates of temperature and momentum downstream of lobed mixers. Past literature has reported that momentum mixing always lags temperature. However, those discoveries were made downstream of confluent mixers, not lobed mixers. This data showed that the relative mixing rates of temperature and momentum downstream of lobed mixers was inconsistent.

List of Abbreviations and Symbols Used

Initials

CFD	Computational Fluid Dynamics
CFL	Courant-Friedrichs-Lewy
CoV	Coefficient of Variance
GCI	Grid Convergence Index
MBTF	Medium Bypass Turbofan Engine
NRC	National Research Council Canada
RANS	Reynolds Averaged Navier-Stokes
SST	Shear Stress Transport
TEC	Turbine Exhaust Casing
TKE	Turbulent Kinetic Energy

Latin Letters

A	Area
C	Coefficient
D	Dimensionality
D_h	Equivalent Diameter
I	Mixing Index
k	Turbulent kinetic energy
m	Mass

P	Pressure
Pr	Prandtl Number
PS	Pressure Side
r	Radius
Re	Reynolds Number
SS	Suction Side
SV	Streamwise Vortex
T	Thrust
Y	Total Pressure Loss
V	Velocity
v	Velocity
Z	Axial Plane, relative to lobed mixer exit

Greek Letters

ρ	Density
ϵ	Turbulent Dissipation, Error
Γ	Circulation
ν	Kinematic Viscosity
ω	Specific Dissipation
σ	Standard Deviation
μ	Dynamic Viscosity
ω	Vorticity

Superscripts

$\dot{x}$	Flux
$\overline{x}$	Mean
$\vec{x}$	Vector

Subscripts

0	Total
∞	Ambient or Surrounding
a	Azimuthal
b	Bypass
c	Core
eff	Effective
i	Reference
j	Jet
r	Radial
ref	Reference
S	Separation
s	Static
s	Streamwise
θ	Tangential
t	Turbulent
z	Axial

Acknowledgements

I would like to thank my supervisors, Dr. Ali Mahallati and Dr. Julio Militzer for standing by me and providing guidance throughout this process.

Thank you to the other members of my examining committee, Dr. Serguei Iakovlev and Dr. Peter Allen.

To the other staff and faculty of the Mechanical Engineering Department and Faculty of Graduate Studies, I want to say how much I appreciate your kindness and help whenever a question needed answering.

I would like to make special acknowledgment to my friend and colleague Dr. Martin Conlon. I found the determination and motivation to continue because of your advice.

I must also thank all of the friends who have been encouraging me through the process. The sometimes tough love was a necessity in this journey and I am glad to have had you all by my side.

Chapter 1

Introduction

1.1 Background

Gas turbine engines have been used in aero applications since the 1960's. At that point in history, economies were booming and fuel was inexpensive. It is now 2019 and the world is facing the realities of climate change. Aviation emissions are a major factor in global carbon emissions and steps are being taken to reduce emissions in any way possible.

One of these steps is reducing the mass of aviation propulsion systems. The exhaust system of medium bypass turbofan engines, commonly used on smaller private and regional craft, has been identified as a candidate for mass reduction through improved design.

The medium bypass turbofan engine exhaust system consists of several parts common to almost all engines in the category. The bypass flow is energized by the fan and flows around the core through a separate duct until it reaches the mixer and interacts with the core exhaust gases. The core flow is a more complicated path through the fan, compressors, combustor, turbines and eventually through the lobed mixer into the mixing duct. Most engines have structural struts downstream of the final low pressure turbine stage (LPT). These struts are known as turbine exhaust casing (TEC) struts and serve two functions: to provide structural support for the core and also to reduce the amount of swirl incident to the mixing duct. Both flows, the bypass and the core, meet at the mixer and are combined in a common nozzle before ultimately being exhausted to the atmosphere. It is the TEC strut and mixer that were identified as parts for weight saving redesigns.

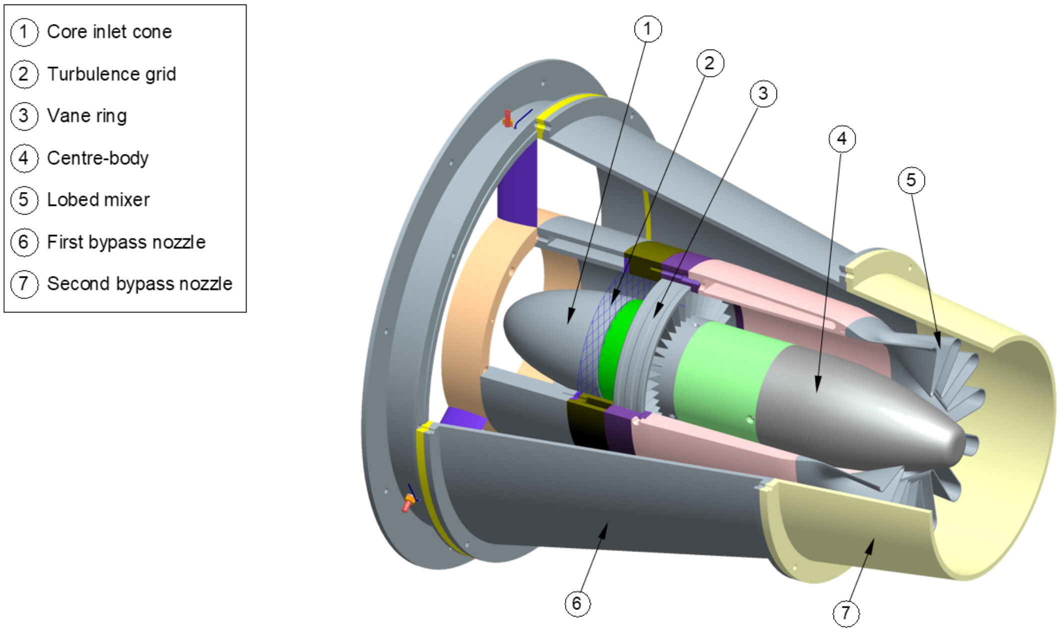

Figure 1.1: Cutaway section of National Research Council Canada low speed test section.

1.1.1 Incompressible Approach

The original approach to this problem was to use a low-speed, concentric, annular internal flow wind tunnel to model the exhaust system of a medium bypass turbofan engine (MBTF) from the LPT downstream to the nozzle and beyond. The original test section relied on 7-hole pressure probe and 4-wire hot wire anemometry to measure the flow. The test section is shown in Figure 1.1. This set up was chosen based on reports in the literature [1, 2, 3, 4, 5, 6] that the rate of mass, momentum and thermal mixing occur at different rates during fluid mixing processes. The literature reports that the mass and energy mixing always leads the momentum mixing. From this, it was inferred by the original researchers that a low-speed isothermal investigation would be applicable to studying the effectiveness of lobed mixers even at compressible non-isothermal conditions such as during engine operation. So long as the momentum mixing was improved, or remained consistent, the rest of the mixing should complete prior to the momentum.

This thesis challenges that inference because the literature did not involve lobed mixers, the focus of this problem.

1.1.2 The Gap in the Literature

The lack of literature specific to the mixing processes and their relative rates produced via lobed mixer provided enough reason to take a closer look and challenge the status quo of the original research approach. Past literature that was used to justify the original approach of examining momentum mixing only was based on studies about concentric mixers. Lobed mixers and concentric mixers produce drastically different flow structures in their wake. Concentric mixers only produce azimuthal vorticity through the Kelvin-Helmholtz instability. Lobed mixers produce streamwise vorticity in addition to the azimuthal vorticity. Their geometry allows for a radial deflection of the inner and outer flow, outward and inward respectively. The viscous nature of the flow results in the development of a convoluted shear layer and the generation of streamwise vorticity in line with the direction of flow. This mechanism creates a bulk movement of fluid from one region to the other.

Scaling from compressible to incompressible flow is usually based on the Reynolds number, which describes the ratio of viscosity to inertia. Generally, the Reynolds number can be kept constant when moving from the compressible to the incompressible regime by modifying the geometric scale of the test section. To do this for the case of the PW615 exhaust system, the model test section would have to be scaled to such a small size that manufacturing tolerances and disturbance of the flow due to probe measurement would render it inaccurate. Therefore, the high Reynolds number environment of the engine operating condition and the subsequent importance of inertia over viscosity means that the flow cannot be simply reduced in speed at the same geometric scale and have the same conclusions drawn about the flow.

This study will take a computational approach to the exhaust system redesign and in doing so shed further light on the trends of mass, momentum and thermal mixing for lobed mixers.

1.2 Computational Approach

Viscous flow mixing is a complex process that is sensitive to probe measurement. Observation of the flow around lobed mixers is particularly difficult via traditional probe-based measurement thanks to the complicated three-dimensional geometry. The flow around lobed mixers is inherently variable and thus probe alignment and accuracy suffers. All three components of velocity must be recorded simultaneously in order to develop an accurate model of the flow. Doing so with probe-measurement-based techniques would be misguided based on the resources available. Computational Fluid Dynamics (CFD) allows for relatively fast and inexpensive investigation of three-dimensional flow fields around complex geometries, like lobed mixers. This research relies on data obtained through CFD simulation.

1.3 Objective

The objective of the research this thesis presents is two-fold. First, there is the problem of aft-end ducting length and second, there is a gap in the literature that had not been considered for previous attempts to solve said problem. This study intends to:

1. Establish a fundamental understanding of free and confined jet flow mixing through review of existing literature.
2. Develop and validate a computational model that can accurately simulate the performance of a turbofan engine lobed mixer.
3. Utilize that model to isolate the effect of flow conditions and hardware designs on turbofan engine exhaust flow mixing.
4. Develop a novel exhaust system design with the intent to reduce aft-end duct length.
5. Analyze supplementary data sets to fill in the gap in the literature.

1.4 Thesis Outline

This thesis is laid out to lead the reader along the path by which the research and discoveries unfolded. The motivations and objectives previously mentioned in this introduction will be expanded on in the text. Chapter 2 presents a summary of the literature review which led to the identification of the gap in knowledge that this thesis shall fill. References to the literature permeate the body of the thesis and will be expanded upon in many of the chapters that follow. Chapter 3 outlines the procedures used during the course of this research. The chapter gives insight on the computational arrangement used to produce the data and how that data was reduced and analyzed. Chapter 4 then displays evidence for the validity of this process via comparison of the computational simulations to past data found in the literature and via data reduction techniques that allow for a quantification of the simulation uncertainty. Chapters 5 through 9 present the analysis of the data. A challenge to the status quo of the original NRC study is presented in Chapter 5 via computational investigation of compressibility effects on the flow structures downstream of and mixing performance of an unscalloped lobed mixer. Chapter 6 continues from those findings to investigate the aerodynamic effect of various scalloping designs of the lobed mixer geometry. Chapter 7 continues further to investigate the sensitivity of unscalloped and scalloped lobed mixers to core flow swirl. Chapter 8 then presents the efficacy of core flow swirl removal hardware (TEC Struts) on overall exhaust system performance and how the hardware in question can be integrated with the lobed mixer to allow for a shorter exhaust duct. The problem this thesis aimed to solve is answered in Chapter 8. Chapter 9 shall fill the gap identified in the literature and present results on the relative mixing rates of fluid flow conservative variables—mass, energy, momentum—when concentric jets are mixed via lobed mixer. Finally, chapter 10 will conclude the thesis with a summary.

Chapter 2

Literature Review

This chapter presents an overview of the current understanding of flow mixing in jets and turbofan lobed mixers. The mixing mechanism of coaxial jets will be reviewed first, followed by focus on the parameters that influence lobed mixer performance.

2.1 Development and Structure of a Free Jet

Jet mixing is an important aspect of turbofan engine operation. The importance of mixing enhancement has led to a large amount of research into achieving optimal jet performance through various mixing enhancement methods. The exhaust systems of low and intermediate bypass ratio turbofan engines typically consist of Turbine Exhaust Casing (TEC) struts, a centre-body, a lobed mixer and a nozzle. In this system, TEC struts remove the majority of swirl from the final low-pressure turbine stage and the mixer enhances mixing between hot core gases and cold bypass air before exiting the nozzle. This enhanced mixing increases the net thrust [7] and reduces the engine jet noise [8]. Exhaust gas discharged through the nozzle expands and mixes with the ambient air.

The jet mixing process in turbofan lobed mixers stems from fundamental understanding of free jet and coaxial jet mixing. The definition of a free jet is the free shear layer that develops between two streams of velocity U_j and U_∞—where U_j, the jet velocity is greater than U_∞, the surrounding velocity—downstream of a nozzle, as shown in Figure 2.1. The surrounding fluid could be ambient with zero velocity or a secondary jet with non-zero velocity—as found in the exhaust of gas turbine engines. A free jet is more unstable than a jet confined by a wall because of the momentum transfer between the unconfined free jet and the surrounding fluid. The free jet is typically turbulent flow; a circular jet becomes a turbulent jet when $Re = \frac{\overline{U} d_o}{\nu} \geq 30$, where d_o is the nozzle diameter and $\overline{U}$ is the mean jet velocity at the nozzle exit. The characteristics of free jets differ between laminar, turbulent and

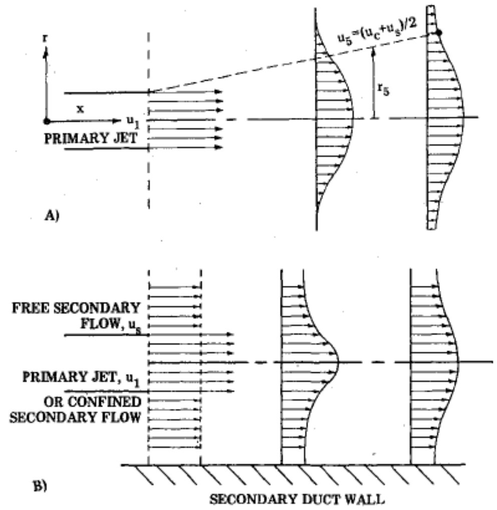

Figure 2.1: Schematic of jet mixing. (A) A primary jet, velocity u_1 mixing with stagnant ambient air. (B) A primary jet, velocity u_1, mixing with a secondary flow, velocity u_S [9].

supersonic/compressible regimes. This literature review will approach the discussion in that order beginning with laminar jet then the transition region to turbulent and finally introducing the supersonic free jet.

The free jet is subject to the development of an outer shear layer immediately upon exiting the nozzle. This shear layer develops due to the velocity gradient at the interface between the two streams—the jet and surrounding fluid. This region is identified in Figure 2.1. In the laminar regime, the mixing layer develops downstream of the nozzle as a result of viscous forces and other instabilities that result from fluid interaction. The laminar mixing layer is dominated by large-scale coherent structures resulting from the Kelvin-Helmholtz instability. Jets in the turbulent regime, on the other hand, are characterized by small-scale perturbations. Eventually, the growth of velocity and vorticity results in the shear layer developing into discrete and coherent vortices. The vortex shedding frequency is dependent on several characteristics of the flow exit velocity profile such as shape, turbulence structure, initial shear layer momentum thickness, and jet exit velocity. It is interesting to note that streamwise vortices develop further downstream because of apparent spanwise instability [10]. These streamwise vortices are arranged in ‘ribs’, as seen in Figure 2.2, and enhance the mixing process between the two fluids. Further downstream of the nozzle exit, the

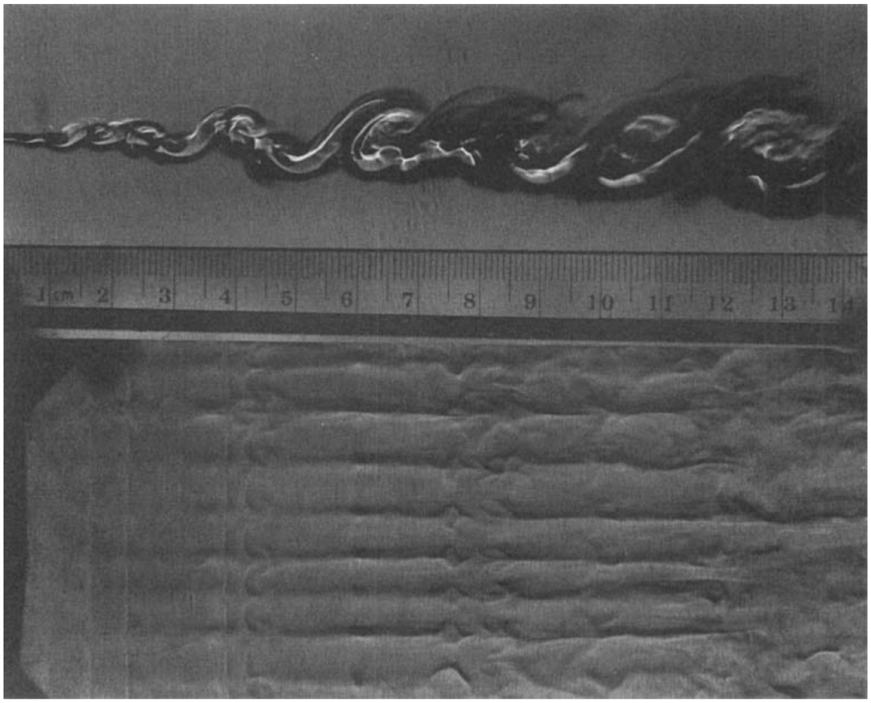

Figure 2.2: Flow visualization showing the streamwise vortices arranged in ribs [10].

interaction of these instabilities leads to an increase of three-dimensional structure in the shear layer and thus the breakdown of the coherent vorticity structures and the genesis of small scale, turbulent structures. Figure 2.3 illustrates the breakdown of large-scale coherent structures. Small eddies develop within the core of the structures themselves creating a turbulent region. A more detailed review can be found in Hussain [11], Bernal and Roshko [10], and Liu [12].

There is a point at which the mixing layer penetrates the jet centre line as the mixing layer grows in thickness downstream from the nozzle. The centre line remains unaffected by the mixing that occurs at the shear layer and the velocity remains equal to that at the nozzle exit up to this point of mixing layer growth. This region is referred to as the potential core, pictured in Figure 2.4. The length of this region is governed by the nozzle exit geometry. It is influenced by the characteristics of mixing as developed by the boundaries of the nozzle itself—a lobed nozzle would have a drastically different potential core than a circular nozzle. The transitional region, where the flow characteristics are governed by jet-column instability and the centreline velocity diminishes rapidly [13], exists immediately downstream of the potential core. The fully turbulent jet is formed beyond the transitional region and is also referred

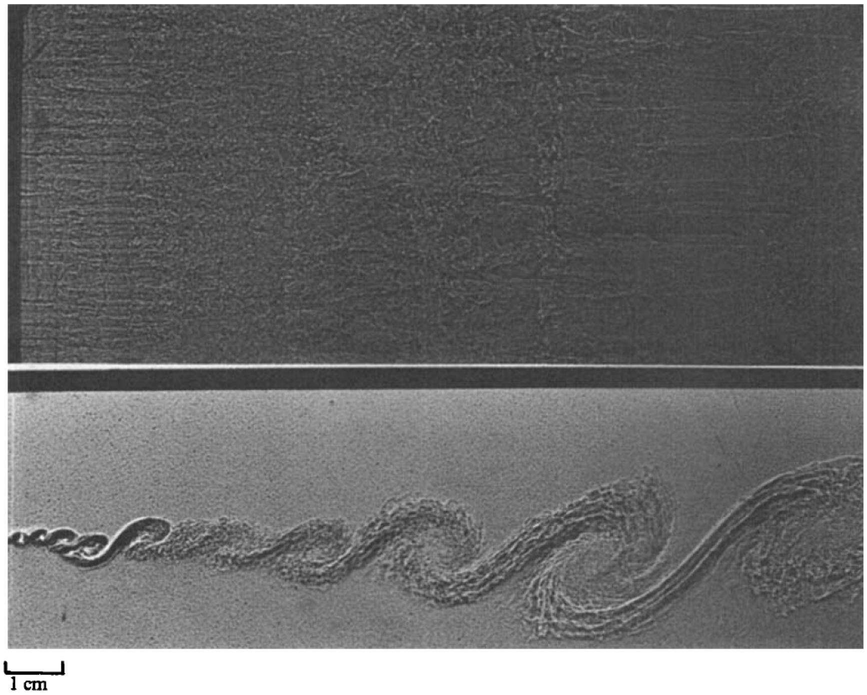

Figure 2.3: Flow visualization showing the generation of small-scale turbulent eddies within large-scale coherent structure [10].

to as the similarity region because the local and mean velocity profiles have become similar at this point.

A large body of research conducted on the development and structure of turbulent jets present evidence that even turbulent jets are the result of large-scale motion generated at the jet boundary or shear layer. These large-scale structures are responsible for the noise produced by jets. There is evidence these large-scale turbulent structures are governed by the same dynamics as the large-scale laminar shear layer

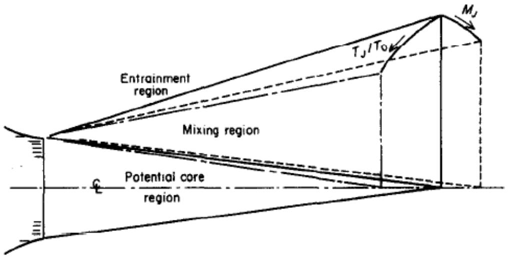

Figure 2.4: The potential core of a free jet [14].

structures. The difference, according to Liu [12], is that the strength of the instabilities come from the more efficient ‘dissipative’ actions of the turbulent eddies rather than viscous dissipation in the laminar structures. More information on turbulent free jets can be found in Liu [12], and Roshko [15].

Supersonic, compressible free jets are fundamentally different from the subsonic, incompressible free jets. The main difference is the presence of a shock cell structure found only for improperly expanded choked jets. If a convergent-divergent nozzle is designed and operated at the proper pressure ratio the jet can be considered supersonic and no shock need be created. The shock cell structure develops in situations of improper operating pressures in which the jet is either overexpanded or underexpanded. The potential core is defined for supersonic jets as the length from the nozzle exit up to the point that these shock cell structures exist. The region downstream of the shock structure is similar to subsonic, incompressible jets.

2.2 Methods of Mixing Enhancement in Coaxial Jets

It is important to understand how to control the coherent structures in terms of their formation, interaction and breakdown in order to enhance the mixing rate of coaxial jets. The methods of enhancement are classified based on the mechanism at work such as breaking up the organized structure, introducing acoustic excitation of instability modes and enhancing the shear stress at the mixing layer. A more detailed review is given by Saddington and Knowles [16], Gutmark et al. [17] and Gutmark and Grinstein [18]. As mentioned earlier, the dynamic development process of laminar jets and turbulent jets is controlled by large-scale coherent structures. Jet mixing efficiency is enhanced when the large-scale coherent flow structures are broken down in to small-scale turbulent structures that accelerate shear layer development. There are several common methods of breaking up the order of large-scale coherent structures, outlined below.

2.2.1 Axis Switching of Vortex Ring

A phenomenon that occurs for non-circular jet flow is axis switching of the azimuthal vortex ring. An azimuthal vortex ring is normally shed at the nozzle trailing edge. As the jet spreads, the cross-section can change through shapes similar to the nozzle with axes rotated at angles characterized by the jet geometry. Several investigations of this phenomenon have been performed on non-circular jets:

- elliptical [19]
- rectangular [20]
- square [20]
- triangular [21]
- and diamond [22].

The underlying mechanism of this phenomenon is that portions of the azimuthal vortex that originate from areas of small radius of curvature will travel downstream faster than other regions of the azimuthal vortex because the small radius allows the azimuthal vortex to interact with itself and develop a pseudo-pump that harnesses the relative counter-rotation of the vortex and accelerates the jet at that particular location. This leads to deformation of the jet cross-section. Figure 2.5 shows how the jet vortex ring formed by the elliptical or rectangular nozzle rotates around the central axis of the jet before switching of the long and short axes occurs. The trend continues downstream resulting in a second axis switch. The location of the first crossover point appears in the form of a set of linear functions of the nozzle aspect ratio [23, 18]. The cross over point downstream of the first is less sensitive to the original nozzle aspect ratio. The vortex deformation appears first at the corners for square, rectangular, and triangular jets due to the extremely small radius of curvature at these points. Small streamwise vortices are created at the corners because of the stretching of the bent vortex by shear stresses [24]. These vortices initiate axis rotation and turbulence amplification at the vertices [25]. There is a thrust loss associated with non-circular compared to circular nozzles. Typical thrust losses of 5% were observed for a rectangular nozzle with an aspect ratio of six [26].

2.2.2 Introduction of the Streamwise Vortex

The entrainment of the surrounding fluid is dominated by the streamwise vortex, a three-dimensional structure in the shear layer. It is desirable to produce these

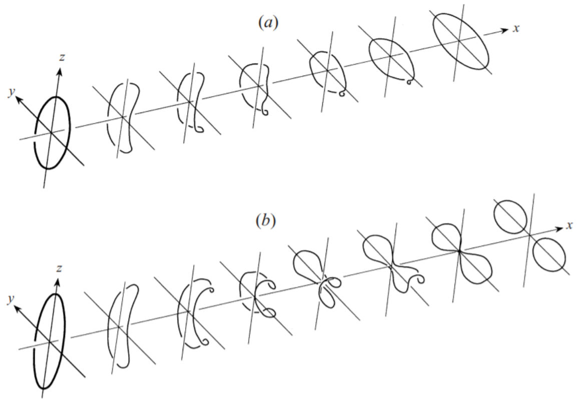

Figure 2.5: Vortex deformation and axis-switching (a) low-aspect-ratio, (b) high-aspect-ratio [27].

streamwise vortices as early as possible: preferably immediately at the nozzle exit. The entrainment of fluid is enhanced by these specific vortices and they also serve to accelerate the breakdown of the organized structure within the shear layer leading to enhanced large-scale and small-scale mixing. Various methods of creating streamwise vortices include notched nozzles [28], crown-shaped nozzles [29], grooves [30], tabs [31] and vortex generation.

Notched nozzles are formed by cutting a V-shaped or rectangular section into a nozzle lip. Crown-shaped nozzles are merely V-shaped notches that overlap. The mechanism at work is similar to the vertices of rectangular nozzles. The vortex ring is bent by shear stress and stretched into a streamwise vortex originating from the notch. Each notch produces a set of counter-rotating streamwise vortices. An alternate benefit of the notched nozzle is a reduction in jet noise; however, there is considerable pressure loss associated with this sort of nozzle. Grooves along the inner surface of the nozzle were successfully proposed to minimize the pressure loss [30], where streamwise vortices are created by semi-circular, rectangular and triangular grooves via the same mechanisms as notched nozzles.

Tabs and vortex generators placed at the exit of axisymmetric and rectangular nozzles produce streamwise vortices. Counter-rotating vortices are developed in the case of tabs, while a half delta wing vortex generator creates a single simple streamwise vortex. An 80% reduction in potential core length was achieved for under-expanded sonic jets using two rectangular tabs [32]. Tabs result in a significant thrust loss, likely due to the increased drag. Lobed mixers also introduce large-scale streamwise

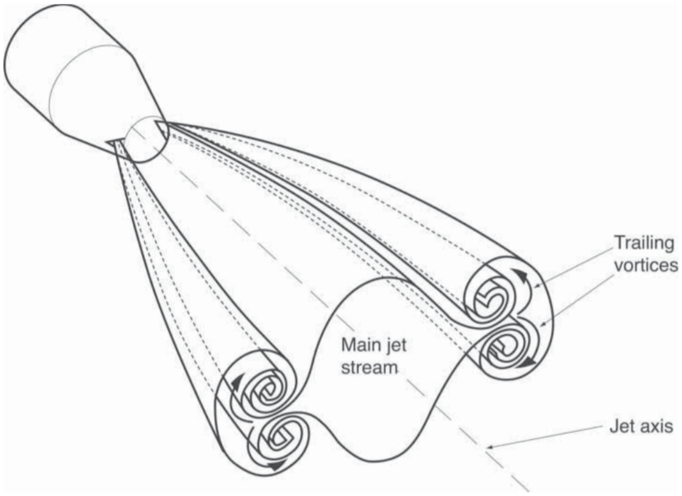

Figure 2.6: Notched nozzle [16].

vortices due to their geometry. They will be investigated in detail in a later section.

2.2.3 Indeterminate Original Nozzle

The term indeterminate origin was proposed by Wlezien and Kibens [33] for nozzles that have either a sloped or stepped exit plane, as shown in figure 2.7. It can also be used to describe nozzles with particularly large notches. The theory behind the indeterminate origin nozzle is that velocity perturbations induced by one shear layer could excite the other if they begin at different axial locations.

2.3 Mixing Rates in Coaxial Jets

Extensive studies of jet mixing characterizing entrainment, large-scale structures and temperature dispersion have been performed on laminar and turbulent coaxial jets. However, few studies have been carried out on the mixing rate of mass, momentum and temperature in coaxial jets. Turbulent subsonic coaxial jet experiments by Forstall and Shapiro [1] in the early 50s showed that mass diffusion is more rapid than momentum. The Schmidt number, relative rates of mass and momentum, was found to be independent of the velocity ratio between jets. Experimental study of turbulent mixing of nonhomogeneous coaxial jets by Alpinieri [2] demonstrated that in mixing regions of unequal density, the product of local density and eddy kinematic viscosity coefficient can be assumed to be dependent upon the axial coordinate of the jet only.

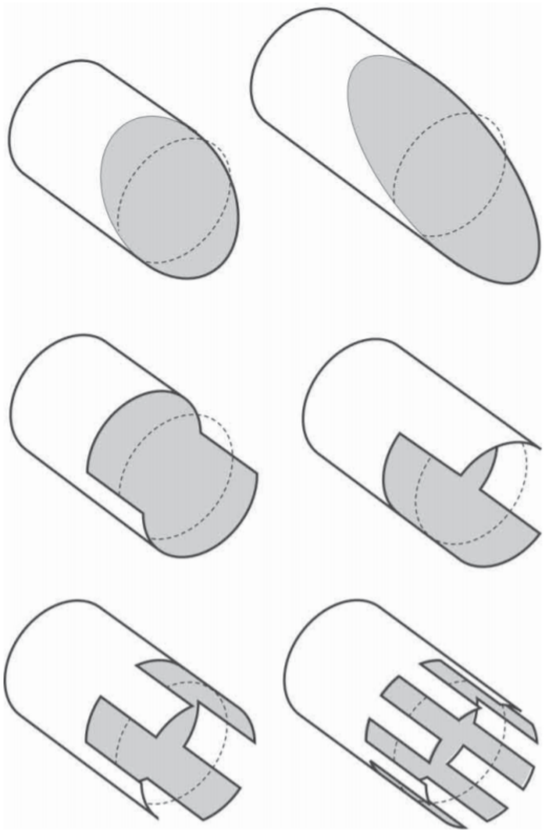

Figure 2.7: Indeterminate origin nozzles [16].

Their measurements also showed that mass diffuses more quickly than momentum, agreeing with Forstall and Shapiro. A qualitative assessment of density effects in turbulent mixing by Brown and Roshko [3] indicated that the density effects are small compared to the compressibility. The amplification rate of Kelvin-Helmholtz instability in a laminar vortex sheet increases the vortex strength by the square root of density ratio but its effect on the turbulent mixing layer was not clear. In an experimental study, Schumaker and Driscoll [4] examined the mixing properties of coaxial jets with large velocity and inverse density ratio. They demonstrated that mixing lengths could be correlated to the momentum flux at high Reynolds numbers. In that scenario, mixing rates were independent of absolute velocity differences and the jet Reynolds numbers. They did conclude, however, that mixing lengths were shorter for low-density jets flowing into higher density ambient fluid than for high-density jets flowing into lower density ambient fluid. All of these studies were performed with confluent mixers. There were no publications found during the several years of literature search that involved this sort of analysis downstream of lobed mixers. This forms the basis of Chapter 9 of this thesis.

2.4 Lobed Mixers

Confluent mixers produce no axial vorticity and the turbulent transport between the core and bypass flows is accomplished solely due to the formation of the Kelvin-Helmholtz vortex sheet in the thin shear layer [34]. The small-scale viscous mixing is much less effective than large-scale mixing induced by the streamwise vortices of lobed mixers. The first application of the lobe-type tailpipe in the aero-engine exhaust system can be traced back about 50 years [35]. Since then, lobed mixers have been used to enhance mixing between hot core gases and cold bypass air before exiting the nozzle, with a resulting increase in engine net thrust [7], a reduction in fuel consumption [36], a reduction in jet noise [8] and in some cases reduced infrared signature [37]. Several parameters determine the compromise between pressure losses, mixing performance and noise reduction in the lobed mixer design. These parameters include the number of lobes, lobe shape and length, lobe radial penetration angles, velocity ratio and turbulence intensity. A review of literature on flow structures, mixing mechanism and major parameters influencing lobed mixers performance are presented here.

Most of the fundamental research on lobed mixers has been carried out on two-dimensional planar corrugated lobes, as seen in Figure 2.8. Werle et al. [38] suggested that flow development in a planar lobed mixer followed a three-step process. First, large scale streamwise vortices arise due to the radially deflected flows from the lobes; the strength of which depends primarily on the lobe geometry [39]. The two counter-rotating streamwise vortices were reported to interact within a small distance downstream of the mixer trailing edge but remain the largest-scale flow structure for three to ten lobe wavelengths downstream [40]. Second, the streamwise and azimuthal vortices, generated due to the shear layer, interact in the wake of the lobes. In the third step, vortices break-down into small-scale turbulent structures, resulting in a significant increase in turbulent mixing and flow uniformity. Experimental observations of Eckerle et al. [41], as well as a computational and experimental study of Elliot et al. [42], supported the above hypothesis. Elliot et al. reported that mixing is enhanced mainly due to the increased interfacial area when the velocity ratio between the streams is close to unity. At higher velocity ratios, contributions of streamwise vortices to mixing become more pronounced than the interfacial area parameter. Flow visualization and hot-film measurements of McCormick and Bennett [43], pressure probe measurements of Yu et al. [44], and laser doppler velocimetry measurements of Yu et al. [45] documented that small-scale periodic vortex structures, known as normal vortices, shed from the lobe trailing edge due to the Kelvin–Helmholtz instability. Normal vortices are deformed by the streamwise vortices such that they eventually pinch-off and breakdown into small scale turbulent structures (Figure 2.9). The shear layer thickness at the lobed mixer trailing edge governs the initial scale of these vortices. McCormick and Bennett [43] also commented on the formation of horseshoe vortices at the leading edge of the lobes, with an insignificant impact on the mixing process. Based on the work of Belovich and Samimy [40], mixing processes downstream of a lobed mixer were concluded to be governed by three primary mechanisms:

- Generation of streamwise vortices due to the lobe geometry
- Increase in interfacial area between the two flow streams
- Small-scale structures occurring in free shear layer due to the Kelvin-Helmholtz

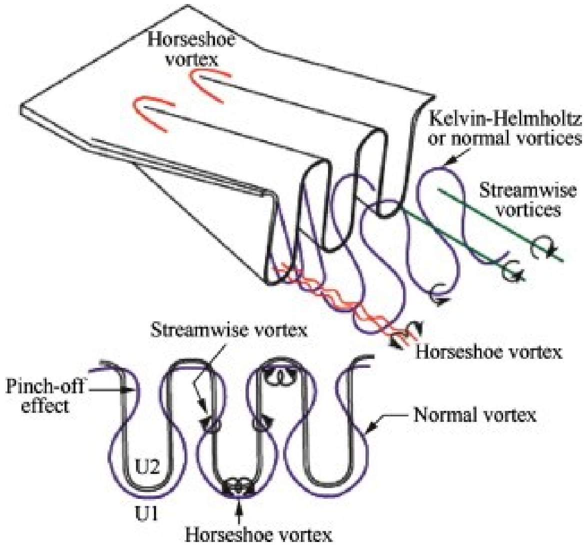

Figure 2.8: Schematic of lobed mixer free shear layer vortical structure [43].

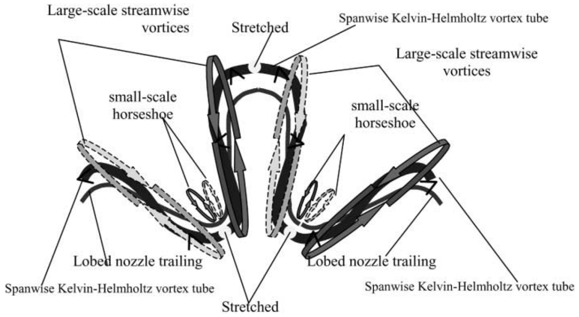
Large-scale streamwise vortices
Stretched
Spanwise Kelvin-Helmholtz vortex tube
Large-scale streamwise vortices
small-scale horseshoe
small-scale horseshoe
Lobed nozzle trailing
Lobed nozzle trailing
Spanwise Kelvin-Helmholtz vortex tube
Spanwise Kelvin-Helmholtz vortex tube
Stretched

Figure 2.9: Lobe mixer vortices and their interaction [46].

instability.

Beyond fundamental research, development of lobed mixers for full engine integration was mainly supported by the NASA Energy Efficient Engine (E3) program in the 1970s and the NASA Noise Reduction Program for Advanced Subsonic Transport in early 2000s. Considerable research has contributed to the understanding of mixing process between the high momentum core flow and the low momentum bypass flow downstream of lobed mixers [43, 42, 47, 48, 49, 50]. Several parameters were found to determine the compromise between pressure losses, mixing performance and noise reduction in the lobed mixer design. These parameters include the number of lobes, lobe shape and length, lobe radial penetration angles, velocity ratio and turbulence intensity. The strength of streamwise vorticity primarily depends on the lobe geometry, especially the penetration angle. Increasing lobe penetration enhances radial mixing and thus improves mixing effectiveness and performance [51]. However, increasing the penetration angle above 30° was reported to result in flow separation at the tip of the mixer lobes, causing a substantial loss in the strength of streamwise vorticity [48, 49].

One geometric modification that reduces the likelihood of boundary-layer separation at high penetration angles is a scalloped edge. Compared to un-scalloped lobed mixers, lobed mixers with scalloped lobes were reported to offer a significant increase in the mixing effectiveness, with essentially no detriment to total pressure loss [8]. Scalloping refers to the removal of a portion of the lobe's parallel sidewalls in the penetration regions of the mixer. Additional streamwise vortices were found to be formed downstream of the scallop, in the same direction as the main streamwise vortices [51]. Additional vortices were suggested to merge with the main streamwise vortices to form a vortex pair that is stronger than that of the un-scalloped mixer [52, 53]. The current author showed that this was not the case and that the additional vortices did not merge with the main streamwise vortices [54]. In the NASA Energy Efficient Engine program test models, a 12-lobe scalloped mixer provided the best trade-off between mixing effectiveness and pressure losses. It produced the highest specific fuel consumption improvement. In ejector systems, the scalloped lobed mixer also produced more thrust and less noise compared to un-scalloped mixers [51]. Yu et al. compared scalloped and un-scalloped planar mixers with the same penetration angle and trailing edge profiles [52, 55]. They showed that the streamwise vorticity was enhanced and its decay rate accelerated in un-scalloped mixers, largely because of the formation of two pairs of streamwise vortices at each lobe. They also reported lower losses for scalloped mixers compared with other configurations, possibly due to their lower wetted surface area within the penetration region. Introducing a deep scallop was also found to reduce mixer noise [56].

Skebe et al. [57] noted that parallel lobe sidewalls tend to produce higher secondary velocities and mix more efficiently than sinusoidally shaped lobes. Salman et al. [58] showed that the scarfed mixer introduced strong flow asymmetries in the azimuthal direction. This caused adjacent vortical structures produced by the alternating short and long gullies of the lobes to interact with each other resulting in slightly higher pressure loss.

Lei et al. [59] explored the effects of core flow swirl on the flow characteristics of a scalloped forced mixer. They showed that the overall streamwise circulation was not necessarily increased after scalloping. The more rapidly decaying streamwise vorticity presented a more effective mixing process because of smaller scale, but stronger, vortices. At low swirl angles, additional streamwise vortices were generated by the deformation of normal vortices due to the scalloped lobes. With core swirl greater than 10°, additional streamwise vortices were generated mainly due to radial velocity deflection rather than stretching and deformation of normal vortices. At high swirl angles, stronger streamwise vortices and rapid interaction between various vortices promoted downstream mixing. Mixing was enhanced with minimal pressure and thrust losses for the inlet swirl angle less than 10°. Wright et al. [54] examined the effects of scalloping on the mixing mechanism of lobed mixers when subjected to highly swirling core flow. They concluded that at high degrees of swirl, an additional vortex is generated in the lobe valley. High inlet swirl resulted in improved mixing but produced higher pressure and thrust losses that were comparable to the zero swirl case.

2.5 Similarity Laws in Lobed Mixers

Performance testing of full-scale lobed mixers at engine operating conditions on a test-stand is expensive and difficult. Accurate performance results and detail flow measurements require specialized and rare equipment. Attempts have been made to test scaled models of lobed mixers at affordable low-speed, isothermal or moderately high core flow temperature conditions for performance. It will be shown in Chapter 5 that the low-speed approach is in violation of similarity laws and the results cannot be used for design validation. Tew et al. [60] examined the effects of compressibility on mixing downstream of a lobe mixer. Their experimental results showed that reduced shear growth rates at higher Mach number give the streamwise vorticity more time to stretch the interface between the two streams. Hence, streamwise vorticity is more effective in the compressible regime than incompressible. Since the vorticity is generated by the interaction of lobe trailing-edge shocks and density gradient across the mixing layer, this vorticity generation may either enhance or reduce the mixing rate depending on the density gradient between the streams. In another study, Waitz et al. [50] measured the exit temperature downstream of a two-dimensional ejector with varying temperature and inlet Mach number. They showed that thermal mixing was completed about five wavelengths downstream of the ejector's throat at low Mach numbers. Thermal mixing was completed at 16 wavelengths at high Mach numbers. Presz and Greitzer [61] used the approximate Munk and Prim similarity principle to show that lobe mixer performance parameters are similar for both full-scale isothermal hot flow and cold flow model tests if the initial Mach numbers and inlet stagnation pressure distributions are simulated. Head et al. [62] compared the test results for a series of 10-percent-scale turbofan lobed mixers from two NASA facilities. Lobe mixers varied in the number of lobes, scallops, lobe penetration depth, the gap between the lobe valley and centrebody and radial wall shape. The two test facilities varied in temperature ratio; 2.5 and 1.35. All parameters kept constant, varying the nozzle pressure ratio at constant temperature ratio had essentially no effect on the nozzle exit temperature profile. By matching the speed of sound at the nozzle exit, Long [63] demonstrated that a helium/air mixture could simulate the essential features of noise radiation of cruise condition hot exhaust in a scaled-down turbofan engine model. The same conditions cannot be simulated in a low-speed environment.

This understanding of the fundamentals of fluid jet mixing as well as the history of the development of the lobed mixer shall serve as the groundwork upon which the analyses presented in this thesis are built. The experiments designed to solve the problem presented for this project drew inspiration from this collection of literature. Upon solution of that problem—reducing the mass of medium bypass turbofan engine exhaust systems—the work continued to fill the aforementioned gap in the literature regarding the relation between temperature and momentum mixing rates downstream of lobed mixers rather than confluent nozzles.

Chapter 3

Computational Set-Up and Procedures

This chapter documents the computational set up, procedures and methodology used to perform the simulations of this investigation. Section 3.1 will provide a brief description of the hardware and software. Section 3.2 will outline the fundamental mathematics governing the simulations.

3.1 Hardware and Software

The simulations were run on a custom-built workstation. The processor was an Intel i7 processor running at a clock speed of 4.1 GHz; the memory was 64 GB of DDR4 RAM running at 2133 MHz; the graphics card was an nVidia GTX 750 Ti with 4 GB of GDDR5 VRAM and a clock speed of 1.06 GHz.

Specialized software was used at many points in the modeling process. The solid models were created using PTC Creo Parametric v4.00. Those models were then meshed using Numeca Hexpress v7.2. After meshing, the fluid flow was simulated via Numeca FINE/Open v7.2, a “multi-purpose unstructured code for 2D and 3D flows in complex geometries”. The simulation data was then visualized and interpreted with the use of Numeca CFView v7.2 as well as Paraview v5.7.4. Data was further reduced using specialized data reduction scripts written in Python v3.6. Each of these software was provided on an academic research based license or, in the case of Paraview and Python, open source licenses.

3.2 Governing Equations

The flow of fluids is governed by the laws of conservation of mass, conservation of energy and balance of momentum. The Navier-Stokes equations combine these governing equations and can be described in their derivative form as:

$$\frac{\partial}{\partial t}\vec{U} + \nabla\vec{F_I} + \nabla\vec{F_V} = \vec{Q} \tag{3.1}$$

$\vec{U}$ is the vector of conservative variables:

$$U = \begin{pmatrix} \rho \\ \rho\vec{v} \\ \rho E \end{pmatrix} \tag{3.2}$$

$\vec{F_I}$ and $\vec{F_V}$ are the inviscid and viscous flux vectors:

$$F_{Ili} = \begin{bmatrix} \rho v_i \\ \rho v_x v_i + p\delta_{xi} \\ \rho v_y v_i + p\delta_{yi} \\ \rho v_z v_i + p\delta_{zi} \\ (\rho E + p)v_i \end{bmatrix} \tag{3.3}$$

$$-F_{Vi} = \begin{bmatrix} 0 \\ \tau_{ix} \\ \tau_{iy} \\ \tau_{iz} \\ q_i + v_j\tau_{ij} \end{bmatrix} \tag{3.4}$$

The shear stress is given by:

$$\tau_{ij} = (\mu + \mu_t)\left[\frac{\partial\overline{v}_i}{\partial x_j} + \frac{\partial\overline{v}_j}{\partial x_i} - \frac{2}{3}(\nabla\vec{\omega})\delta_{ij}\right] \tag{3.5}$$

The heat flux is:

$$q_i = (\kappa + \kappa_t)\frac{\partial}{\partial x_i}\tilde{T} \tag{3.6}$$

The total energy, E, is given by:

$$E = e + \frac{1}{2}\tilde{\omega}_i\tilde{\omega}_i \tag{3.7}$$

Q contains the source terms:

$$Q = \begin{bmatrix} 0 \\ \rho\vec{f_e} \\ W_f \end{bmatrix} \tag{3.8}$$

where $\rho\vec{f_e}$ describes the effects of external forces and W_f describes the work of those forces.

Reynolds Averaged Navier-Stokes Equations

The Navier-Stokes equations describe both laminar and turbulent flow. Turbulence is a non-linear phenomenon with a wide range in time and spatial scale. As a result, direct simulation of turbulent flow is computationally costly and therefore not suited to most applications of engineering. It is possible to ease this computational demand by splitting the flow field into a mean and fluctuating partition. This produces the Reynolds Averaged Navier-Stokes (RANS) equations. The density and pressure are time averaged:

$$q = \overline{q} + q' \tag{3.9}$$

where $\overline{q}$ is the time averaged value and q' contains the fluctuating values. The energy, temperature and velocity components are density-weighted averages as described by:

$$\tilde{q} = \frac{\overline{\rho q}}{\overline{\rho}} \tag{3.10}$$

The RANS equations describe turbulent flow but at the expense of introducing six new variables to the system of equations. These new variables are known as the Reynolds stresses and require the use of an empirically developed turbulence model to achieve closure of the system.

3.3 Fluid Model

The simulations in this investigation used the “air as a perfect gas” fluid model. This model allows for density changes important to compressible simulation.

3.4 Turbulence Modeling

Turbulence models for RANS solvers provide closure to the system of equations by solving for the Reynolds stress variables. These models combine understanding of the flow physics and some degree of empirical tuning. Models are selected based on the experience of the user and the type of flow to be simulated. These decisions are informed by desired accuracy and computational cost. All turbulence models in FINE/Open begin with a first-order closure model base on the Boussinesq assumption—which introduces the concept of eddy viscosity and considers a linear connection between the Reynolds-stress tensor and the mean flow strain.

$$-\overline{(\rho\vec{v}\otimes\vec{v})} = \mu_t\left[2\overline{\overline{S}} - \frac{2}{3}\left(\vec{\nabla}\cdot\vec{\tilde{v}}\right)I\right] - \frac{2}{3}\overline{\rho}kI \tag{3.11}$$

where $-\overline{(\rho\vec{v}\otimes\vec{v})}$ is the Reynolds stress tensor. This expression contains all of the effects of turbulence on the averaged momentum conservation and appears as a result of the Reynolds averaging on the momentum and energy equations. $\overline{\overline{S}}$ is the mean stress tensor and μ_t is the turbulent eddy viscosity.

$$\overline{\overline{S}} = \frac{1}{2}\left(\vec{\nabla}\otimes\vec{\tilde{v}} + \left(\vec{\nabla}\otimes\vec{\tilde{v}}\right)^T\right) \tag{3.12}$$

k is the turbulent kinetic energy.

$$\overline{\rho}k = \overline{\rho\frac{|\vec{v}|^2}{2}} \tag{3.13}$$

Turbulent heat flux also needs to be modeled to solve the flow. The Prandtl number, Pr_t, connects the eddy viscosity, μ_t, to the thermal conductivity, κ_t:

$$\overline{\rho h''\vec{v}} = -\kappa_t\vec{\nabla}T \tag{3.14}$$

where

$$\kappa_t = \frac{\mu_t c_p}{\mathrm{Pr}_t} \tag{3.15}$$

The RANS equations return to the original Navier-Stokes system of equations after the Boussinesq assumption except that dynamic viscosity, μ, is replaced by $\mu + \mu_t$ and thermal conductivity, κ, is replaced by $\kappa + \kappa_t$. The static pressure, $\overline{P_s}$ is modified by adding the last term in the mean flow strain correlation and the averaged total energy, $\overline{E}$, also contains the turbulent kinetic energy term, k.

$$\bar{\tilde{\tau}}_T = (\mu + \mu_t)\left[2\overline{\overline{S}} - \frac{2}{3}\left(\vec{\nabla} \cdot \vec{\tilde{v}}\right) I\right] \tag{3.16}$$

$$\vec{\bar{q}}_T = -\left(\kappa + \kappa_t\right) \vec{\nabla} T \tag{3.17}$$

$$\overline{P_s}^* = \overline{P_s} + \frac{2}{3}\overline{\rho} k \tag{3.18}$$

$$\overline{E} = \overline{e} + \overline{\rho}\frac{|\vec{\overline{v}}|^2}{2} + k \tag{3.19}$$

Turbulence Model Order

The most widely used turbulence models calculate the Reynolds stresses as a linear function of shear stress. Other more computationally expensive models use non-linear relationships to calculate the Reynolds stresses but will not be expanded on since they were not considered for this application. The linear models in question can be categorized as zero-, one- or two- equation models.

Zero-equation models are also known as algebraic models. They are robust and computationally inexpensive because they are based solely on the gradients of local flow properties. Accuracy is sacrificed for their simplicity, so they are best used as a starting point.

One-equation models solve one turbulent transport equation and are more accurate than zero-equation models. Spalart-Allmaras is an example of such a model. This model does not directly involve the turbulent kinetic energy, k, so its contribution is neglected and static pressure and energy are not modified as expected for Equations 3.18 and 3.19.

Two-equation models are more accurate than zero- and one-equation models and more popular as a result. As expected by their name, these models solve two turbulent transport equations. Most models will solve for the turbulent kinetic energy, k, with one of the equations; while the second equation will solve for turbulent dissipation, ϵ, as in the case of aptly named $k - \epsilon$ models, or the specific dissipation, ω, in the $k - \omega$ models. Each of these base two-equation models have several versions that feature minor modifications to alter their accuracy in certain flow regimes. A study was conducted to determine the most appropriate turbulence model for the investigation outlined in this thesis. Three models were compared: the one-equation model Spalart-Allmaras, the two-equation model Yang-Shih $k-\epsilon$ and the two-equation model $k-\omega$ Shear Stress Transport (SST). These models were chosen based on their availability in FINE/Open and suggestions from my supervisor. The conclusion of that study was that the SST model was best suited to this application [64].

k-ω (M-SST) Turbulence Model

This model was developed by Menter in 1994 to overcome the shortcomings of the k-ω model. According to the FINE/Open Theory manual, the worst shortcoming of these models is their extreme sensitivity to the small free stream value of ω in the free-shear and adverse-pressure-gradient boundary flows. To overcome these shortcomings, Menter devised a method to combine the k-ω and k-ϵ two-equation models through a blending function. In order to blend these models, the k-ϵ model is reformulated into a k-ω expression. The blending function F_1, Equation 3.27, is used to weight the original k-ω model while $1 - F_1$ is used to weight the transformed k-ϵ; the result is then summed to produce the new model.

$$\phi = F_1\phi_1 + (1 - F_1)\phi_2 \tag{3.20}$$

The turbulent kinematic viscosity, ν_t, is defined as a limited function of the turbulent kinetic energy, k, and the specific dissipation rate of the turbulent frequency, *omega*:

$$\nu_t = \min\left(\frac{\alpha_1 k}{\max\left(\alpha_1\omega_1\sqrt{2}SF_2\right)}; 5000\nu\right) \tag{3.21}$$

The two equations of the M-SST turbulence model are:

$$\frac{\partial k}{\partial t} + u_j\frac{\partial k}{\partial x_j} = P_k - \beta^* k\omega + \frac{\partial}{\partial x_j}\left[\left(\nu + \frac{\nu_t}{\sigma_k}\right)\frac{\partial k}{\partial x_j}\right] \tag{3.22}$$

and

$$\frac{\partial \omega}{\partial t} + u_j\frac{\partial \omega}{\partial x_j} = \frac{\Upsilon}{\nu_t} - \beta\omega^2 + \frac{\partial}{\partial x_j}\left[\left(\nu + \frac{\nu_t}{\sigma_\omega}\right)\frac{\partial \omega}{\partial x_j}\right] + (1 - F_1)\, 2\frac{\rho\sigma_{\omega_2}}{\omega}\frac{\partial k}{\partial x_j}\frac{\partial \omega}{\partial x_j} \tag{3.23}$$

where the eddy viscosity, production and shear terms are defined:

$$S = \sqrt{s_{ij}s_{ij}} \text{ with } s_{ij} = \frac{1}{2}\left(\frac{\partial u_i}{\partial x_j} + \frac{\partial u_j}{\partial x_i}\right) \tag{3.24}$$

$$P_k = \min\left(\tau_{ij}\frac{\partial u_i}{\partial x_j}, 20\beta * \rho\omega k\right) \tag{3.25}$$

$$\tau_{ij} = \mu_t\left(2S_{ij} - \frac{2}{3}\frac{\partial u_k}{\partial x_k}\delta_{ij}\right) - \frac{2}{3}\rho k\delta_{ij} \tag{3.26}$$

$$F_1 = \tanh\left[\left(\min\left[\max\left(\frac{\sqrt{k}}{\beta^*\omega d}, \frac{500\nu}{d^2\Omega}\right), \frac{4\sigma_{\omega^2}k}{CD_{k\omega}d^2}\right]\right)^4\right] \tag{3.27}$$

and

$$CD_{k\omega} = \max\left(\frac{2\rho\sigma_{\omega 2}}{\omega}\frac{\partial k}{\partial x_j}\frac{\partial \omega}{\partial x_j}, 10^{-10}\right) \tag{3.28}$$

$$F_2 = \tanh\left[\max\left(2\frac{\sqrt{k}}{\beta^*\omega d}, \frac{500\nu}{d^2\omega}\right)\right] \tag{3.29}$$

The standard coefficients for k and ω by Menter (1994):

$$\sigma_{\kappa 1} = 1.176,\ \sigma_{\omega 1} = 2,\ \gamma_1 = 0.5532,\ \beta_1 = 0.075,\ \beta^* = 0.09$$
$$\sigma_{\kappa 2} = 1.0,\ \sigma_{\omega 2} = 1.168,\ \gamma_2 = 0.4403,\ \beta_2 = 0.0828,\ a_1 = 0.31$$

3.5 Boundary Conditions

Figure 3.1 indicates the locations of each boundary type. These boundaries were set to provide numerical stability to the simulation.

3.5.1 Incompressible Boundary Conditions

The boundary conditions specified for the low-speed, incompressible simulations were as follows:

- Inlets
  - Core and Bypass: these subsonic boundary conditions had an explicit mass flow imposed, along with the velocity vector direction. The direction was specified in terms of $v_x/|\vec{v}| = 0$, $v_y/|\vec{v}| = 0$ and $v_z/|\vec{v}| = 1$.
  - Free Stream: this subsonic boundary condition had the total quantities of pressure and temperature imposed. The velocity direction was defined to be normal to the inlet and the magnitude of the absolute velocity was extrapolated from the interior field such that, $\vec{v_0}/|\vec{v_1}| = -\vec{n}$. $\vec{v_0}$ represents

the absolute velocity at the inlet; $|\vec{v_1}|$ is the velocity norm inside the domain and $\vec{n}$ is the normal vector.

- Outlet

  - An average static pressure was imposed at the outlet boundary. The interior field was extrapolated onto the boundary and translated such that the computed average matched that which was specified in the simulation set up.

- Walls

  - The test section walls were adiabatic with conditions such that the velocity vector at the boundary was $\vec{v_w} = 0$. The temperature and pressure at the wall were set such that the gradient between the boundary and the interior of the domain was equal to zero: $p_w = p_1$ and $T_w = T_1$.

  - For the far-field wall condition, the velocity must be tangential to the wall such that the wall velocity equaled the velocity of the nearest cell. The pressure and density were obtained via zero order extrapolation as well, $p_w = p_1$ and $T_w = T_1$.

3.5.2 Compressible Boundary Conditions

The boundary conditions for the high-speed, compressible simulations were similar to those of the incompressible simulations except that all three inlet boundaries were defined with total quantities of pressure and temperature imposed, like the free stream inlet of the incompressible simulation.

Specific details on the boundary conditions are provided in Chapter 5.

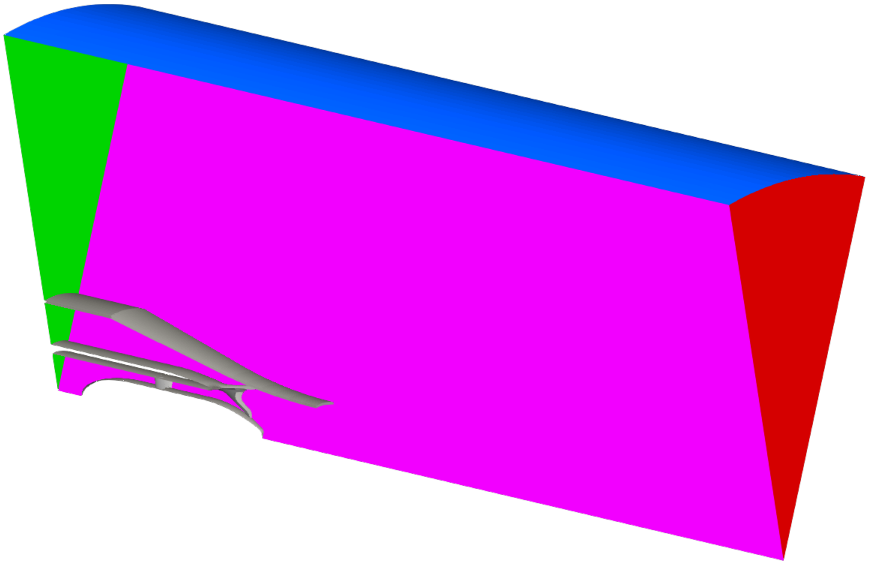

Figure 3.1: Boundary conditions for the simulations. Inlet: Green, Outlet: Red, Periodic: Pink, Solid: Gray, Full-slip solid: Black

3.6 Discretization

Space

Spatial discretization in FINE/Open is based on a cell centered finite volume approach. This can be formulated in the discrete form as:

$$\int_{\Omega} \frac{\partial u}{\partial t} \mathrm{d}\Omega + \sum_{S} \vec{F_I} \vec{\Delta S} + \sum_{S} \vec{F_V} \vec{\Delta S} = \int_{V} Q \mathrm{d}V \tag{3.30}$$

where Ω represents the control volumes, S represents the surface of the volume and F_V and F_I represent the viscous (diffusive) and inviscid (convective) fluxes respectively.

The viscous fluxes are determined centrally and the gradients must be evaluated on the cell faces; this is done via the application of Gauss' theorem:

$$\vec{\nabla}\Phi = \frac{1}{\Omega} \int \vec{\nabla} Q \mathrm{d}\Omega = \frac{1}{\Omega} \int Q \mathrm{d}\vec{S} \tag{3.31}$$

A diamond shaped control volume is formed by the face and the points created by the neighbouring cell centres, as shown in Figure 3.2.

The inviscid numerical flux across the face k bounded by two cells is expressed as:

$$\left(\vec{F}^{*} \cdot \vec{n}\right)_k = \frac{1}{2}\left(\left(\vec{F} \cdot \vec{n}\right)_L + \left(\vec{F} \cdot \vec{n}\right)_R\right) - \frac{1}{2} d_k \tag{3.32}$$

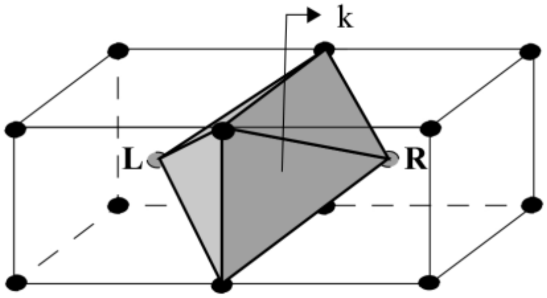

Figure 3.2: Diamond control volume approach for gradient computation on faces [65].

where d_k is known as the numerical dissipation term. This study uses a central difference scheme for inviscid fluxes and so d_k is an artificial dissipation. Or, an alternative formulation can be used based on the averaged unknowns:

$$\left(\vec{F}^{*} \cdot \vec{n}\right)_k = \vec{F}\left(\frac{U_L + U_R}{2}\right) \cdot \vec{n} - \frac{1}{2} d_k \tag{3.33}$$

FINE/Open uses these alternative formulae in different circumstances. Flux averaging is used for internal faces and solution averaging is used for boundary faces.

The numerical dissipation term, d_k, was defined based on the formulation by Jameson, Schmidt and Turkel (1981):

$$d_k = \epsilon_k^{(2)} \delta U_k + \epsilon_R^{(4)} \delta^2 U_R - \epsilon_L^{(4)} \delta^2 U_L \tag{3.34}$$

This is a blend of second and fourth order differences of the conservative variables where scalar coefficients are given as:

$$\epsilon_k^{(2)} = \kappa^{(2)} \lambda_k^{*} \max\left(\nu_L, \nu_R\right) \tag{3.35}$$

$$\epsilon_k^{(4)} = -\max\left(0, \kappa^{(4)} \lambda_k^{*} - \epsilon_k^{(2)}\right) \tag{3.36}$$

The coefficients $\kappa^{(2)}$ and $\kappa^{(4)}$ are user defined parameters of artificial diffusion set within FINE/Open as 1.0 and 0.1 respectively.

Time

A multi-grid accelerated Runge-Kutta scheme is used to perform a pseudo-time integration in the FINE/Open solver. This allows for the desired steady-state solution to be achieved by calculating the unsteady form of the RANS equations. Marching through time allows for a spatially-accurate approximation of the steady-state solution. An explicit q-stage Runge-Kutta scheme is applied to

$$\frac{\mathrm{d}F}{\mathrm{d}t} = F(U) \tag{3.37}$$

and can be written

$$\begin{aligned} U^1 &= U^n + \alpha_1 \Delta t F(U^n) \\ U^2 &= U^n + \alpha_2 \Delta t F(U^1) \\ &\cdots \\ U^q &= U^n + \Delta t F(U^{q-1}) \\ U^{n-1} &= U^q \end{aligned} \tag{3.38}$$

where α_q are coefficients used to determine the stability and order of accuracy of the Runge-Kutta scheme. For the 4-stage central scheme—as used in this study—they are specified as:

$$\begin{aligned} \alpha_1 &= 0.125 \\ \alpha_2 &= 0.306 \\ \alpha_3 &= 0.587 \\ \alpha_4 &= 1.0 \end{aligned} \tag{3.39}$$

The local time step for inviscid calculations is then given as:

$$\left(\frac{\Delta t}{\Omega}\right)_I = \frac{\mathrm{CFL}}{\begin{array}{r} \left|\vec{v}\cdot\Delta\vec{S}_\xi\right| + \left|\vec{v}\cdot\Delta\vec{S}_\eta\right| + \left|\vec{v}\cdot\Delta\vec{S}_\zeta\right| \\ + c\cdot\left(\left|\Delta\vec{S}_\xi\right| + \left|\Delta\vec{S}_\eta\right| + \left|\Delta\vec{S}_\zeta\right|\right) \end{array}} \tag{3.40}$$

where Ω is the cell volume, $\vec{v}$ is the velocity and c is the speed of sound in the cell. The CFL is the Courant-Friedrichs-Lewy number—the non-dimensional time-step, or the time it takes for a virtual particle to travel one cell width. Finally, the $\vec{S}$ terms correspond to the cell normals. The local time step for viscous calculations:

$$\left(\frac{\Delta t}{\Omega}\right)_V = \frac{\mathrm{CFL}\rho\Omega}{\left[8\mu_{\mathrm{eff}}\left[\begin{array}{l} \left|\Delta\vec{S}_\xi\right|^2 + \left|\Delta\vec{S}_\eta\right|^2 + \left|\Delta\vec{S}_\zeta\right|^2 \\ \quad + 2\left(\left|\Delta\vec{S}_\xi\cdot\Delta\vec{S}_\eta\right| + \left|\Delta\vec{S}_\xi\cdot\Delta\vec{S}_\zeta\right| + \left|\Delta\vec{S}_\eta\cdot\Delta\vec{S}_\zeta\right|\right) \end{array}\right]\right]} \tag{3.41}$$

where μ_{eff} is the effective viscosity and ρ is the density in the cell where the time step is evaluated. When viscous flows are simulated, FINE/Open uses a “harmonic-like” mean of the inviscid and viscous local time steps:

$$\left(\frac{\Delta t}{\Omega}\right) = \frac{\left(\frac{\Delta t}{\Omega}\right)_I \left(\frac{\Delta t}{\Omega}\right)_V}{\left(\frac{\Delta t}{\Omega}\right)_V + \left(\frac{\Delta t}{\Omega}\right)_I} \tag{3.42}$$

The CFL is defined by the user. A larger CFL can accelerate solution convergence at the cost of stability. All results presented were run with CFL of 3. A simulation campaign was performed to determine the appropriate CFL number to balance simulation stability and time-to-convergence.

Multigrid Strategy

This study uses a Full Multigrid solution strategy. In this strategy, the simulation will be solved to a certain accuracy on the coarsest grid first. Upon satisfying the accuracy requirements specified, the solution of the coarser grid is then interpolated onto the finer grid as its initial condition. The process continues until the finest grid is solved. For this study, 4 levels of multigrid coarseness were used to accelerate the propagation of boundary conditions throughout the domain.

Low Reynolds Number Treatment

The low speed simulations of this investigation used the preconditioning method developed by Hakimi in 1997. This preconditioning scheme is quite general and can be applied to any type of fluid including the air as a perfect gas model. The Preconditioned RANS equations are:

$$\int_\Omega \Gamma^{-1}\frac{\partial Q}{\partial t}\mathrm{d}\Omega + \int_S \vec{F}\cdot\vec{S} = \int_\Omega S_T \mathrm{d}\Omega \tag{3.43}$$

and

$$\Gamma^{-1} = \begin{bmatrix} \frac{1}{\beta^2} & 0 & 0 & 0 & 0 & 0 & 0 & 0 & \cdots & 0 \\ \frac{(1+\alpha)\mathrm{u}}{\beta^2} & \rho & 0 & 0 & 0 & 0 & 0 & 0 & \cdots & 0 \\ \frac{(1+\alpha)\mathrm{v}}{\beta^2} & 0 & \rho & 0 & 0 & 0 & 0 & 0 & \cdots & 0 \\ \frac{(1+\alpha)\mathrm{w}}{\beta^2} & 0 & 0 & \rho & 0 & 0 & 0 & 0 & \cdots & 0 \\ \frac{\alpha\vec{\mathrm{v}}^2+\mathrm{E_g}}{\beta^2}(-1)^* & 0 & 0 & 0 & \rho & 0 & 0 & 0 & \cdots & 0 \\ 0 & 0 & 0 & 0 & 0 & 1 & 0 & 0 & \cdots & 0 \\ 0 & 0 & 0 & 0 & 0 & 0 & 1 & 0 & \cdots & 0 \end{bmatrix} \tag{3.44}$$

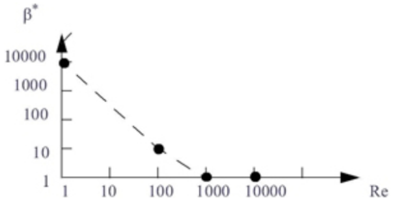

Figure 3.3: Typical variation of the preconditioning parameter, β^*, with Reynolds number [65].

The preconditioning parameter β is imposed by defining the coefficient β^* and characteristic velocity V_{ref} such that:

$$\beta^2 = \beta^* V_{\text{ref}}^2 \tag{3.45}$$

The value of β^* used in this investigation is 3, the default. This value was chosen based on a desire for numerical stability at the beginning of the simulations. β^* values are correlated to the Reynolds number of the flow according to Figure 3.3. The flows investigated have average Reynolds numbers above 1000, at which point $\beta^* = 1$ is accepted. However, certain local areas with low flow velocities will have Reynolds numbers below this threshold and therefore a slightly larger value of β^* is desired for stability. It is important to avoid arbitrarily increasing the value of β^* as high values will introduce excessive artificial dissipation.

Chapter 4

Data Reduction and Simulation Validation Studies

This chapter will outline how the data obtained from the computational simulations has been reduced from raw data to understandable units and the validity of said data. The first sections will discuss the manipulation of the data and how it will be used to determine conclusions about exhaust system design performance. The chapter will then progress to illustrate evidence that the simulations performed are in fact worth examining and can be confidently assumed to reflect the real world. Mesh and iterative convergence studies will be presented, followed by an uncertainty analysis. The uncertainty analysis will provide a measure of accuracy to the results of the simulations. This is a necessary step to prove the confidence of the simulations.

4.1 Data Reduction Methods

The data produced via FINE/Open simulation were reduced using a combination of Python 2.7 scripting language and proprietary commands related to the Numeca post-processing program CFView v12.2. The code for these routines will be provided in Appendix A.

4.1.1 Equations of Interest

FINE/Open is able to output several useful data points at each node of the computational mesh. These data include velocity, vorticity, total pressure, static pressure, total temperature, Mach number, density and more. This information is helpful when analyzing a single simulation to assess the flow fields and performance in isolation. This study will present many simulations and so requires the data to be prepared for comparison. Two reference planes have been indicated downstream of the swirling vanes and upstream of the mixer and any deswirling hardware: one plane in the core and one plane in the bypass, indicated in Figure 4.1. Averaged values of velocity, total pressure, static pressure and dynamic pressure from these planes were

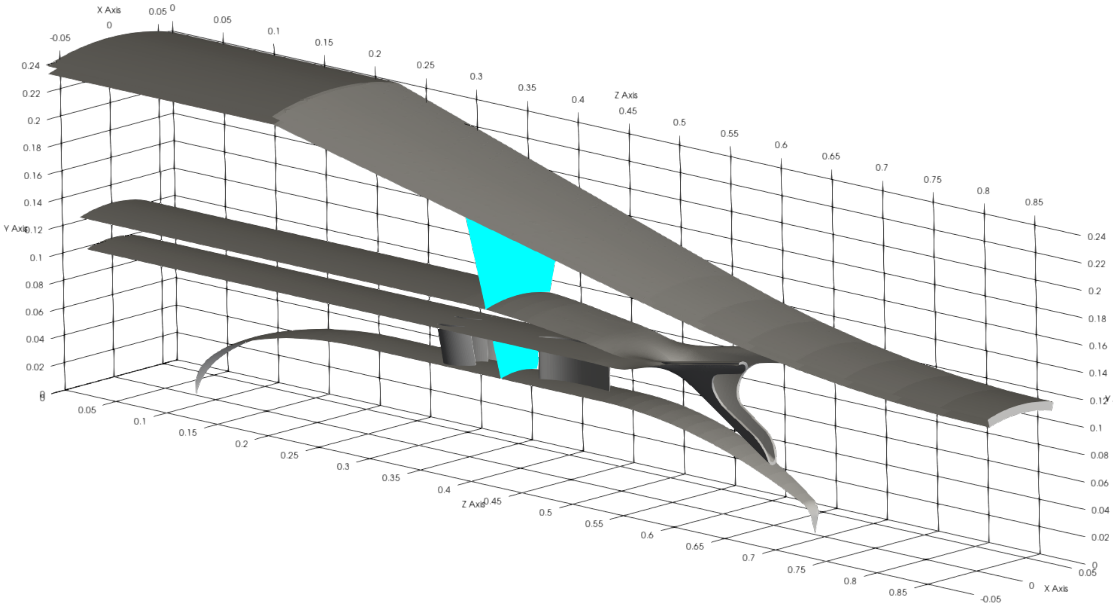

Figure 4.1: Reference planes highlighted within the domain.

used to normalize performance parameters and allow for clearer comparison between simulations.

Normalized Velocity

$$\overline{\vec{V}} = \frac{\vec{V}}{\overline{V_{z_{ic}}}} \tag{4.1}$$

Normalized Velocity is a simple way of comparing flow fields between each case. It is calculated via the division of the Velocity vector by the mass-averaged axial velocity component at the core reference plane. A similar factor is the velocity coefficient which is defined with the axial component of the velocity vector in the numerator: $CV = \frac{V_z}{\overline{V_{z_{ic}}}}$.

Vorticity Coefficients

$$C_{\omega s} = \frac{\omega_z \mathrm{D_h}}{\overline{V_{zi}}} \tag{4.2}$$

$$C_{\omega a} = \frac{\sqrt{\omega_r^2 + \omega_\theta^2}\,\mathrm{D_h}}{\overline{V_{zi}}} \tag{4.3}$$

Vorticity is the curl of the velocity vector field. The magnitude of vorticity describes the strength of vortex cores, or vortices, within the flow field. The streamwise vorticity is considered to be equal to the axial vorticity—the vector for which the magnitude points along the z-axis—while the azimuthal vorticity is the sum of radial and tangential components of the vector field. The units of vorticity are s^{-1}, so the magnitudes of vorticity are normalized by the core reference velocity and the characteristic length of the system, achieving a non-dimensional coefficient of vortex strength that can be directly compared between each case. The characteristic length in this case is measured as the equivalent diameter, D_h, of the lobed mixer. The magnitude of the coefficient indicates the strength of the vortex, while the sign of the measurement indicates the direction of rotation.

Swirl Angle

$$\Theta = \tan^{-1}\left(\frac{V_\theta}{V_z}\right) \tag{4.4}$$

Some basic trigonometry is used to determine the swirl at a given point in the flow field. The swirl angle is used to measure how much flow turning is produced by each hardware component. Thrust is directly proportional to the amount of swirl in the flow.

Circulation

$$\Gamma = \iint \vec{\omega} \cdot \vec{n} \mathrm{dA} \tag{4.5}$$

Circulation is the amount of force that is acting on a fluid element along a closed path. According to Stokes' theorem, circulation is an indication of the overall strength of vorticity in a region. In the case of a lobed mixer, the clockwise streamwise circulation is calculated along the closed path covering the right half of each lobe (looking upstream), and vice versa for the counterclockwise circulation. For non-swirling flow, the circulation in both directions should be equal and decay at similar rates. Flows with swirl will have asymmetrical circulation. Circulation decays along with the vorticity strength.

Pressure Coefficients

$$Y = \frac{\left(\overline{P_{0i}} - \overline{P_0}\right)}{\left(\overline{P_{0i}} - \overline{P_{si}}\right)} \tag{4.6}$$

$$C_{Ps} = \frac{\left(P_s - \overline{P_{si}}\right)}{\left(\overline{P_{0i}} - \overline{P_{si}}\right)} \tag{4.7}$$

$$C_{Ps} = \frac{\left(P_0 - \overline{P_{si}}\right)}{\left(\overline{P_{0i}} - \overline{P_{si}}\right)} \tag{4.8}$$

The total pressure loss coefficient provides a quantitative value to compare the efficiency of each case.

The static and total pressure coefficients provide the ability to make qualitative comparisons of the flow fields between each case.

Mixing Index

$$I_P = \sqrt{\frac{\iint \rho V_z \overline{\phi}^2 \mathrm{dA}}{\iint \rho V_z \mathrm{dA}}} \tag{4.9}$$

The mixing index is a dimensionless parameter that characterizes the mixing between the core and bypass streams and thus compare the mixing performance of each case. Each parameter is defined as $\phi = \left(X - \overline{X_m}\right) / \left(\overline{X_i} - \overline{X_m}\right)$, where X is any scalar parameter of the flow, the subscript m refers to the plane of measurement. The factor reduces to zero for fully uniform flow where the point values of the scalar are identical to the average value at the measurement plane.

Turbulent Kinetic Energy

$$\mathrm{TKE} = \frac{\sqrt{k}}{\overline{V_{zi}}} \tag{4.10}$$

Turbulent Kinetic Energy is generated where large scale flow structures break down into smaller scale turbulent flow. That breakdown is important to local mixing rates. These regions and the sources of those interactions can be identified by observing regions of increased TKE in the flow field.

Thrust

$$T = \dot{m}\overline{V_z} + (P_s - P_\infty)A_n \tag{4.11}$$

$$C_T = \frac{T_n}{T_c + T_b} \tag{4.12}$$

The most important performance parameter of a jet engine exhaust system is the thrust. This thrust coefficient is calculated in such a way to also serve as an indicator into the performance of the lobed mixer across each case. The thrust calculated at the nozzle outlet is normalized by the sum of expected thrusts measured based on flow conditions at the upstream reference plane, $Z = -1.02$, in the core and bypass streams. This indicates the effectiveness of the mixer and any deswirling hardware found in the flow. Normalizing based on the upstream values means that despite each case having different hardware in the flow, no individual case is penalized because of extra hardware impeding the flow.

These parameters will provide the necessary information to draw conclusions about the performance and flow physics of each case included in this study.

4.2 Computational Simulation Validation

CFD is inherently uncertain when presented in isolation. CFD simulations must be subject to a general and rigorous validation procedure. There are many choices to make when setting up a CFD simulation: the discretization scheme, the mesh density, how many iterations to run, initial conditions, boundary conditions, etc.,. Many of these choices have been outlined in Chapter 3, Computational Set-Up and Procedures. This section will outline the process of the Mesh Independence and Iterative Convergence studies used to validate the simulation and determine the uncertainty for each parameter investigated.

4.2.1 Uncertainty Analysis

A Richardson Extrapolation based technique called the Grid Convergence Index [GCI] as explained by Roache [66] was used to determine a confidence interval for each result parameter presented in this thesis. The GCI is used to ‘uniformly report grid-convergence tests’. A great feature of the Richardson Extrapolation is that it applies to both point-by-point solution values as well as solution calculations such as thrust coefficient.

The procedure for calculating the GCI is outlined by Roache [67] and summarized for unstructured simulations as follows:

- Multiple meshes are generated with cell counts of N_1 and N_2 referring to the fine and coarse meshes, respectively.
- An effective refinement ratio is calculated based on the equation:

  $$r_{\text{effective}} = \left(\frac{N_1}{N_2}\right)^{\frac{1}{D}} \tag{4.13}$$

  where D is the dimensionality of the simulations, 3.
- The fine grid solution error is calculated as:

  $$\epsilon = \frac{f_2 - f_1}{f_1} \tag{4.14}$$

  where f refers to the corresponding grid solution value.
- Finally, the GCI is calculated using the formula

  $$\text{GCI} = \frac{3|\epsilon|}{r^p_{\text{effective}} - 1} \tag{4.15}$$

  with p corresponding to the order of the discretization method used, 2.

The GCI method for quantifying uncertainty of CFD simulations allows for a conservative and consistent report of solution precision. CFD precision is often inconsistently reported if reported at all.

GCI values are reported for relevant solution values in the following sections of this document.

4.2.2 Mesh Independence

Three meshes were generated and solutions converged for the mesh independence study. Their cell counts are listed in Table 4.1 and representative samples are shown in Figures 4.2, 4.3 and 4.4.

Figures 4.5, 4.6 and 4.7 present pitchwise average values of Total Pressure Coefficient, Static Pressure Coefficient and Axial Velocity respectively at six planes between the lobed mixer exit plane, $Z = 0.000$, and the nozzle exit plane, $Z = 1.000$. While, finally, Tables 4.2 and 4.3 present tabulated errors between mesh densities of Nozzle Pressure Loss, Y, and Nozzle Thrust, T_N, respectively.

The radial pitchwise plots indicate very close agreement in calculation between the Medium, Fine and Finer mesh densities. Certain parameters, such as the Static Pressure Coefficient and Nozzle Thrust, diverged when the mesh density was increased to the Finer level. This divergence could be attributed to the 'Coastline Problem', where taking ever smaller units of measurement can lead to a fractal-like increase in magnitude measured. However, this divergence was in no way representative of true error in the mesh convergence and could be considered as a bias error. Bias errors were mitigated through the comparative nature of the analyses presented throughout the discussion chapters of this thesis. A mesh density strategy nearest to the fine mesh presented in this section was chosen for the simulations investigated because it achieved a balance between acceptable accuracy, precision and computational cost.

Table 4.1: Number of cells in each mesh.

Mesh	Number of Cells
Coarse	4 355 996
Medium	9 762 421
Fine	25 521 764
Finer	36 233 788

Table 4.2: Relative error of nozzle pressure loss.

Simulation	Nozzle Pressure Loss	$\|\epsilon\|$
Coarse	80.68	—
Medium	64.72	24.6%
Fine	64.56	0.248%
Finer	64.277	0.440%

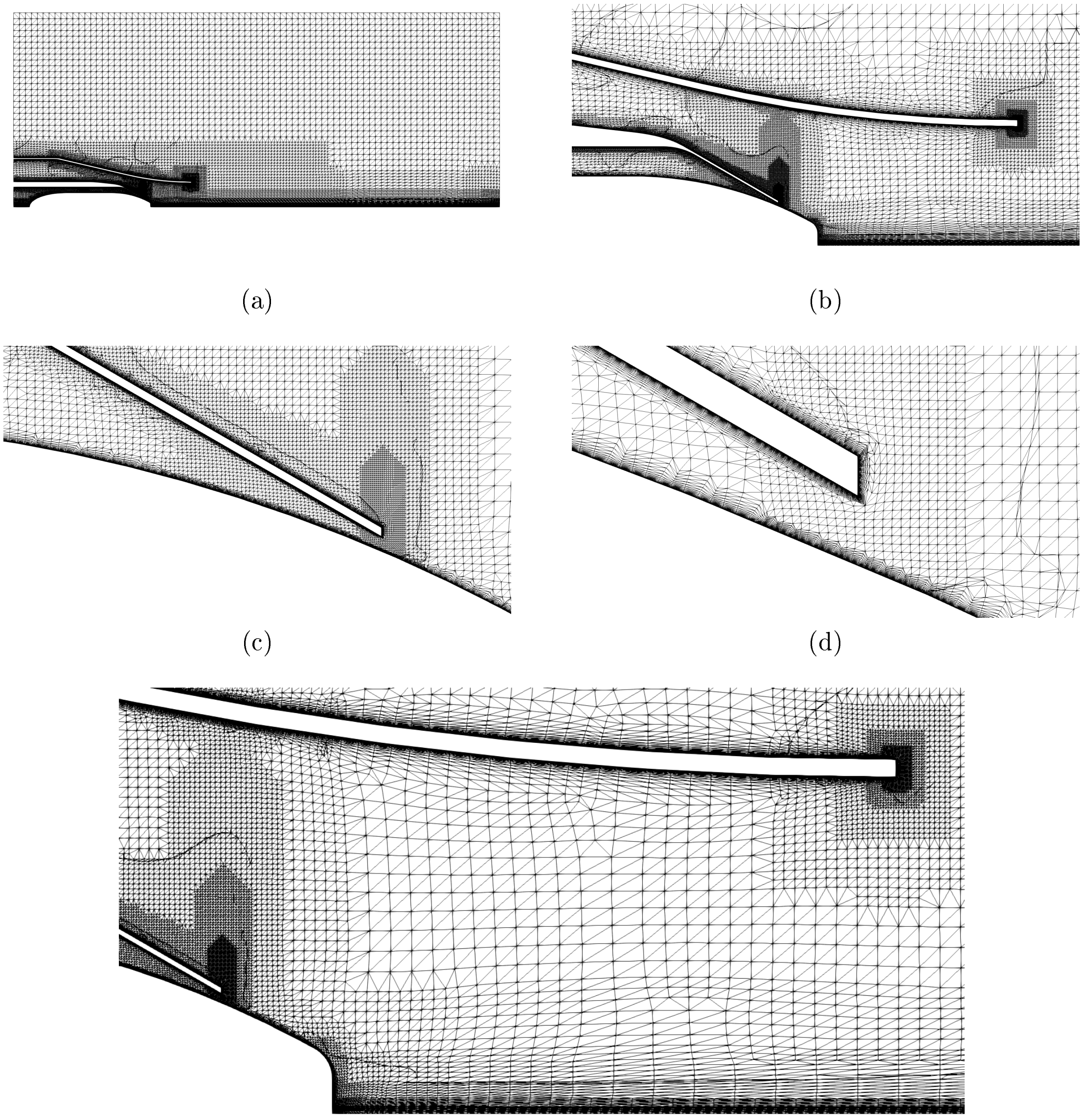

(a)

(b)

(c)

(d)

(e)

Figure 4.2: Coarse mesh, 4 355 996 cells.

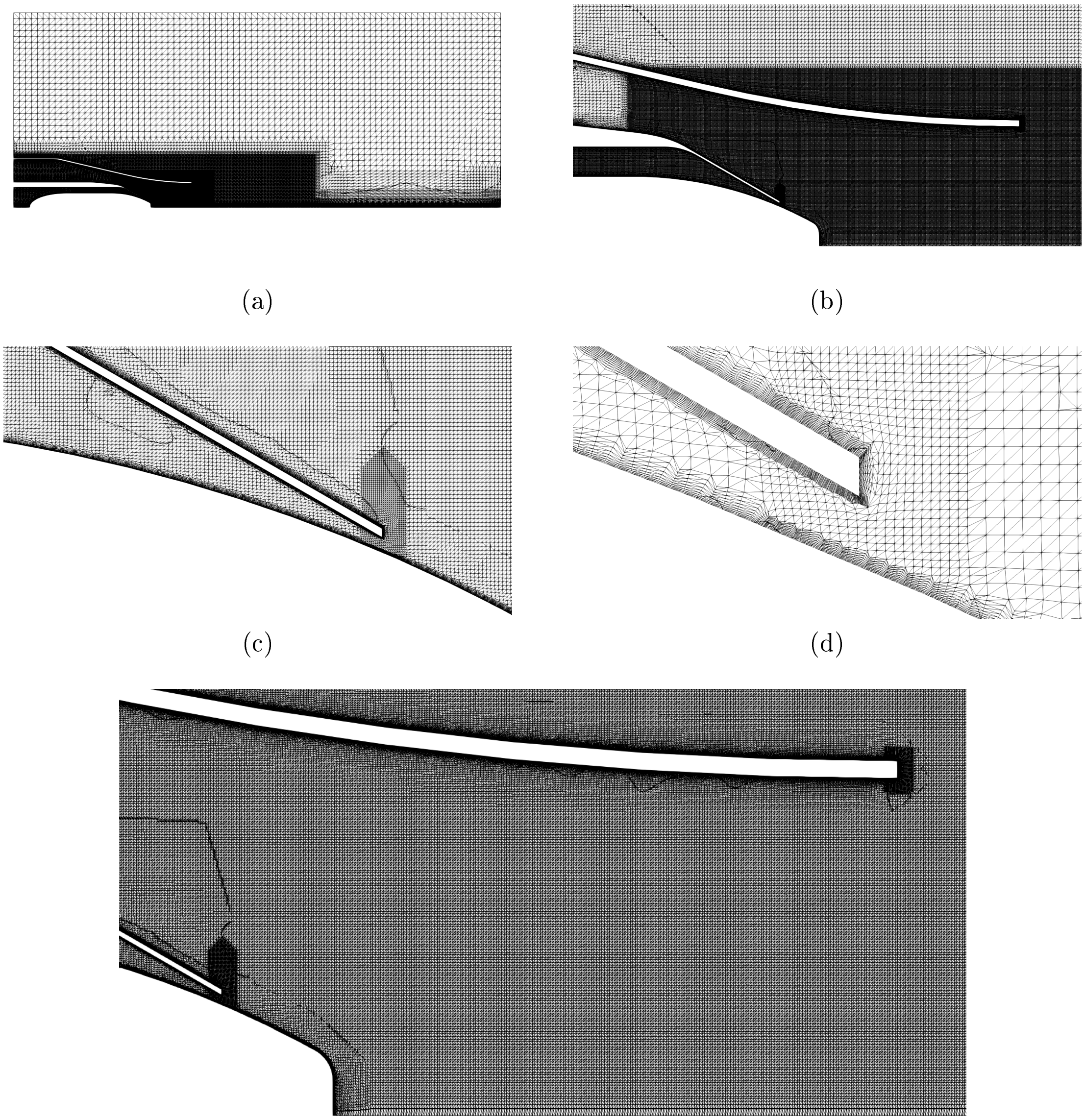

(a)

(b)

(c)

(d)

(e)

Figure 4.3: Medium mesh, 9 762 421 cells.

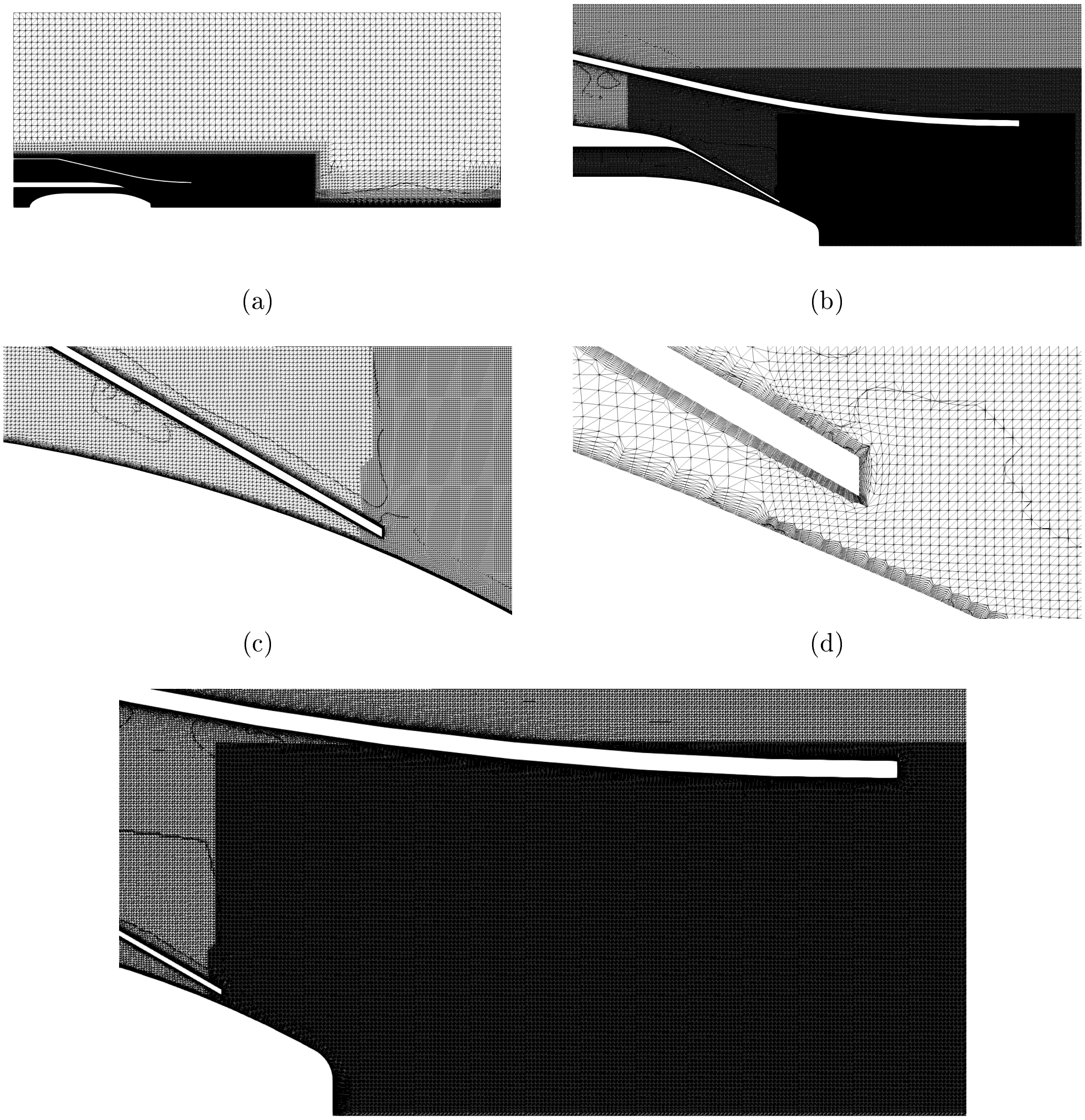

(a)

(b)

(c)

(d)

(e)

Figure 4.4: Fine mesh, 25 521 764 cells.

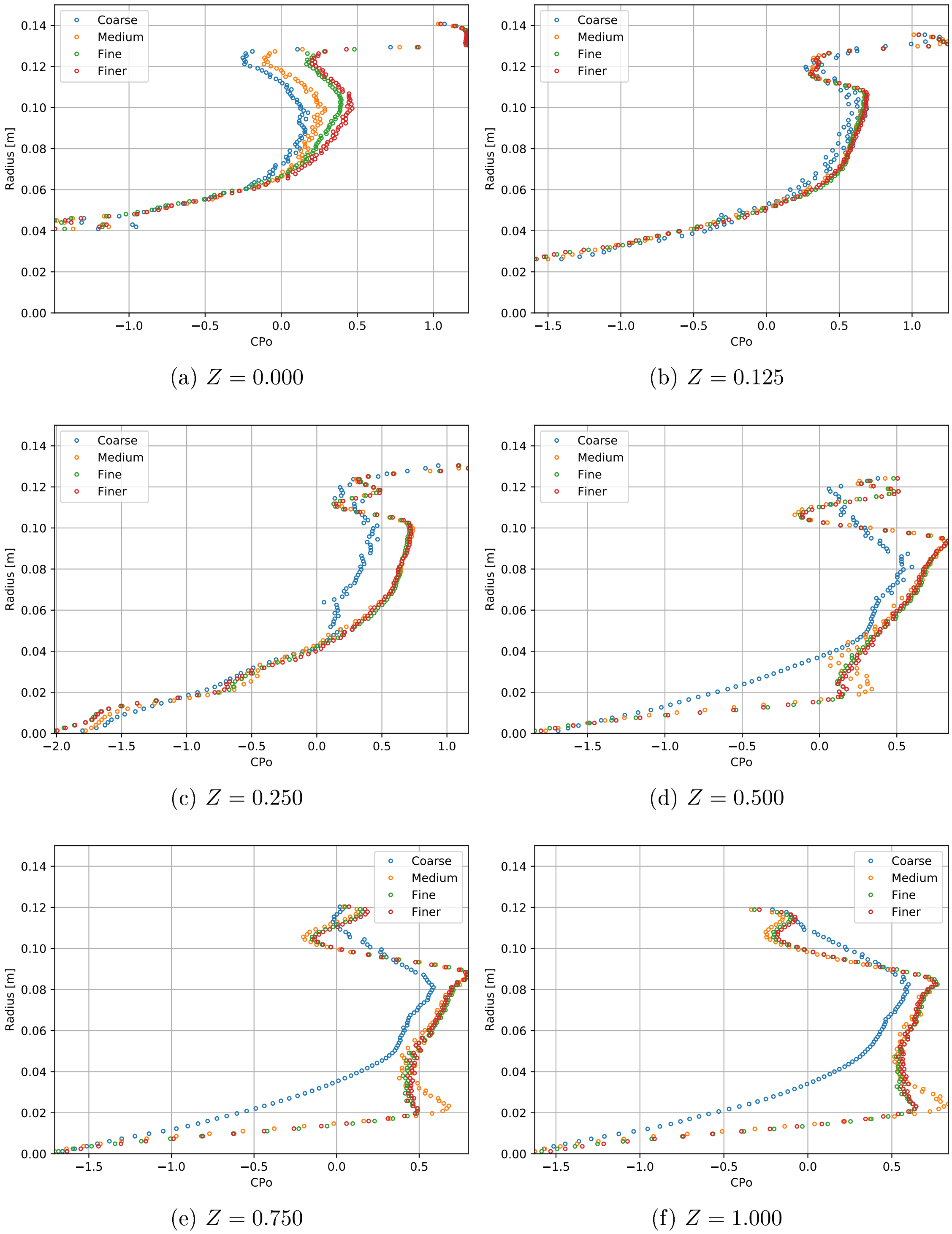

(a) $Z = 0.000$

(b) $Z = 0.125$

(c) $Z = 0.250$

(d) $Z = 0.500$

(e) $Z = 0.750$

(f) $Z = 1.000$

Figure 4.5: Pitchwise average total pressure coefficient at selected axial planes.

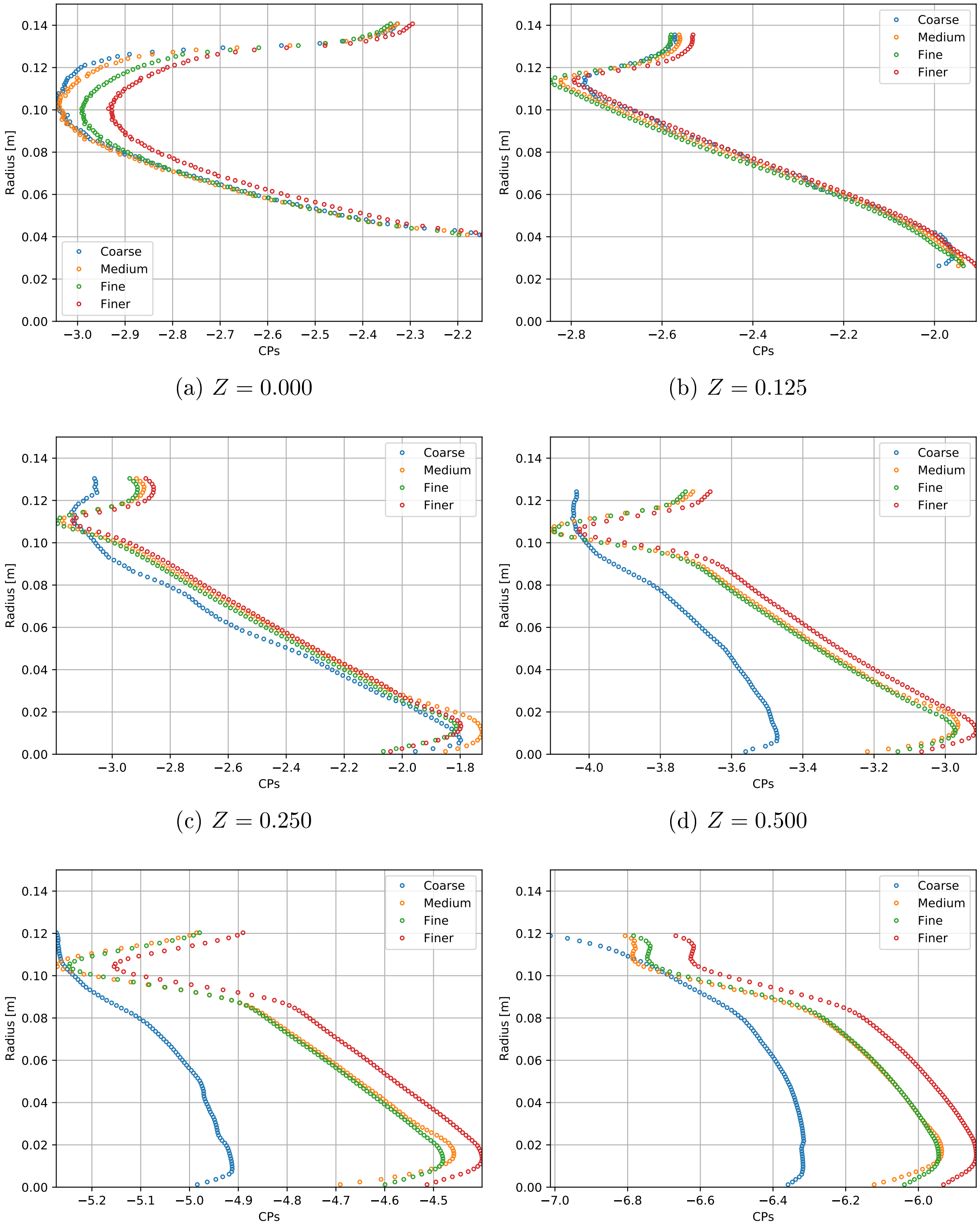

(a) $Z = 0.000$

(b) $Z = 0.125$

(c) $Z = 0.250$

(d) $Z = 0.500$

(e) $Z = 0.750$

(f) $Z = 1.000$

Figure 4.6: Pitchwise average static pressure coefficient at selected axial planes.

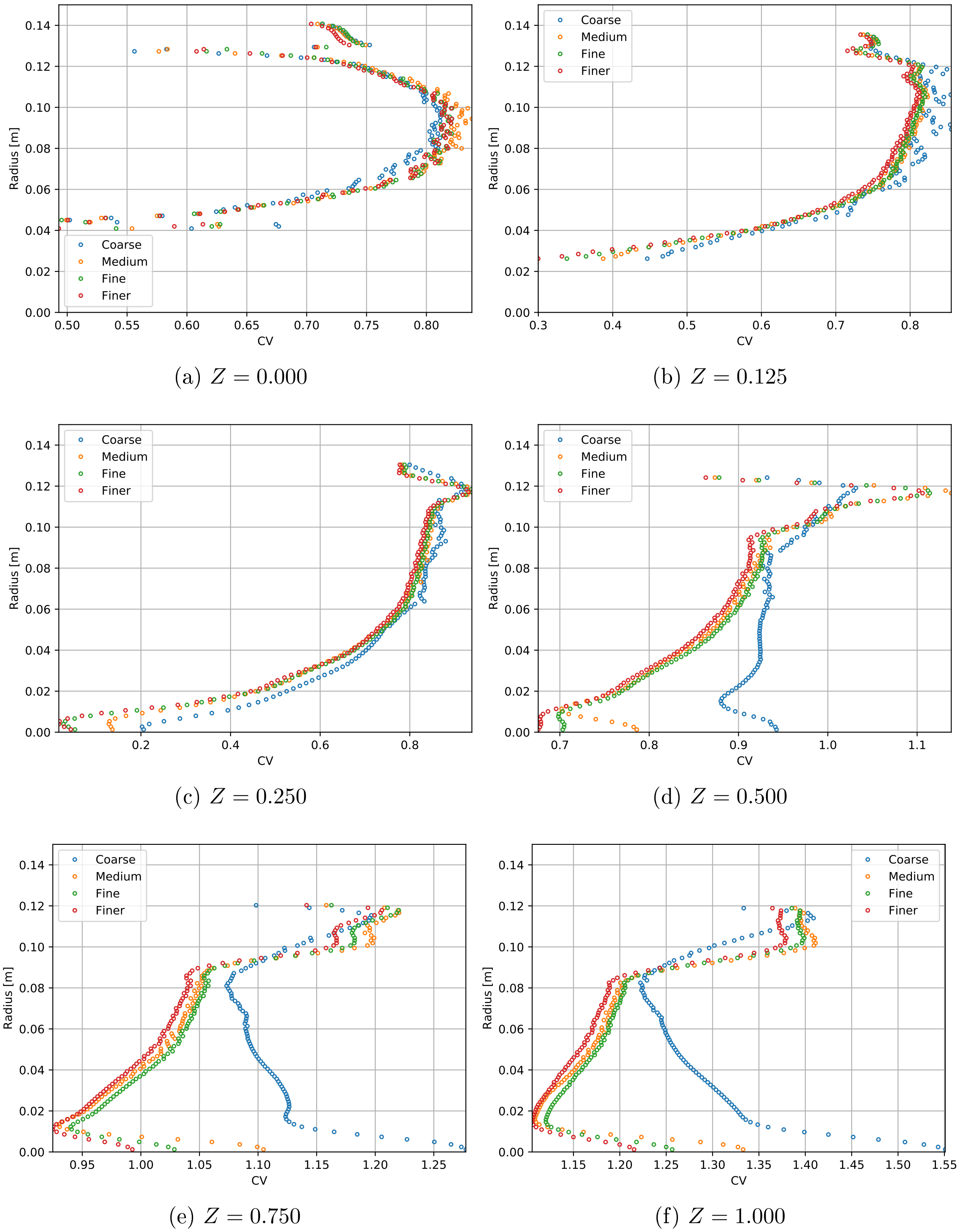

(a) $Z = 0.000$

(b) $Z = 0.125$

(c) $Z = 0.250$

(d) $Z = 0.500$

(e) $Z = 0.750$

(f) $Z = 1.000$

Figure 4.7: Pitchwise average axial velocity coefficient at selected axial planes.

Table 4.3: Relative error of nozzle thrust.

Simulation	Nozzle Thrust	$\lvert\epsilon\rvert$
Coarse	1628.164	—
Medium	1628.133	1.90E-3%
Fine	1628.135	1.23E-4%
Finer	1628.788	4.01E-2%

4.2.3 Iterative Convergence

The simulations in the mesh convergence study were run to 2000 iterations from their initial conditions. The fine mesh was then subject to an iterative convergence study to determine an appropriate number of iterations required to achieve results to the desired accuracy. The data presented in Figures 4.8, 4.9 and 4.10 of radial pitchwise average total pressure coefficient, static pressure coefficient and axial velocity at six planes downstream of the lobed mixer exit plane agree with the data in Tables 4.4 and 4.5 of nozzle pressure loss and thrust, respectively, that iterative convergence was achieved with as few as 250 iterations with the computational strategy chosen.

Table 4.4: Relative error of thrust coefficient.

Iterations	Nozzle Pressure Loss	$\lvert\epsilon\rvert$
250	63.80	—
500	65.00	1.84%
1000	65.02	0.031%

Table 4.5: Relative error of thrust coefficient.

Iterations	Thrust Coefficient	$\lvert\epsilon\rvert$
250	62.84	—
500	62.74	0.160%
1000	62.74	0.00%

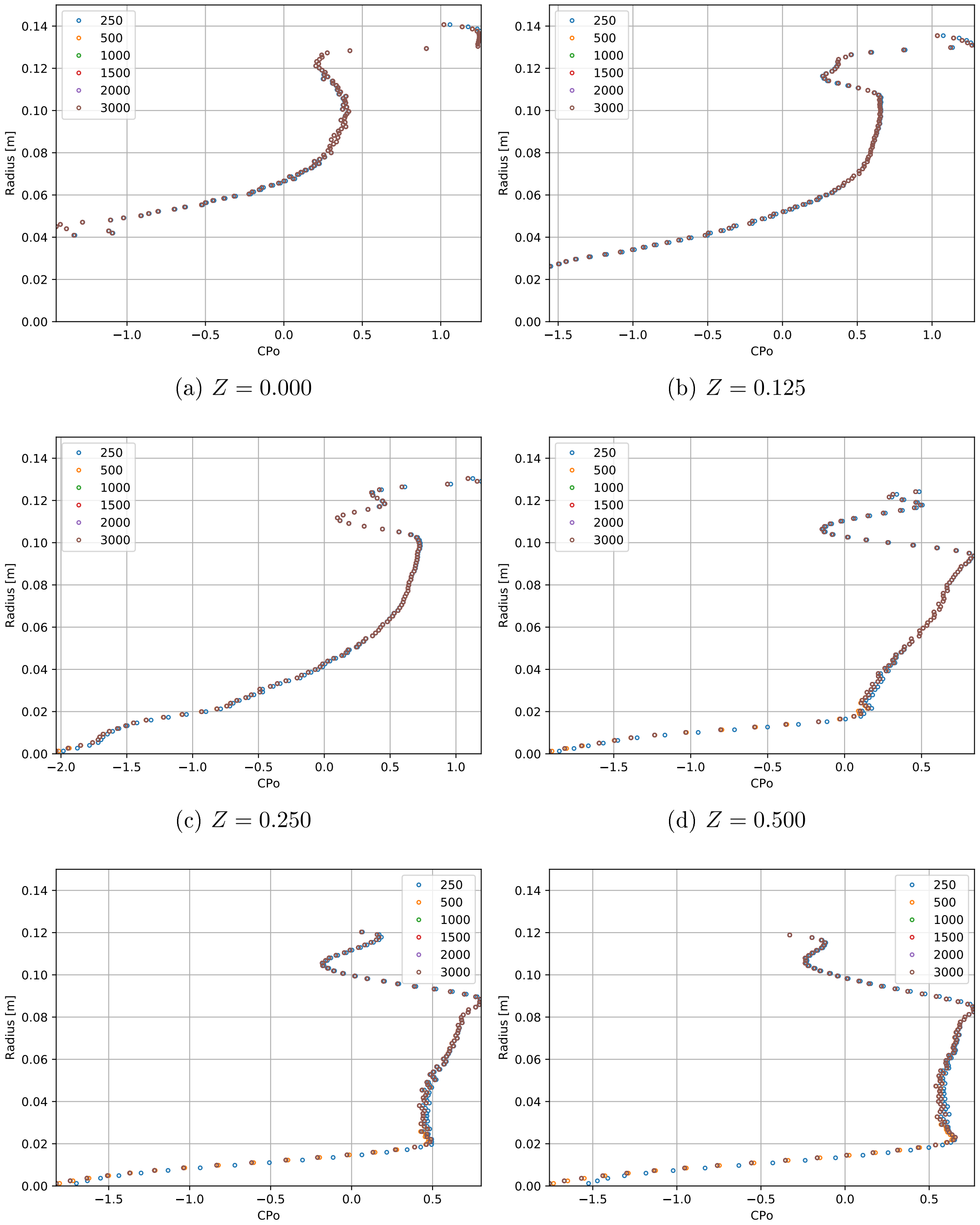

(a) $Z = 0.000$

(b) $Z = 0.125$

(c) $Z = 0.250$

(d) $Z = 0.500$

(e) $Z = 0.750$

(f) $Z = 1.000$

Figure 4.8: Pitchwise average total pressure coefficient at selected axial planes.

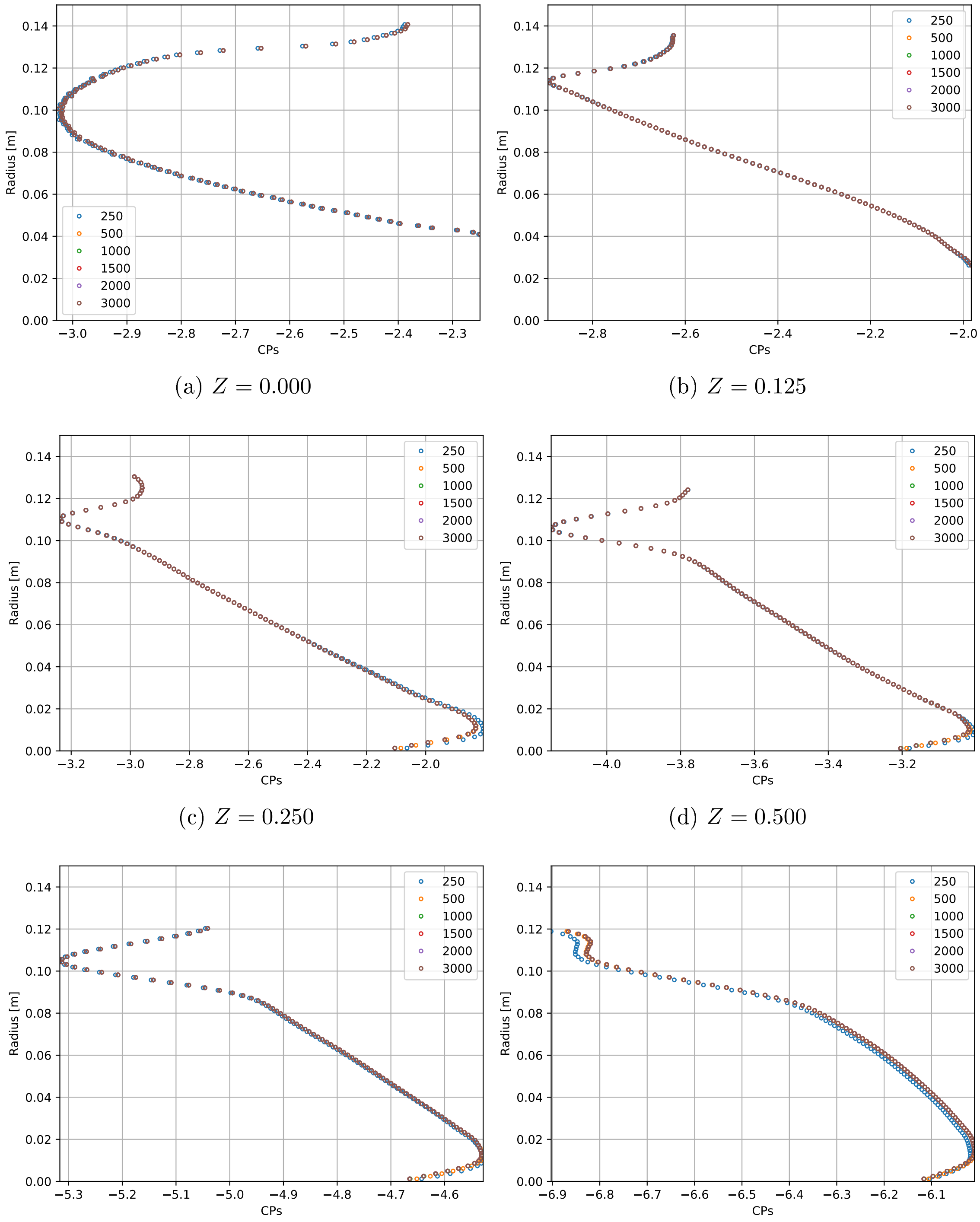

(a) $Z = 0.000$

(b) $Z = 0.125$

(c) $Z = 0.250$

(d) $Z = 0.500$

(e) $Z = 0.750$

(f) $Z = 1.000$

Figure 4.9: Pitchwise average static pressure coefficient at selected axial planes.

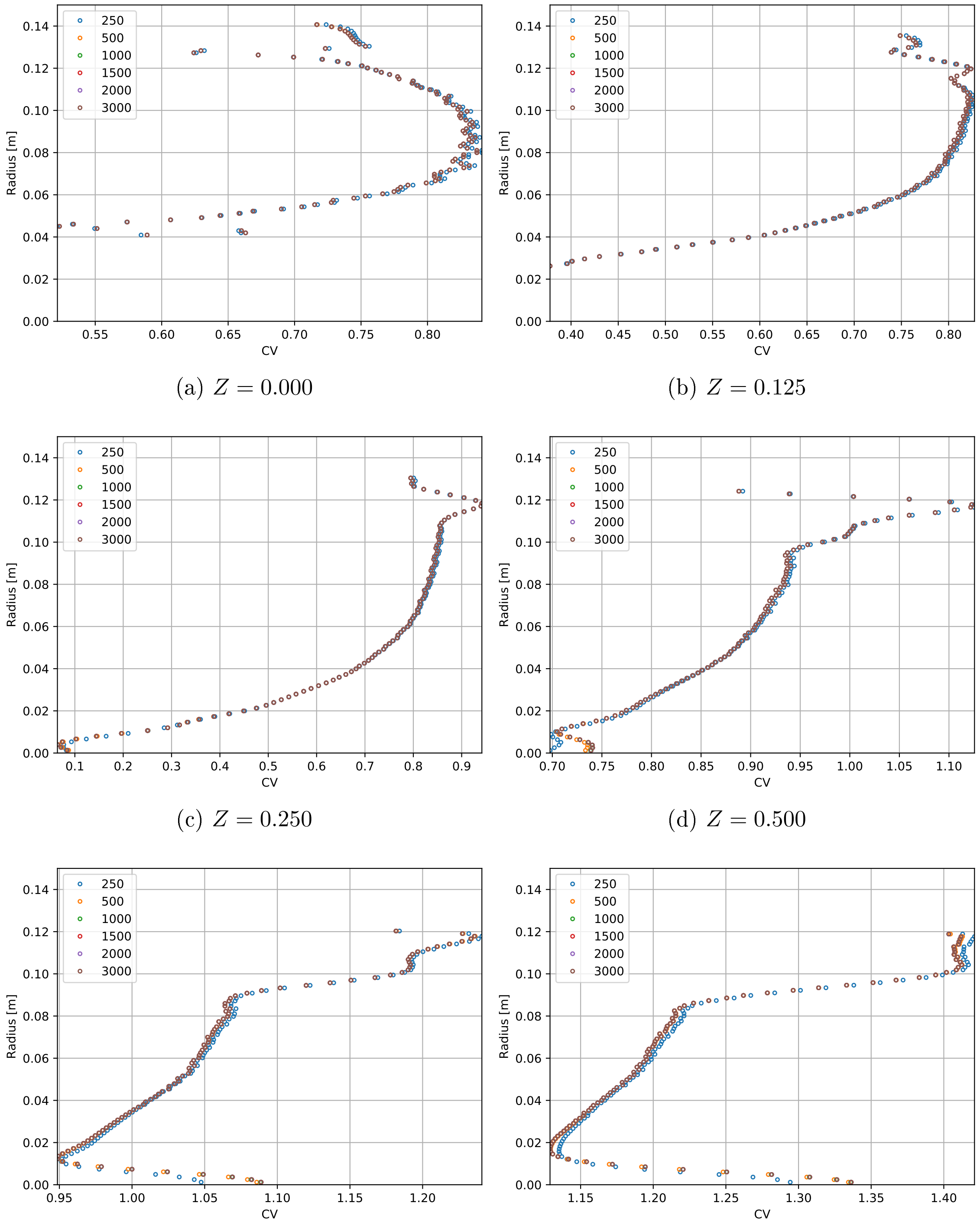

(a) $Z = 0.000$

(b) $Z = 0.125$

(c) $Z = 0.250$

(d) $Z = 0.500$

(e) $Z = 0.750$

(f) $Z = 1.000$

Figure 4.10: Pitchwise average axial velocity coefficient at selected axial planes.

4.3 Experimental Comparison

Finally, the simulations were compared against data obtained from low-speed experiments performed by Lei and Mahallati, published in 2012 [59]. The lobed mixers used in that experiment also consisted of 12 lobes of similar dimensions. However, the centrebody had a smaller radius and there was a larger gap between the lobed mixer valley and the centrebody surface. That gap allowed increased levels of swirl to reside in the flow downstream of the lobed mixer in the experimental data.

Figure 4.11 presents measured contour plots of velocity coefficient, streamwise vorticity coefficient and azimuthal vorticity coefficient at axial planes downstream of the lobed mixer. Figure 4.12 presents computational predictions of the same flow parameters at equivalent axial planes. The qualities of the flow features measured in the experiment are also predicted via the simulation. Similar streamwise vorticity is observed at acceptable magnitudes and with acceptable development downstream of the mixer.

Further data is presented in Figures 4.13 and 4.14 for flow fields downstream of the scalloped mixer with 30° core flow swirl on axial planes. The influence of the residual swirl through the lobed mixer valley-centrebody gap is evident despite it being accurately predicted to be weaker in the simulation. The overall distortion of the residual swirl was captured in both the experiment and simulation. It should be noted by the reader that the measurements were made in stages and without the full nozzle included downstream of the mixer. That was necessary in order to facilitate probe measurement near the lobed mixer exit plane but reduced the total accuracy of the experiment as a model of an engine exhaust system. This note is important because of the clear impingement of the streamwise vortex on the nozzle in the simulations which was not possible to be measured in the experiment.

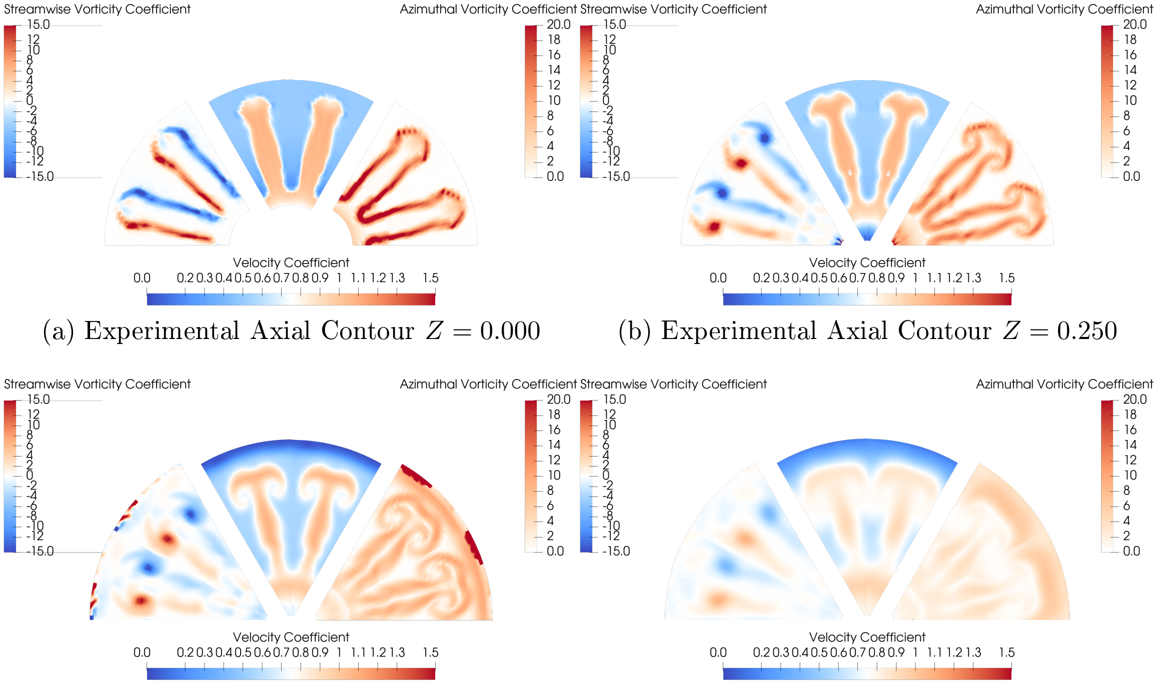

(a) Experimental Axial Contour $Z = 0.000$

(b) Experimental Axial Contour $Z = 0.250$

(c) Experimental Axial Contour $Z = 0.500$

(d) Experimental Axial Contour $Z = 1.000$

Figure 4.11: Measurement of an incompressible model with 0° core flow swirl, measured by Lei [59].

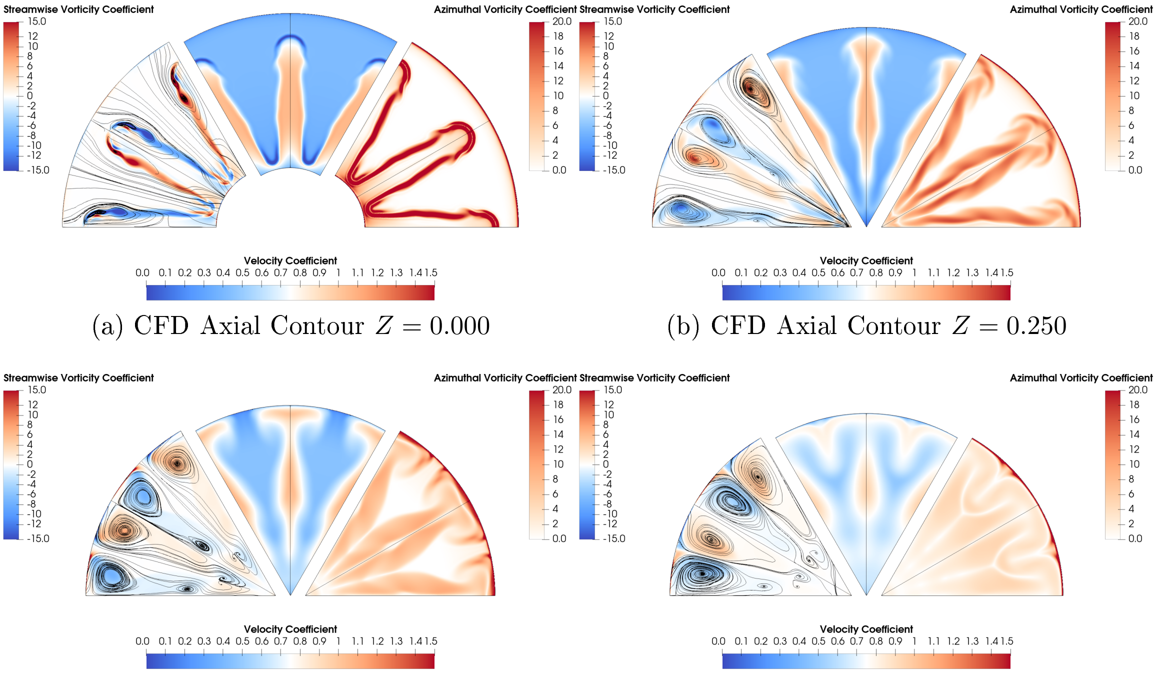

(a) CFD Axial Contour $Z = 0.000$

(b) CFD Axial Contour $Z = 0.250$

(c) CFD Axial Contour $Z = 0.500$

(d) CFD Axial Contour $Z = 1.000$

Figure 4.12: CFD predicted streamwise vorticity, velocity and azimuthal vorticity coefficients with 0° core flow swirl.

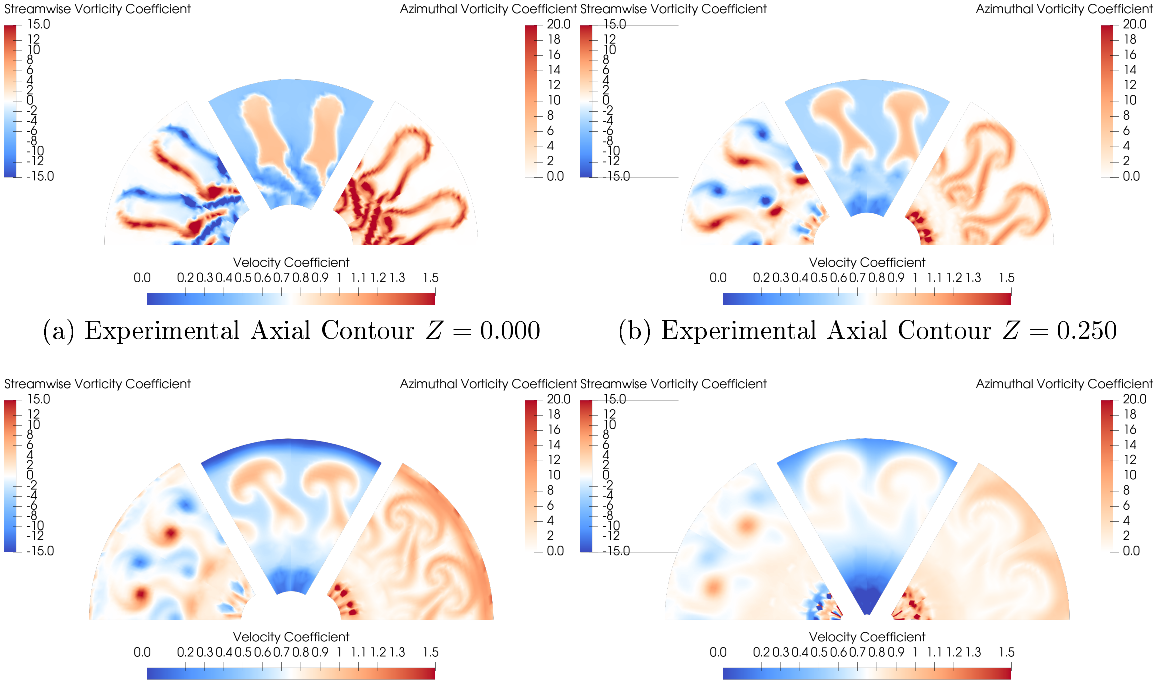

(a) Experimental Axial Contour $Z = 0.000$

(b) Experimental Axial Contour $Z = 0.250$

(c) Experimental Axial Contour $Z = 0.500$

(d) Experimental Axial Contour $Z = 1.000$

Figure 4.13: Measurement of an incompressible model with 30° core flow swirl, measured by Lei [59].

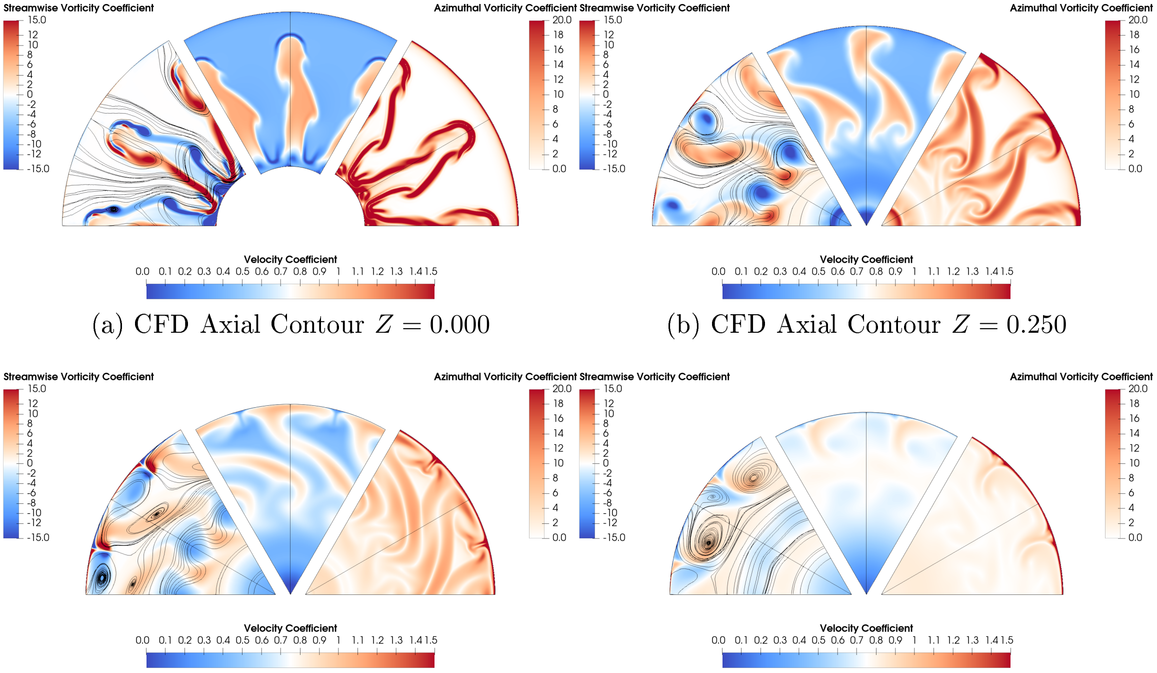

(a) CFD Axial Contour $Z = 0.000$

(b) CFD Axial Contour $Z = 0.250$

(c) CFD Axial Contour $Z = 0.500$

(d) CFD Axial Contour $Z = 1.000$

Figure 4.14: CFD predicted streamwise vorticity, velocity and azimuthal vorticity coefficients with 30° core flow swirl.

Chapter 5

Compressibility Effects

The previous chapters have set up the problem and identified a gap in the knowledge that surrounded the development of a solution. This chapter begins the analysis of data obtained as outlined in Chapters 3 and 4 and concludes that isothermal incompressible flow experimentation and simulation should not be used to model the exhaust flow of a medium bypass turbofan engine (MBTF) with a lobed mixer nor infer design decisions based on those results. The actual conditions of a MBTF exist within the compressible flow regime and display a large thermal gradient between core and bypass flows. Isothermal, incompressible models are attractive due to their simpler design and relative cost compared to full engine condition matching, but are not accurate enough.

5.1 Introduction

It is difficult to find a viable scaling criteria for such a flow because there are multiple streams with varied fluid characteristics. The core and bypass flow of the engine exhibit differing Reynolds numbers, Mach numbers, densities, velocities, viscosities, temperatures, pressures and characteristic lengths. The NRC experiment, which used low-speed incompressible conditions to model the flow, matched the velocity ratio between the core and bypass flow; the ratio is approximately 4 : 1. The Reynolds number of the flow was changed dramatically because the experiment was scaled only to match the velocity ratio. The Reynolds number, $Re = \frac{\rho V D}{\mu}$, depends on a characteristic length of the flow geometry as well as fluid density, velocity and viscosity. The Reynolds numbers are tabulated in Table 5.1.

Reynolds number scaling via geometry has been a practice of turbine and compressor aerodynamics for decades. Losses in these systems—as well as in the exhaust system under current investigation—are dominated by viscous effects. Therefore it would be sensible to apply the same logic here and perform geometric scaling on

Table 5.1: Core and bypass Reynolds numbers at incompressible and compressible conditions.

		Reynolds Number
Incompressible	Core	701 000
	Bypass	152 000
Compressible	Core	245 000
	Bypass	473 000

the exhaust system. That is not practical given the effect the drop in temperature and velocity has on the Reynolds number at incompressible conditions. The Bypass geometry would need to shrink by a quarter scale and the core enlarged by a factor of nearly 3. This redesign is impractical and so another direction was taken in the experimental test.

Geometric scaling was avoided altogether and, as mentioned previously, the velocity ratio was maintained. The justification for this choice was found in the literature. It suggests that thermal and mass mixing of two non-isothermal gases is completed before momentum mixing [5, 6]. It was a reasonable engineering decision to use this as justification to develop a low-cost, low-speed isothermal experiment to examine lobed mixer performance. However, upon further review of the literature, all of these studies focused on coaxial mixers and none touched on lobed mixers.

The literature review in Chapter 2 presented the knowledge that lobed mixers produce streamwise vortex structures in addition to the normal vortex that develops, in common with coaxial mixers, along the trailing edge. This chapter includes a description of the flow physics that govern the development of the streamwise vortex to provide further context for the effect of compressibility and thermal gradient on the flow structures and performance.

The next section outlines the investigation performed to answer the question of accuracy regarding low-speed incompressible experiments when making MBTF exhaust system design decisions.

5.2 Methodology

The four simulations presented in this chapter were chosen to illustrate the significant difference between the outcomes of modifications to incompressible or compressible simulations. The same performance trends must be observed at both conditions for incompressible flow to be a useful model. Boundary condition changes produced major changes in fluid characteristics such as: density, viscosity, velocity and temperature. Analysis of the four simulations presented provided insight on how these changes affected the miscibility of the core and bypass flows.

The comparative nature of this analysis reduced the impact of bias error on the conclusion. Computational simulation cut down on many of the outside effects that would have been worrisome with an experimental simulation. It was clear the absolute magnitude of the performance parameters would be different between the two sets of conditions, but observation of the results at different core swirl conditions allowed observation of trends which reduced the difference in absolute performance magnitude. Other potential environmental errors were minimized by the computational nature of the analysis; but, numerical errors in mesh density, artificial dissipation, discretization in time and space and overall validity of the results came in to question. Chapter 4 presents arguments to mitigate concern over the quantification of such computationally related sources of error.

5.2.1 Boundary Conditions

This chapter presents data from four simulations of the same unscalloped lobed mixer at different conditions—incompressible and compressible flow regime, with and without swirl in the core flow. The incompressible boundary conditions are outlined in Table 5.2 and the compressible boundary conditions are outlined in Table 5.3. These conditions were chosen because they represent general cruise conditions for the compressible condition and the incompressible conditions were chosen because they allow for a match in the velocity ratio at the core bypass mixer interface. Figure 5.2 illustrates the overall computational domain with boundaries labeled. Green indicates inlet type boundaries, Gray indicates no-slip solid type boundaries, Red indicates the outlet type boundary, Blue indicates a solid boundary with full-slip condition and

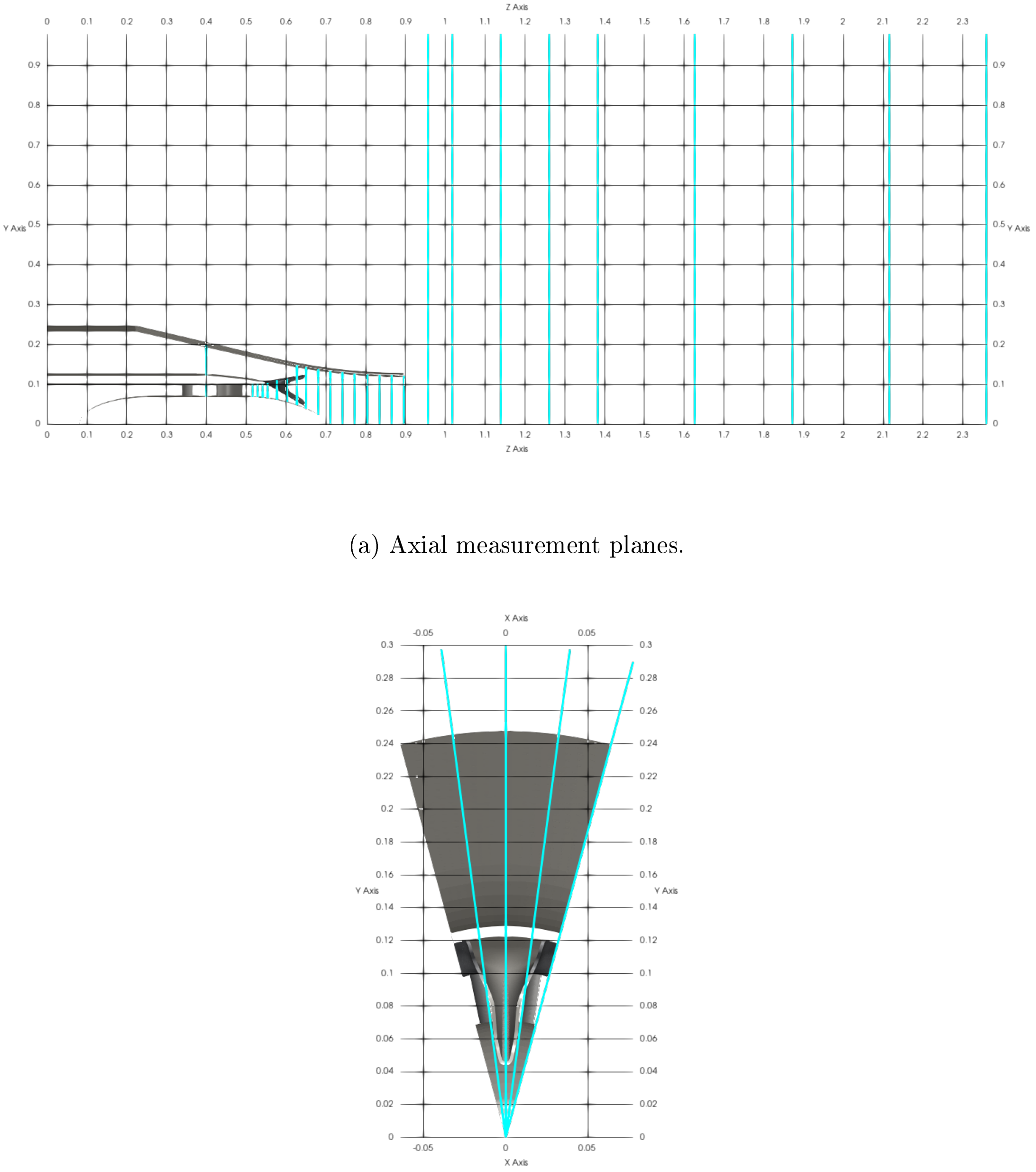

(a) Axial measurement planes.

(b) Meridional measurement planes.

Figure 5.1: Measurement planes highlighted within the computational domain.

Table 5.2: Low-speed incompressible boundary conditions based on matching core to bypass velocity ratio of actual engine.

Boundary	Type	Value
Core	Mass Flow	$1.2\,\mathrm{kg\,s^{-1}}$
	Static Temperature	$293\,\mathrm{K}$
	V_x/V	0
	V_x/V	0
	V_x/V	1
	k	$3.75\,\mathrm{m^2\,s^{-2}}$
	ϵ	$4500\,\mathrm{m^2\,s^{-3}}$
Bypass	Mass Flow	$1.2\,\mathrm{kg\,s^{-1}}$
	Static Temperature	$293\,\mathrm{K}$
	V_x/V	0
	V_x/V	0
	V_x/V	1
	k	$0.8\,\mathrm{m^2\,s^{-2}}$
	ϵ	$4.5\,\mathrm{m^2\,s^{-3}}$
Free Stream	Total Pressure	101.325 kPa
	Total Temperature	$293\,\mathrm{K}$
	k	$5\,\mathrm{m^2\,s^{-2}}$
	ϵ	$30\,000\,\mathrm{m^2\,s^{-3}}$
Outlet	Average Static Pressure	101.325 kPa

Pink indicates the periodic type boundaries. The figure also indicates the relative sizes of the free-stream and open exhaust region of the computational domain.

5.2.2 Test Geometries

One lobed mixer geometry was used for all simulations in this chapter.

Unscalloped Mixer

There are many potential alterations to the lobed mixer geometry as outlined in Chapter 2. The unscalloped mixer was chosen for this analysis because it represented a baseline lobed mixer geometry. The mixer is illustrated in Figure 5.3.

The lobed mixer used for these simulations had a rise angle of 10° and a fall angle of 30°. The crest radius was 10 mm and the valley radius set such that the sidewalls

Table 5.3: High-speed compressible boundary conditions based on comparable commercial engine cruise conditions.

Boundary	Type	Value
Core	Total Pressure	43.0 kPa
	Total Temperature	728 K
	k	$5\,\mathrm{m^2\,s^{-2}}$
	ϵ	$30\,000\,\mathrm{m^2\,s^{-3}}$
Bypass	Total Pressure	45.1 kPa
	Total Temperature	273 K
	k	$5\,\mathrm{m^2\,s^{-2}}$
	ϵ	$30\,000\,\mathrm{m^2\,s^{-3}}$
Free Stream	Total Pressure	18.9 kPa
	Total Temperature	223 K
	k	$5\,\mathrm{m^2\,s^{-2}}$
	ϵ	$30\,000\,\mathrm{m^2\,s^{-3}}$
Outlet	Average Static Pressure	18.8 kPa

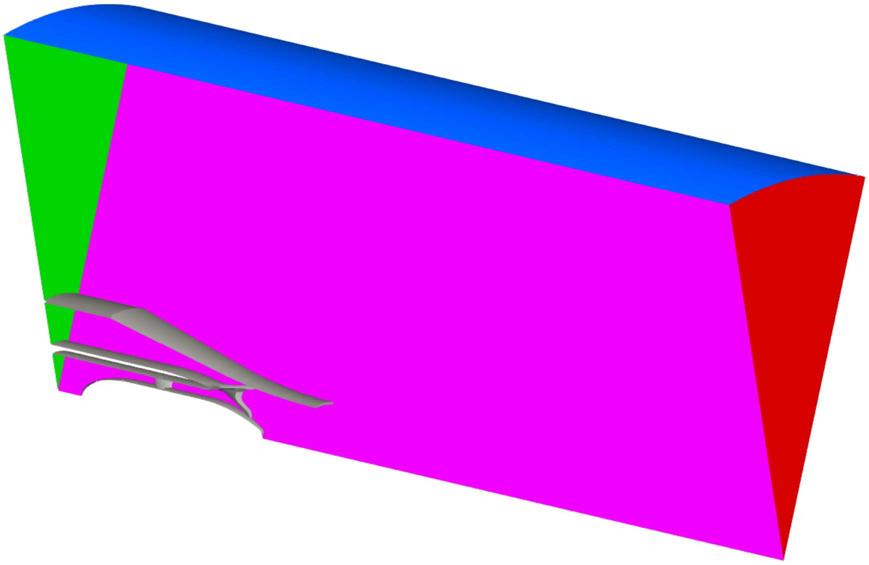

Figure 5.2: Computational domain indicating various boundary conditions.

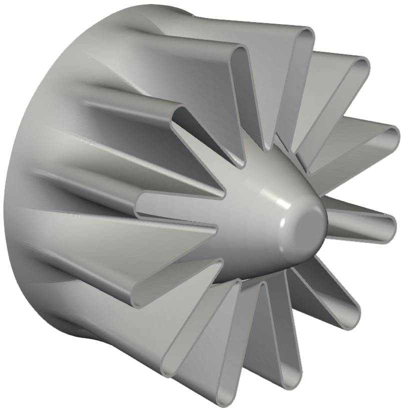

Figure 5.3: The unscalloped mixer.

remained parallel and tangent to the crest. The trailing edge thickness was 1 mm.

The next section discusses the flow fields and exhaust system performance that arose from the combination of these boundary conditions with this lobed mixer.

5.3 Flow Fields

The results were analyzed to determine the effect of flow compressibility on the flow structures developed in the wake of a lobed mixer. This section begins with analysis of the flow fields developed during incompressible flow: first for a baseline case with no swirl within the core flow then at a high swirl case with 30° swirl within the core flow. The cases with compressible flow are presented after the cases of incompressible flow.

5.3.1 Incompressible Flow

These incompressible flow cases are presented as a representation of the experimental set up devised by NRC to model the exhaust performance of a medium bypass turbofan engine.

Baseline

Figure 5.4 illustrates the baseline incompressible flow fields measured computationally at eight axial planes: two upstream of the mixer outlet plane, $Z = 0.000$, and five downstream to the nozzle outlet plane, $Z = 1.000$. The quantities presented are, from left to right, the streamwise vorticity coefficient, $C_{\omega s}$, with surface velocity streamlines; total pressure coefficient, CP_0, and azimtuhal vorticity coefficient, $C_{\omega a}$. Their definitions are found in equations 4.2, 4.3 and 4.8, respectively. The vorticity coefficients are measures of the vortex strength normalized by the core flow reference dynamic pressure. The total pressure coefficient is a measure of local total pressure normalized by the core flow reference dynamic pressure. These normalized coefficients help when making comparisons of simulations with differing boundary and flow conditions. The viewer's perspective is looking upstream from the nozzle outlet plane toward the mixer.

The first flow features to be discussed are the streamwise vortices. These structures were the result of the radial velocity gradient applied to the flow as it traverses the lobed mixer. The bypass flow was deflected radially inward and the core flow was deflected radially outward. The interaction of the core and bypass flow at the mixer trailing edge, $Z = 0.000$, produced an axial component of the vorticity vector. Figure 5.4 represents counterclockwise vorticity with positive magnitude with red colouring and clockwise vorticity with negative magnitude and blue colouring. Flow absent of streamwise vorticity is represented in white. The two vortices that were developed in this case, and illustrated as SV_1 and SV_2 in Figure 5.4c, began with a length-scale on the order of the lobe height. The surface streamlines assist the reader in observing their development into coherent vortex cores in Figure 5.4e and further downstream.

The streamwise vortices interacted directly with the azimuthal vortex. The contour plots of Figure 5.4 illustrate clearly that the normal vortex, whose magnitude is represented in red, became distorted at locations that correspond to the presence of the strongest streamwise vorticity. The distortion is indicated in Figure 5.4d. The azimuthal vortex was fully detached from itself, or pinched off into separate structures, because of the distortion. The pinch points are indicated in Figure 5.4e. The mutual destruction of the vortex structures is a key aspect to flow mixing in the wake of lobed mixers. The goal is to have fully uniform flow as quickly as possible. The best way to achieve that is to produce strong vorticity that provides bulk fluid exchange between core and bypass and then dissipates into small scale turbulent structures. After all, the fully uniform flow does not contain distinct, coherent flow structures.

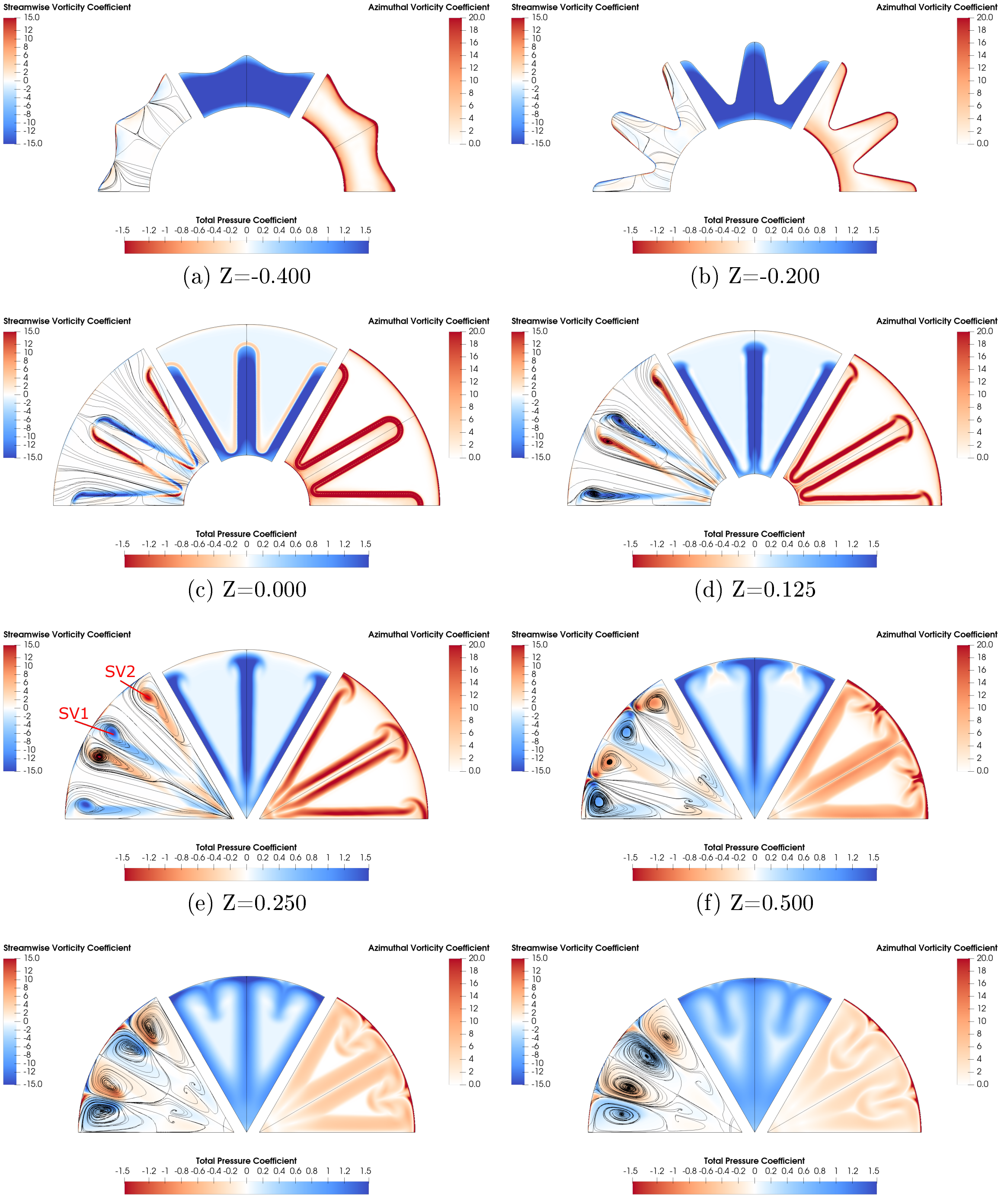

(a) Z=-0.400

(b) Z=-0.200

(c) Z=0.000

(d) Z=0.125

(e) Z=0.250

(f) Z=0.500

(g) Z=0.750

(h) Z=1.000

Figure 5.4: Contour plots of streamwise vorticity coefficient, total pressure coefficient and azimuthal vorticity coefficient at the incompressible baseline case.

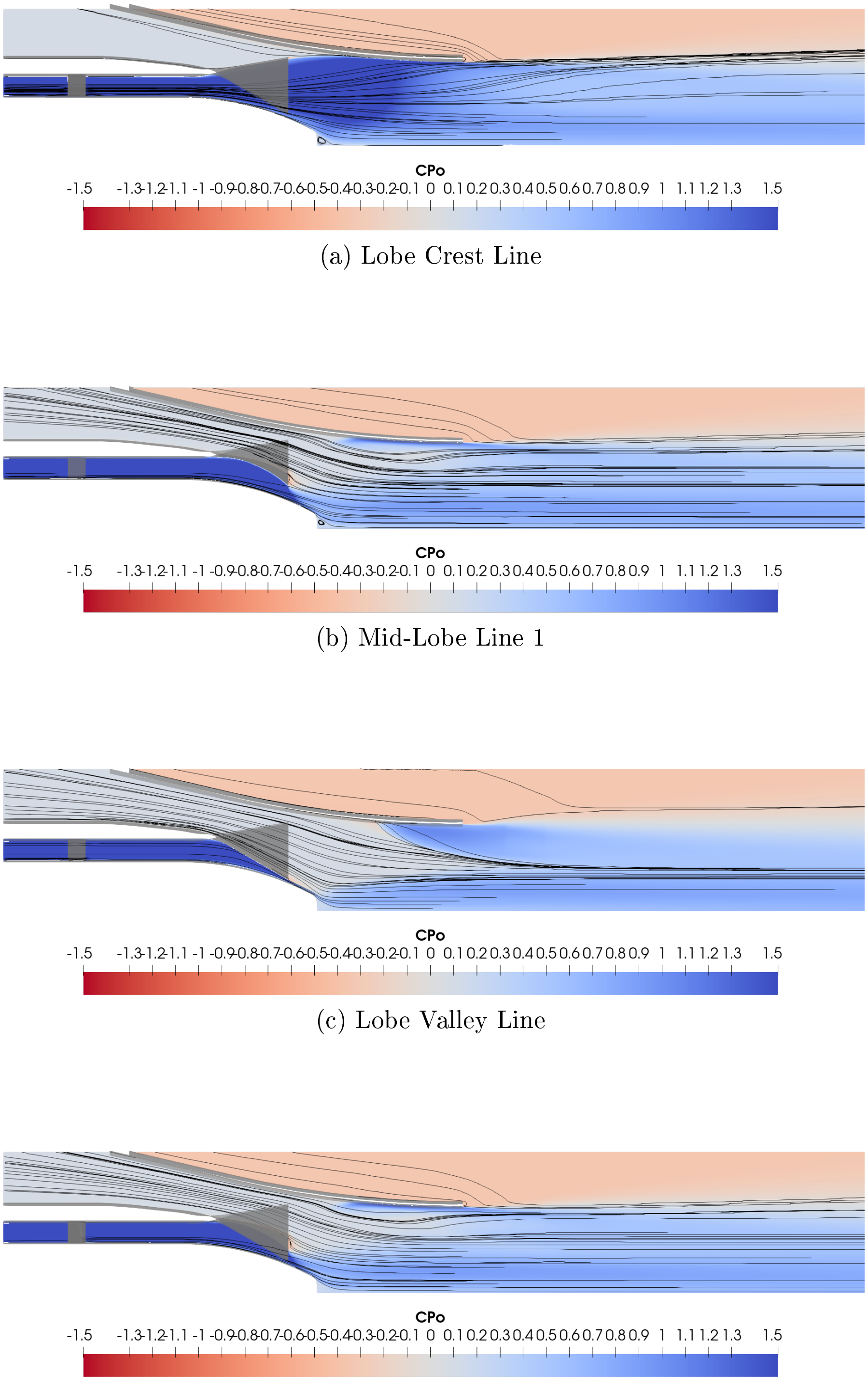

(a) Lobe Crest Line

(b) Mid-Lobe Line 1

(c) Lobe Valley Line

(d) Mid-Lobe Line 2

Figure 5.5: Meridional contours of total pressure coefficient at the incompressible baseline case.

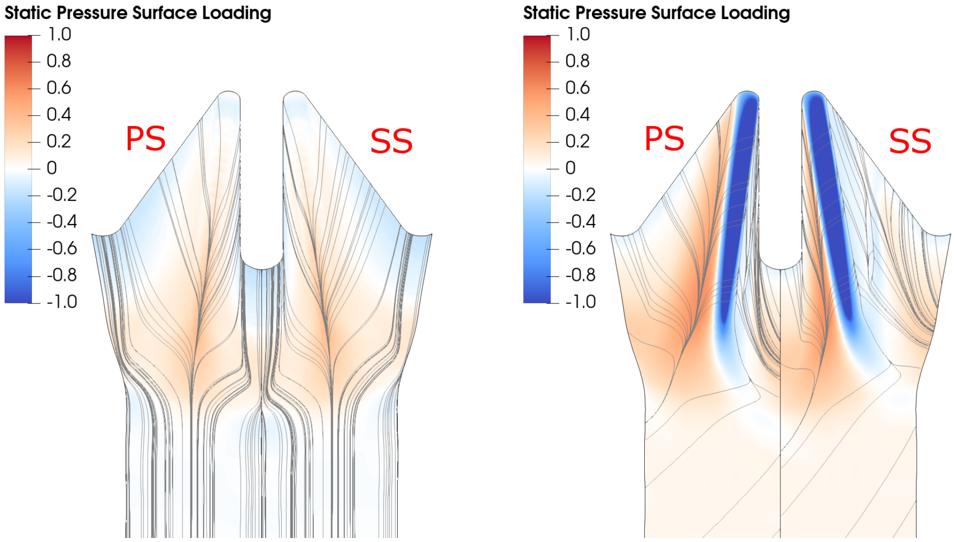

(a) Baseline

(b) 30° Swirl

Figure 5.6: Static pressure loading on the core side of the lobed mixer for the incompressible cases.

The central sector of Figure 5.4 shows the total pressure coefficient. These plots show how the relatively higher pressure core flow extended and dissipated into the lower pressure bypass fluid. The plots show the streamwise vortices impinged on the inner surface of the nozzle, better illustrated in Figure 5.5, which limited their ability to produce mixing. Figure 5.5 shows the total pressure coefficient at four meridional planes. Finally, Figure 5.6a shows the static pressure loading on the core side of the mixer with the viewers perspective looking downstream toward the mixer from the inlets. This plot indicates that the core flow accelerated around the valley of the lobes and diffuses along the crest. These loading Figures became important points of illustration when swirl was included in the core flow.

30° **Swirl**

The flow physics that produce the flow fields did not change when swirl is introduced to the core flow. What did change was how that flow interacted with the passive lobed mixer device. Figure 5.6 clearly illustrates the change. When swirl was introduced, the core flow impinged on what is labeled PS, the pressure side of the lobe. A saddle point developed and the fluid that leaked around the valley encountered a strong adverse pressure gradient and separated from the mixer on the suction side, labeled

SS. Figure 5.7 illustrates the effect that separation had on the flow structures.

The planes upstream of the mixer show a region of strong positive streamwise vorticity that developed where the flow began to separate. The three-dimensional nature of the separation is apparent because it also induced azimuthal vorticity upstream of the mixer trailing edge. Further to this, the total pressure coefficient plot also indicates a loss of energy within the separation as well. This new streamwise vortex shall be referred to as the separation streamwise vortex and labeled as SV_S in the figures for all cases that it appears.

In this case, there were now two distinct and coherent positive regions of streamwise vorticity. Both interacted with the azimuthal vortex as indicated in Figure 5.7d but only SV_1 was the result of shear layer interaction with the bypass flow. Therefore, it is proposed that the extra vortex did not assist with bulk flow mixing in anyway, but only contributed to viscous dissipation of other flow structures.

The wake of the centrebody was another point of interest, especially in the total pressure coefficient plots. A substantial drop in total pressure was observed in the wake of the centrebody when swirling core flow was present. Figure 5.8 indicates a recirculation zone in the wake that added to the total pressure loss of this particular system. The low total pressure coefficient seen downstream of the centrebody was not due to the entrainment of the lower pressure bypass flow, but rather viscous losses because of that recirculation zone. The recirculation developed was due to residual swirl—evident in Figure 5.7d—that persisted downstream of the mixer. The residual swirl's tangential component of velocity was accelerated because of the conservation of angular momentum as the centrebody radius reduced.

The effect of swirl on the overall performance of the exhaust system at incompressible conditions will be examined in Section 5.4.

5.3.2 Compressible Flow

The change to the compressible flow regime again did not alter the flow physics behind the flow structure development, but it did alter the physical parameters that governed how the mixing developed. In this condition, the viscosity and density of the fluid were reduced, the temperature was increased, and the Reynolds number changed. The following sections outline the effects these changes had on the flow structures

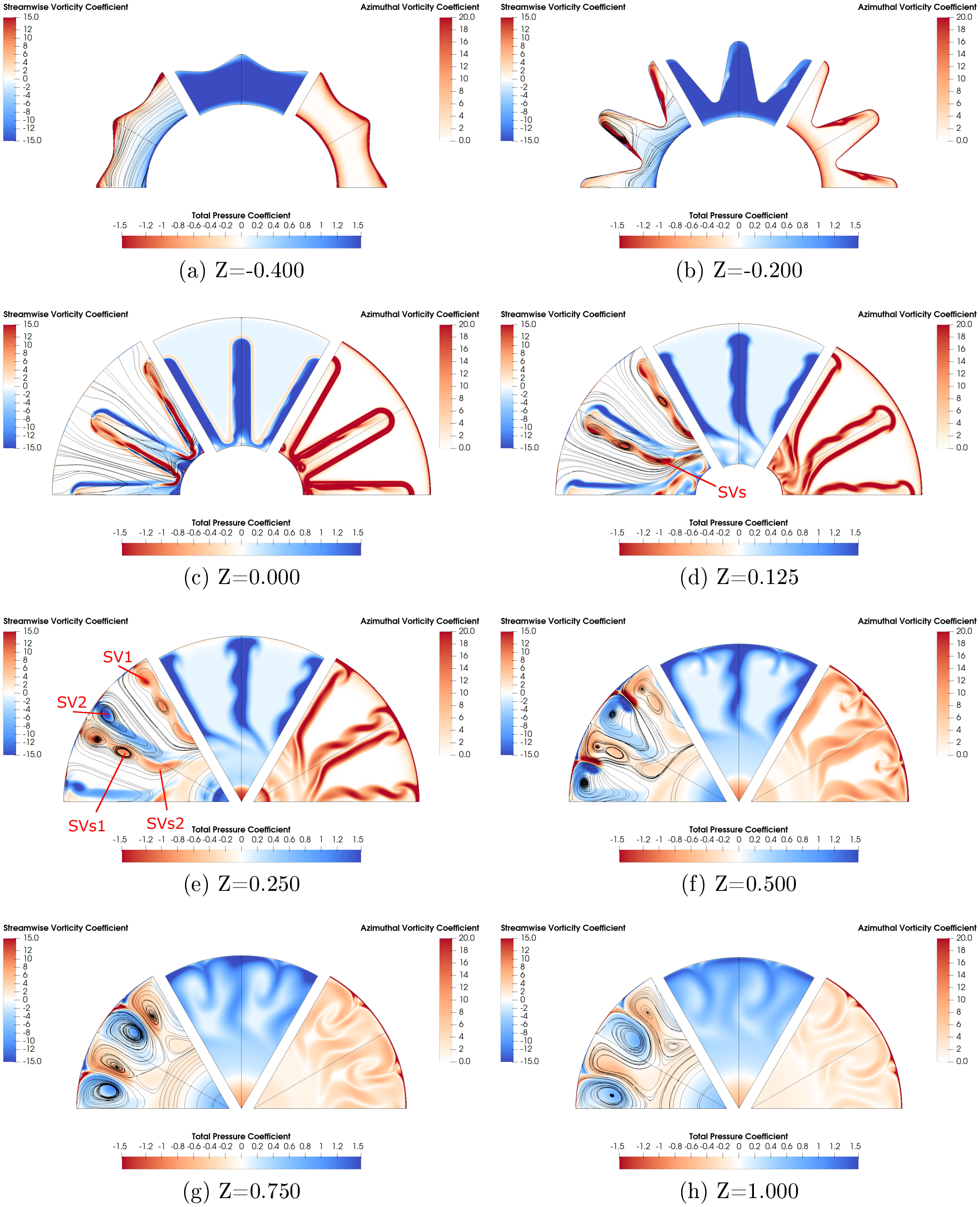

(a) Z=-0.400

(b) Z=-0.200

(c) Z=0.000

(d) Z=0.125

(e) Z=0.250

(f) Z=0.500

(g) Z=0.750

(h) Z=1.000

Figure 5.7: Contour plots of streamwise vorticity coefficient, total pressure coefficient and azimuthal vorticity coefficient at the incompressible 30° swirl case.

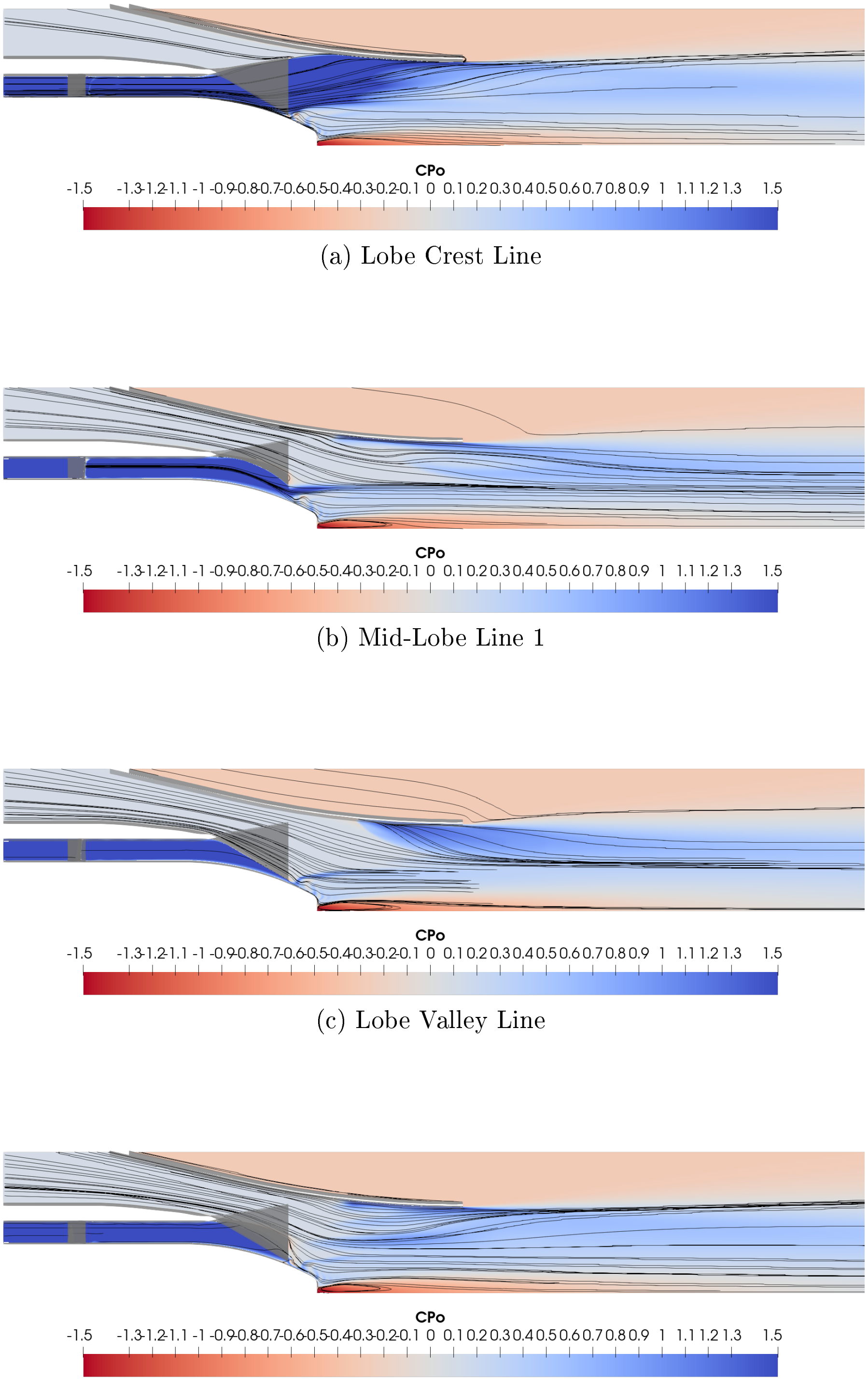

(a) Lobe Crest Line

(b) Mid-Lobe Line 1

(c) Lobe Valley Line

(d) Mid-Lobe Line 2

Figure 5.8: Meridional contours of total pressure coefficient at the incompressible 30° swirl case.

and their development.

Baseline

There were many changes to the flow features between incompressible and compressible conditions as seen in Figure 5.9. The first that should be noticed is the total pressure values for the compressible condition were higher in the bypass flow than the core flow. This is the expected arrangement, but for incompressible cases this was reversed in order to match the core to bypass velocity ratio.

The streamwise vorticity developed similarly to the incompressible condition; the initial length scale of the two vortices was of the order of the lobe height. These regions of strong vorticity quickly coalesced to distinct vortex cores at $Z = 0.250$ and persisted downstream to $Z = 1.00$. The streamwise and azimuthal vortex also interacted in a similar fashion. The azimuthal vortex was distorted at $Z = 0.125$ and pinched off at $Z = 0.250$. The main difference, however, is that the streamwise vortices did not impinge on the nozzle surface so quickly. That allowed for unimpeded bulk flow mixing between the core and bypass flow as illustrated in Figure 5.10. The total pressure coefficient contour plots along the meridional planes indicate much more of the core flow was entrained near the nozzle surface than during the incompressible case, especially at the mid-lobe planes.

At baseline, the loading on the mixer was practically indistinguishable between incompressible and compressible conditions. However, the presence of swirl resulted in a major change. The lobed mixer surface static pressure loading, shown in Figure 5.11b, indicates the expected separation but also a flow reattachment and second separation. A truly complex flow field.

30° **Swirl**

Figure 5.12 illustrates the creation and development of the many flow structures that arose from the simulation of 30° swirl in the core flow at compressible conditions. The separation and reattachment described previously is visible to the reader as regions of strong positive vorticity and azimuthal vorticity as seen in Subfigure 5.12b. The two separation induced vortices are labeled on the figure as SV_{S1} and SV_{S2}. The vortex core nearest the valley tip was strong enough and large enough to entrain the

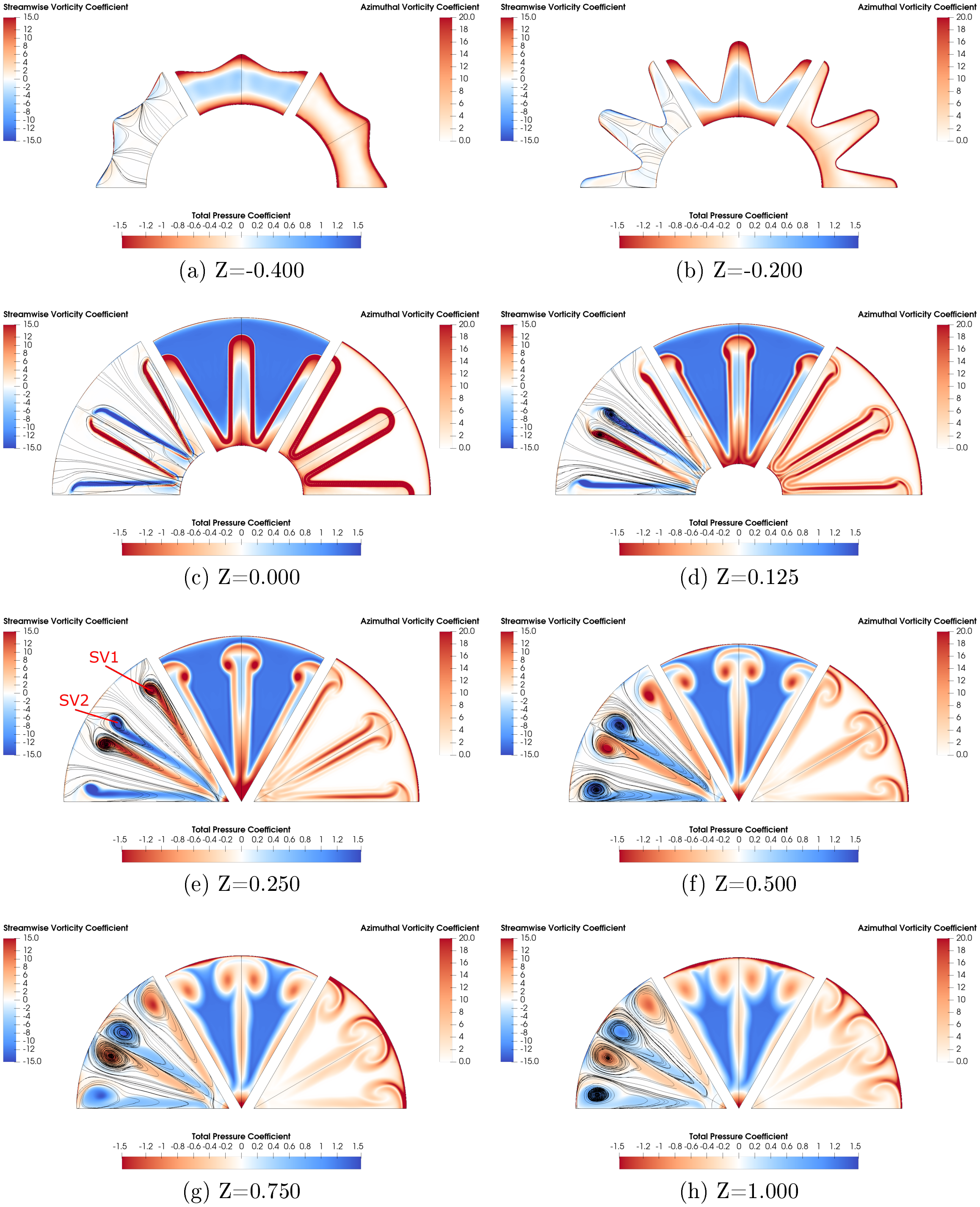

(a) Z=-0.400

(b) Z=-0.200

(c) Z=0.000

(d) Z=0.125

(e) Z=0.250

(f) Z=0.500

(g) Z=0.750

(h) Z=1.000

Figure 5.9: Contour plots of the streamwise vorticity coefficient, total pressure coefficient and azimuthal vorticity coefficient for the compressible baseline case.

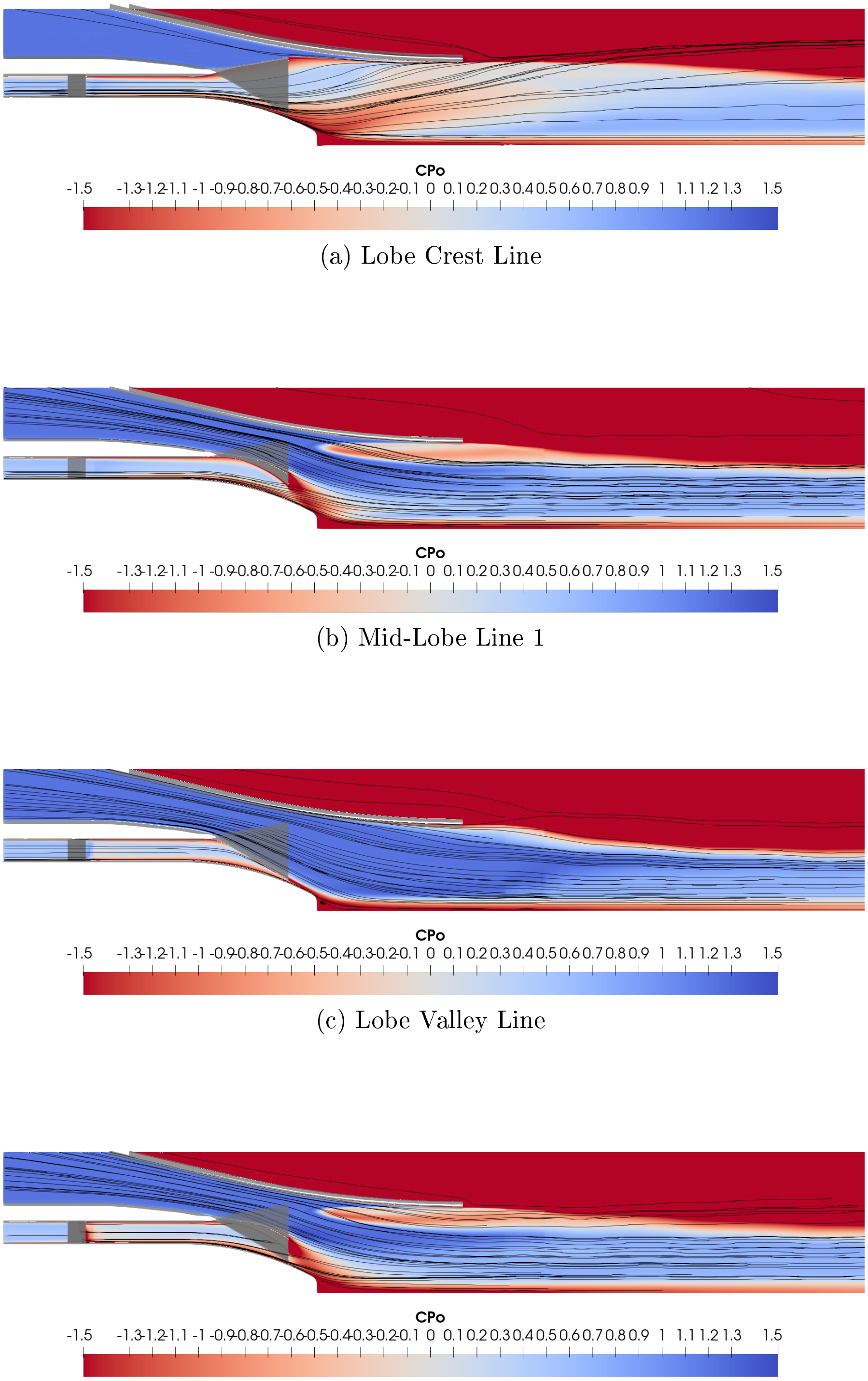

(a) Lobe Crest Line

(b) Mid-Lobe Line 1

(c) Lobe Valley Line

(d) Mid-Lobe Line 2

Figure 5.10: Meridional contours of total pressure coefficient for the compressible baseline case.

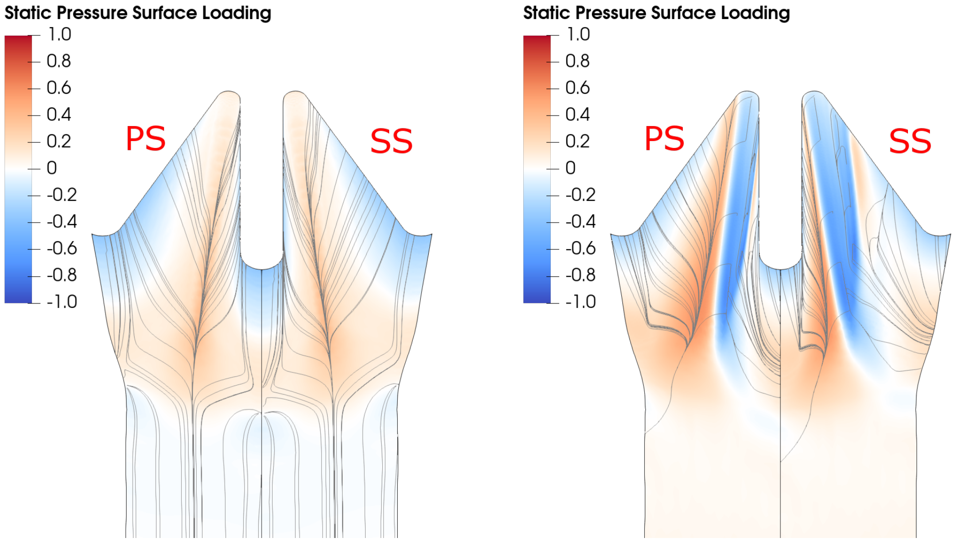

(a) Baseline

(b) 30° Swirl

Figure 5.11: Static pressure loading on the core side of the lobed mixer for the compressible cases.

fluid that was active in the azimuthal vortex on the opposite side of the lobe. This is indicated on Subfigure 5.12d. The strength of SV_{S1} is also shown to have generated a counter-rotating paired vortex, indicated as SV_{SP}.

The residual swirl also caused a large low pressure zone in the wake of the centre-body at this condition, observable in both axial and meridional planes.

Now that the flow fields and development of flow structures have been described for each case, it is prudent to remind the reader of the contents of Table 5.1. The shift from incompressible to compressible conditions resulted in the core Reynolds number dropping and the bypass Reynolds number increasing by factors of 2.8 and 3.11 respectively. These changes in Reynolds number mean that the core flow became more sensitive to viscous effects because of its lower momentum. The bypass flow changed in the opposite sense; it was less sensitive to viscous effects and possessed relatively more momentum than the incompressible condition.

Examining the Reynolds number effects help explain several of the flow field differences described previously. For instance, the impingement of the core on the nozzle at incompressible conditions was due to its high momentum at that condition.

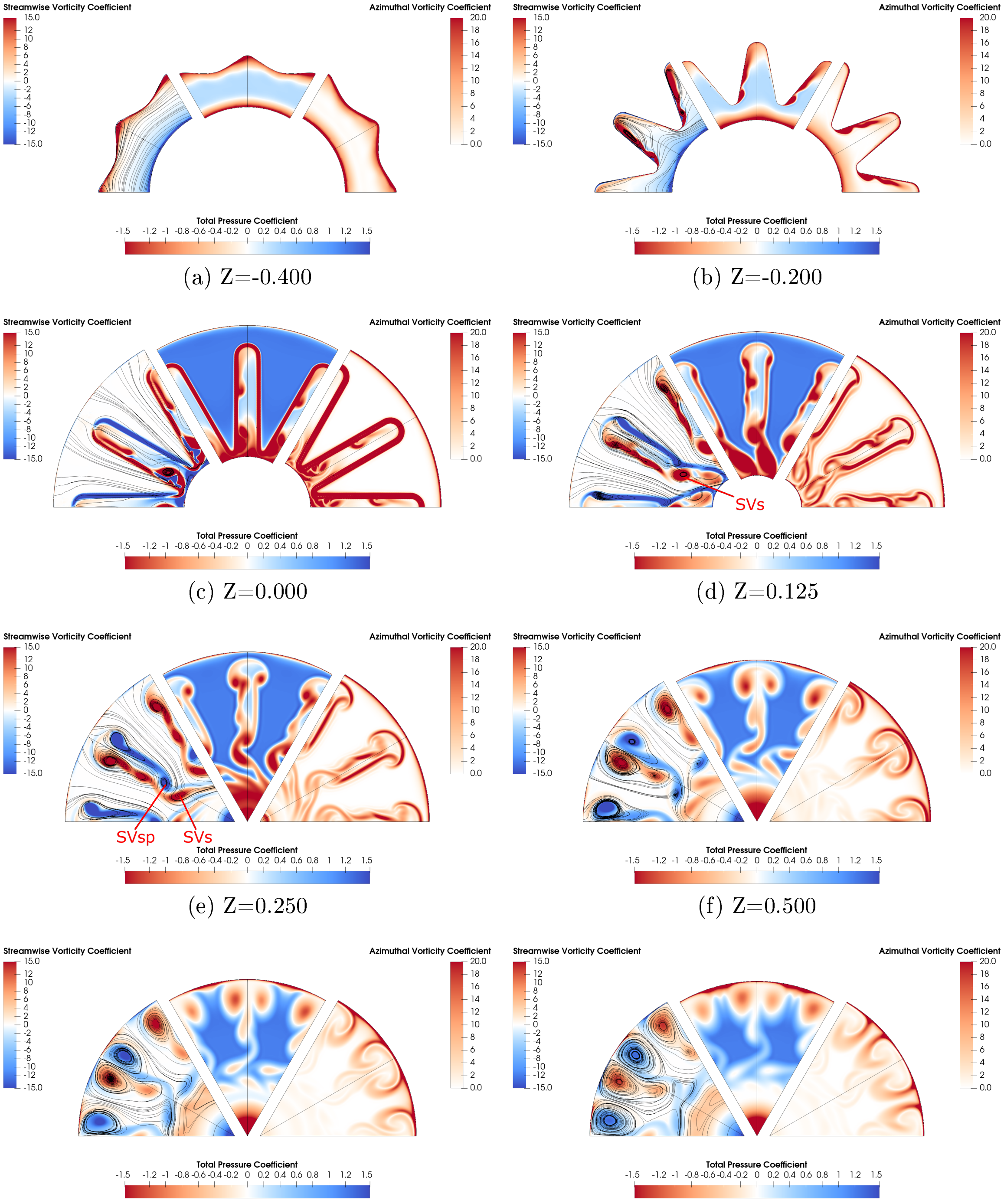

(a) Z=-0.400

(b) Z=-0.200

(c) Z=0.000

(d) Z=0.125

(e) Z=0.250

(f) Z=0.500

(g) Z=0.750

(h) Z=1.000

Figure 5.12: Contour plots of streamwise vorticity coefficient, total pressure coefficient and azimuthal vorticity coefficient at the compressible 30° swirl case.

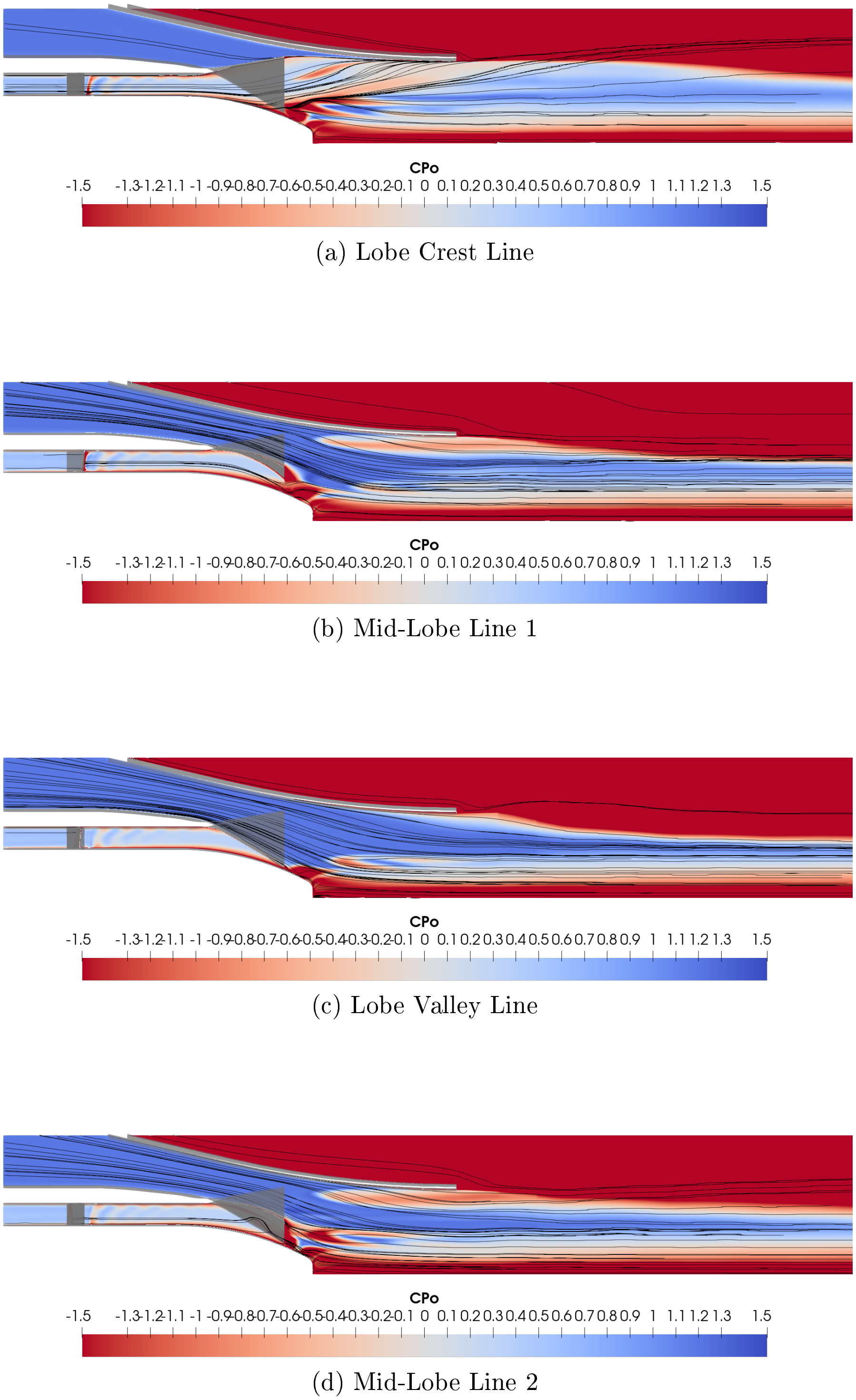

(a) Lobe Crest Line

(b) Mid-Lobe Line 1

(c) Lobe Valley Line

(d) Mid-Lobe Line 2

Figure 5.13: Meridional contours of total pressure coefficient at the compressible 30° swirl case.

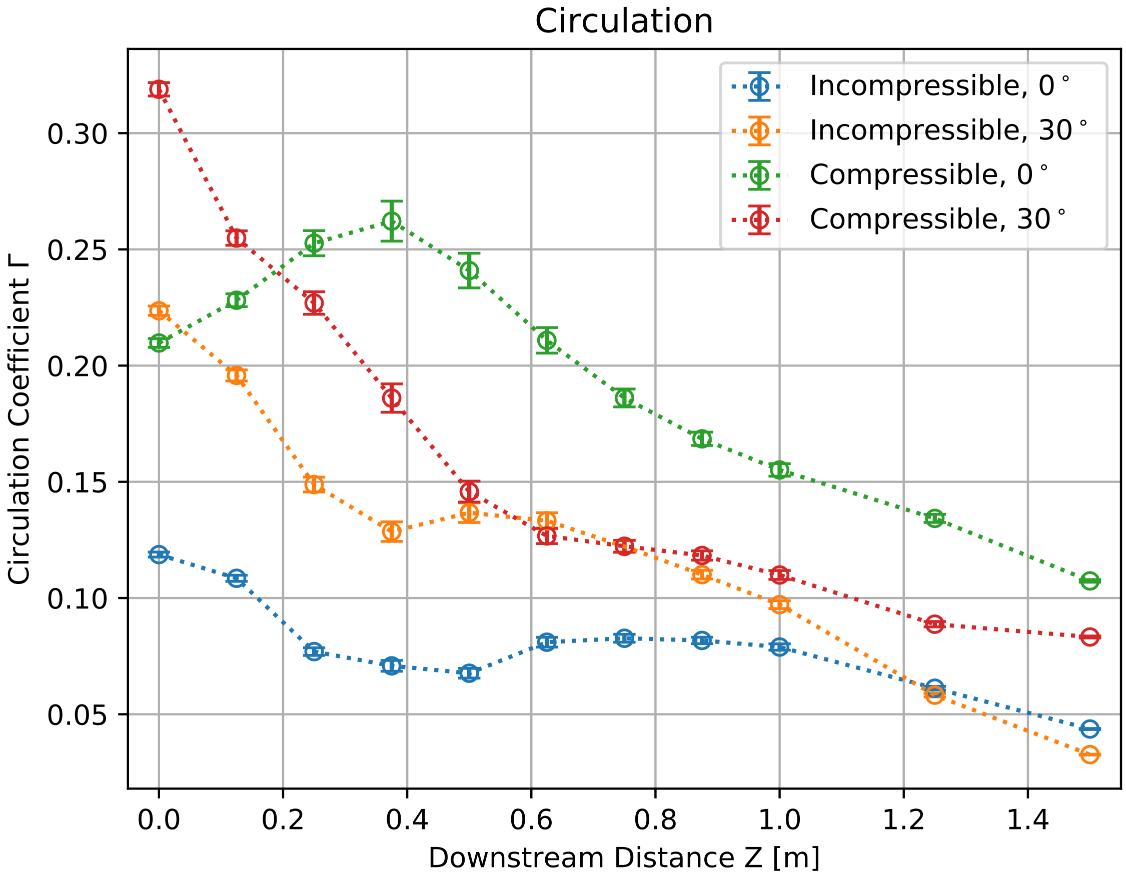

Figure 5.14: Comparison of circulation values at each boundary condition.

5.4 Performance

This section presents the effect that the change in the flow regime had on the overall performance of the exhaust system.

Circulation, Γ, is measured as the surface integral of vorticity normal to a two-dimensional plane. For measurements on the axial planes that is the same as the streamwise vorticity. The measurements were calculated over a plane covering one half lobe wavelength. Counterclockwise circulation corresponds to the side of the lobe that produced positive, counterclockwise vorticity from the perspective of Figures such as Figure 5.4. Clockwise circulation corresponds to the opposite side where negative vorticity was observed. Circulation is an indication of bulk flow mixing at a particular axial location due to the streamwise vorticity. Ideally circulation will begin with a large magnitude to indicate rapid mixing, then fall quickly as the fluid

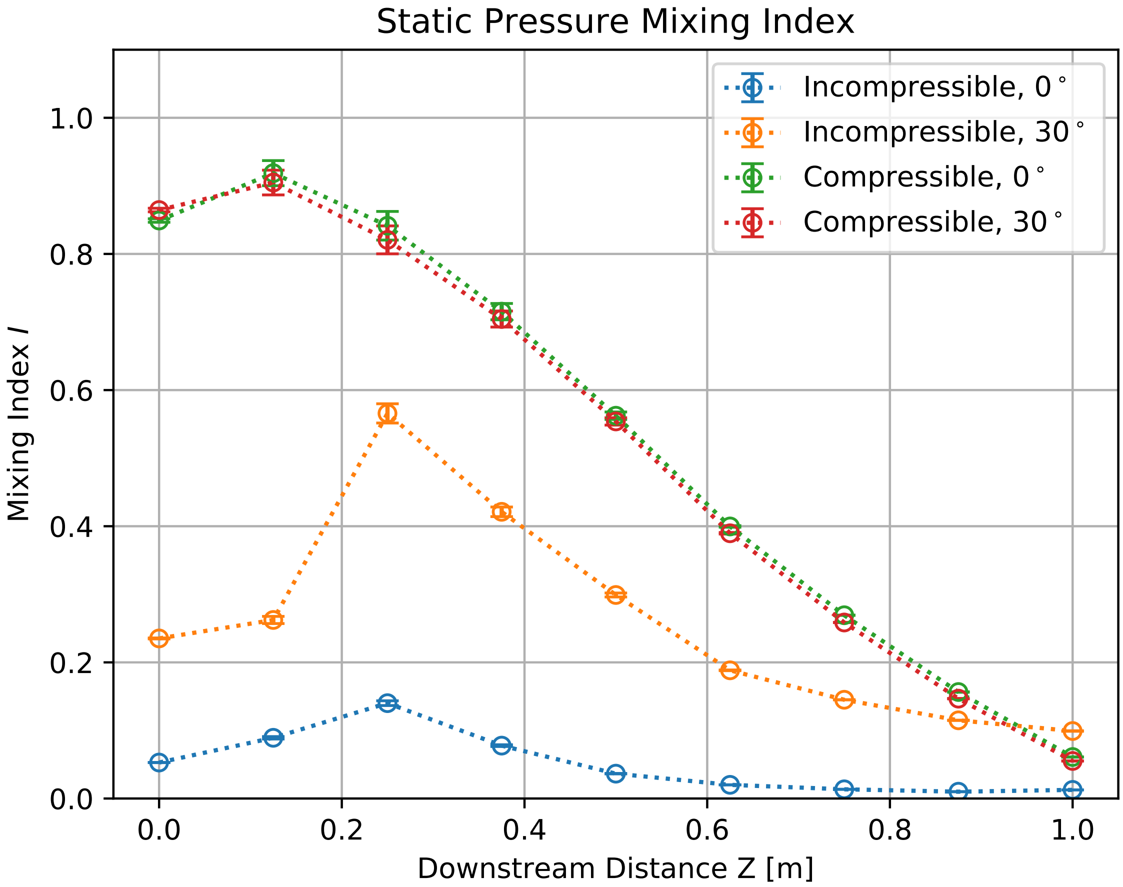

Figure 5.15: Comparison of static pressure mixing index at each boundary condition.

becomes mixed and more homogenous.

Figure 5.14 shows that incompressible conditions had slightly higher circulation values at the mixer trailing edge than at the nozzle exit plane. Case B exhibited stronger circulation thanks to the residual swirl, which manifested as positive circulation in the surface integral. The axial trends were similar for both incompressible cases. The compressible cases had higher overall circulation than their incompressible counterparts. However, the axial trends were not similar for the compressible cases. The circulation observed in case C was shown to rise steadily up to $Z = 0.375$, then decline gradually until the nozzle exit. Case D did not show the initial rise in circulation, but rather a steady drop from mixer trailing edge until the nozzle exit. Again, the increase in circulation can be explained by the residual swirl. This is a strong indication that trends between incompressible and compressible regimes are not consistent.

As circulation indicated the overall strength of the mixing mechanisms, the mixing index of static pressure, I_{PS}, provides information about the effectiveness and completeness of the mixing. Its formulation is very similar to a statistical variance which conveys information on how far any individual data point may be from the mean of a population. That feature of the mixing index offers two insights into the mixing and uniformity of the flow. A high mixing index indicated a highly variant and likely active mixing flow. A low mixing index, approaching zero, indicated a more uniform flow with consistent measurement throughout the plane. Like circulation, this measurement ideally peaks early in the mixing duct and falls quickly toward zero.

The plots in Figure 5.15 show the static pressure mixing index for the four cases presented in this chapter. The incompressible cases once again show similar trends but with different magnitudes. The static pressure mixing index increased up to $Z = 0.250$ where the mixing rate reached the maximum, then dropped throughout the nozzle. The incompressible cases, on the other hand, show remarkable similarity in axial trend and magnitude. The presence of swirl showed no effect on the static pressure mixing index for incompressible conditions.

The nozzle pressure loss coefficient, Y, as defined in Equation 4.6, measures the change in average total pressure from the reference plane upstream of the mixer to the measurement plane. This indicates the efficiency of the exhaust system by quantifying friction and viscous losses.

Table 5.4 shows that the losses increased with core inlet swirl for both incompressible and compressible cases. This is a situation where the trends matched regardless of compressibility. Higher core flow swirl produced greater losses under both conditions, as expected from analysis of the flow fields.

Finally, Table 5.4 summarizes the thrust coefficients of each case. The thrust coefficient, as calculated according to equations 4.11 and 4.12, is the most important performance parameter for the engine. According to the data, there was not a significant change in the thrust coefficient when the core flow swirl increased at either flow condition.

Table 5.4: Nozzle total pressure loss and thrust coefficient performance comparison.

Flow	Swirl	Y	C_T
Incompressible	0° Swirl	34.1	51.9
	30° Swirl	39.4	52.0
Compressible	0° Swirl	63.3	62.8
	30° Swirl	69.7	62.9

5.5 Conclusions

The purpose of this chapter was to provide evidence whether incompressible flow conditions were able to accurately provide a model for medium bypass turbofan engine exhaust systems which operate in the compressible flow regime. This chapter provided insight into the various flow structures developed in the mixing region of the exhaust system. Flow field parameters were presented in the form of contour plots of streamwise vorticity, azimuthal vorticity and total pressure coefficient. System performance data was presented through scatter plots of circulation, static pressure mixing index and total pressure loss versus distance downstream of the mixer to the nozzle.

The data showed that the trends in exhaust system performance when operating at either incompressible or compressible flow regimes diverged for certain parameters like static pressure mixing index but agreed for overall performance parameters like total pressure loss. When considered in conjunction with the flow field data—which showed clear differences between flow regimes—it has been concluded that compressible condition simulations should be the main consideration moving forward. The original assumption had been based on research that did not include lobed mixers. Those assumptions have been investigated further and presented in Chapter 9.

The next chapter shall build from this information and utilize compressible flow simulations to determine the effect of scalloping on exhaust system performance. Scalloping refers to the removal of a portion of the lobe side wall to increase the trailing edge perimeter and also reduce mixer weight. It is the next step in the process of solving the problem posed in this thesis.

Chapter 6

Effects of Scalloping Depth

The previous chapter confirmed the status quo modeling procedure was insufficient for simulating the performance of MBTF exhaust systems with lobed mixers. A proper simulation requires the flow regime to be similar to real world conditions: compressible and non-isothermal. This chapter will utilize that discovery to begin the inquest for the answer to the problem at hand. The MBTF exhaust system design is a candidate for reductions in mass and therefore overall fuel consumption of the engine. The study begins by investigating the lobed mixer geometry in more detail, specifically scalloping. Scalloping is shown to introduce further flow structures into the mixing field and improve flow uniformity at the nozzle exit.

6.1 Introduction

Chapter 5 showed that large-scale counter-rotating streamwise vortices are generated due to the radially defected core and bypass flow through the mixer lobes. Those vortices tended to stay toward the outer portion of the jet—near the nozzle wall—regardless of the flow regime. The mixing should be improved by the generation of streamwise vorticity that remains nearer to the core of the jet. Scalloping, the removal of a portion of the parallel side walls within the penetration region of the mixer, could achieve that goal.

The strength of streamwise vorticity has been shown to be a function of the lobed mixer geometry [45, 49]. Mixers with scalloped lobes have been reported to offer a significant increase in mixing effectiveness with minimal impact on total pressure loss [8, 68]. Additional streamwise vortices were found to be formed along the inner edge of the scallop, co-rotating along with the primary vortices on their respective sides of the lobe [51]. There are extensive studies of scalloped mixers in the literature but, apart from the research group at National Research Council Canada (NRC), there has been little investigation on the performance of scallops when the core flow had swirl. Swirling flows have been shown to decrease thrust and increase specific fuel consumption [68]. This chapter will advance the investigations already completed at NRC [59, 54] with their incompressible modeling and look at the performance of various scalloping depths when presented with 30° swirl within the core at compressible and non-isothermal flow conditions.

This chapter presents data on the flow fields and structures within, the strength of vorticity, the overall circulation, the overall pressure loss and other performance parameters. Data is presented on ten cases of varying scallop depths and core swirl conditions which will be expanded upon in the next section.

6.2 Methodology

There are ten simulations presented in this chapter, five different mixer geometries and two different core flow swirl values. These simulations are organized in a way to illustrate the effects and effectiveness of lobed mixer scalloping on MBTF exhaust system flow structures and performance. All ten cases were simulated with the same compressible boundary conditions outlined in the next section. The investigation was designed to reveal a causal relationship between the scallop depth and the changes to flow structures and system performance.

6.2.1 Boundary Conditions

Chapter 5 concluded that accurate simulations of MBTF exhaust systems are conducted using compressible boundary conditions. Those boundary conditions are tabulated in Table 6.1. These conditions were chosen because they represent a general cruise condition for the MBTF model.

6.2.2 Test Geometries

There are two baseline cases presented that match the compressible cases previously discussed in Chapter 5. These baseline cases showcase the flow field and performance of the unscalloped mixer at both ideal inlet conditions with 0° core swirl and off-design conditions with 30° core swirl. Each subsequent mixer geometry is presented with both swirl conditions side-by-side for comparison. The mixers tested have gradually

Table 6.1: High-speed compressible boundary conditions based on comparable commercial engine cruise conditions.

Boundary	Type	Value
Core	Total Pressure	43.0 kPa
	Total Temperature	728 K
	k	$5\,\mathrm{m^2\,s^{-2}}$
	ϵ	$30\,000\,\mathrm{m^2\,s^{-3}}$
Bypass	Total Pressure	45.1 kPa
	Total Temperature	273 K
	k	$5\,\mathrm{m^2\,s^{-2}}$
	ϵ	$30\,000\,\mathrm{m^2\,s^{-3}}$
Free Stream	Total Pressure	18.9 kPa
	Total Temperature	223 K
	k	$5\,\mathrm{m^2\,s^{-2}}$
	ϵ	$30\,000\,\mathrm{m^2\,s^{-3}}$
Outlet	Average Static Pressure	18.8 kPa

increasing scalloping depths from 25% up to 75% of the total mixer length. Finally, a partially-optimized scallop profile is presented. The mixers were tested with and without swirl in order to confirm the proper amount of scalloping to be used in solving the problem posed in this thesis. The final scalloped mixer was designed based on the analyses presented in this chapter and previous literature.

The test geometries used in this chapter were based on the unscalloped mixer used in Chapter 5. The five geometries in total feature that unscalloped mixer as a baseline, three test geometries and one final geometry. Figure 6.2 presents the Baseline and Test mixer geometries. As mentioned previously, the lobed mixers used for these simulations have a total length of 100 mm, a rise angle of 10° and a fall angle of 30°. The crest radius is 10 mm and the valley radius set such that the sidewalls remain parallel and tangent to the crest. The trailing edge thickness is 1 mm.

The scallop profile was designed with certain rules in mind:

1. The scallop depth was prescribed based on a percentage of the total mixer length.

2. The outer edge of the profile must remain parallel to the lobe crest line.

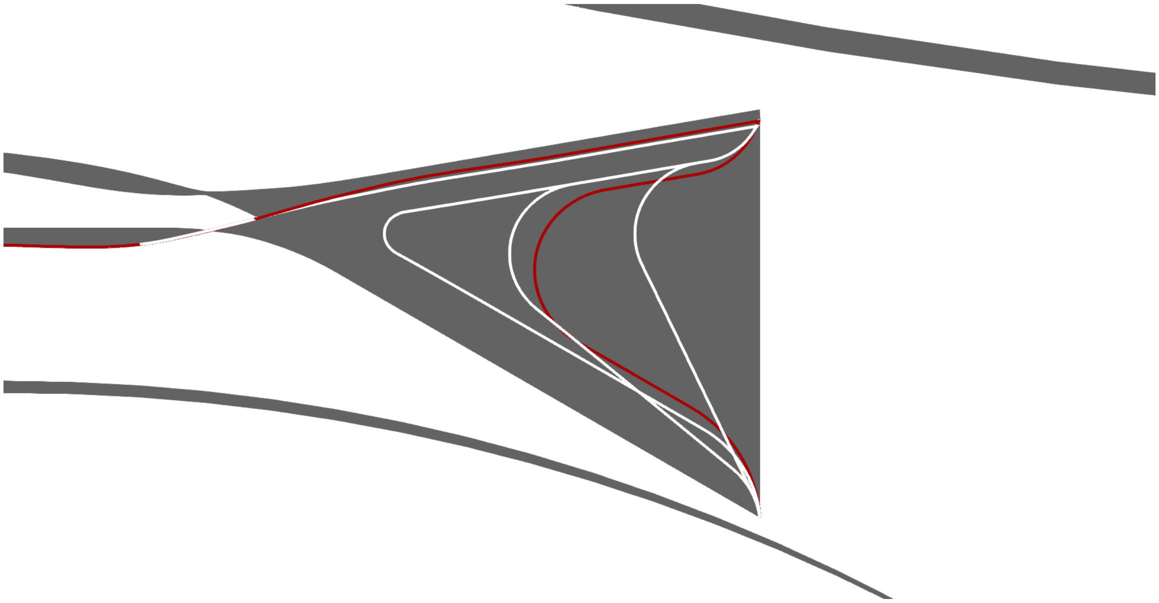

Figure 6.1: The side view outline of the lobed mixer scalloping profiles.

3. The outer edge of the profile must be offset from the crest line by 10 mm.

4. The inner edge of the profile may create a positive angle with the valley line but must not pass parallel.

5. The radius of curvature on the upstream edge must be no larger than 20 mm but may be reduced to maintain preceding rules.

The scallop profiles that resulted from these design rules are shown in Figure 6.1. The test geometry profiles are presented in white, while the final profile is presented in red. Scalloping allows for a larger trailing edge perimeter compared to an unscalloped mixer with the same overall dimensions. The deeper the scallop, the larger the perimeter and therefore interfacial area for core and bypass flow to interact.

Shallow Scalloped Mixer

The first test mixer has a scallop that extends 25 mm upstream from the unscalloped trailing edge. This produced a shallow scallop with an inner edge that is not near parallel with the mixer valley line as seen in Figures 6.1 and 6.2b.

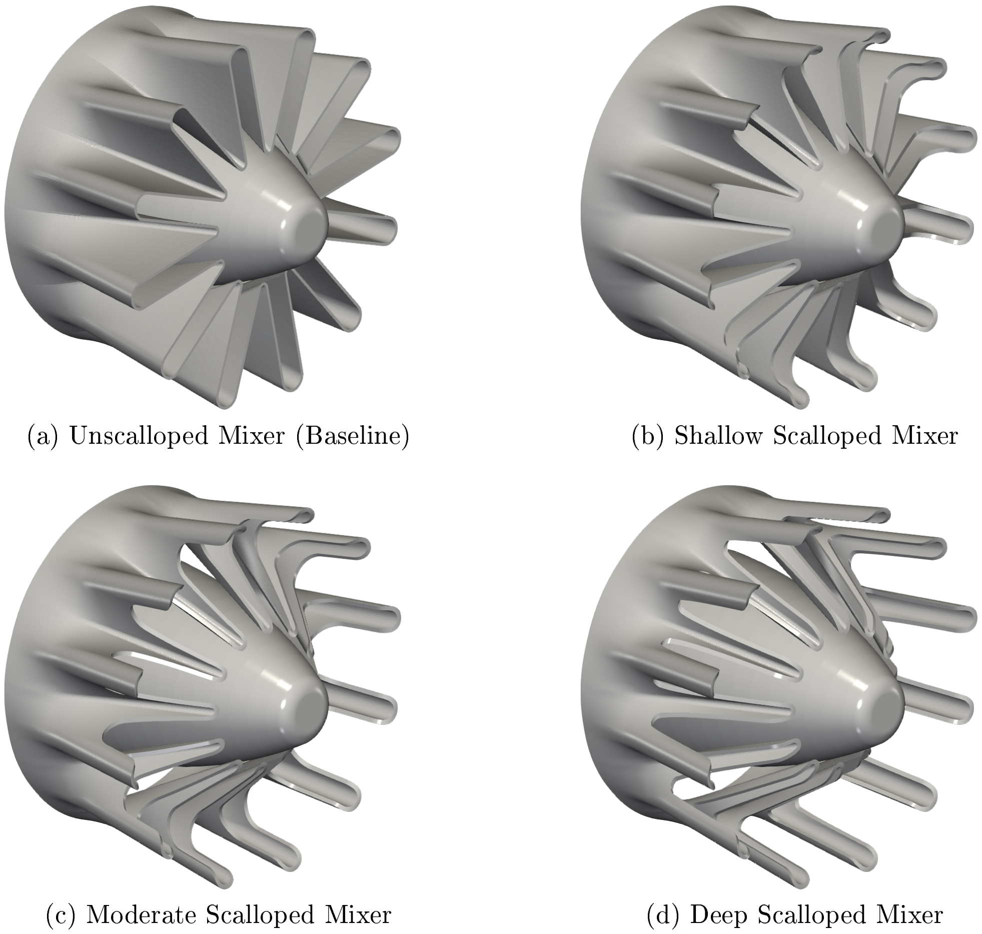

(a) Unscalloped Mixer (Baseline)

(b) Shallow Scalloped Mixer

(c) Moderate Scalloped Mixer

(d) Deep Scalloped Mixer

Figure 6.2: Full 12-lobed mixers used in the scalloping investigation.

Moderate Scalloped Mixer

The second test mixer has a scallop that extends 50 mm upstream from the unscalloped trailing edge. This produced a moderate scallop with an inner edge nearing parallel with the valley line as seen in Figures 6.1 and 6.2c.

Deep Scalloped Mixer

The third test mixer has a scallop that extends 75 mm upstream from the unscalloped trailing edge. This produced a deep scallop with a reduced radius of curvature in order to maintain parallel with the valley line as seen in Figures 6.1 and 6.2d.

Parallel Moderate Scalloped Mixer

The final scallop profile, shown in Figure 6.3, was devised based on the findings presented in the earlier parts of this chapter. The reader may notice that it embraces features of each test geometry like a moderate scallop and an inner edge parallel to the valley line. These features will be expanded on in Section 6.3.6.

The next section discusses the exhaust system flow fields and performance that results from the above mentioned modifications to the lobed mixer.

6.3 Results and Discussion

The results of the ten simulations were analyzed to discuss the influence of scalloping on vortical structures and jet-flow mixing. As mentioned, three levels of scalloping were simulated and compared against each other and the baseline unscalloped mixer under no swirl and swirl conditions. The highest swirl of 30° was chosen to represent the swirl condition.

6.3.1 Baseline Flow Field

Unscalloped Mixer

This case is the same as the Compressible Baseline case described in Section 5.3.2. A detailed description of the baseline flow field is found there. To summarize, the streamwise vortex begins developing immediately at the mixer trailing edge,

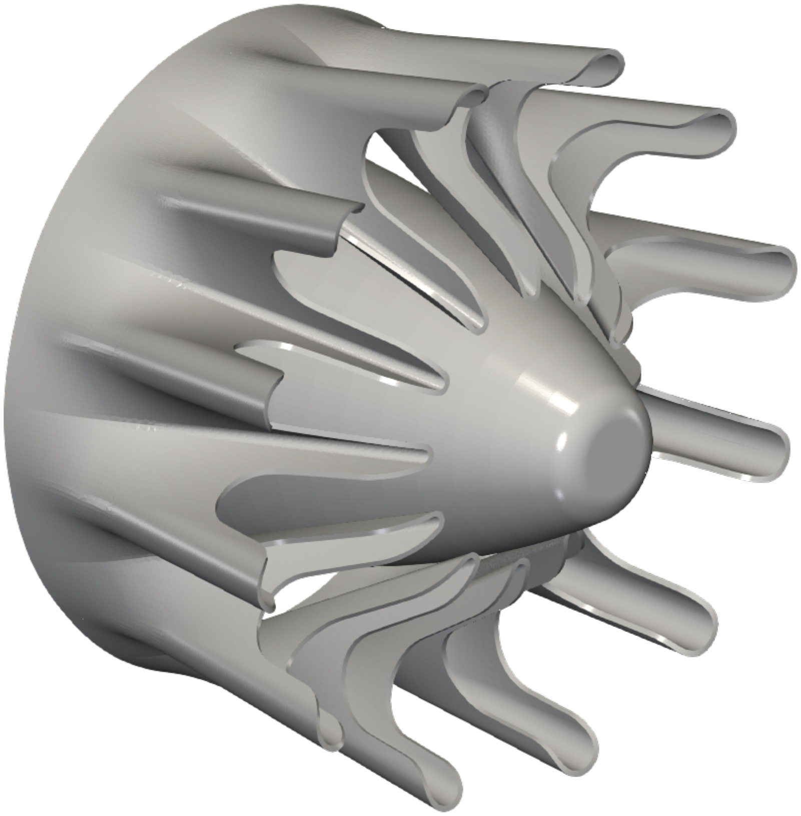

Figure 6.3: The parallel moderate scalloped mixer.

$Z = 0.000$, at a length scale approximately equal to the lobe height. The streamwise vortices, SV_1 and SV_2 quickly formed distinct vortex cores, marked at $Z = 0.250$. The streamwise vortex and the azimuthal vortex interacted with each other which resulted in the azimuthal vortex becoming distorted and pinched into distinct regions of vorticity, marked at $Z = 0.500$. The meridional planes indicated in Figure 6.5 display the degree of bulk flow mixing that was provided via the interaction of streamwise and azimuthal vorticity.

Figures 6.4 and 6.5 have been reprinted for the benefit of the reader to make easier comparisons to the upcoming test cases with various scallop depths.

6.3.2 Test Cases

The three test cases are presented in order of scallop depth: shallowest to deepest. First is the Shallow Scallop, which extends 25 mm upstream of the lobed mixer trailing edge at its deepest point.

Shallow Scallop

There are few changes to the flow field because of the shallow scallop. The most remarkable differences between Figure 6.4 and 6.6 are visible at $Z = 0.000$ where the contours of the three coefficients are no longer as uniform along the lobed mixer's trailing edge. The scallop allows the flow structures to begin interacting at an advanced point in the ducting. That early interaction can be observed in the development rate of the structures as compared to the unscalloped mixer. The vorticity strength and development is leading that of the unscalloped mixer.

The other clear difference is the shape of the structures. The total pressure of the bypass flow is higher than that of the core flow. This pressure differential drives the bypass fluid to expand into the core fluid. The marker on Figure 6.6d makes this clear as the flow structures appear pinched toward each other in the direction of the core fluid. The Mid-Lobe lines of Figure 6.7 also assist the illustration of that point. The bypass fluid makes a distinct curve downward toward the core in the wake of the scallop.

Such a shallow scallop was able to produce distinct changes to the flow field.

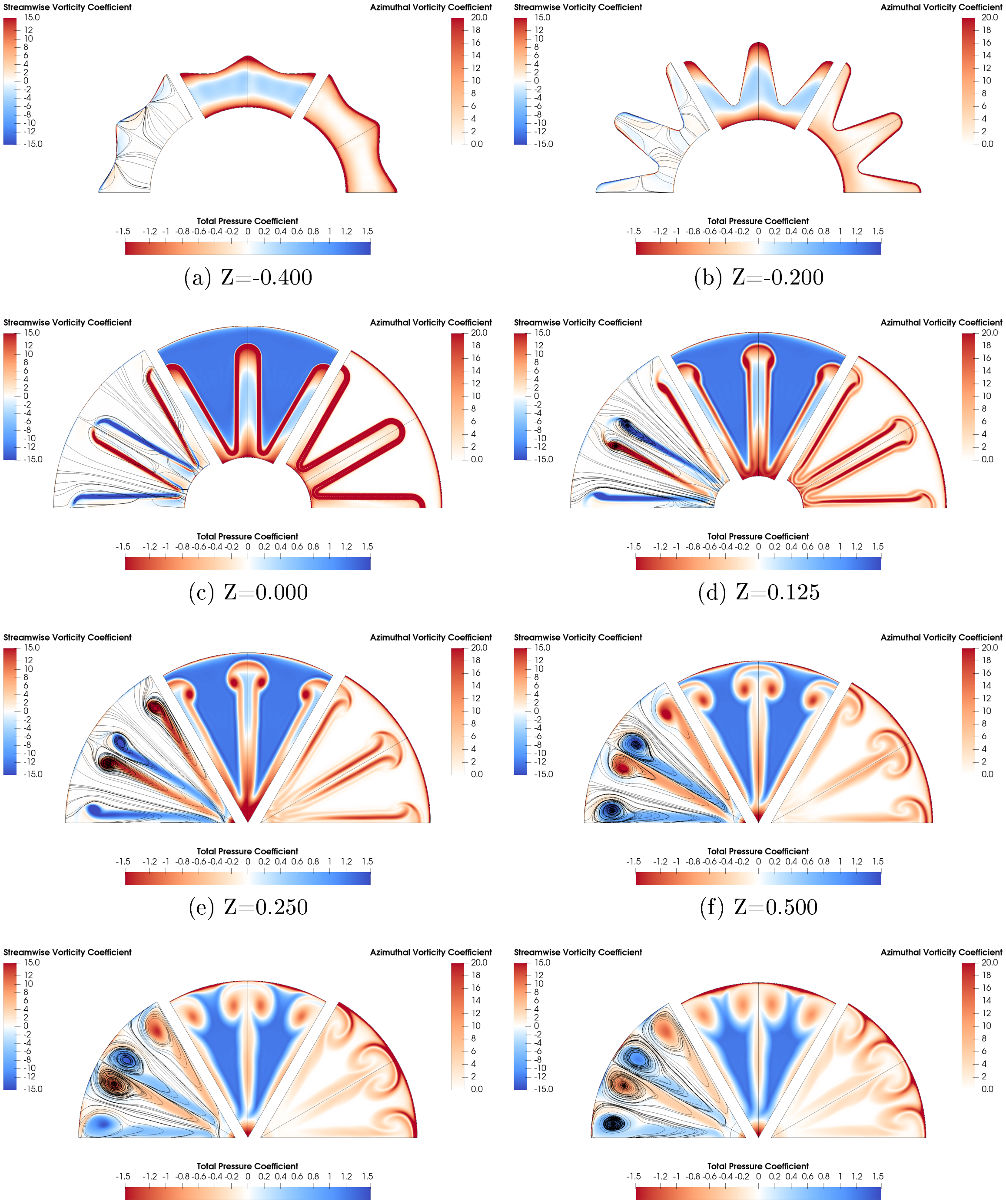

(a) Z=-0.400

(b) Z=-0.200

(c) Z=0.000

(d) Z=0.125

(e) Z=0.250

(f) Z=0.500

(g) Z=0.750

(h) Z=1.000

Figure 6.4: Contour plots of streamwise vorticity coefficient, total pressure coefficient and azimuthal vorticity coefficient, unscalloped mixer, no swirl.

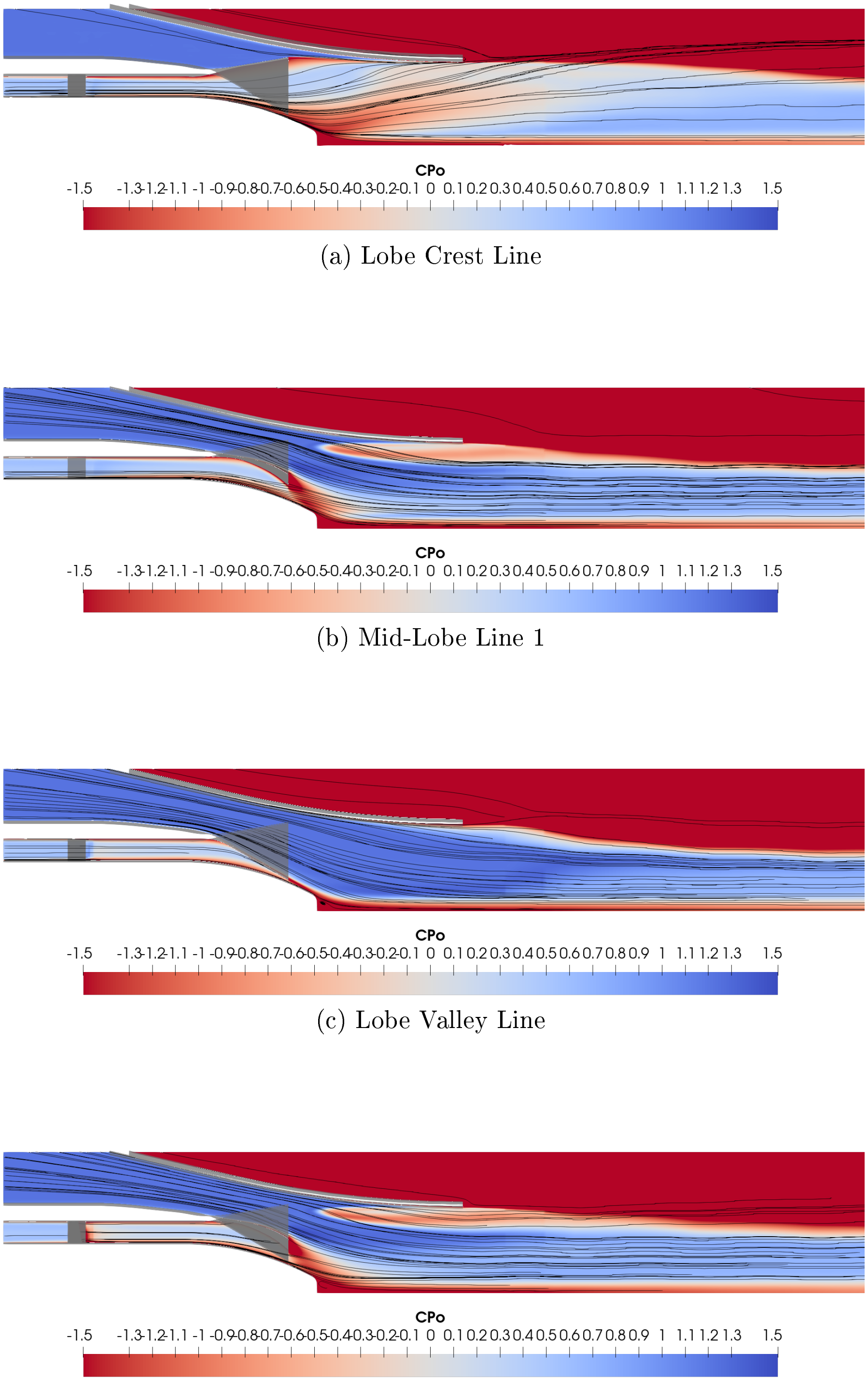

(a) Lobe Crest Line

(b) Mid-Lobe Line 1

(c) Lobe Valley Line

(d) Mid-Lobe Line 2

Figure 6.5: Meridional contours of total pressure coefficient, unscalloped mixer, no swirl.

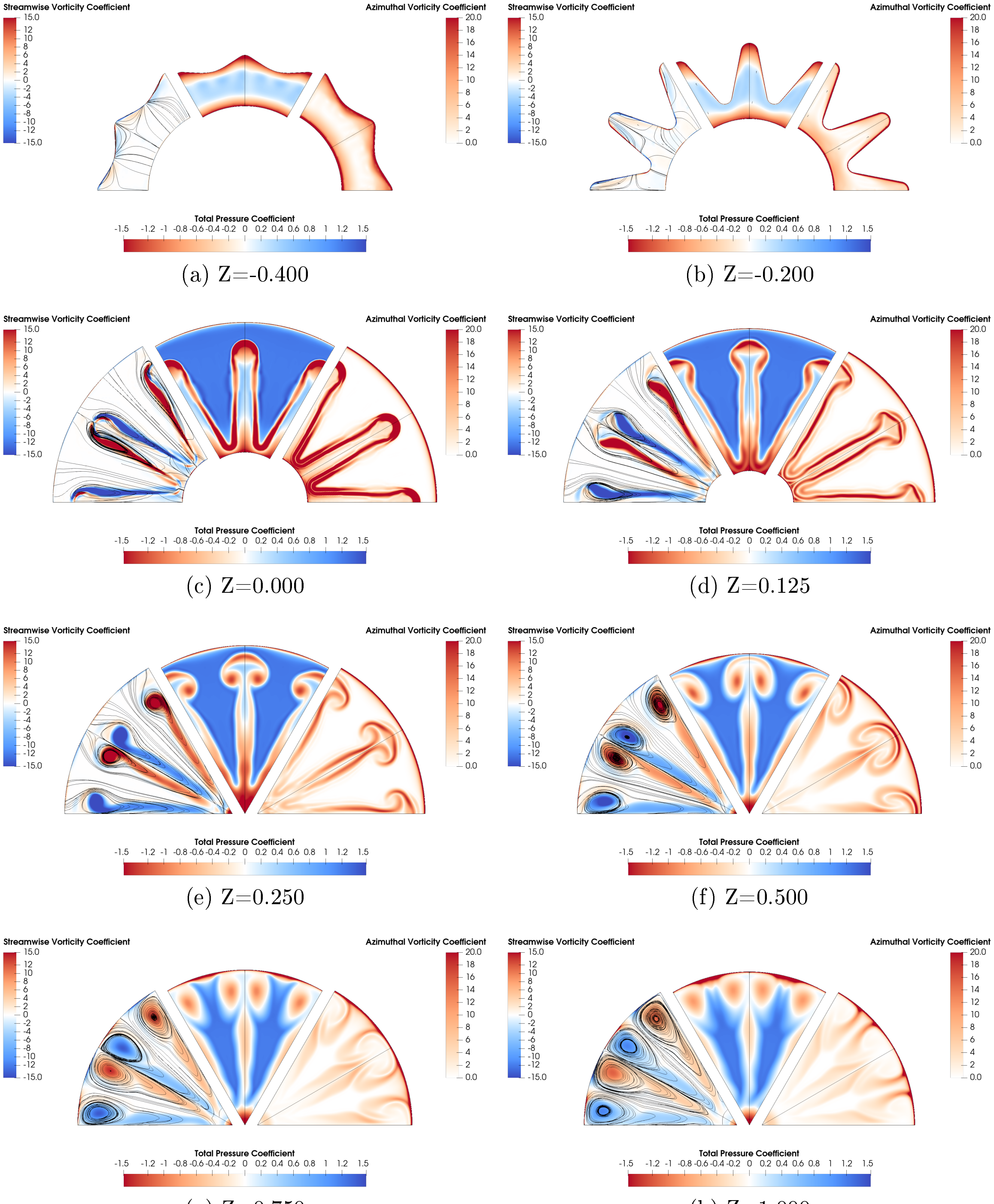

(a) Z=-0.400

(b) Z=-0.200

(c) Z=0.000

(d) Z=0.125

(e) Z=0.250

(f) Z=0.500

(g) Z=0.750

(h) Z=1.000

Figure 6.6: Contour plots of streamwise vorticity coefficient, total pressure coefficient and azimuthal vorticity coefficient, shallow scallop, no swirl.

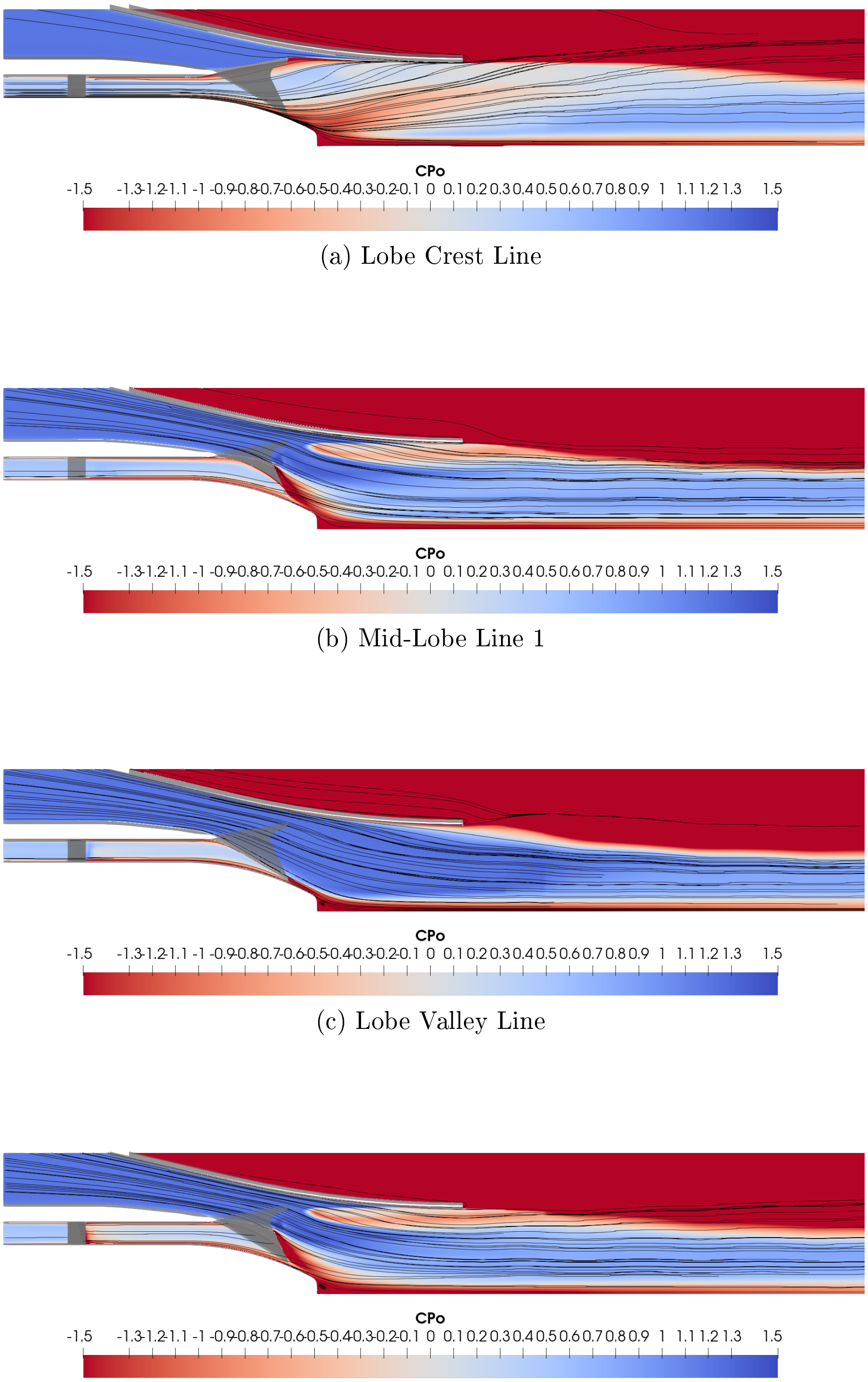

(a) Lobe Crest Line

(b) Mid-Lobe Line 1

(c) Lobe Valley Line

(d) Mid-Lobe Line 2

Figure 6.7: Meridional contours of total pressure coefficient, shallow scallop, no swirl.

Moderate Scallop

The moderate scallop lobed mixer flow fields are presented in Figures 6.8 and 6.9. Figure 6.1 illustrates that the scallop becomes much more pronounced at this depth. The lower edge was nearing parallel with the valley and a much larger area of the lobed mixer side wall was removed.

The core and bypass fluid was able to interact upstream of the $Z = -0.200$ plane as shown in Figure 6.8b. The even earlier interaction of the vortices left the azimuthal vortex notably weaker at the $Z = 0.125$ plane as compared to the same axial location for the shallow scallop. New streamwise vortex structures were generated near the center of the jet as denoted at the $Z = 0.250$ plane. These new streamwise vortices, labeled SV_3 and SV_4, were generated because of the angle of the scallop's lower edge with respect to the flow direction. The direction of the counter-rotating vortices indicate that they were also a result of the radially deflected flows of core and bypass fluids. However, they did not merge or interact with the main streamwise vortices, SV_1 and SV_2, nearer to the nozzle. They did interact with the azimuthal vortex and resulted an another region of distortion and 'pinching-off' as labeled at plane $Z = 0.500$. The new vortices were weaker and dissipated by the time the flow reached $Z = 0.750$, as illustrated by the limiting streamlines of velocity vector. At that point, they had dissipated into small scale turbulence.

The deeper scallop allowed the low total pressure zone in the wake of the mixer to have begun dissipating and mixing out by the time the fluid reached the $Z = 0.000$ plane.

The remarkable difference between the shallow and moderate scallop lobed mixer flow fields served as an indicator that deeper scalloping should produce further differences to the flow features. Next is the deep scallop in which the deepest point of the scallop extended 75 mm upstream of the unscalloped lobed mixer trailing edge, also referred to as the mixer exit plane.

Deep Scallop

The streamwise vortices, SV_1 and SV_2, began forming coherent cores at the $Z = -0.200$ plane—well before the mixer exit plane. The cores can be identified in the streamwise vorticity and total pressure coefficient plots. The azimuthal vortex was

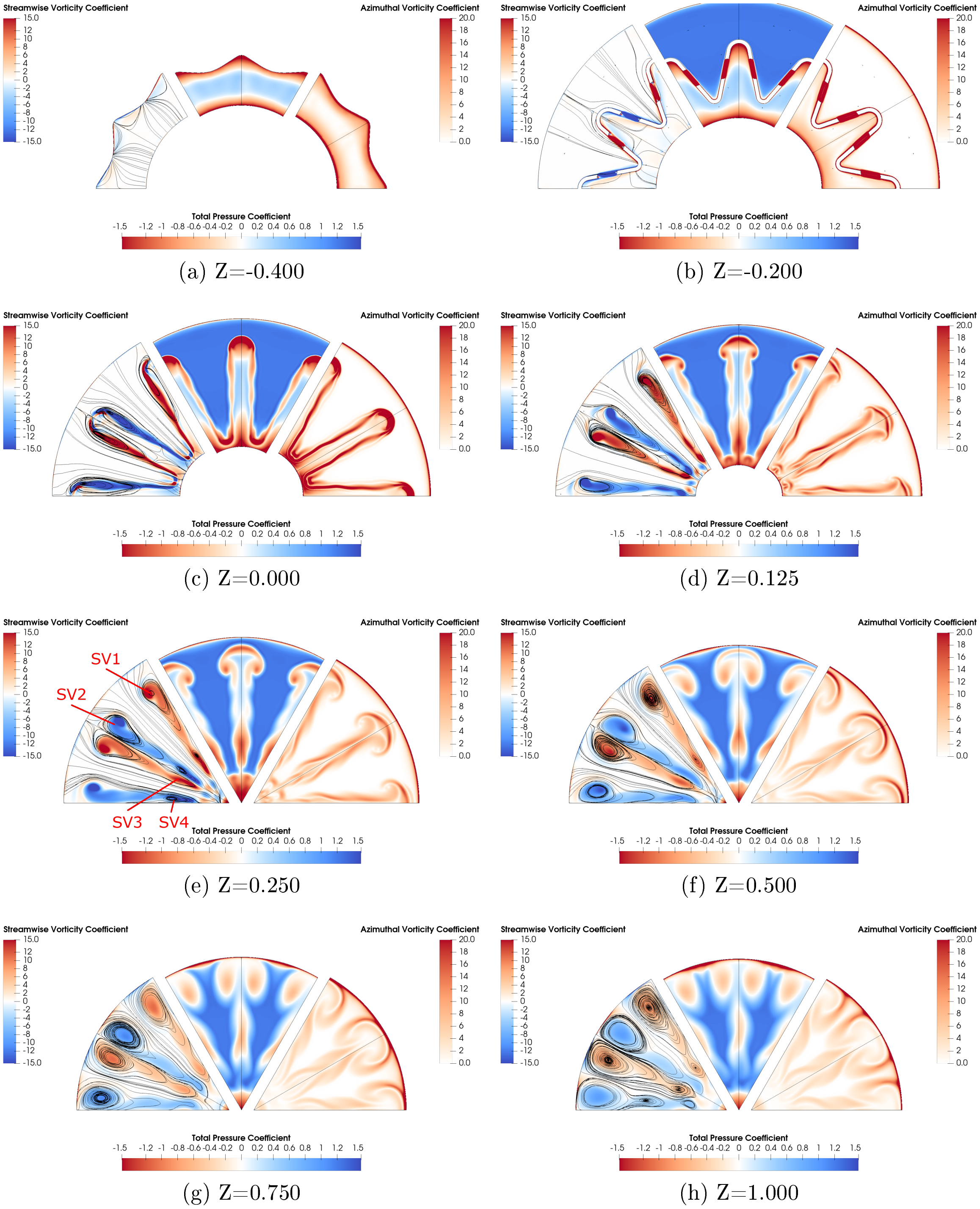

(a) Z=-0.400

(b) Z=-0.200

(c) Z=0.000

(d) Z=0.125

(e) Z=0.250

(f) Z=0.500

(g) Z=0.750

(h) Z=1.000

Figure 6.8: Contour plots of streamwise vorticity coefficient, total pressure coefficient and azimuthal vorticity coefficient, moderate scallop, no swirl.

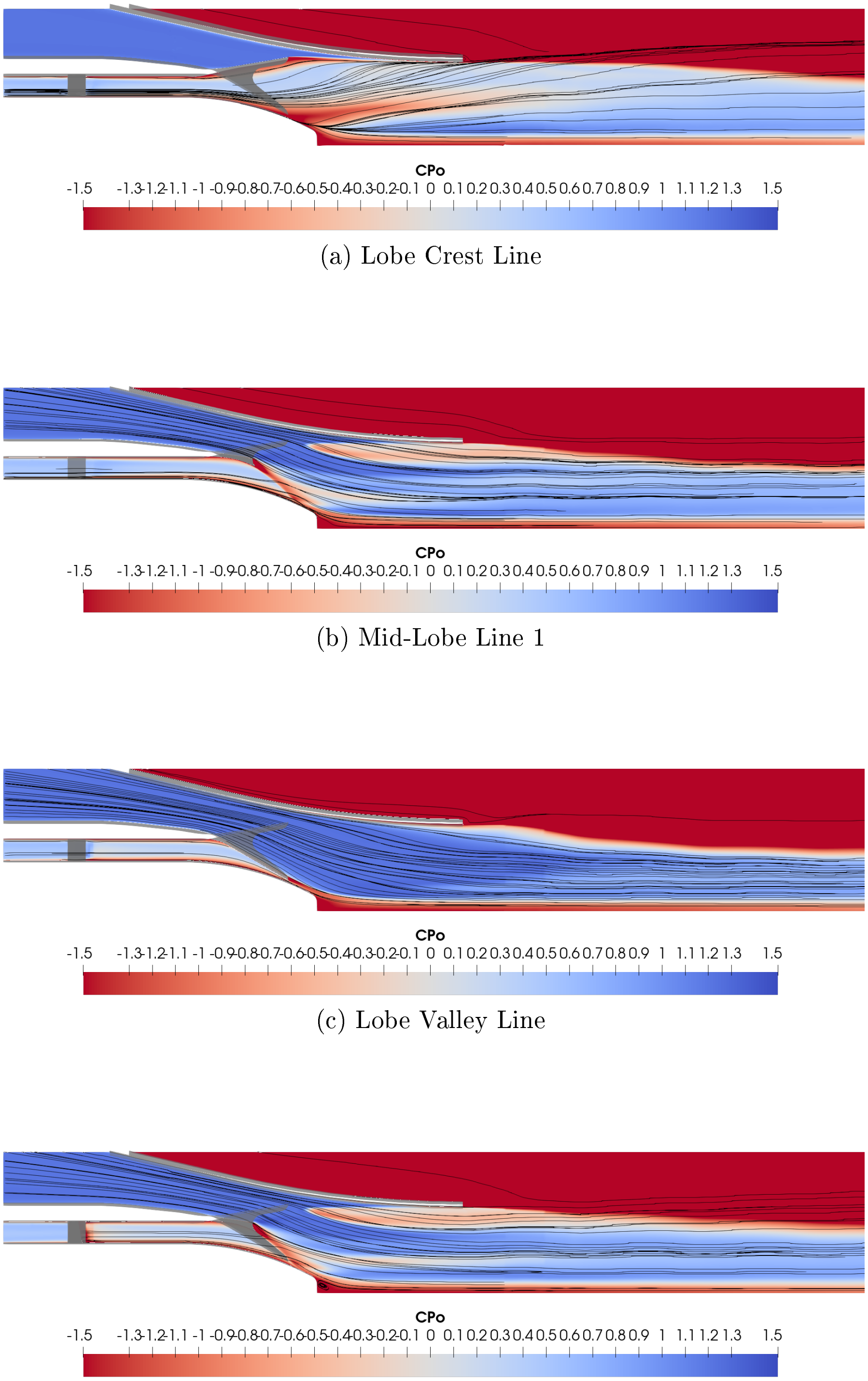

(a) Lobe Crest Line

(b) Mid-Lobe Line 1

(c) Lobe Valley Line

(d) Mid-Lobe Line 2

Figure 6.9: Meridional contours of total pressure coefficient, moderate scallop, no swirl.

already distorted by the entrainment of the streamwise vortices. At $Z = 0.000$, the azimuthal vortex had already been 'pinched-off' and split into separate, discrete structures. The mixer exit plane also shows the development of more streamwise vortices developing at the radial locations where the outer and inner edges of the scallop reside. The fifth and sixth cores, labeled SV_5 and SV_6, were observed to interact and merge with the first cores developed. The process can be seen by following the development of the streamwise vorticity coefficient contour plots from plane $Z = 0.000$ to $Z = 0.500$, at which point only four vortex cores remain. SV_3 and SV_4 remain as coherent structures further downstream for this deep scallop than what was seen for the moderate scallop.

The flow field within the mixing duct of a MBTF exhaust system has been shown to be affected by lobed mixer scalloping at a condition with no swirl in the core flow. The next section presents the same progression of lobed mixer scalloping—from unscalloped to a deep scallop—when presented with 30° swirl in the core flow.

6.3.3 Baseline, High Swirl

This case of the unscalloped lobed mixer subjected to 30° core swirl is the same as that presented in Section 5.3.2, where a detailed description of the flow field exists.

Unscalloped

To summarize the flow field description in Chapter 5:

- A separation formed on the 'suction side' of the lobed mixer because of the core flow's 30° angle of attack.
- The separation formed a region of strong positive streamwise vorticity, SV_{S1}.
- The strength of SV_{S1} induced a counter-rotating paired vortex, SV_{SP}.
- The residual swirl induced a large low-pressure zone in the wake of the centrebody, seen in Figure 6.13.

Let us now move on to review the data on the effect that scalloping produces within the flow field when the core flow is swirling.

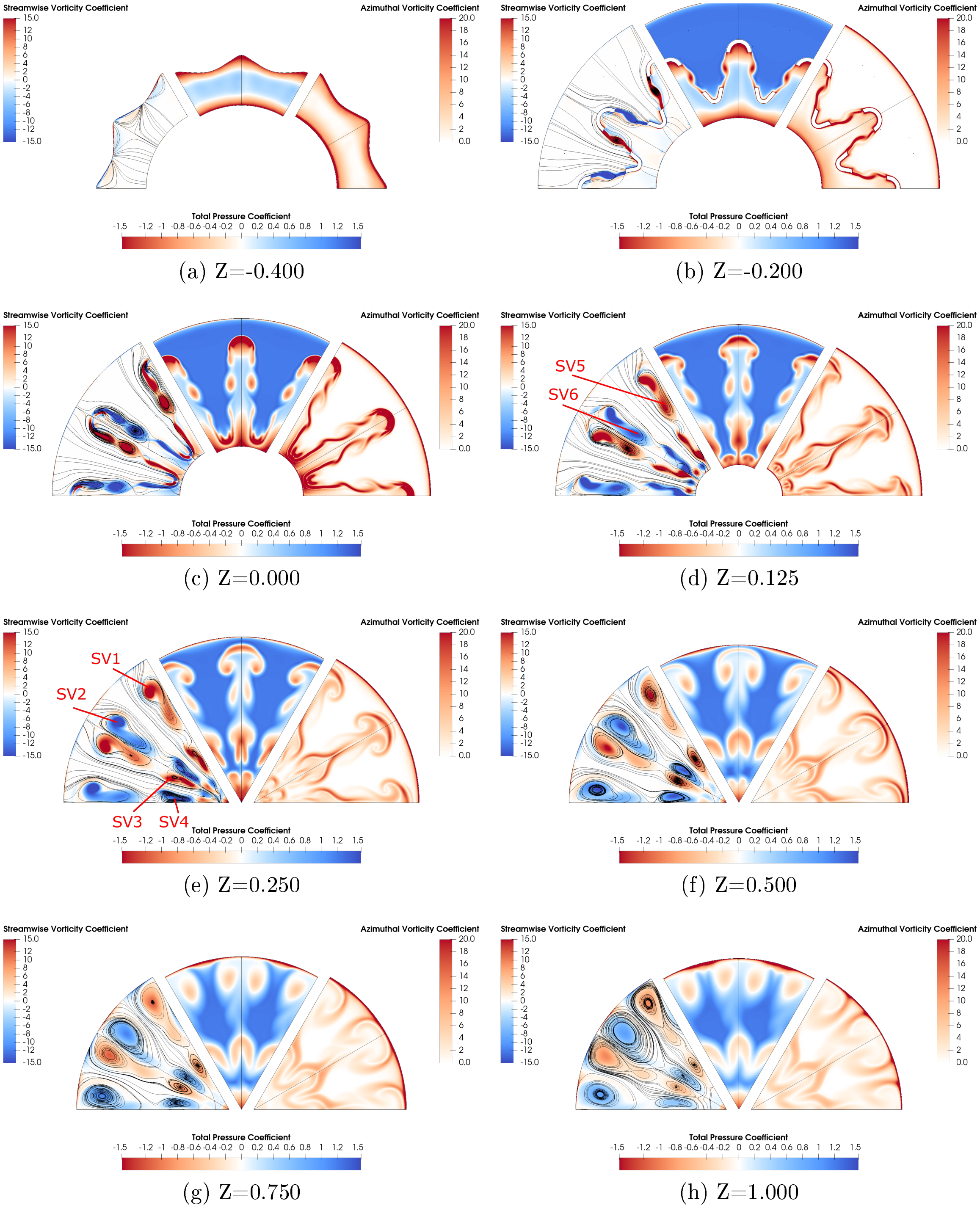

(a) Z=-0.400

(b) Z=-0.200

(c) Z=0.000

(d) Z=0.125

(e) Z=0.250

(f) Z=0.500

(g) Z=0.750

(h) Z=1.000

Figure 6.10: Contour plots of streamwise vorticity coefficient, total pressure coefficient and azimuthal vorticity coefficient, deep scallop, no swirl.

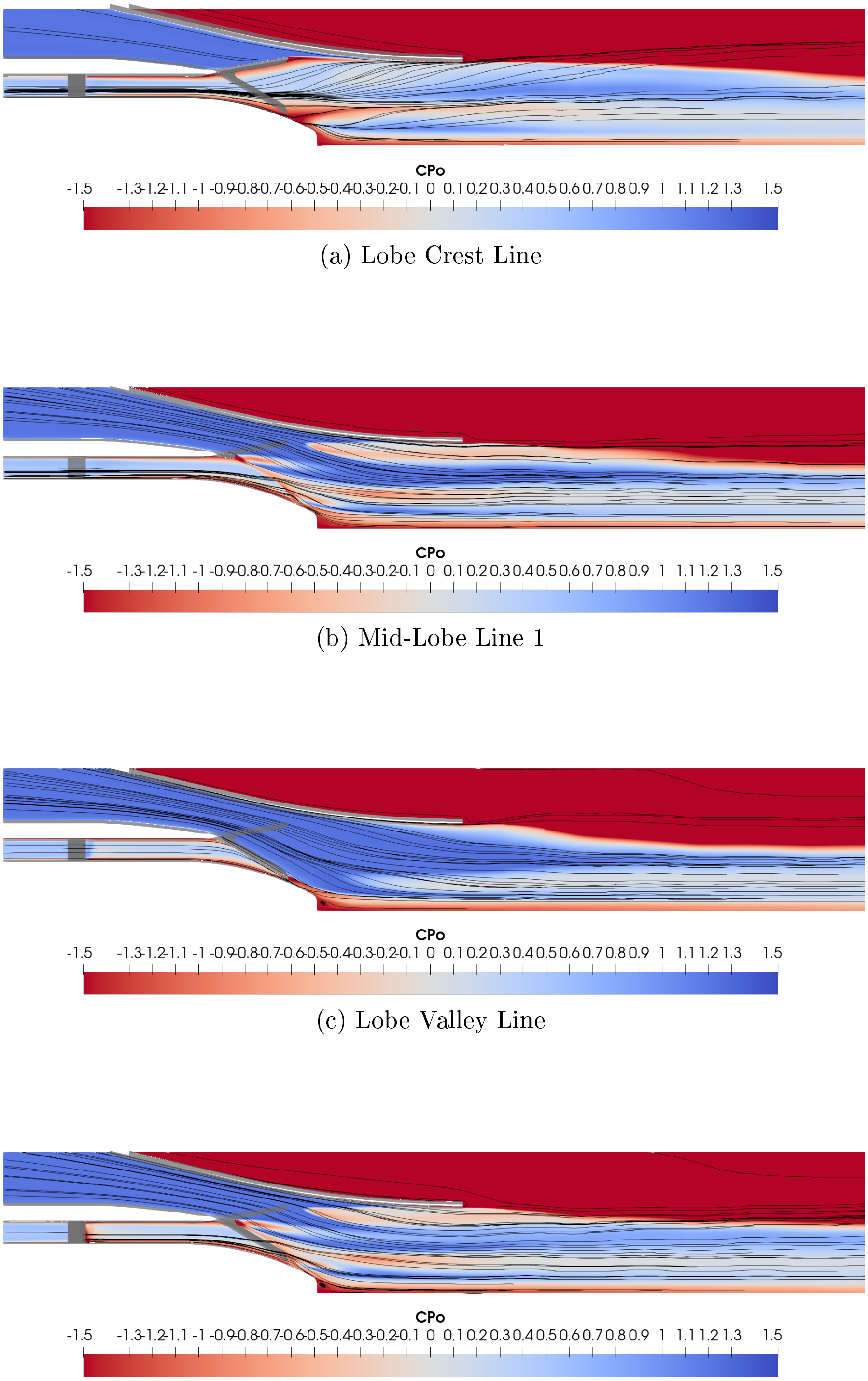

(a) Lobe Crest Line

(b) Mid-Lobe Line 1

(c) Lobe Valley Line

(d) Mid-Lobe Line 2

Figure 6.11: Meridional contours of total pressure coefficient, deep scallop, no swirl.

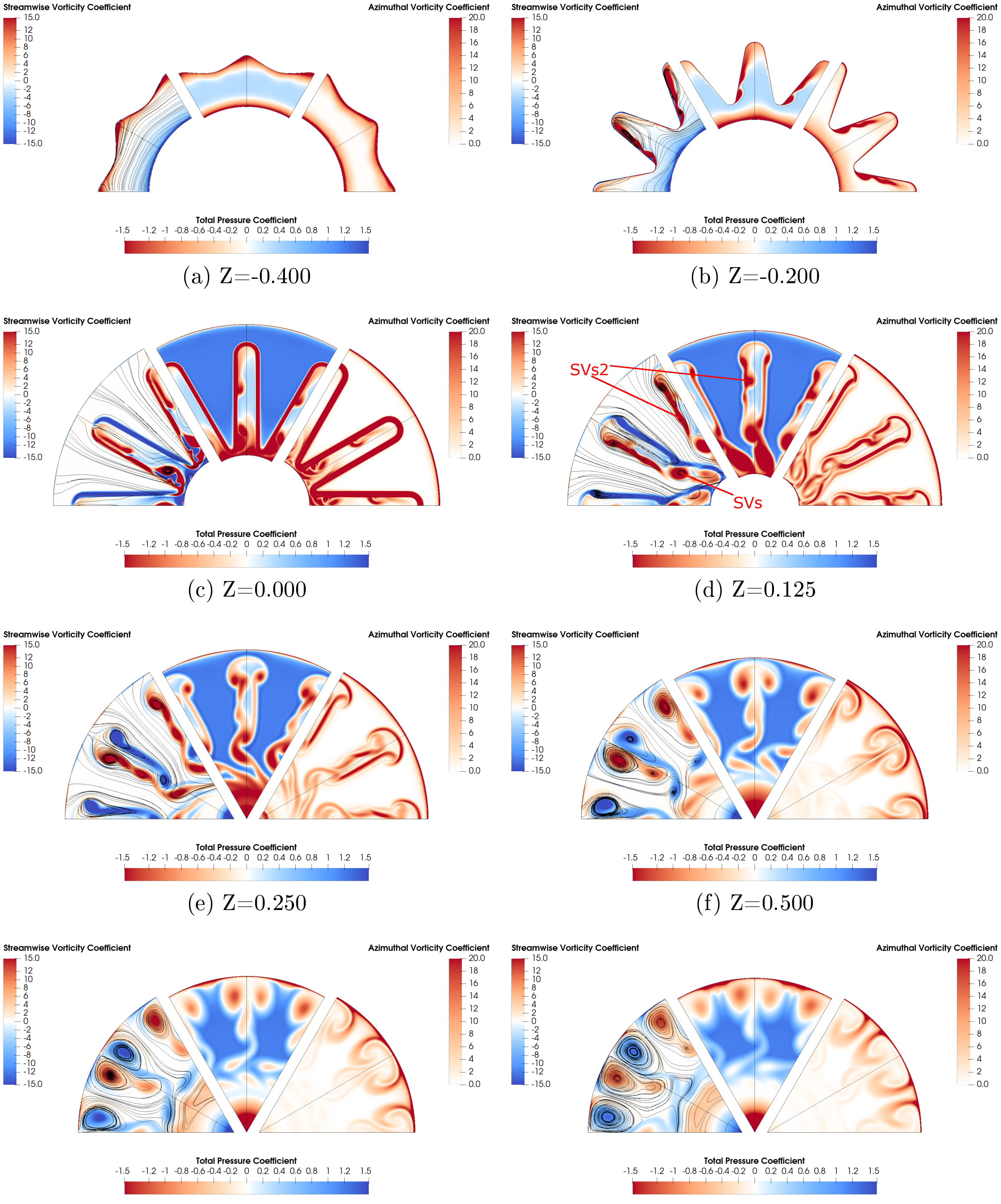

(a) Z=-0.400

(b) Z=-0.200

(c) Z=0.000

(d) Z=0.125

(e) Z=0.250

(f) Z=0.500

(g) Z=0.750

(h) Z=1.000

Figure 6.12: Contour plots of streamwise vorticity coefficient, total pressure coefficient and azimuthal vorticity coefficient, unscalloped, 30° swirl.

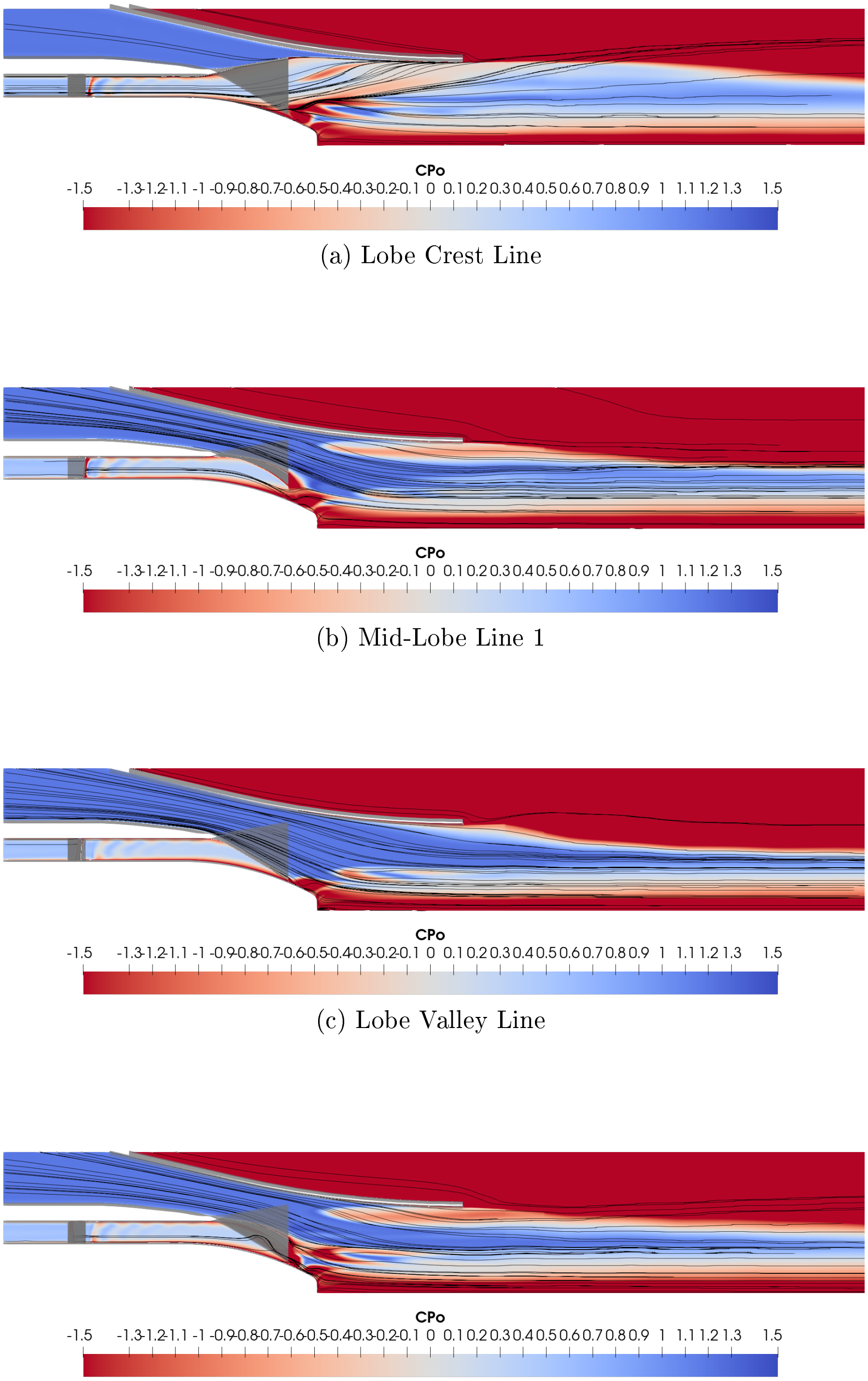

(a) Lobe Crest Line

(b) Mid-Lobe Line 1

(c) Lobe Valley Line

(d) Mid-Lobe Line 2

Figure 6.13: Meridional contours of total pressure coefficient, unscalloped, 30° swirl.

6.3.4 Test Cases

The test cases are again presented in order from shallow to deep scallop. As the baseline case indicated, the separation due to the swirling incident flow produced an asymmetric flow field within the core lobe of the mixer.

Shallow Scallop

First, a focus on the streamwise vorticity. Figure 6.14b shows the separation had generated a strong region of positive vorticity along the 'suction-side' of the lobe. Apart from SV_{S1}, the streamwise vorticity appears symmetrical along the outer regions of the lobe at $Z = 0.000$. This is expected due to the general flow turning performed by the mixer and the shallowness of the scallop not allowing for the swirl to have major effects around the outer regions of the jet. However, the symmetry is broken near the centre of the jet because of the residual swirl that persists between the lobed mixer valley and exhaust centrebody. The SV_{S1} was still strong enough to induce SV_{SP}, but was quickly entrained to the centre of the jet thanks to the pressure gradient produced via the swirling flow in the wake of the centrebody. This entrainment is clear in Figure 6.14e.

The azimuthal vorticity and total pressure coefficient contour plots indicate the same general development as observed with the unscalloped mixer save for one major difference. Where the unscalloped mixer provided a surface for the core flow to reattach briefly, the shallow scallop did not. The structure noted in Figure 6.12d is noticeably absent from the contour plots of Figure 6.14.

The next section presents the flow fields observed when the deeper Moderate scallop was subject to a 30° core flow swirl.

Moderate Scallop

Let us begin, again, with a discussion of the streamwise vorticity coefficient contour plots show in Figure 6.16. Close inspection of the $Z = -0.200$ plane shows the development of a small counter-rotating vortex pair within the scallop on the 'suction-side' of the lobe. The separation produced a large region of positive streamwise vorticity in the unscalloped and shallow scallop cases. Whereas the 'pressure-side' of

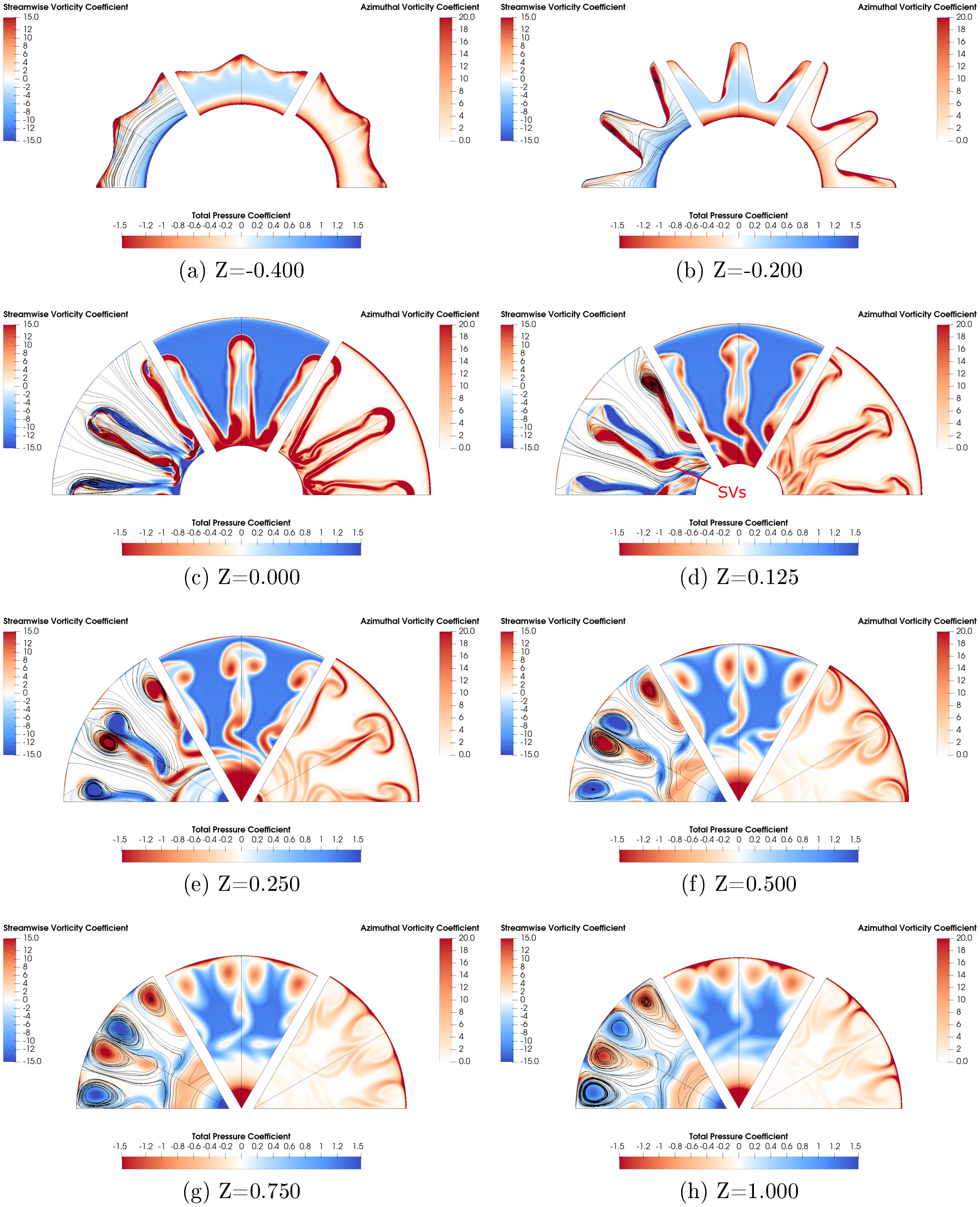

(a) Z=-0.400

(b) Z=-0.200

(c) Z=0.000

(d) Z=0.125

(e) Z=0.250

(f) Z=0.500

(g) Z=0.750

(h) Z=1.000

Figure 6.14: Contour plots of streamwise vorticity coefficient, total pressure coefficient and azimuthal vorticity coefficient, shallow scallop, 30° swirl.

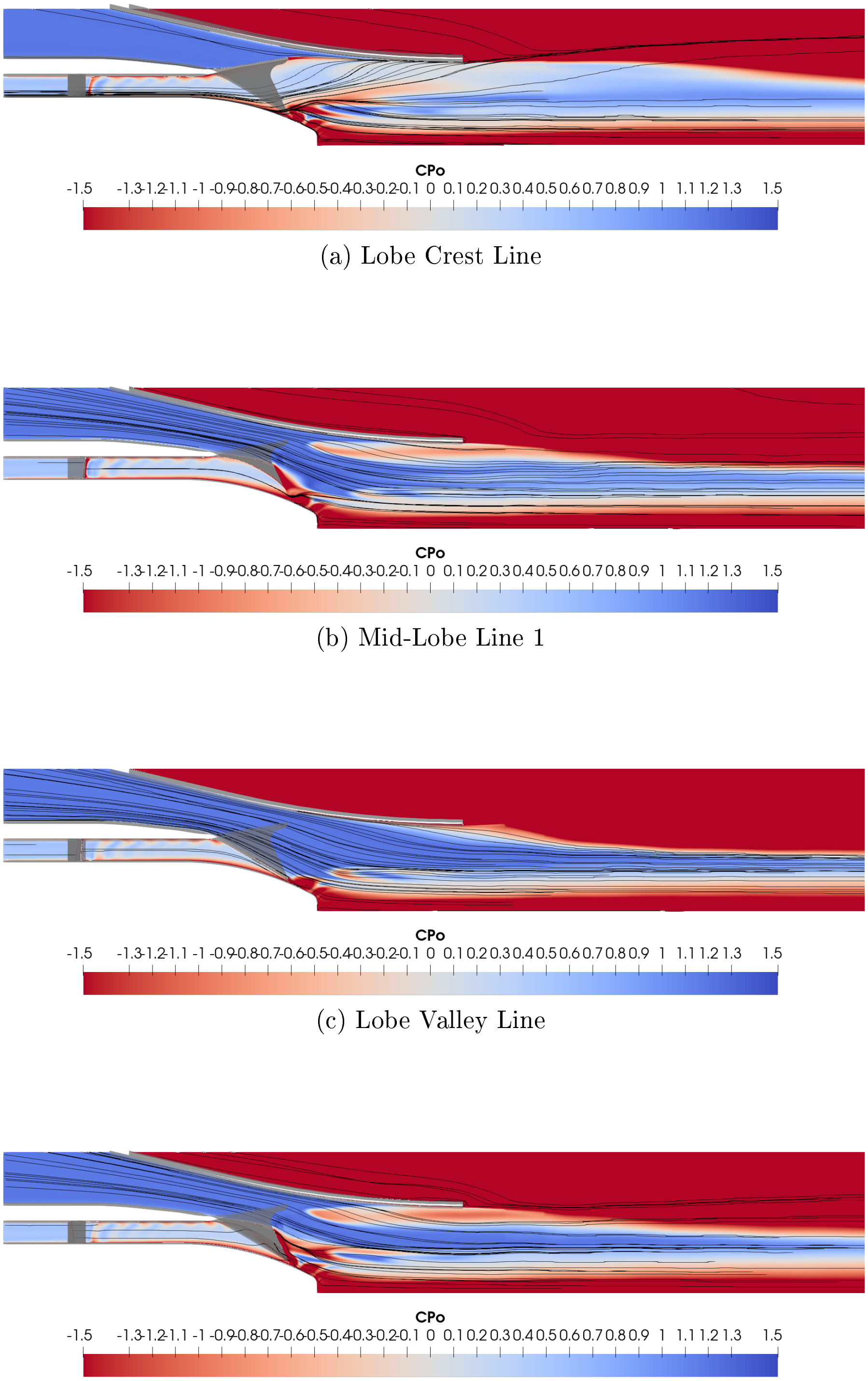

(a) Lobe Crest Line

(b) Mid-Lobe Line 1

(c) Lobe Valley Line

(d) Mid-Lobe Line 2

Figure 6.15: Meridional contours of total pressure coefficient, shallow scallop, 30° swirl.

the lobe indicates only negative vorticity developing as one would expect from the direction of the radial velocity gradients. The $Z = 0.000$ plane indicates that SV_{S1} developed into a coherent vortex core and at $Z = 0.125$ a paired counter-rotating vortex developed near SV_{S1}. This paired vortex is not SV_{SP}, but rather SV_4. It developed along the lower edge of the scallop on the 'pressure-side'. The contour plots confirm this because of the clear coherence of the vortex at $Z = 0.125$, rather than at $Z = 0.250$ in the case of SV_{SP}, and its persistence downstream where it is still a coherent, albeit weaker, structure at $Z = 1.000$.

There was a clear asymmetry in the total pressure coefficient as indicated in Figure 6.16c. This differs from the shallow scallop case where the total pressure drop was clearly weaker, but still symmetric across both sides of the lobe. In this case the 'pressure-side' wake displays higher total pressure values than the 'suction-side' wake. Curiously, this did not translate into asymmetric strength of the azimuthal vortex, indicated in Figure 6.8d. Both contours indicate that residual swirl managed to pass through the scallop and into the mixing zone. Figure 6.16 shows the distortion of the flow structures downstream of the scallop in the direction of the swirl.

The flow fields downstream of the deep scallop lobed mixer shall be discussed in the next section.

Deep Scallop

Figure 6.18 reveals a complex flow field with many structures to discuss. The interaction of the swirling core flow incident on the mixer with such deep lobes produced a streamwise vorticity field unlike any seen in previous sections of this thesis. The discussion shall begin at $Z = -0.200$ where the limiting streamlines of the velocity vector indicate that a coherent counter clockwise streamwise vortex had already developed within the 'suction-side' scallop. However, unlike the case without swirl, there was no matching coherent vortex on the opposite side. This structure is labeled SV_1 because it was formed via the interaction of the radially deflected core and bypass flow, much like that seen in Figure 6.10. Though there was a region of negative streamwise vorticity within the 'pressure-side' scallop, it did not form a coherent core. The absence of SV_2 remained downstream of the mixer. It was clearly inhibited by

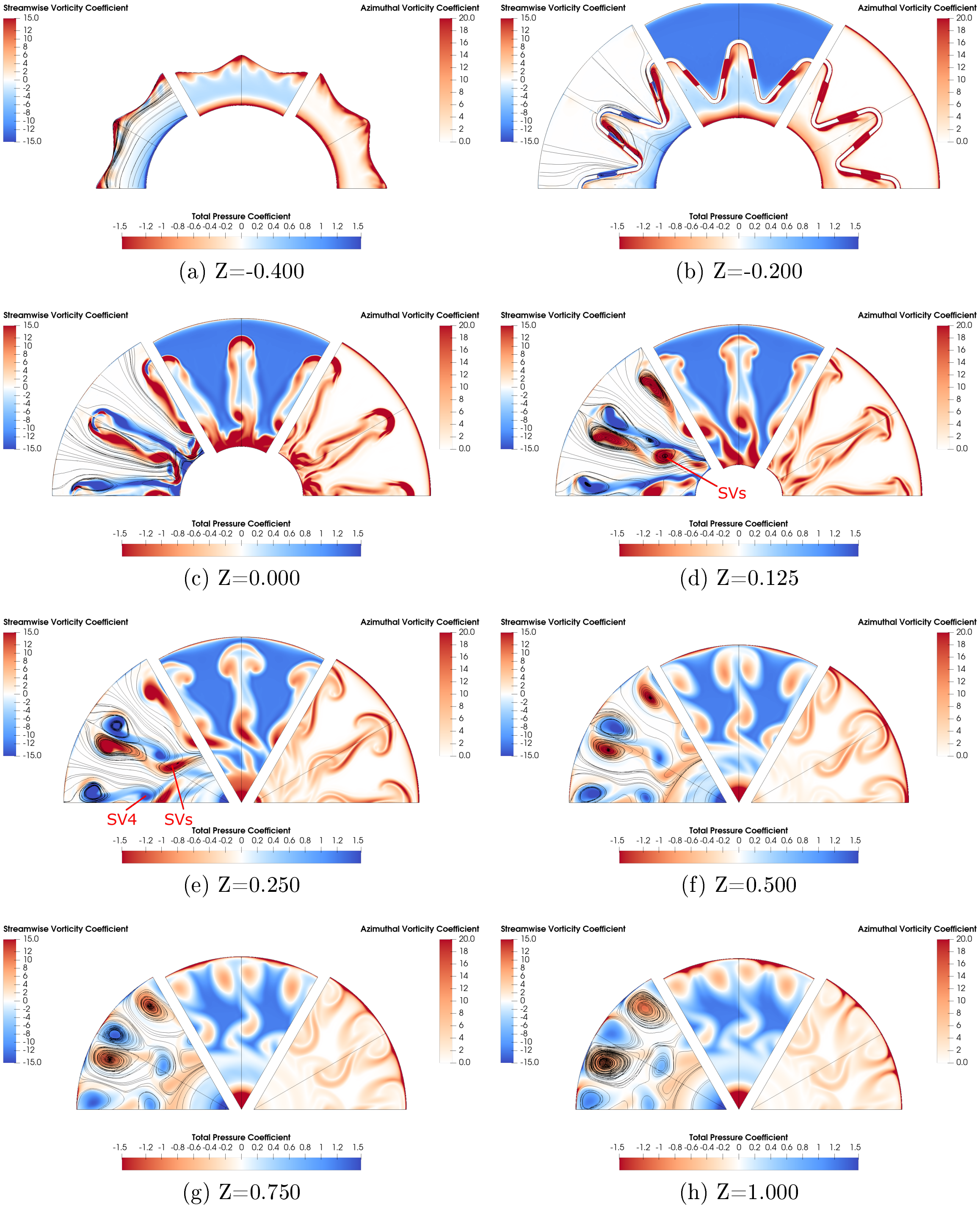

(a) Z=-0.400

(b) Z=-0.200

(c) Z=0.000

(d) Z=0.125

(e) Z=0.250

(f) Z=0.500

(g) Z=0.750

(h) Z=1.000

Figure 6.16: Contour plots of streamwise vorticity coefficient, total pressure coefficient and azimuthal vorticity coefficient, moderate scallop, 30° swirl.

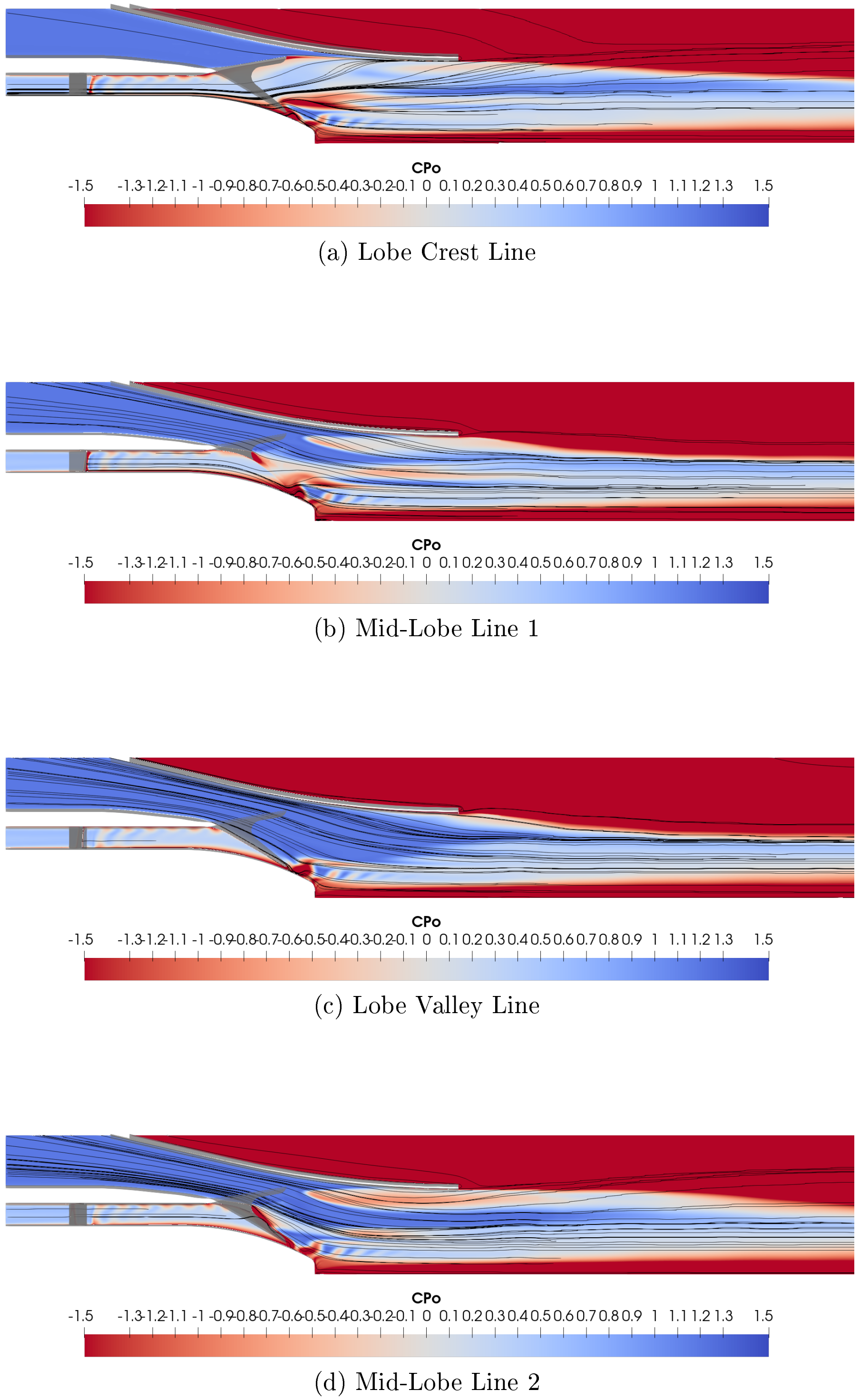

(a) Lobe Crest Line

(b) Mid-Lobe Line 1

(c) Lobe Valley Line

(d) Mid-Lobe Line 2

Figure 6.17: Meridional contours of total pressure coefficient, moderate scallop, 30° swirl.

the swirling flow. At $Z = 0.000$, the inner and outer scallop edge vortices have developed into discrete and coherent vortex cores as well. They are labeled as SV_3, SV_4 and SV_5. The separation induced vortex was also developed, labeled SV_{S1}. It was quickly entrained by the residual swirling flow at the centre of the jet in the wake of the centrebody. SV_5 and SV_6 remain mostly coherent until $Z = 1.000$, but the other vortices become too weak and break down due to interactions with the azimuthal vortex and each other. The streamlines show little radial velocity near the centre of the jet in the final two planes shown in Figure 6.18.

Such complex streamwise vorticity fields can be translated into equally complex total pressure and azimuthal vorticity fields. The total pressure coefficient contour plot assists in the identification of coherent vortex cores via the clear low pressure regions that correspond to the centre of the vortex. There are generally also clear low pressure regions in the wake of hardware as well. Figure 6.18b shows that the wake of the scallop on the 'pressure-side' had already begun mixing out and dissipating because of the azimuthal vortex. The low pressure regions within the cores persists further downstream than those produced because of wake. Quite interestingly, the low pressure region indicated at $Z = 0.125$ completely disappeared in plane $Z = 0.250$. That zone corresponded with SV_3 which broke down and became incoherent between these planes. That breakdown was due to the interaction with the azimuthal vortex, which is shown to have been distorted and weakened in the same region, and with SV_{S1}, a co-rotating streamwise vortex in close proximity. The nature of vorticity results in co-rotating vortices to dissipate due to viscous losses when their cores are close enough to interact. That results in a rapid breakdown of the coherent structure into small scale turbulent structures and heat. The rapidity of this process should not go unnoticed.

Analysis of the flow fields provides context for the effects of lobe scalloping on the overall performance parameters calculated from these simulations.

6.3.5 Overall Performance

The counterclockwise circulation is shown in Figure 6.20 and was calculated via the integral of streamwise vorticity on the right hand—or 'suction-side'—of the lobe within the computational domain. For the cases with 0° core swirl, all of the circulation was

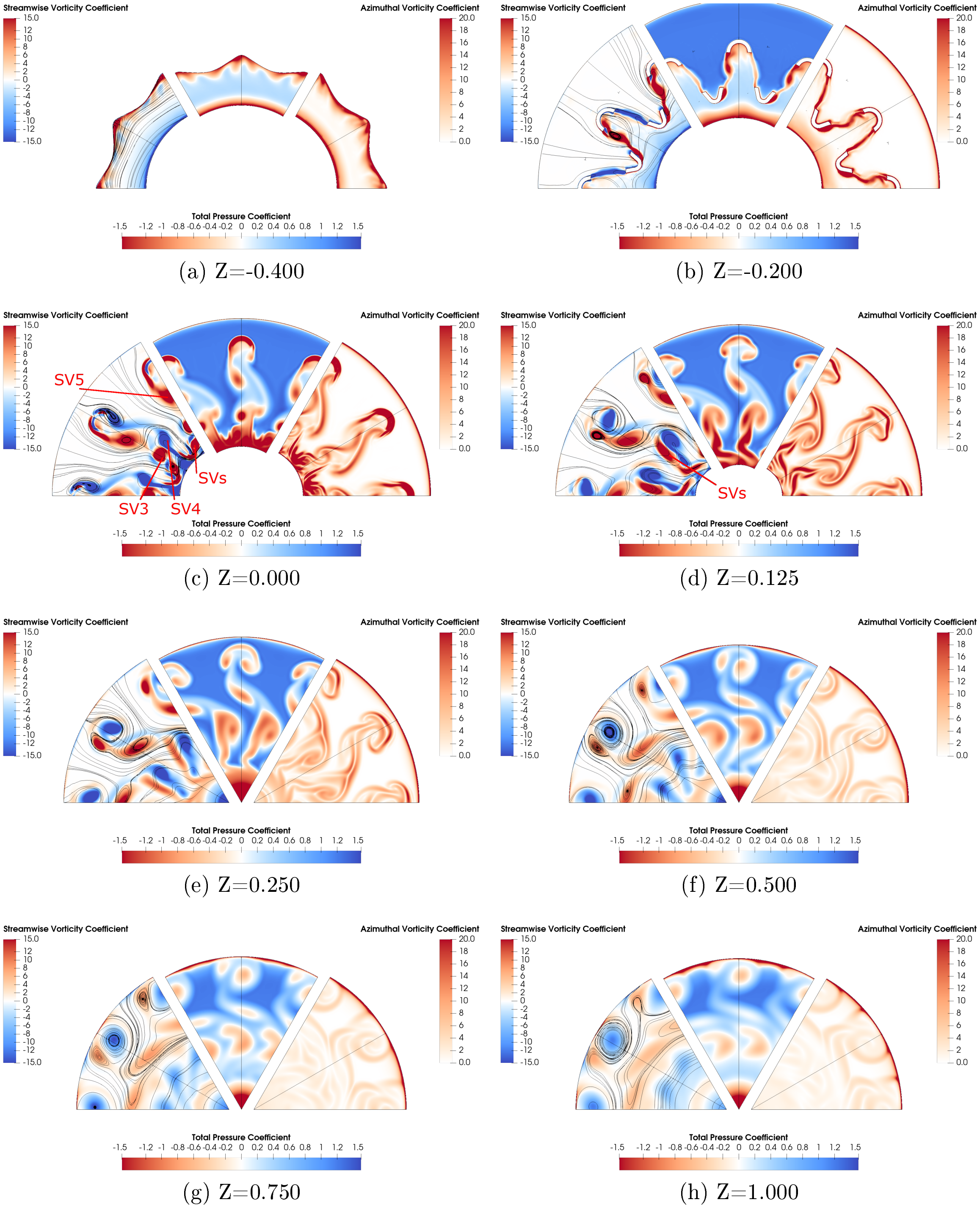

(a) Z=-0.400

(b) Z=-0.200

(c) Z=0.000

(d) Z=0.125

(e) Z=0.250

(f) Z=0.500

(g) Z=0.750

(h) Z=1.000

Figure 6.18: Contour plots of streamwise vorticity coefficient, total pressure coefficient and azimuthal vorticity coefficient, deep scallop, 30° swirl.

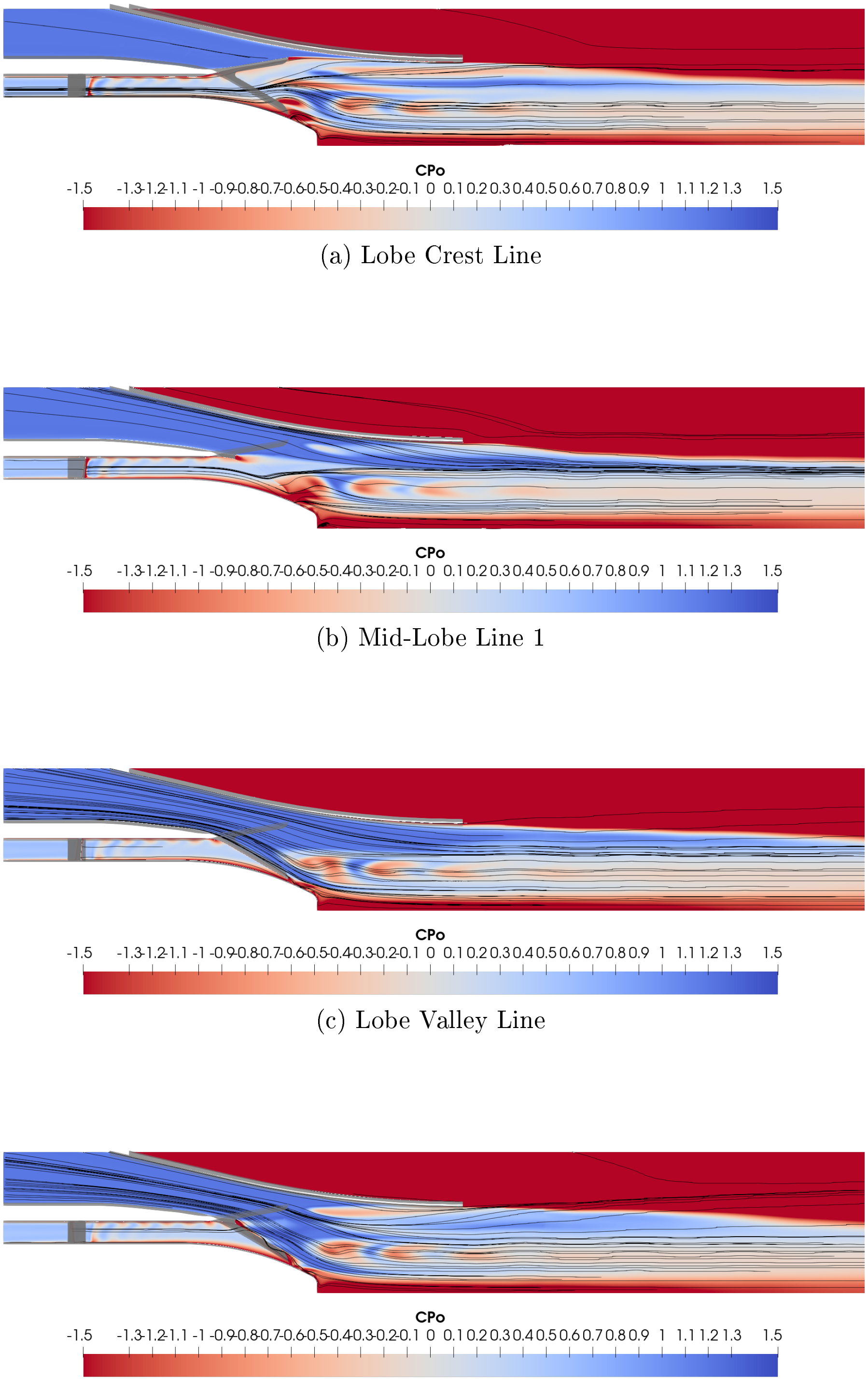

(a) Lobe Crest Line

(b) Mid-Lobe Line 1

(c) Lobe Valley Line

(d) Mid-Lobe Line 2

Figure 6.19: Meridional contours of total pressure coefficient, deep scallop, 30° swirl.

Table 6.2: Peak circulation values for various scalloping depths.

(a) No Swirl

Scallop Depth	Peak Location	Peak Value
Unscalloped	0.375	0.26
Shallow	0.25	0.30
Moderate	0.25	0.27
Deep	0.125	0.26
Final	0.25	0.25

(b) 30° Swirl

Scallop Depth	Peak Location	Peak Value
Unscalloped	0.000	0.32
Shallow	0.000	0.37
Moderate	0.000	0.32
Deep	0.000	0.26
Final	0.000	0.31

produced via the streamwise vorticity. When the core swirl was increased to 30°, that had the effect of introducing residual swirl into the mixing duct. That residual swirl produced negative vorticity downstream of the mixer in the wake of the centrebody, affecting the circulation output.

As indicated in Table 6.2, the shallow scallop produces the maximum circulation in either case of no swirl or 30° swirl. The unscalloped mixer peaks the latest. After each circulation peak, the cases settle into a regular order of strength that does not change from $Z = 0.325$ up to $Z = 1.000$. That order, from weakest circulation to strongest is: Deep, Final, Moderate, Unscalloped then Shallow. This trend confirms the streamwise vortex was strongest downstream of the shallow scallop lobed mixer and the strength of the streamwise vorticity downstream of the moderate scallop lobed mixer was no stronger than that of the unscalloped or shallow mixer, despite producing more discrete vortex cores. When swirl was introduced, it became clear that a deeper scallop was more sensitive and allowed more residual swirl to persist downstream of the scallop. As mentioned, the residual swirl is mathematically indistinguishable from negative—clockwise from the perspective of the reader—streamwise vorticity. That is very clear when observing the circulation downstream of the deep scallop lobed mixer subject to inlet swirl dropped below zero at $Z = 0.250$.

The performance of the final scallop profile is included in this section as well. The design was based on observations of the flow fields and the performance of the other test case scallop lobed mixers. Figure 6.20a and Table 6.2 show the final scallop lobed mixer produced the lowest peak circulation. The circulation is just an integral of the streamwise vortex strength in a particular area. Stronger vortices lead to more bulk mixing, but are more difficult to breakdown into small scale turbulent flow, which is important in this application. The circulation alone cannot be used to conclude the efficacy of a lobed mixer. The static pressure mixing index, I_{P_S}, is presented next and provides further context into mixing performance.

The static pressure mixing index provides an indication of both how rapidly the flow is being mixed and the uniformity of the flow. Theoretically, a perfectly uniform flow will have a mixing index of zero which means there is no variation in the flow and therefore no flow mixing is possible. The mixing index is a similar calculation to the statistical variance.

Figure 6.21 shows the parallel moderate scallop lobed mixer produced the highest mixing index of static pressure at all planes in both cases of swirl, down to $Z = 1.000$ where each case converges on a value near 0.05. This suggests the parallel moderate scallop produced rapid mixing throughout the nozzle with little detriment to the final outcome. That detriment can be quantified as the Total Pressure Loss Coefficient, Y, which is presented next in Table 6.3.

The total pressure loss coefficient measured at the nozzle exit plane, $Z = 1.000$, is a good summary of the efficiency of the exhaust system as a whole. This value encapsulates all losses within the flow from frictional losses against the solid walls, to viscous losses where flow structures interact and break down. Lower losses are better and exhaust systems yielding lower losses require less fuel for equal output. Table 6.3 summarizes the Total Pressure Loss Coefficient as well as the overall Thrust Coefficient measured at $Z = 1.000$. The Thrust Coefficient, defined in equations 4.11 and 4.12, is the most important performance parameter and describes how much force the exhaust system jet can exert.

The parallel moderate scallop lobed mixer achieved the lowest losses under both

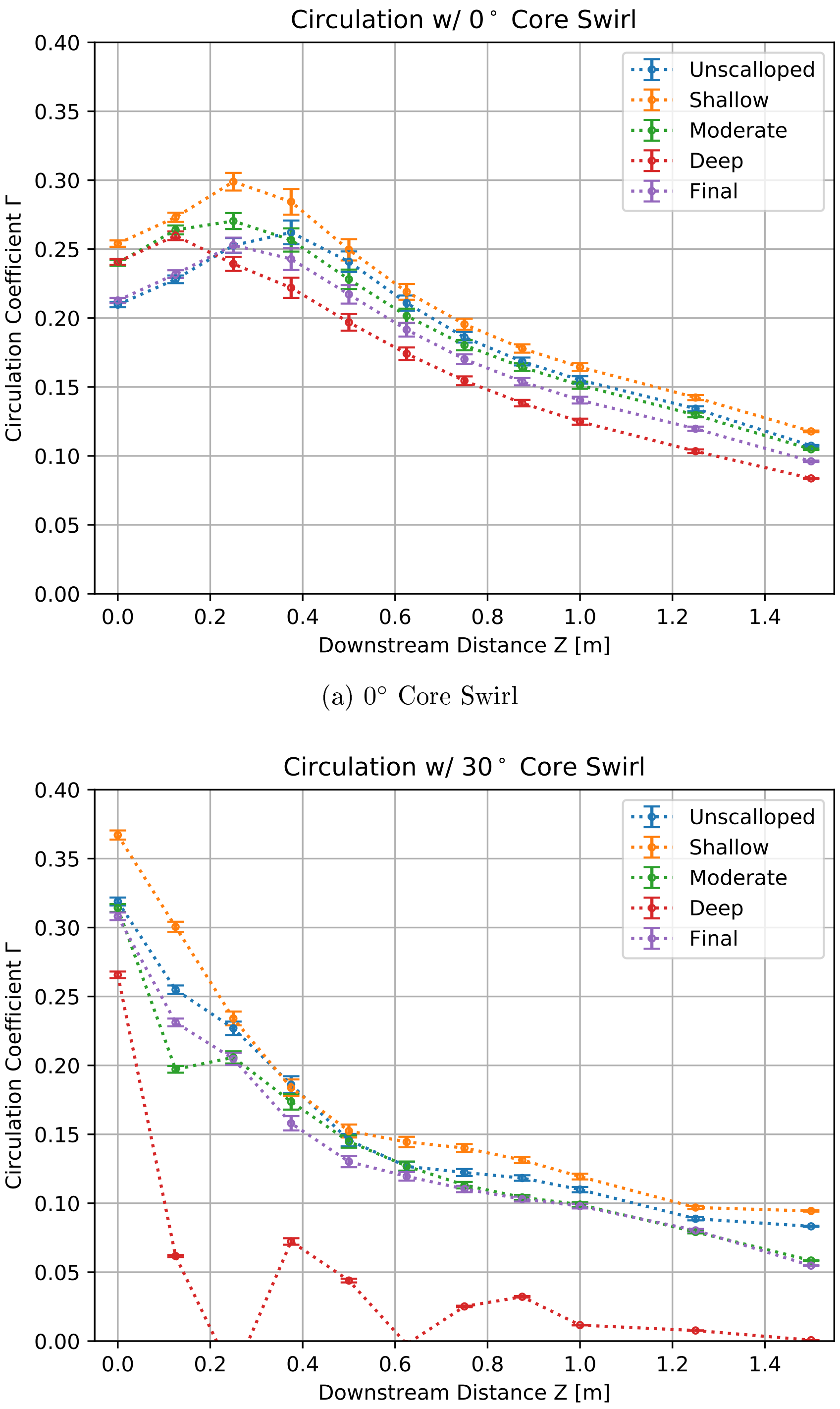

(a) 0° Core Swirl

(b) 30° Core Swirl

Figure 6.20: Clockwise circulation for various scalloping depths.

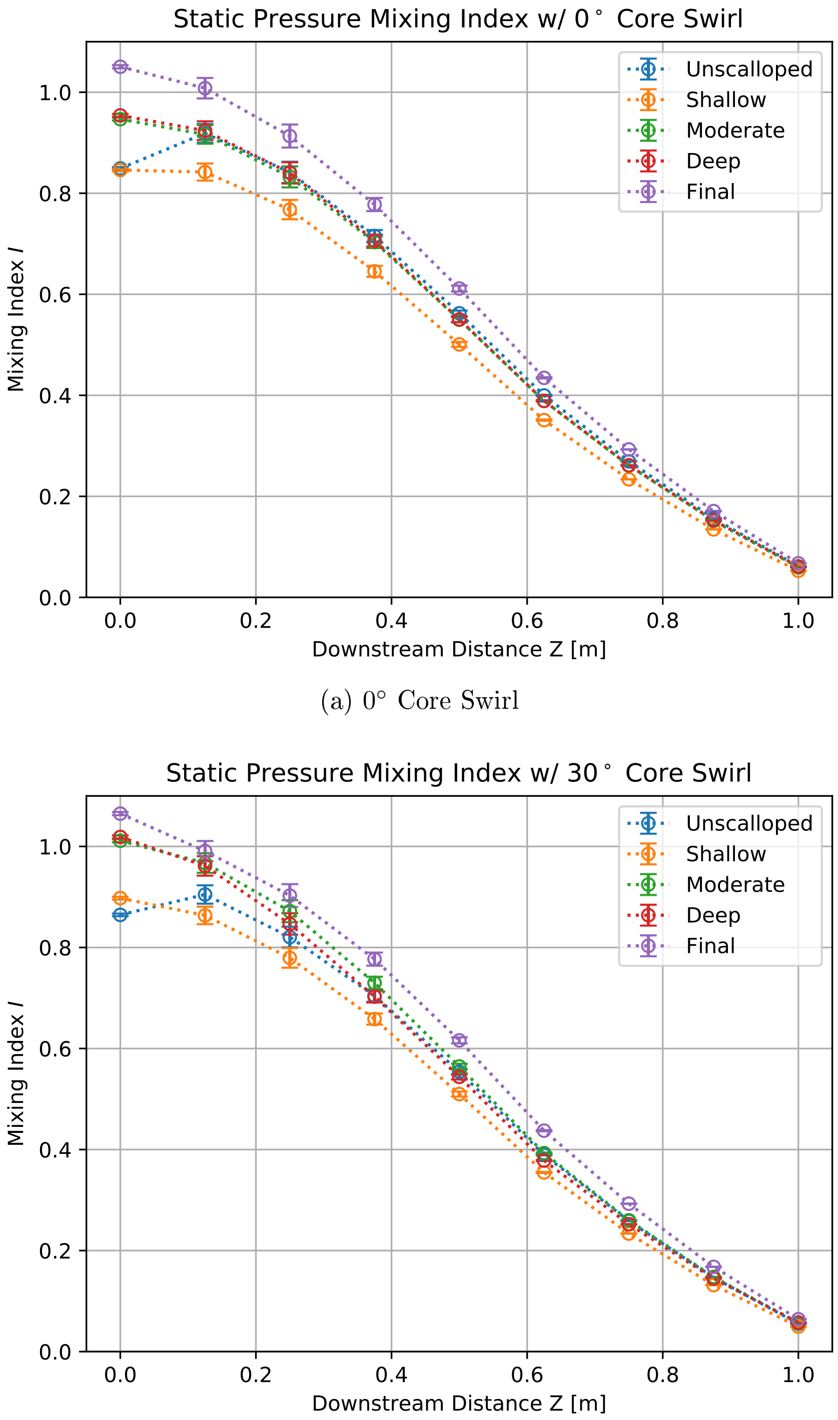

(a) 0° Core Swirl

(b) 30° Core Swirl

Figure 6.21: Static pressure mixing index for various scalloping depths.

Table 6.3: Pressure loss, Y and thrust coefficient C_T for various scallop depths.

(a) No Swirl

Scallop Depth	Y	C_T
Unscalloped	63.3	62.8
Shallow	66.5	62.7
Moderate	60.3	63.0
Deep	58.2	63.2
Final	57.5	63.0

(b) 30° Swirl

Scallop Depth	Y	C_T
Unscalloped	69.7	62.8
Shallow	72.4	62.5
Moderate	69.3	62.5
Deep	70.0	62.7
Final	67.9	62.9

core flow conditions. It achieved the second highest thrust with no swirl in the core flow, behind the deep scallop, but came out on top when the core flow had swirl. The additional residual swirl through the deep scallop was detrimental to the thrust output, which relies on the axial component of velocity.

6.3.6 Parallel Moderate Scallop

The design of the parallel moderate scallop was based on the data presented in this chapter, as well as information from the literature review in Chapter 2. The moderate depth of the scallop was chosen to enhance the amount of material trimmed from the unscalloped mixer, while maintaining structural integrity and overall stiffness that would have been sacrificed with a deep scallop. The deeper the scallop, the earlier the core and bypass flow may interact thus providing a head-start for fluid mixing within the nozzle. The other important design choice was to make the inner edge of the scallop parallel to the valley in the same way that the outer edge was parallel to the crest. This allowed SV_3 and SV_4 to shed from the inner edges of the scallop on either side of the lobe. The additional vortices provided enhanced mixing near the centre of the jet while the primary streamwise vortices, SV_1 and SV_2, facilitated mixing nearer to the nozzle surface. This scallop design was used for the investigations of Chapter 7 and Chapter 8.

The flow fields downstream and performance output of the parallel moderate scallop lobed mixer are presented in detail in Chapter 7, which investigates the sensitivity of the Unscalloped and Scalloped mixer to various levels of core flow swirl.

6.4 Conclusions

The purpose of this chapter was to examine the effect of increasing scallop depth on the performance of a lobed mixer and devise a design for the optimal mixer to be used in further investigations marching toward the solution of the problem set forth in Chapter 1. Three scallop depths were compared against the unscalloped mixer with no swirl in the core flow and 30° swirl in the core flow, each.

The evidence suggests that deeper scallops allowed for mixing to begin further upstream than cases with shallow or no scallop. The earlier mixing meant that the flow was more uniform and the mixing rates within the nozzle were lower in most cases. However, review of the literature and the results presented in this chapter suggest that there are downsides to too-deep scallops. These range from mechanical issues of structural integrity and vibration, to purely aerodynamic reasons like increased residual swirl at off-design conditions. The thin protrusions of the deep scalloped mixer are not as stiff as the mixer with shallower scallops. Vortex shedding and other aerodynamic effects can induce vibration and reduce the lifecycle of the mixer.

The final scallop design was produced based on the data analyzed in this study. That scallop had a moderate depth and inner and outer edges that were parallel to the mixer valley and crest protrusions, respectively. This mixer did not perform the best in all categories when considered in isolation, but was able to provide the best overall performance when all cases and parameters were considered.

Chapter 7

Mixer Sensitivity to Core Flow Swirl

The results of the previous chapter have indicated that the flow mixing of a MBTF exhaust system is improved by scalloped lobed mixers up to a certain degree. Further, it showed that scallops reduce the robustness of the mixer when presented with highly swirling core flow. This chapter presents an investigation into the sensitivity of unscalloped and scalloped lobed mixers to various quantities of core flow swirl. Core flow swirl is shown to be detrimental to exhaust system performance for large degrees, but beneficial to mixing when kept below 10°.

7.1 Introduction

Any loss of axial velocity in the flow of a MBTF exhaust system translates directly into a loss of thrust. From this, the reader can infer that allowing swirl to remain downstream of the final low-pressure turbine rotor (LPT) would diminish the performance of the engine. Past research at NRC has shown that swirling core flows improved aspects of mixing at the cost of increased pressure losses and reduced thrust output [69, 54, 59]. Turbine designers tend to design the final LPT stage with approximately 30° of exit swirl. Large turbine exhaust casing (TEC) struts downstream of the LPT provide structural support for the core hardware and centrebody and do work on the flow to convert any tangential velocity component to axial. The Zweifel coefficient, a measure of turbine blade lift, suggests that more energy can be extracted from a turbine rotor if the flow turning is increased.

The previous chapters have shown that the lobed mixer does some flow turning work on the core flow itself, regardless of the presence of the TEC struts. This feature of the lobed mixer could be exploited to reduce the reliance on TEC struts to turn the flow. The engine designer could then make choices to develop an exhaust system with TEC struts that do no work on the flow, or ideally without TEC struts at all. Avoidance of TEC struts would provide an immediate and obvious reduction of the aft-end duct mass.

This chapter presents data on the structures with the flow fields, the strength of vorticity, the inlet and outlet average swirl, the overall circulation, the overall pressure loss and other performance parameters. Data was acquired from ten cases: five core inlet swirls of 0°, 5°, 10°, 20° and 30° imposed on two mixers, unscalloped and scalloped. The cases are expanded upon in the next section.

7.2 Methodology

This chapter presents an investigation into the sensitivity of the lobe mixer to gradually increasing amounts of core flow swirl. The investigation was designed to probe the understanding of how increases in core swirl from 0° to 30° affects the performance of MBTF exhaust systems with lobed mixers. The knowledge gained in the previous chapters also indicated that while the core flow swirl would affect the performance in some way, the lobed mixer would also affect the distribution of the swirl as the flow traversed the mixer. The performance of the unscalloped mixer will be compared directly to the final scalloped mixer throughout this chapter. Each mixer was subject to five varying levels of inlet swirl. This study has been included in the overall investigation so that any impact of core flow swirl can be examined before moving on to Chapter 8 where core flow swirl was removed via TEC struts.

The range of swirl values was chosen based on the expected LPT exhaust swirl for optimal power extraction. The 0° case served as a baseline for both unscalloped and scalloped mixers. As in all of the simulations examined for this thesis, the core flow swirl was generated by swirling vanes. There were 36 vanes modeled in total for the full exhaust system annulus which resulted in three being captured within the 15° sector that comprised the computational domain.

7.2.1 Boundary Conditions

Chapter 5 concluded that accurate simulations of MBTF exhaust systems are conducted using compressible boundary conditions. Those boundary conditions are tabulated in Table 7.1. These conditions were chosen because they represent a general cruise condition for the MBTF model.

Table 7.1: High-speed compressible boundary conditions based on comparable commercial engine cruise conditions.

Boundary	Type	Value
Core	Total Pressure	43.0 kPa
	Total Temperature	728 K
	k	$5\,\mathrm{m}^2\,\mathrm{s}^{-2}$
	ϵ	$30\,000\,\mathrm{m}^2\,\mathrm{s}^{-3}$
Bypass	Total Pressure	45.1 kPa
	Total Temperature	273 K
	k	$5\,\mathrm{m}^2\,\mathrm{s}^{-2}$
	ϵ	$30\,000\,\mathrm{m}^2\,\mathrm{s}^{-3}$
Free Stream	Total Pressure	18.9 kPa
	Total Temperature	223 K
	k	$5\,\mathrm{m}^2\,\mathrm{s}^{-2}$
	ϵ	$30\,000\,\mathrm{m}^2\,\mathrm{s}^{-3}$
Outlet	Average Static Pressure	18.8 kPa

7.2.2 Test Geometries

The two mixer geometries used were the standard unscalloped mixer and the final scalloped mixer as shown in Figure 7.1. These were chosen to model the sensitivity to swirl in the absence and presence of the scallop since it was shown that scalloping has an effect on the flow. This choice isolated for effects of scalloping versus effects of the mixer alone.

The swirl vanes were designed by a colleague in a previous study [69] to produce a uniform swirl profile from the centrebody hub to the turbine exhaust casing in the core flow. The cross sectional profile for the swirling vanes is shown in Figure 7.2.

Figure 7.3 presents the radial swirl profile produced via each swirling vane ring.

This chapter presents a systematic approach looking at various inlet swirl magnitudes and lobed mixer scalloping. The systematic increase of core flow swirl will allow for incremental observation of effects and outcomes on mixer performance regardless of scalloping. This study characterizes the impacts of swirl on exhaust system performance with the purpose of confirming the hypothesis that swirl removal is a necessary part of the hardware design of MBTF exhaust systems.

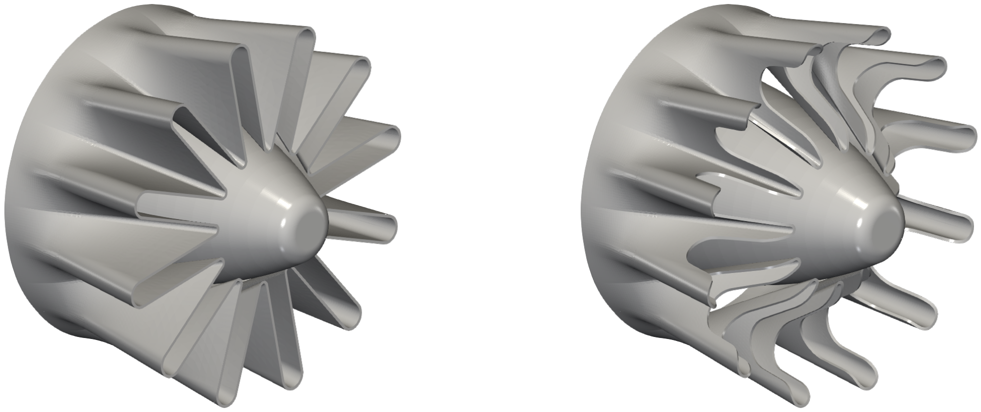

(a) Unscalloped Mixer

(b) Scalloped Mixer

Figure 7.1: Unscalloped and scalloped mixers used in simulations for Chapter 7.

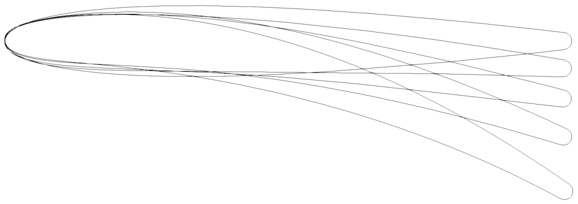

Figure 7.2: Cross sectional profiles for 0°, 5°, 10°, 20° and 30° swirl vanes.

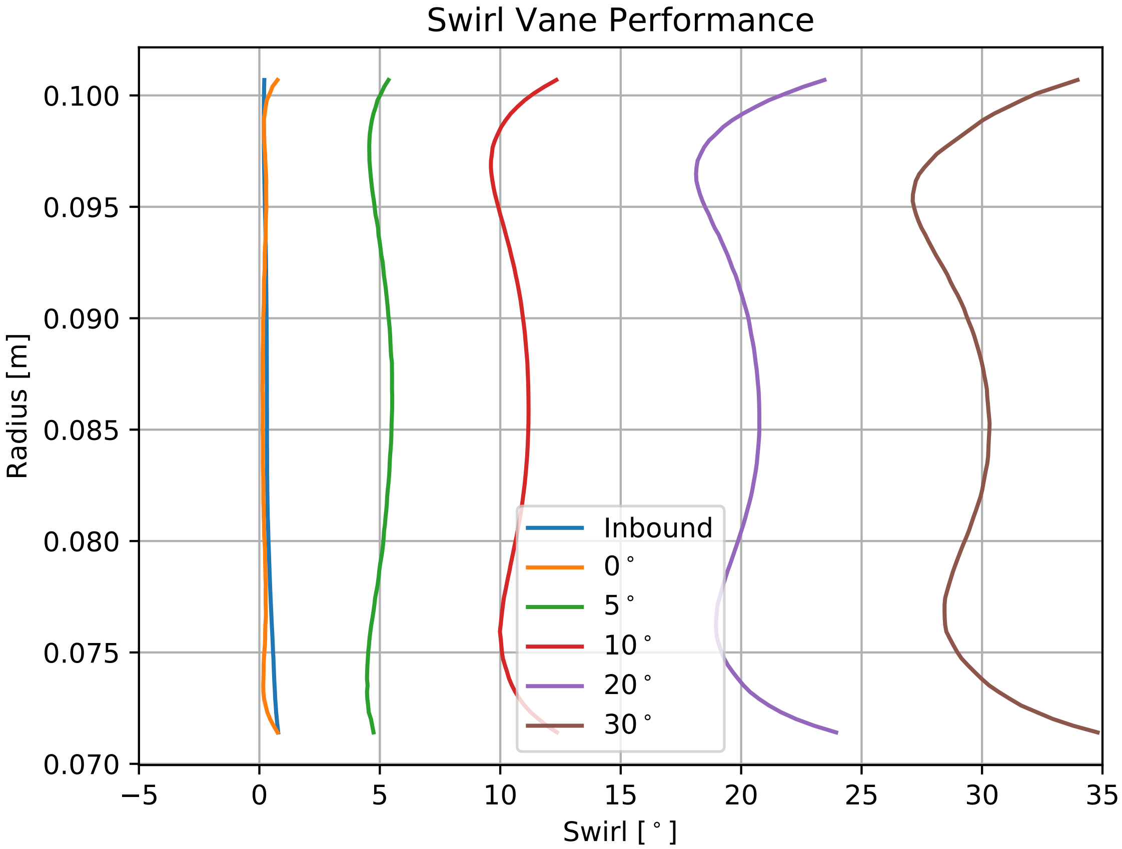

Figure 7.3: Swirl vane inlet and outlet values for the five swirl values tested.

7.3 Discussion

7.3.1 Unscalloped Flow Field Sensitivity

This section presents discussion of the flow fields downstream of the unscalloped mixer subject to 5°, 10° and 20° swirl in the core flow. This mixer has already been presented in detail for the cases of 0° and 30° core flow swirl; they are not repeated here. Their discussions are found in Section 5.3.2. The main takeaway from those discussions is that, at 0° swirl, the radial deflection of the core and bypass flow through the lobed mixer produces streamwise vorticity as the streams interact at the shear layer. The streamwise vorticity then coalesces into two distinct counter rotating vortex cores that originate from the radial side walls of the lobe. They persist downstream, losing energy to viscous losses and mixing. A further streamwise vortex core emerged when the core flow swirl was 30°. That streamwise vortex emerged from the separation which occurred on the 'suction-side' of the mixer and was analogous to a wing-tip vortex.

5 Degrees

The flow fields that resulted from subjecting the unscalloped lobed mixer to 5° core flow swirl matched expectations that they would only differ slightly from the case with 0° core flow swirl. There is a perceptible asymmetry to the flow structures and a small deflection near the centre of the jet in the direction of the residual swirling flow.

10 Degrees

Core flow swirl of 10° did not change the flow fields drastically either. They become slightly more asymmetrical but the overall strength and development of the flow structures cannot be observed to change drastically through view the flow fields alone.

20 Degrees

The further doubling of the core flow swirl to 20° produced more interesting effects on the flow fields downstream of the lobed mixer. The separation induced vortex,

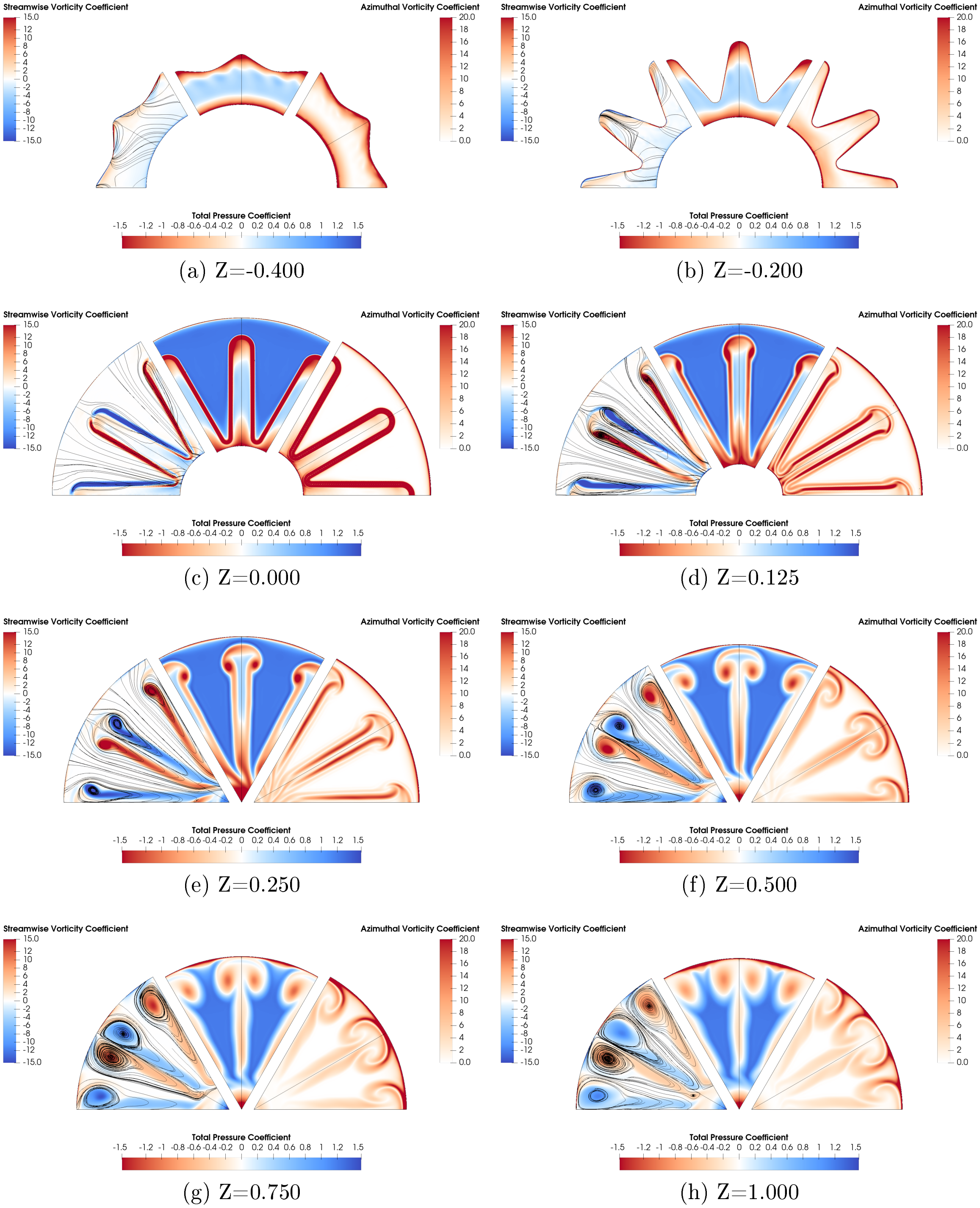

(a) Z=-0.400

(b) Z=-0.200

(c) Z=0.000

(d) Z=0.125

(e) Z=0.250

(f) Z=0.500

(g) Z=0.750

(h) Z=1.000

Figure 7.4: Contour plots of streamwise vorticity coefficient, total pressure coefficient and azimuthal vorticity coefficient, 5°, unscalloped.

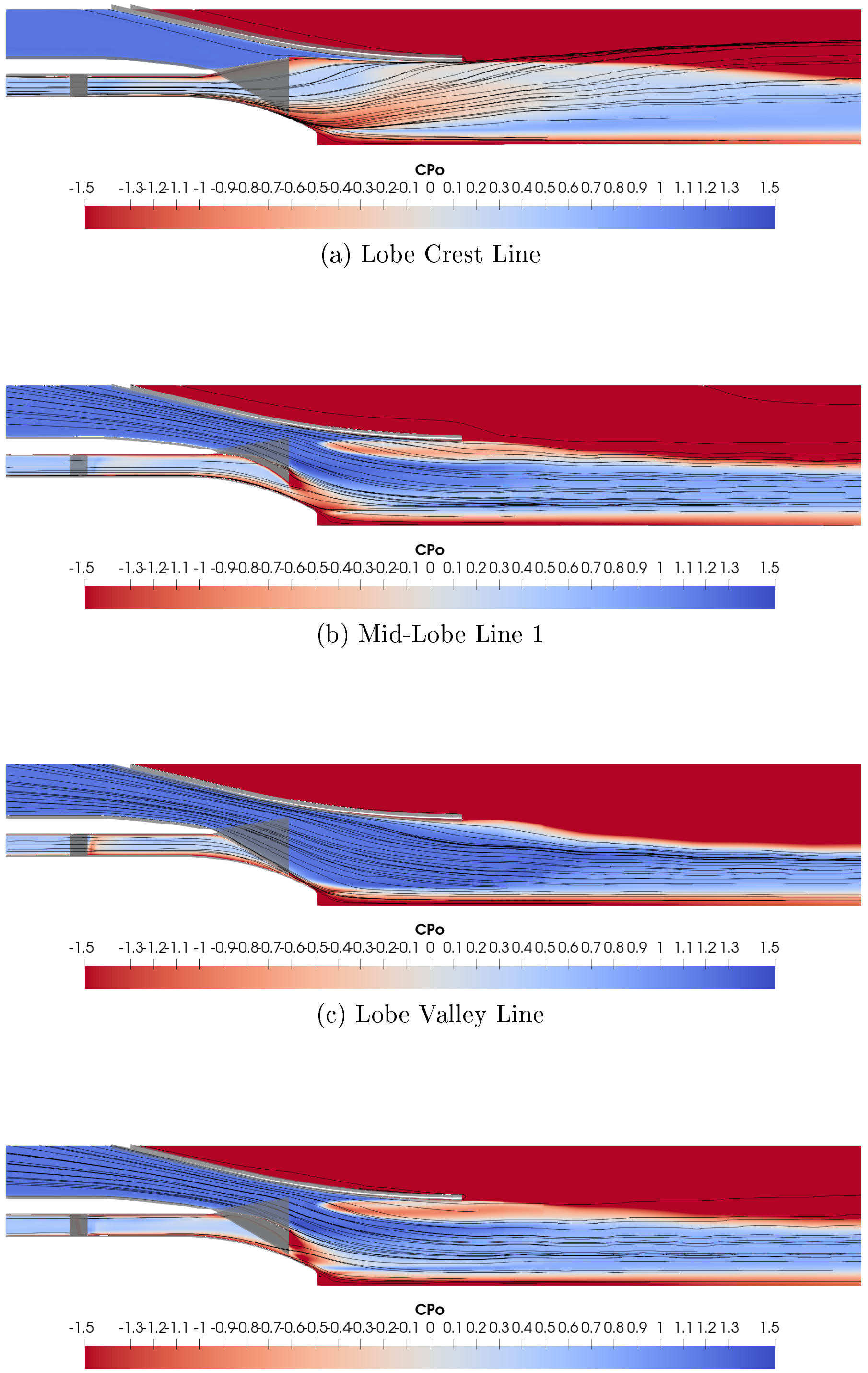

(a) Lobe Crest Line

(b) Mid-Lobe Line 1

(c) Lobe Valley Line

(d) Mid-Lobe Line 2

Figure 7.5: Meridional contours of total pressure coefficient, 5°, unscalloped.

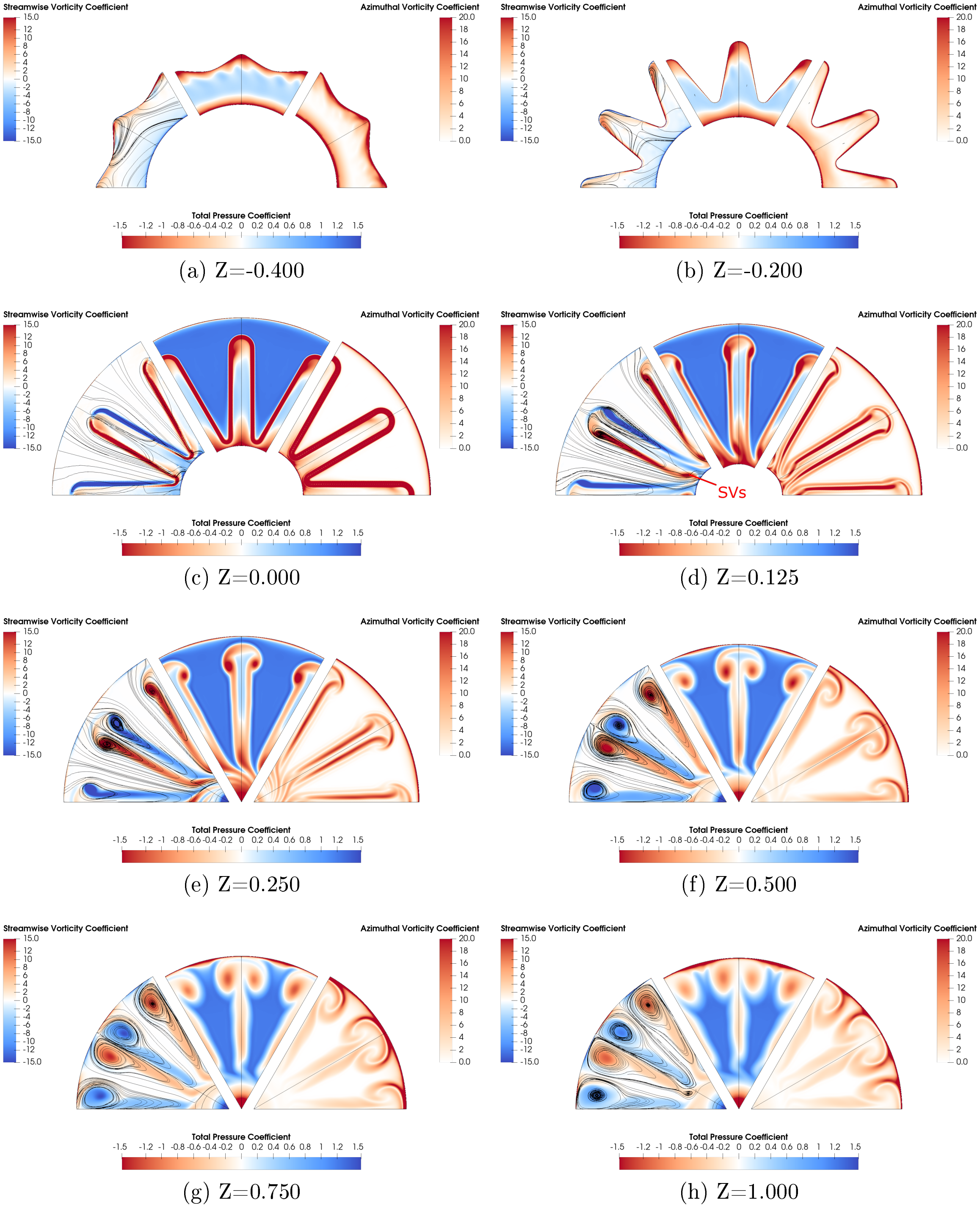

(a) Z=-0.400

(b) Z=-0.200

(c) Z=0.000

(d) Z=0.125

(e) Z=0.250

(f) Z=0.500

(g) Z=0.750

(h) Z=1.000

Figure 7.6: Contour plots of streamwise vorticity coefficient, total pressure coefficient and azimuthal vorticity coefficient, 10°, unscalloped.

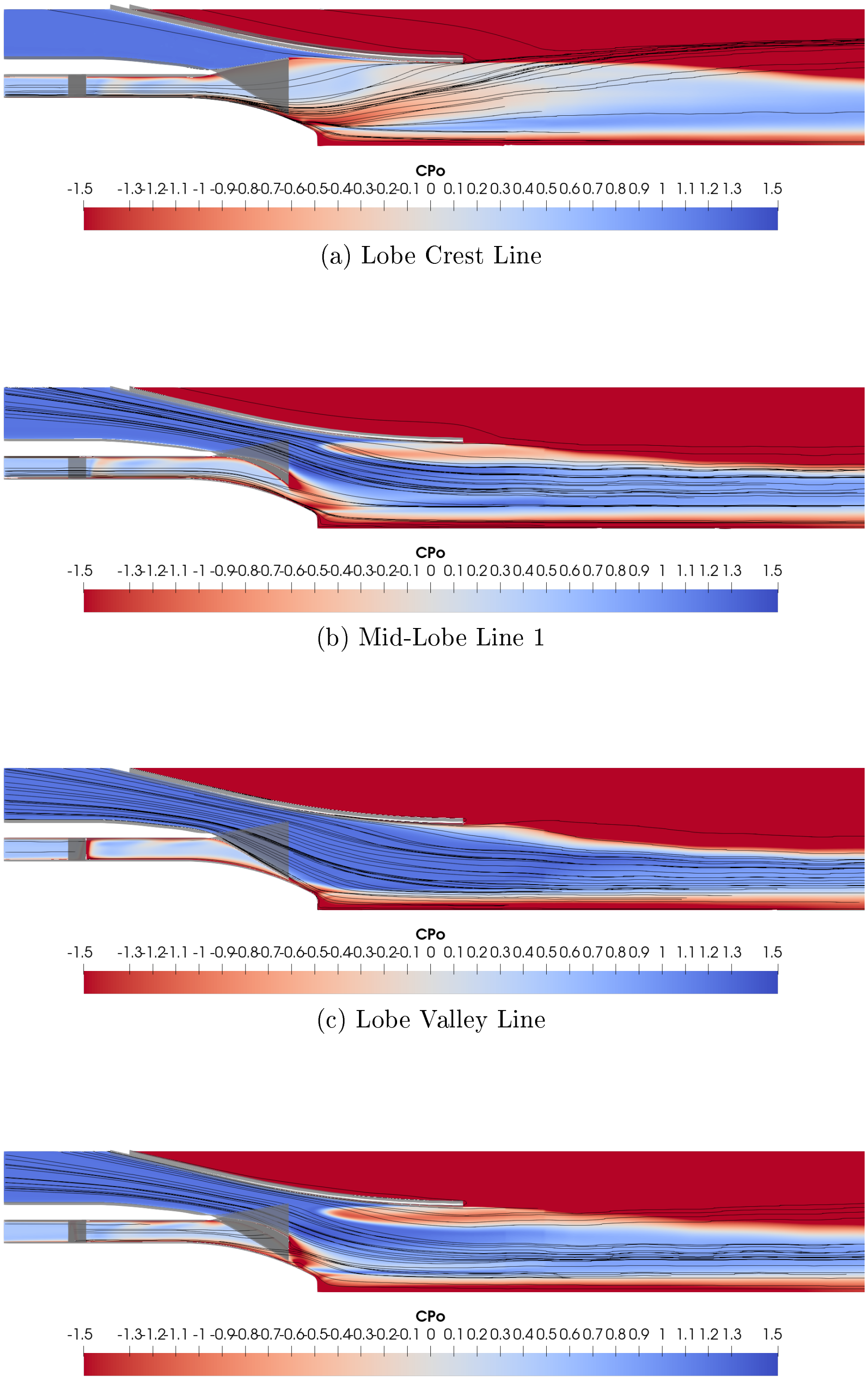

(a) Lobe Crest Line

(b) Mid-Lobe Line 1

(c) Lobe Valley Line

(d) Mid-Lobe Line 2

Figure 7.7: Meridional contours of total pressure coefficient, 10°, unscalloped.

SV_{S1}, can be observed at the plane $Z = 0.000$. That suggests that for this particular lobed mixer design, the core flow would separate if the core flow swirl is somewhere between 10° and 20°. The rest of the flow fields were similar to that when the core flow swirl had 30° swirl. The second separation induced streamwise vortex, SV_{S2}, was not produced.

Mixer Loading

Figure 7.10 shows the limiting streamlines and surface static pressure loading along the inner surface of the unscalloped lobed mixer for all five swirl values investigated. A saddle point along the valley of the mixer is clearly illustrated by the limiting streamlines when the core flow swirl is 0°. The saddle point moved toward the 'pressure-side' of the lobed mixer as the core flow swirl increased. The separation that occurred when the core flow swirl was 20° or 30° is also illustrated by the limiting streamlines and has been highlighted in the Figure.

Turbulent Kinetic Energy Production

The turbulent kinetic energy contour plots indicate regions in the flow where turbulence intensity is increased, indicating the breakdown of large-scale structure like the streamwise and azimuthal vortices into small-scale turbulent structures. These contours in particular, shown in Figure 7.11, show that turbulence generation mostly occurs where the streamwise and azimuthal vortex interact and break each other down. However, the cases with higher swirl show very high turbulent kinetic energy in the wake of the separation on the 'suction-side' of the lobes and in the wake of the centrebody.

Streamlines

An axial view of the velocity streamlines, coloured with total temperature values, has been included in Figure 7.12 to provide a sense of the flow structures' shape and size. The unscalloped mixer showed little sensitivity to core flow swirl up to angles around 10°, beyond which a flow separation occurred and the flow fields disturbed passed minor deflection and asymmetry. The next section presents flow field data to

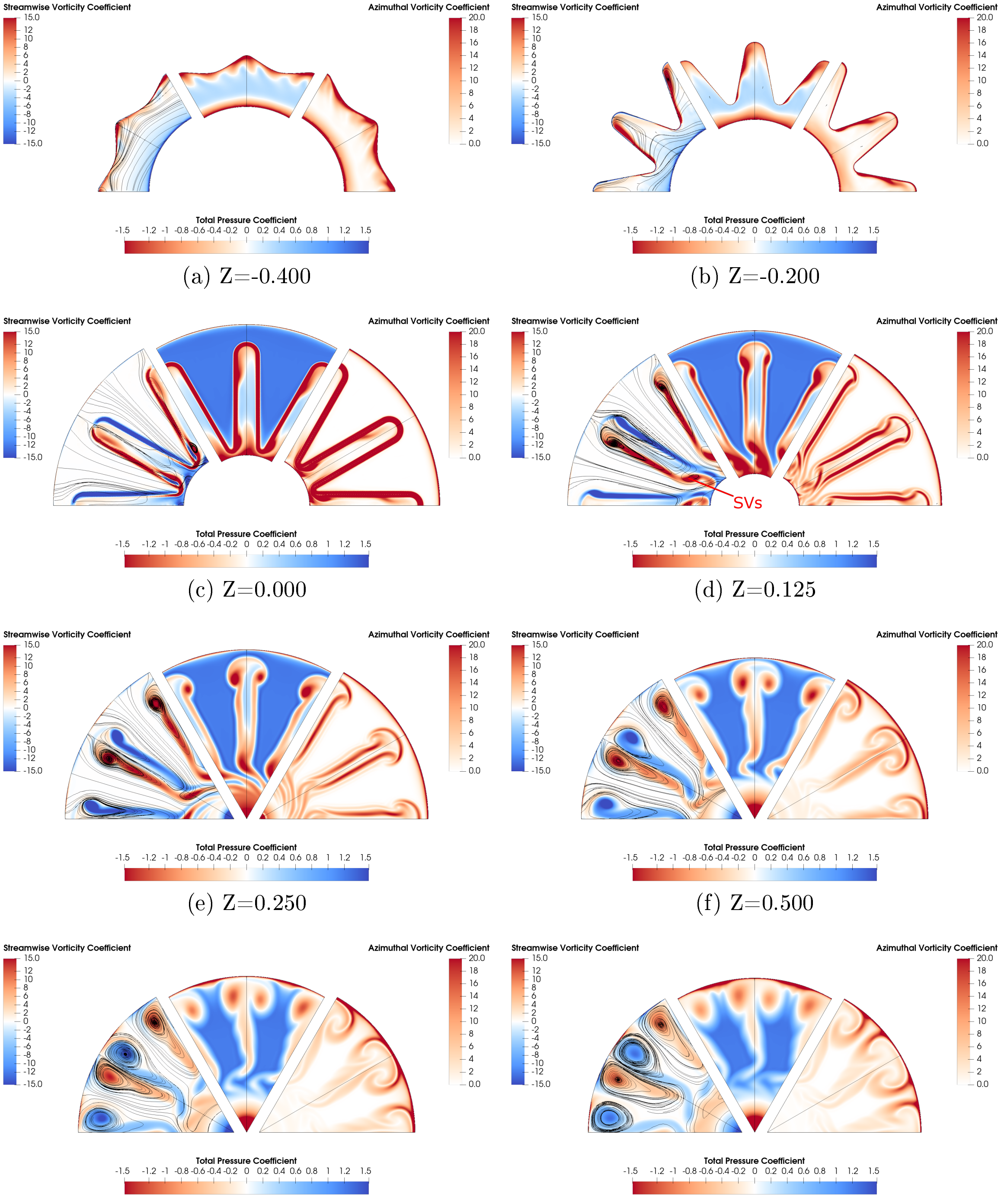

(a) Z=-0.400

(b) Z=-0.200

(c) Z=0.000

(d) Z=0.125

(e) Z=0.250

(f) Z=0.500

(g) Z=0.750

(h) Z=1.000

Figure 7.8: Contour plots of streamwise vorticity coefficient, total pressure coefficient and azimuthal vorticity coefficient, 20°, unscalloped.

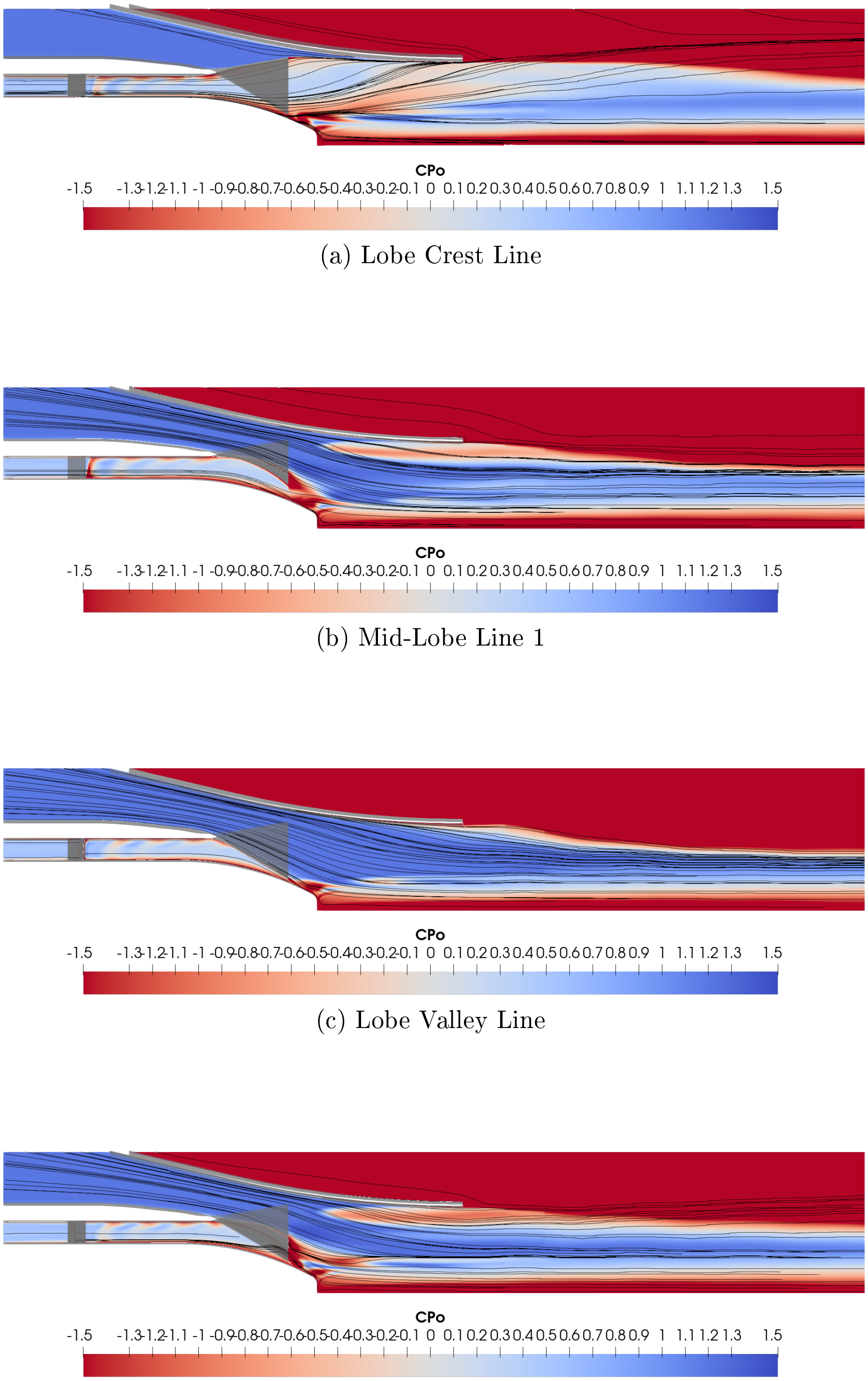

(a) Lobe Crest Line

(b) Mid-Lobe Line 1

(c) Lobe Valley Line

(d) Mid-Lobe Line 2

Figure 7.9: Meridional contours of total pressure coefficient, 20°, unscalloped.

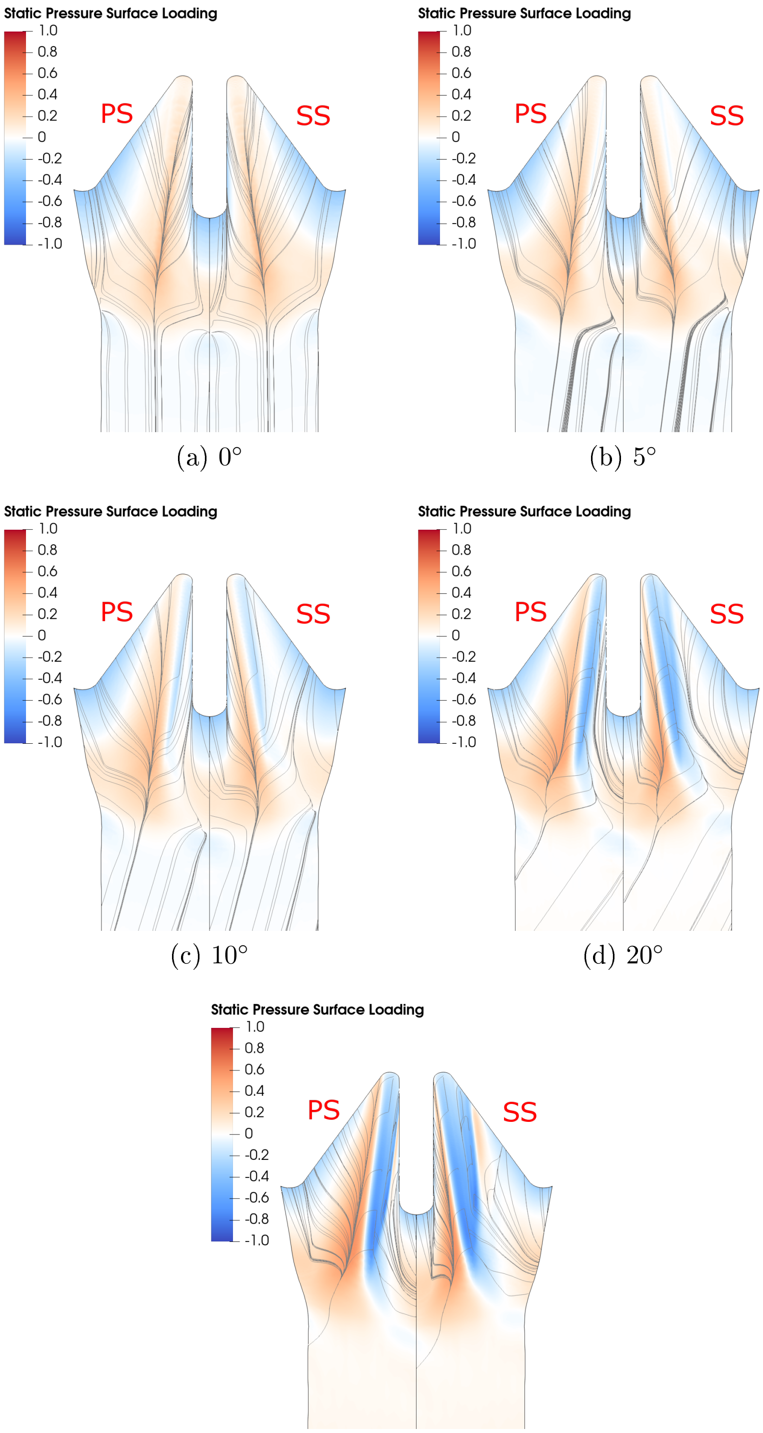

(a) 0°

(b) 5°

(c) 10°

(d) 20°

(e) 30°

Figure 7.10: Surface static pressure loading and limiting streamlines on the core surface of unscalloped lobed mixer with various core flow swirl.

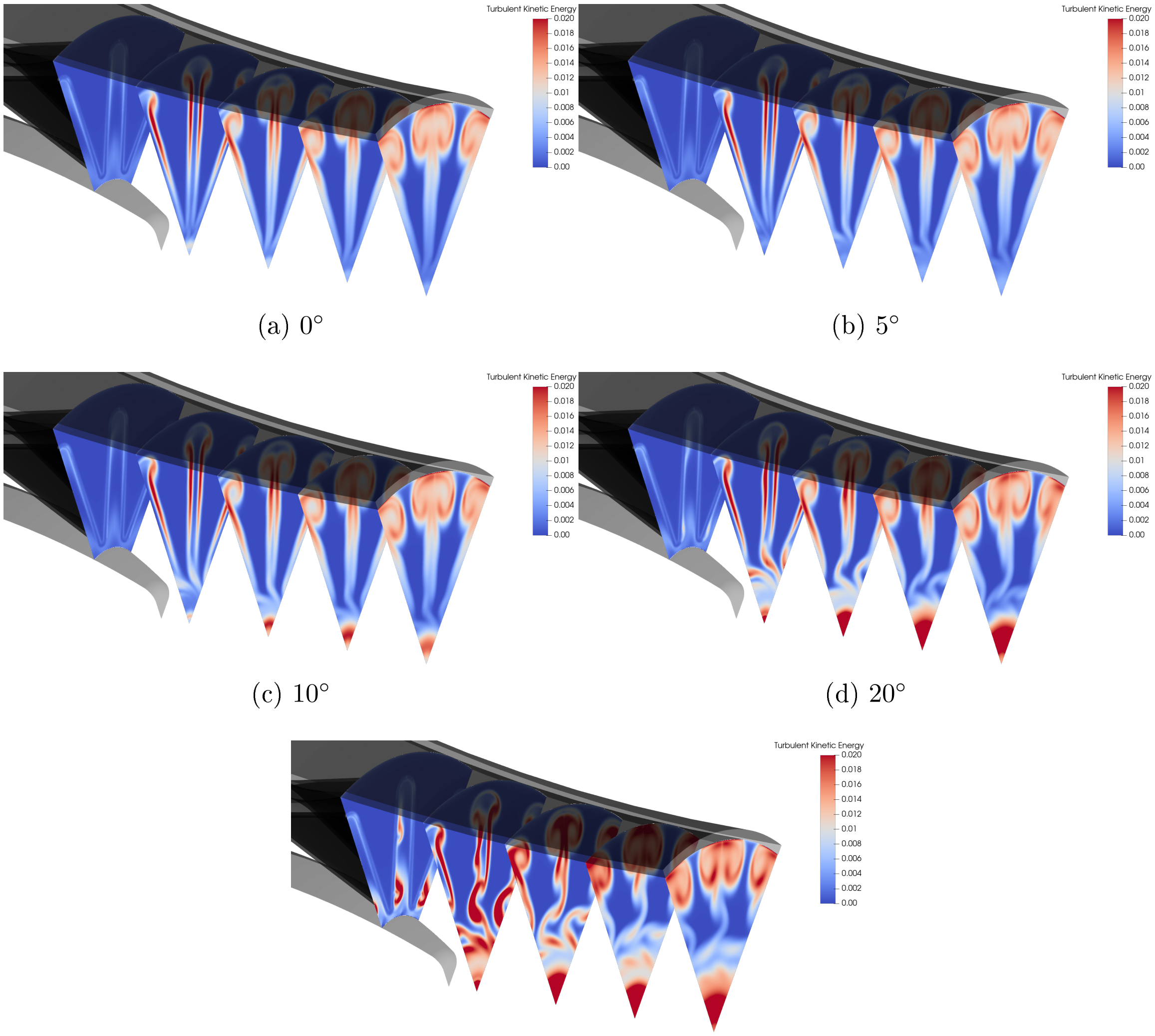

(a) 0°

(b) 5°

(c) 10°

(d) 20°

(e) 30°

Figure 7.11: Turbulent kinetic energy contour plots downstream of unscalloped lobed mixer with various core flow swirl.

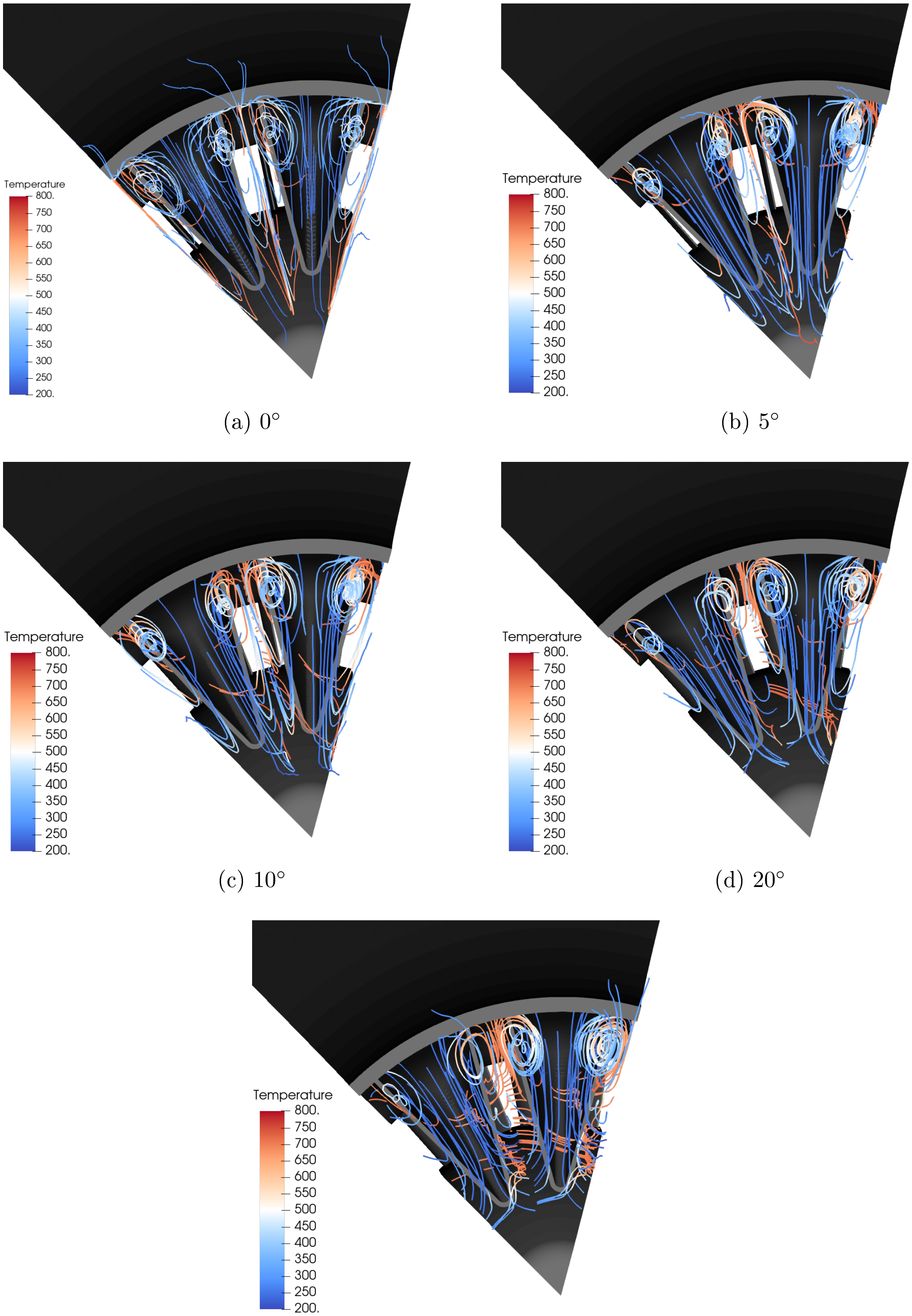

(a) 0°

(b) 5°

(c) 10°

(d) 20°

(e) 30°

Figure 7.12: Velocity streamlines, coloured by total temperature, downstream of unscalloped lobed mixer with various core flow swirl.

provide context on the sensitivity of the scalloped lobed mixer to increased core flow inlet swirl.

7.3.2 Scalloped Flow Field Sensitivity

This section presents the first time that the flow fields downstream of the 'Final' scalloped lobed mixer, heretofore referred to simply as the scalloped lobed mixer, shall be discussed.

0 Degree

Figure 7.13 illustrates the flow field downstream of the scalloped lobed mixer at the ideal exhaust system condition where all of the fluid flowing into the lobed mixer is purely axial, with no tangential component to the velocity vector in either the core or the bypass. Four distinct vortex cores were developed: the two main vortices expected from a comparable unscalloped mixer and two additional vortices near the valley of the lobes where co-rotating pairs of the main vortices were developed because of the shape of the scallop and the flow around it. These features lose strength, grow in size, break down and mix out as they propagate downstream of the mixer toward the end of the nozzle, $Z = 1.000$.

5 Degrees

Just as in the unscalloped lobed mixer flow fields, a core flow inlet swirl of 5° produced only minor changes. The flow fields shown in Figure 7.15 display a slight asymmetry and deflection of structures near the centre of the jet. Otherwise, the relative strength of vorticity streamwise and azimuthal appear unchanged.

10 Degrees

Increasing the core flow swirl to 10° showed the same effects as the unscalloped lobed mixer. Further asymmetry and deflection of structures is illustrated in Figure 7.17.

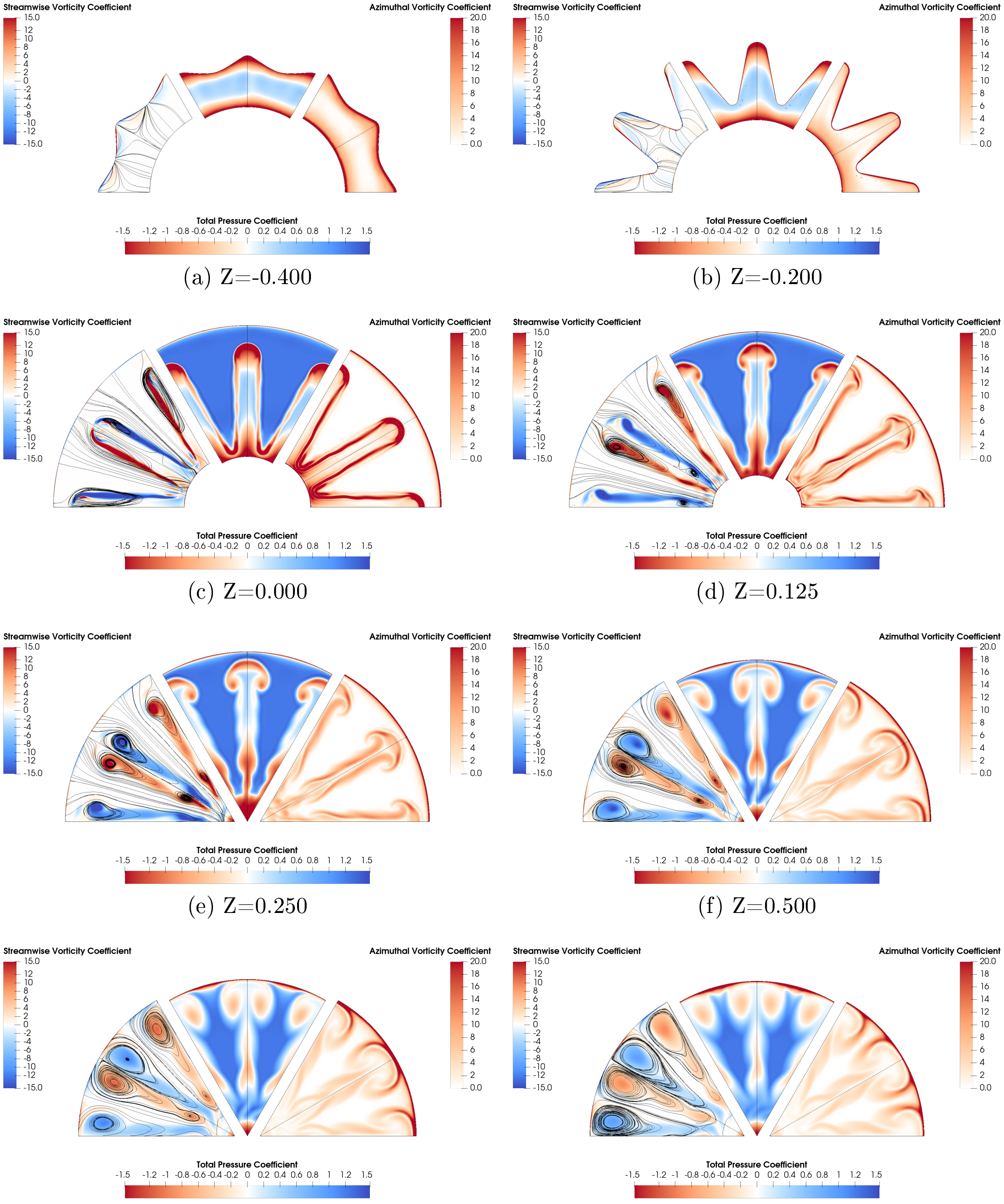

(a) Z=-0.400

(b) Z=-0.200

(c) Z=0.000

(d) Z=0.125

(e) Z=0.250

(f) Z=0.500

(g) Z=0.750

(h) Z=1.000

Figure 7.13: Contour plots of streamwise vorticity coefficient, total pressure coefficient and azimuthal vorticity coefficient, no swirl, scalloped.

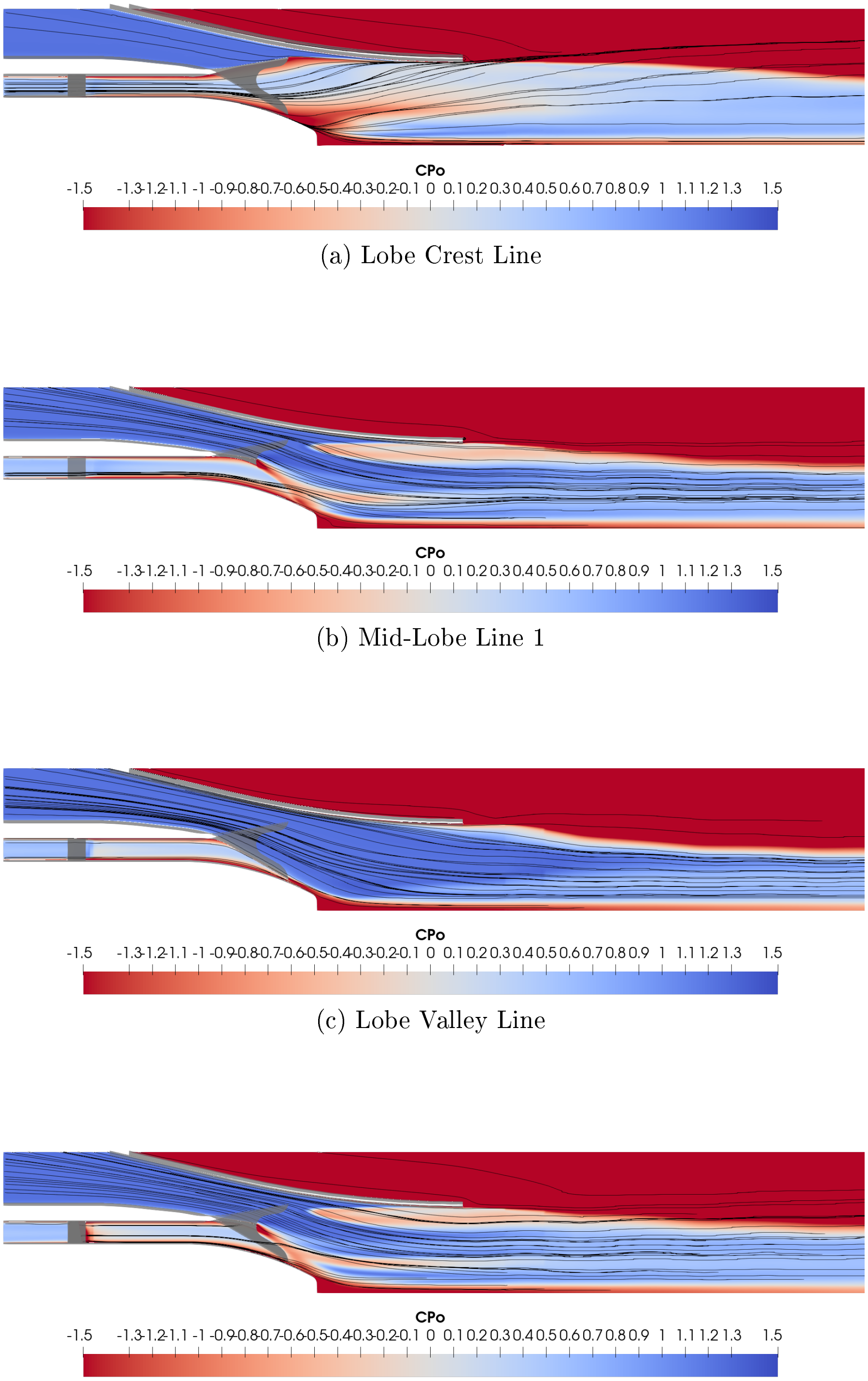

(a) Lobe Crest Line

(b) Mid-Lobe Line 1

(c) Lobe Valley Line

(d) Mid-Lobe Line 2

Figure 7.14: Meridional contours of total pressure coefficient, no swirl, scalloped.

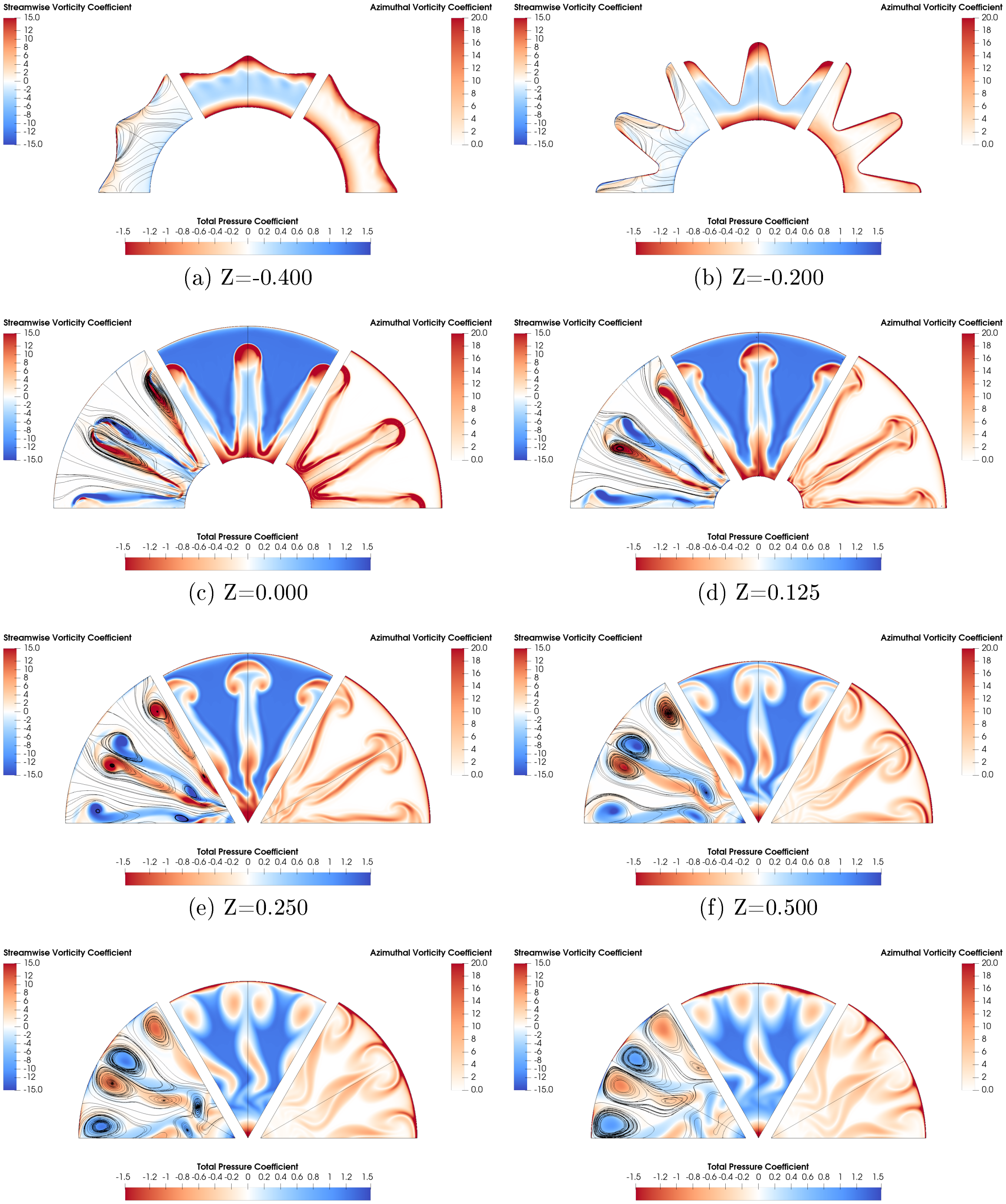

(a) Z=-0.400

(b) Z=-0.200

(c) Z=0.000

(d) Z=0.125

(e) Z=0.250

(f) Z=0.500

(g) Z=0.750

(h) Z=1.000

Figure 7.15: Contour plots of streamwise vorticity coefficient, total pressure coefficient and azimuthal vorticity coefficient, 5° swirl, scalloped.

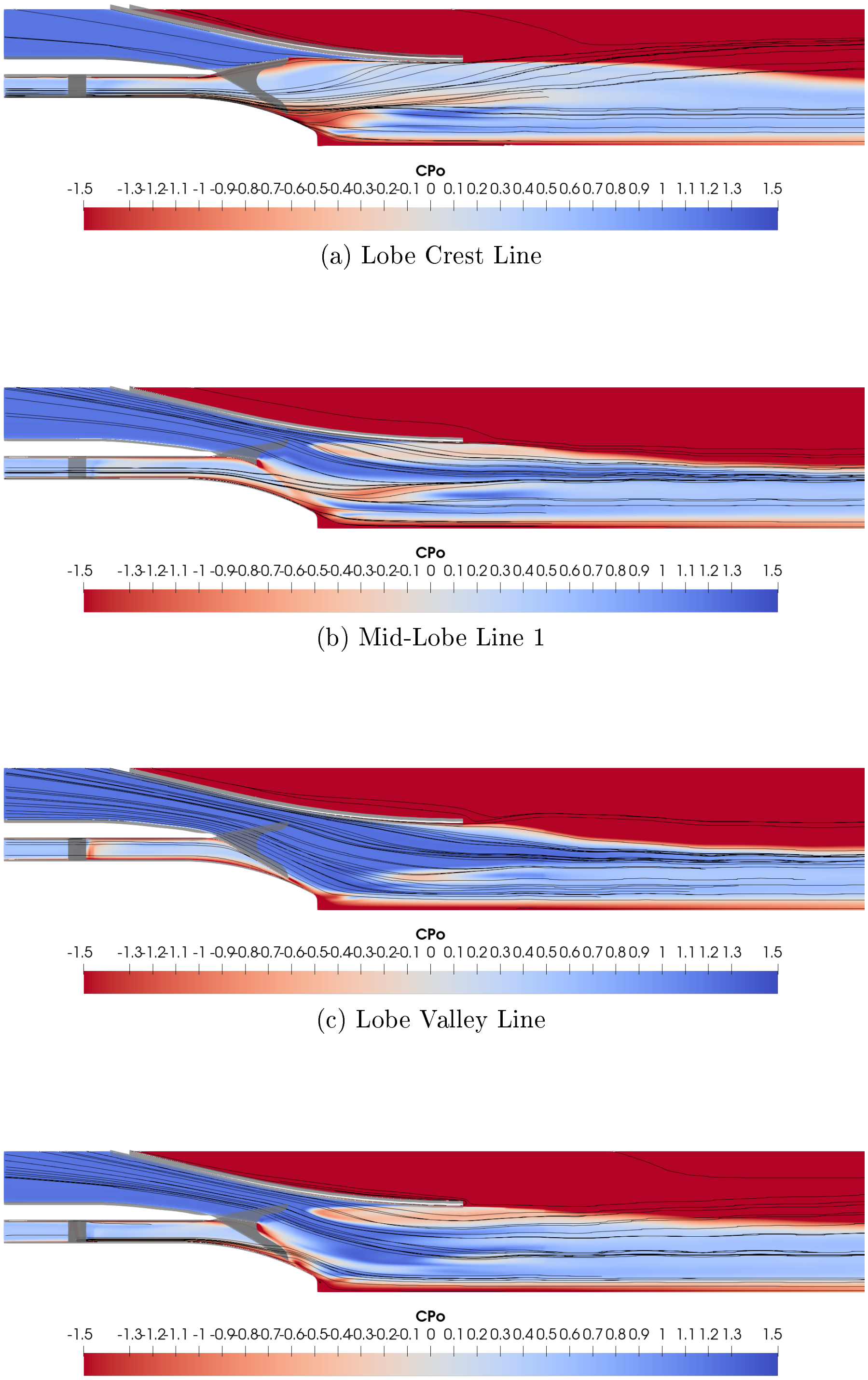

(a) Lobe Crest Line

(b) Mid-Lobe Line 1

(c) Lobe Valley Line

(d) Mid-Lobe Line 2

Figure 7.16: Meridional contours of total pressure coefficient, 5° swirl, scalloped.

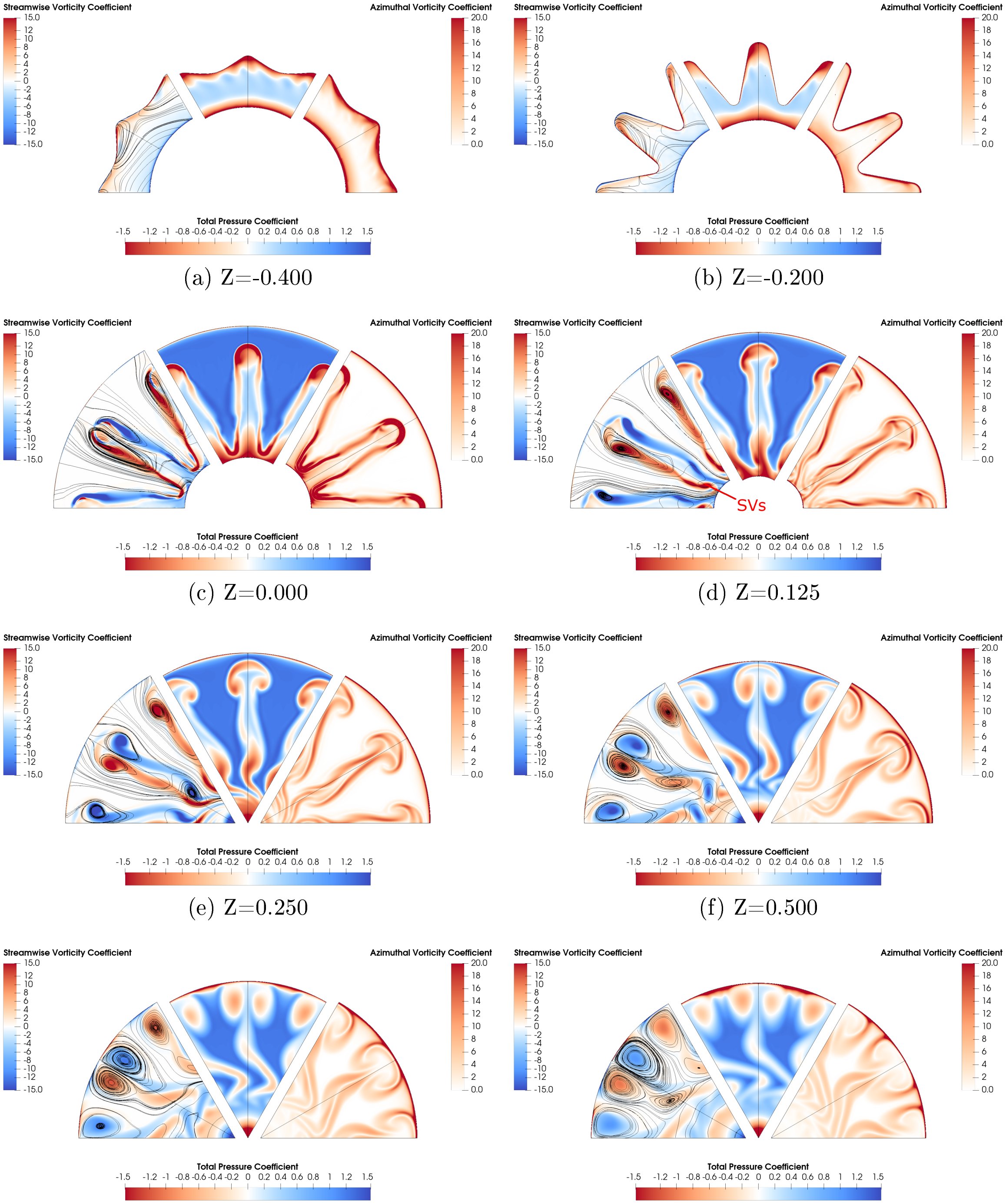

(a) Z=-0.400

(b) Z=-0.200

(c) Z=0.000

(d) Z=0.125

(e) Z=0.250

(f) Z=0.500

(g) Z=0.750

(h) Z=1.000

Figure 7.17: Contour plots of streamwise vorticity coefficient, total pressure coefficient and azimuthal vorticity coefficient, 10° swirl, scalloped.

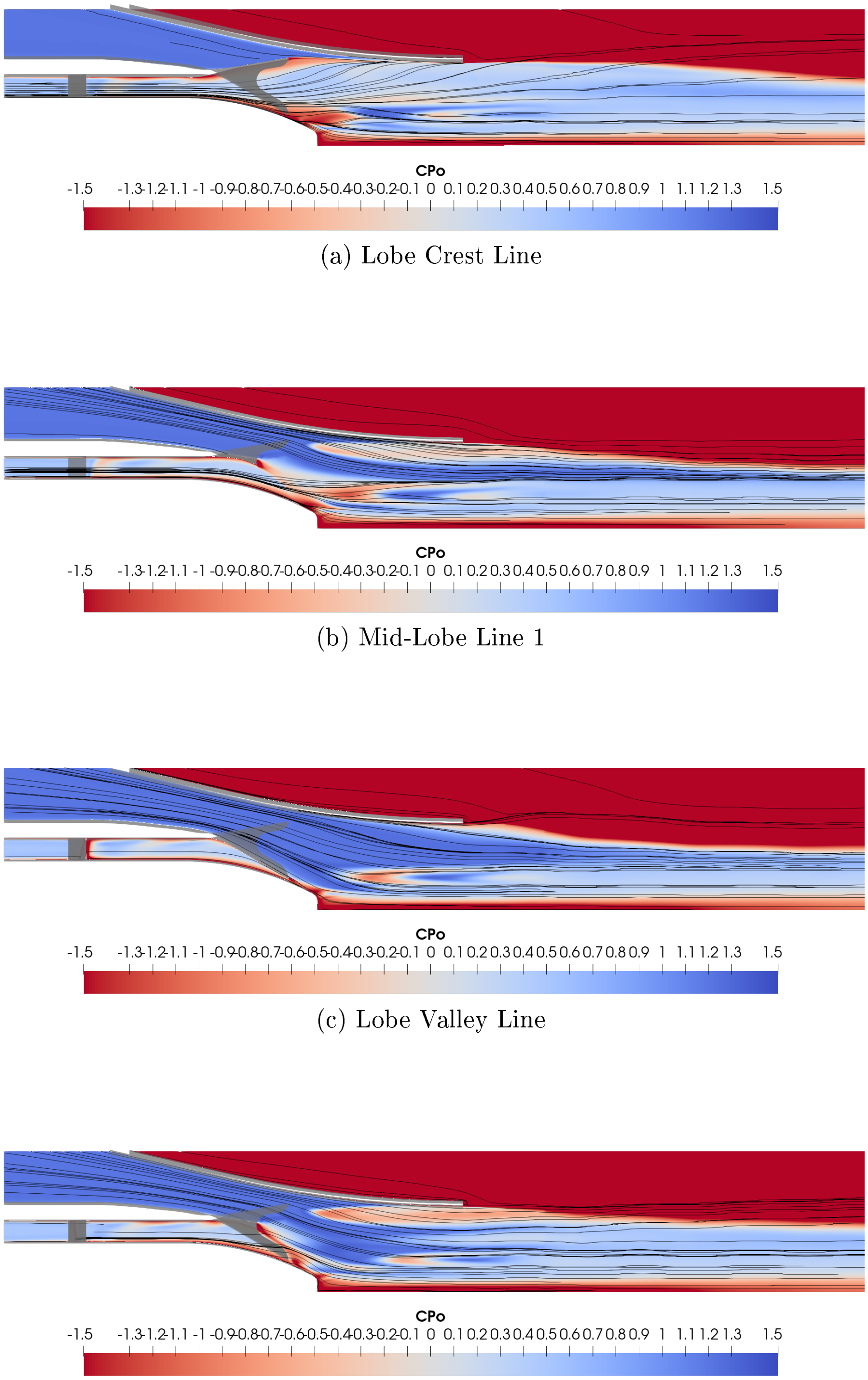

(a) Lobe Crest Line

(b) Mid-Lobe Line 1

(c) Lobe Valley Line

(d) Mid-Lobe Line 2

Figure 7.18: Meridional contours of total pressure coefficient, 10° swirl, scalloped.

20 Degrees

The separation induced vortex, SV_{S1}, appeared again when the scalloped lobed mixer was operating with 20° core flow swirl—along with all of its associated low pressure zones and azimuthal vortex interaction. A greater asymmetry was also observed. Plane $Z = 0.000$ of Figure 7.19 illustrates the lower pressure zone within the wake of the scallop on the 'suction-side' of the mixer as compared to the wake of the 'pressure-side'. The secondary streamwise vortices, SV_3 and SV_4, developed as well. All three streamwise vortices near the centre of the jet interacted with each other which resulted in a radial stacking of the vortices as indicated on plane $Z = 0.250$. These vortices became incoherent and lost their structure around plane $Z = 0.750$.

30 Degrees

Figure 7.21 shows that the separation induced vortex was produced with a very strong core, labeled on plane $Z = 0.000$. That vortex inhibited SV_3 from forming its distinct core along the inner edge of the scallop. Unlike the 20° core flow swirl case, where three streamwise vortices emerged near the centre of the jet and interacted to produce a radial stack of vortices, the two vortices were not able to interact to form such a stack and did not fully dissipate at the nozzle exit plane, $Z = 1.000$. The residual swirl through the gap between the valley and the centrebody produced a very strong low pressure zone in the centre of the jet.

Mixer Loading

The surface static pressure loading and limiting streamlines of velocity on the inner mixer surface shown in Figure 7.23 identify which levels of core swirl produced separation on the 'suction-side' of the lobes. Separation was observed for core flow swirls of 20° and 30°, agreeing with the observations noted about the flow fields.

Turbulent Kinetic Energy Production

Figure 7.24 shows the turbulent kinetic energy downstream of the scalloped lobed mixer with various core flow swirl values. The higher swirl cases of 20° and 30°

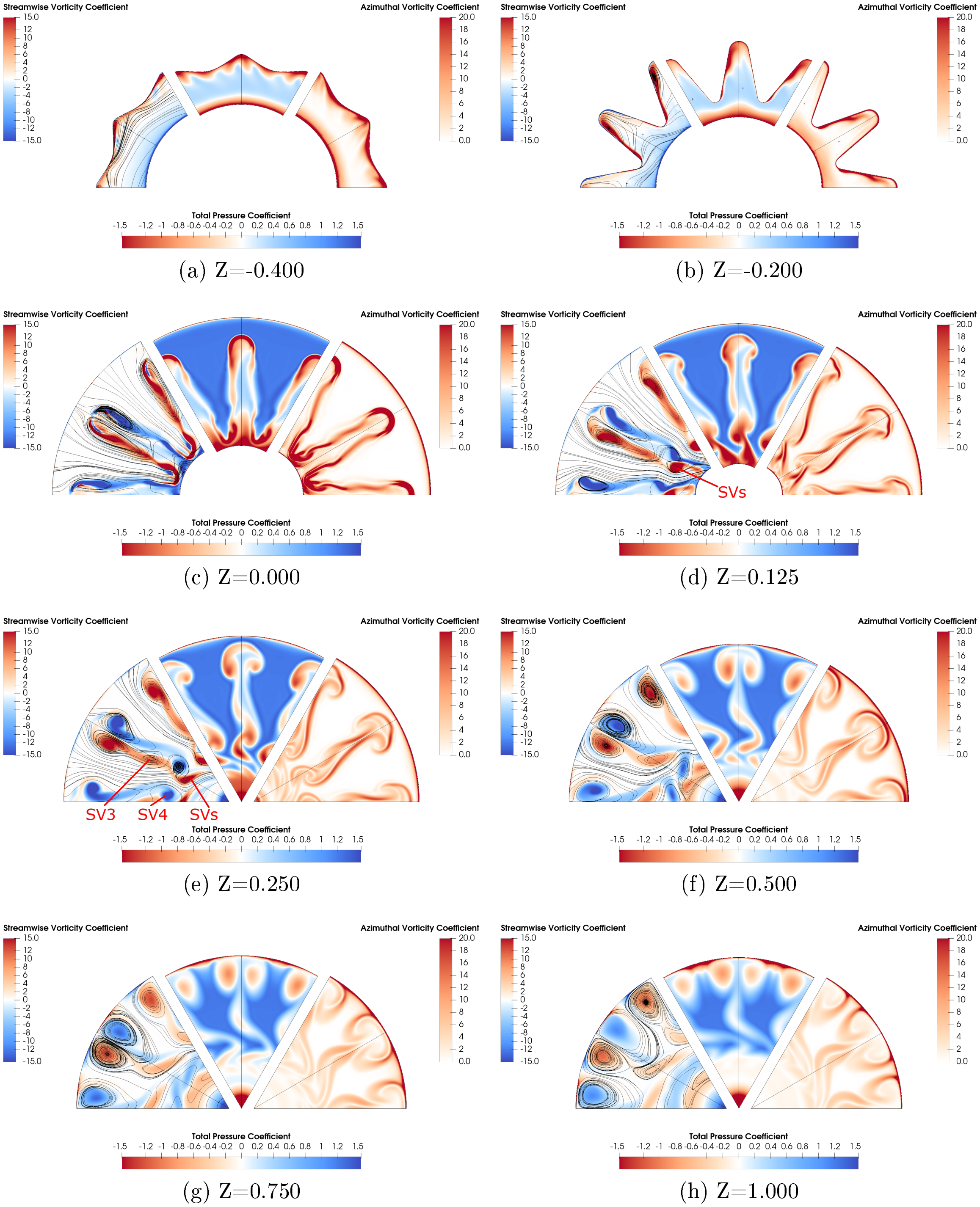

(a) Z=-0.400

(b) Z=-0.200

(c) Z=0.000

(d) Z=0.125

(e) Z=0.250

(f) Z=0.500

(g) Z=0.750

(h) Z=1.000

Figure 7.19: Contour plots of streamwise vorticity coefficient, total pressure coefficient and azimuthal vorticity coefficient, 20° swirl, scalloped.

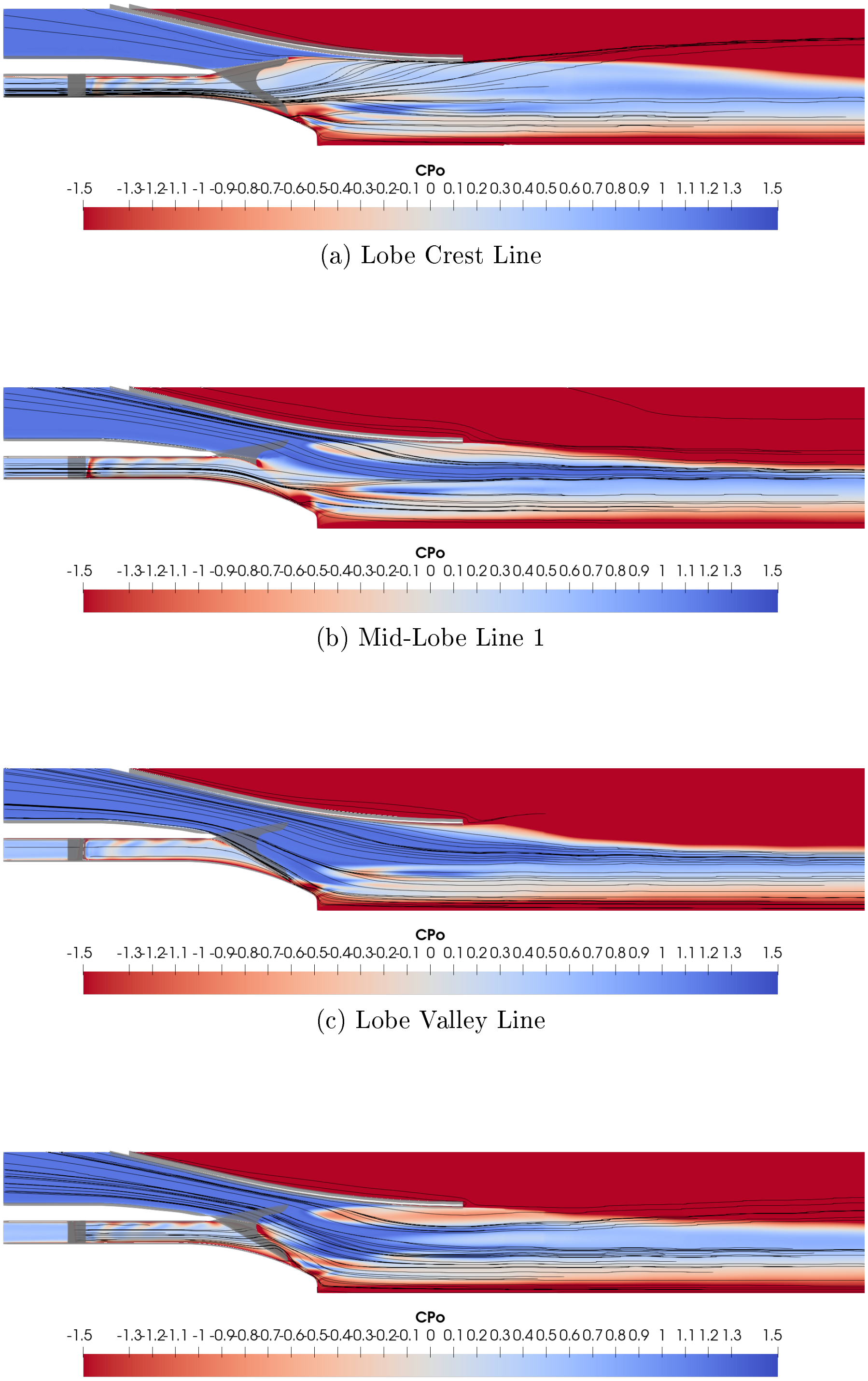

(a) Lobe Crest Line

(b) Mid-Lobe Line 1

(c) Lobe Valley Line

(d) Mid-Lobe Line 2

Figure 7.20: Meridional contours of total pressure coefficient, 20° swirl, scalloped.

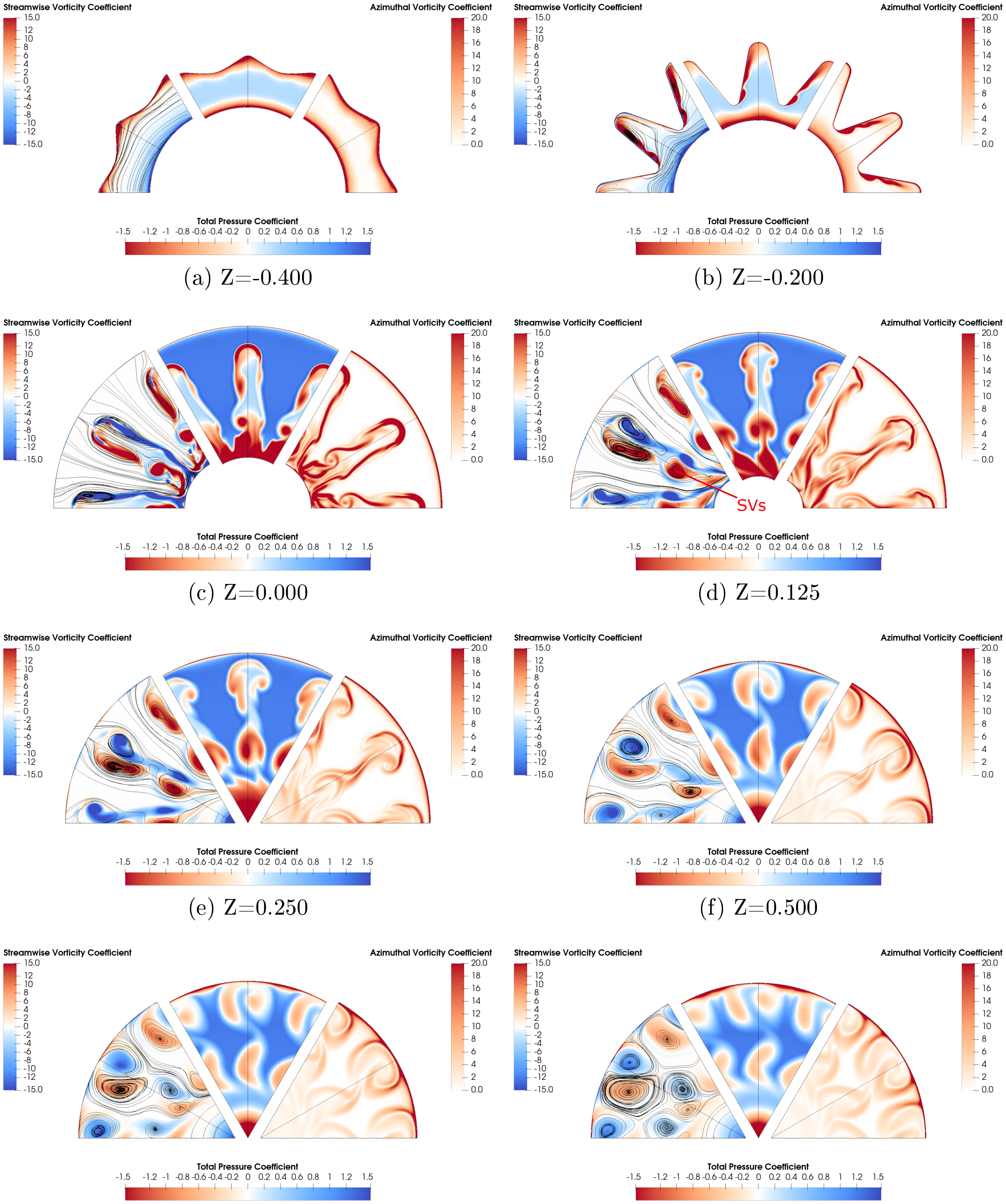

(a) Z=-0.400

(b) Z=-0.200

(c) Z=0.000

(d) Z=0.125

(e) Z=0.250

(f) Z=0.500

(g) Z=0.750

(h) Z=1.000

Figure 7.21: Contour plots of streamwise vorticity coefficient, total pressure coefficient and azimuthal vorticity coefficient, 30° swirl, scalloped.

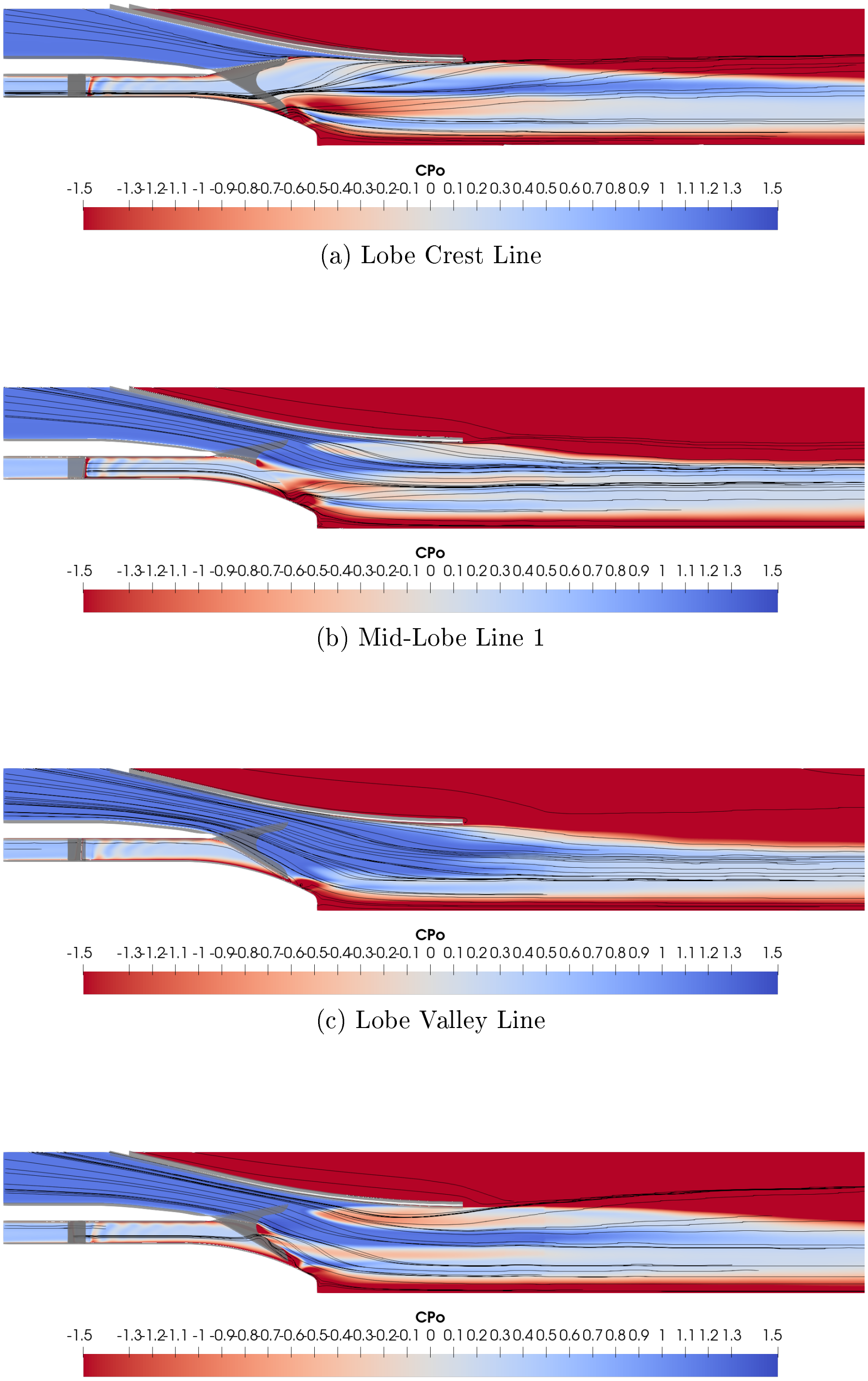

(a) Lobe Crest Line

(b) Mid-Lobe Line 1

(c) Lobe Valley Line

(d) Mid-Lobe Line 2

Figure 7.22: Meridional contours of total pressure coefficient, 30° swirl, scalloped.

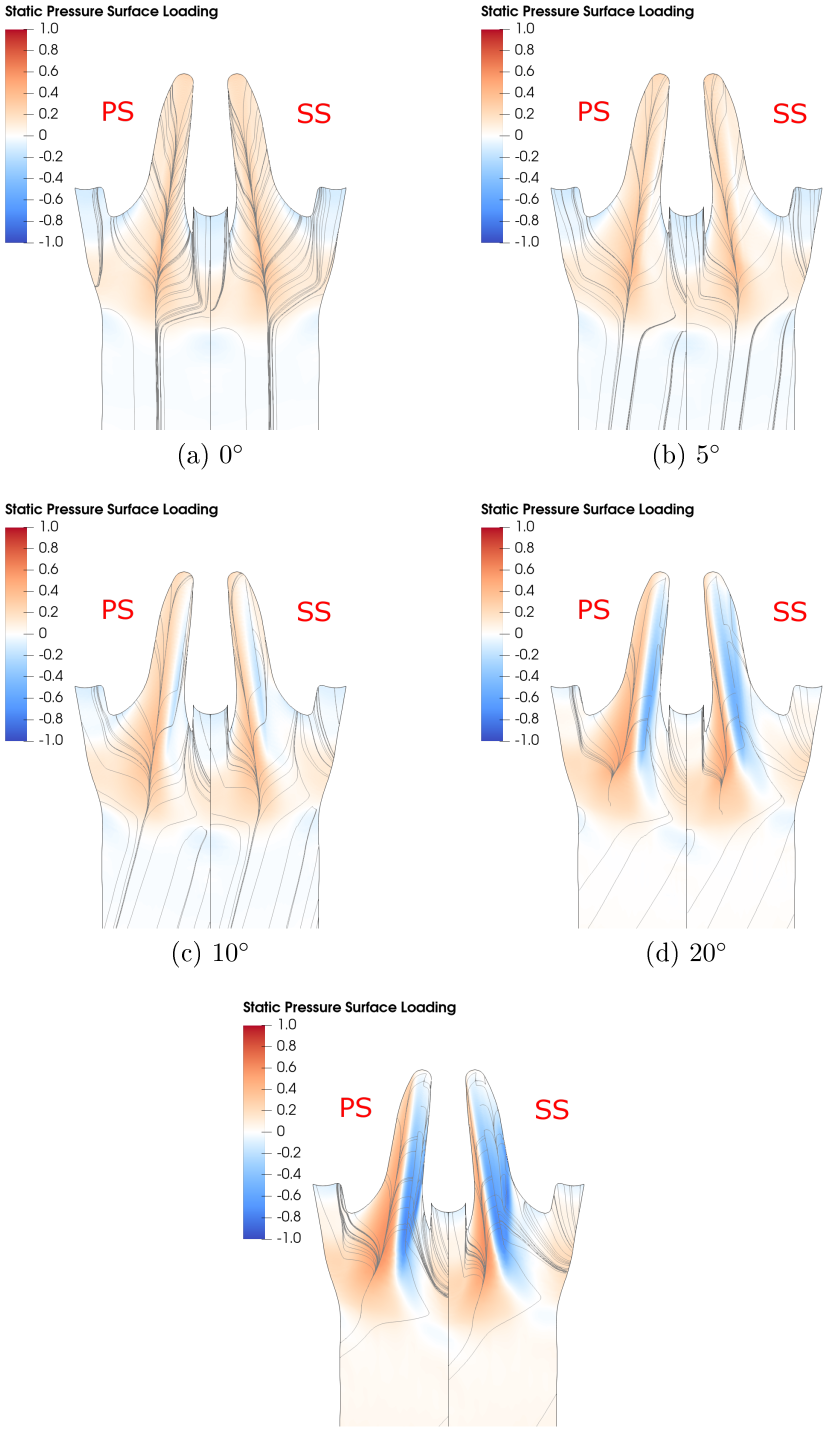

(a) 0°

(b) 5°

(c) 10°

(d) 20°

(e) 30°

Figure 7.23: Surface static pressure loading and limiting streamlines on the core surface of scalloped lobed mixer with various core flow swirl.

produced exceptionally high levels of turbulent energy throughout the mixing duct, especially in regions that correspond to the flow separation.

Streamlines

Figure 7.25 provides an illustration of the three dimensional velocity streamlines downstream of the scalloped lobed mixer.

7.3.3 Performance

Circulation

The positive, counterclockwise circulation is presented for the unscalloped and scalloped lobed mixers in Figure 7.27. The residual swirl that persisted downstream of the mixer, whether through the gap between the valley and centrebody or through the scallop, was recorded in this calculation as positive vorticity and therefore positive circulation. This is the first time reporting circulation Figures for the unscalloped lobed mixer with 5°, 10° and 20° core flow swirl, in Figure 7.27a. The circulation settled into a trend from the greatest with no core flow swirl to the lowest with 30° core flow swirl downstream of the unscalloped lobed mixer. Figure 7.27b tells a different story downstream of the scalloped lobed mixer. The circulation for the 30° core flow swirl case began as the strongest circulation right at the mixer exit plane. It then became the weakest of all the cases shortly downstream of the lobed mixer, but at $Z = 0.625$ plane began to maintain strength as compared to the 10° and 20° core flow inlet swirl cases. It even overtakes the 5° case at the nozzle exit plane, $Z = 1.000$. That circulation trend matches the observation in the streamwise vorticity coefficient contour plots where the inner vortex cores were coherent through to $Z = 1.000$.

Static Pressure Statistics

The static pressure data obtained via these simulations painted an interesting picture as well. The primary static pressure value is the mixing index, shown in Figure 7.28. There was little difference between the cases for both unscalloped and scalloped lobed mixers. What's more interesting is the plot of minimum static pressure observed downstream of the lobed mixers, shown in Figure 7.30. There was a large drop in the

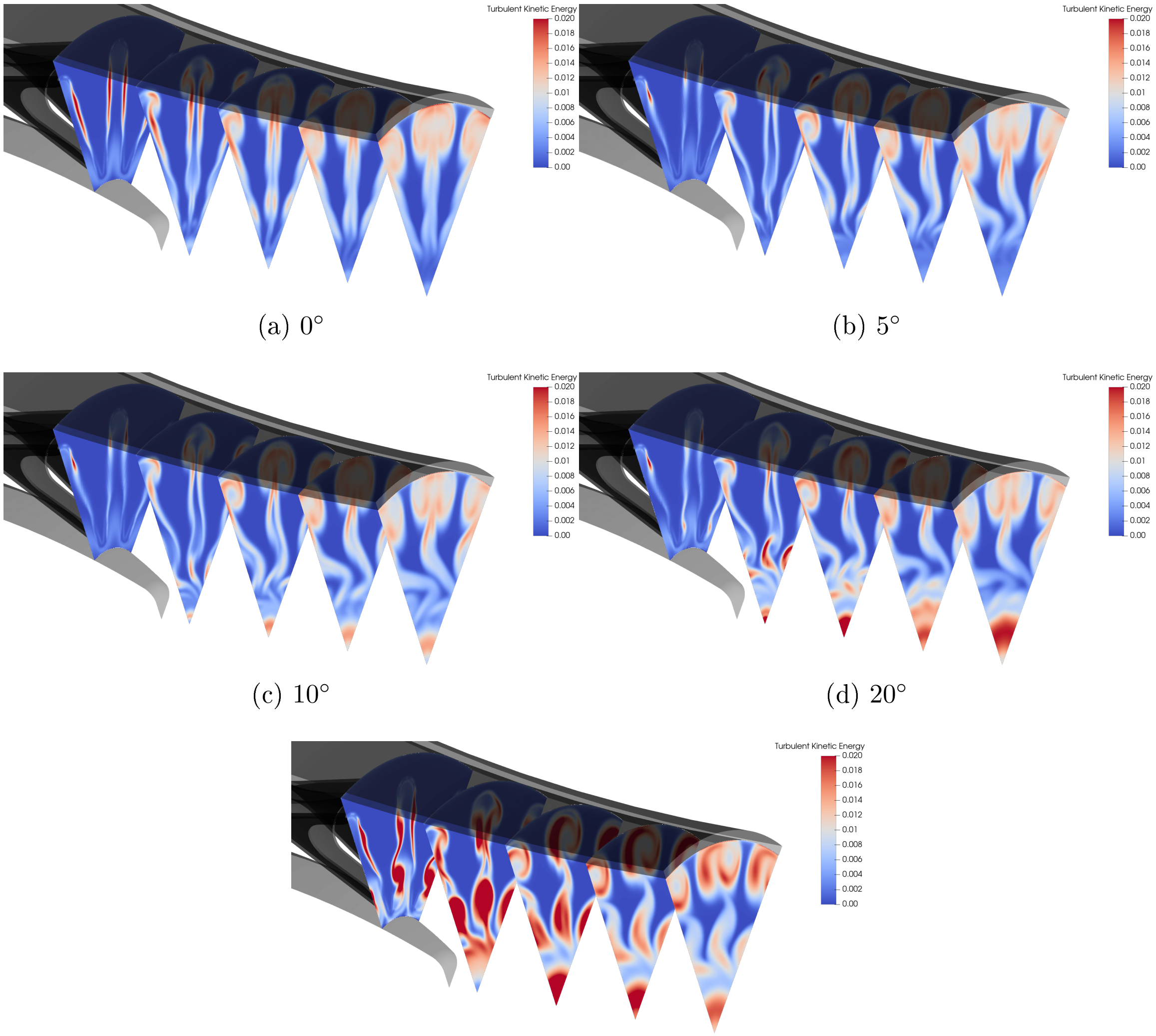

(a) 0°

(b) 5°

(c) 10°

(d) 20°

(e) 30°

Figure 7.24: Turbulent kinetic energy contour plots downstream of scalloped lobed mixer with various core flow swirl.

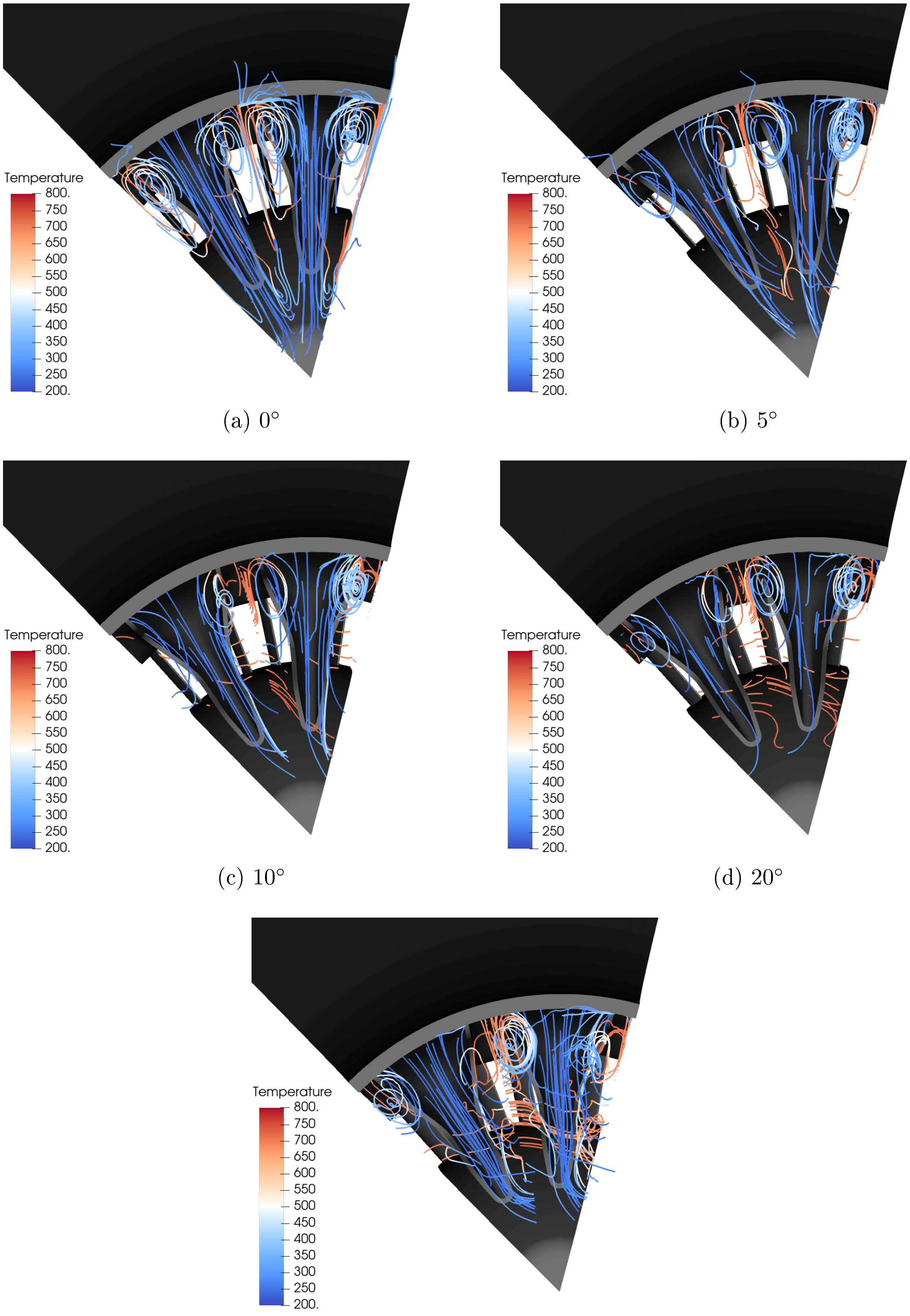

(a) 0°

(b) 5°

(c) 10°

(d) 20°

(e) 30°

Figure 7.25: Velocity streamlines, coloured by total temperature, downstream of scalloped lobed mixer with various core flow swirl.

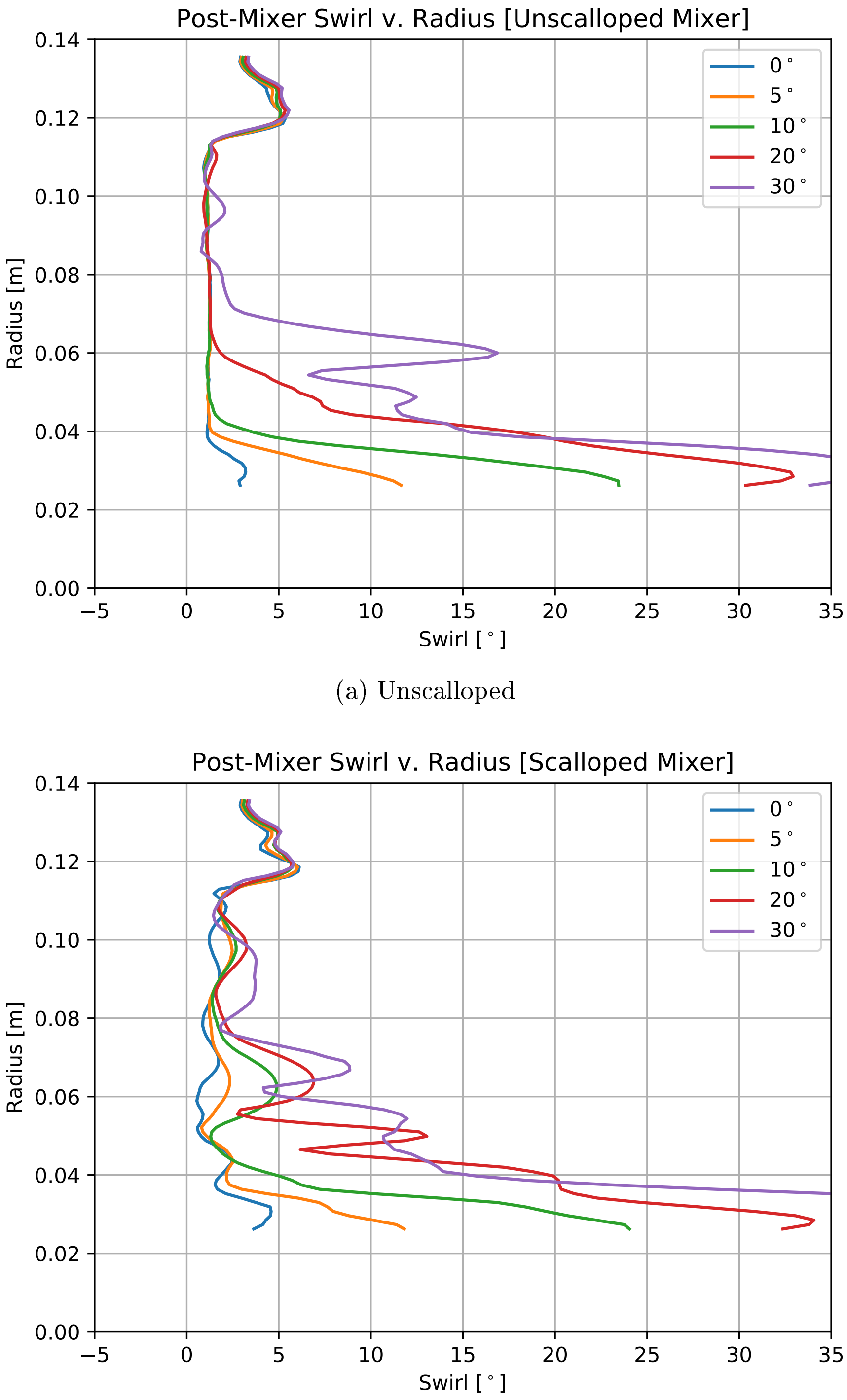

(a) Unscalloped

(b) Scalloped

Figure 7.26: Mixer outlet swirl with various core flow swirl angles.

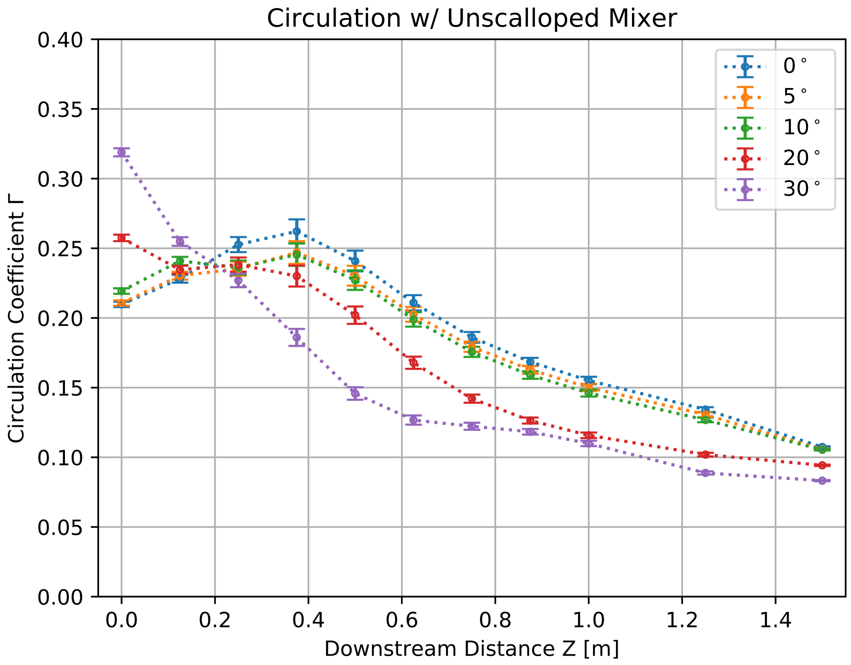

(a) Unscalloped

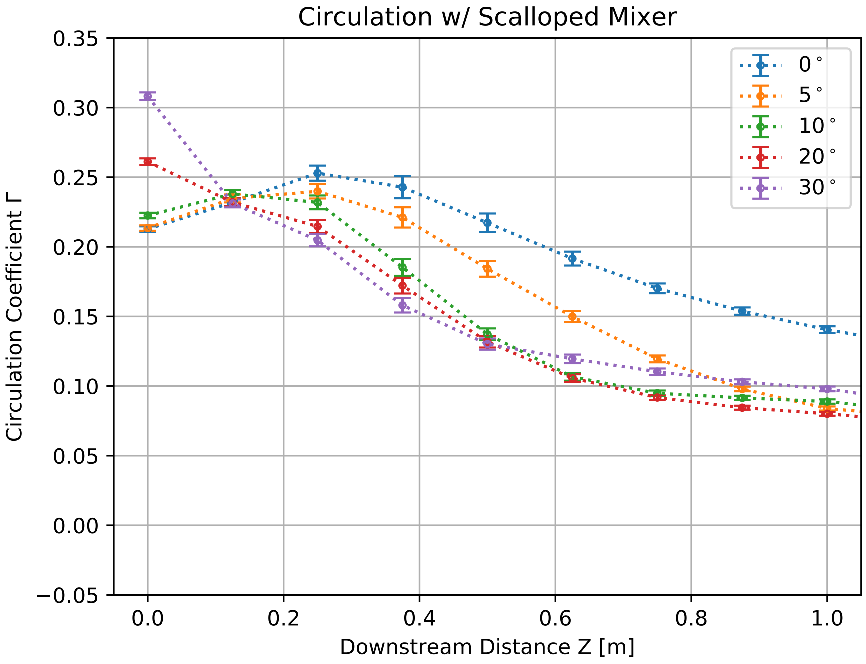

(b) Scalloped

Figure 7.27: Counterclockwise circulation downstream of the mixer with various core flow swirl angles.

minimum static pressure calculated at the $Z = 0.250$ plane downstream of both lobed mixers for cases with core flow swirl greater than 10°. That large drop ocurred in the wake of the centrebody and was due to the interaction of the swirling flow with the falling radius. Conservation of angular momentum commands that a fluid element with tangential velocity component should experience an increase of that tangential velocity component as the distance of the fluid element from the centre of rotation diminishes. That is exactly the case that happened with core flow swirl downstream of the centrebody.

Pressure Loss and Thrust Coefficient

The prime performance parameters of pressure loss and thrust coefficients, listed in Table 7.2, give a clear indication into the true sensitivity of each mixer to various degrees of core flow inlet swirl. In all ten cases, the thrust coefficient was clearly not sensitive to core flow swirl. All cases produced values within the margin of error of the simulations. The pressure loss coefficient was more sensitive to inlet swirl. As mentioned previously, the high degree swirl cases predicted large low pressure zones and high turbulent kinetic energy in the separation zones downstream of the mixer and centrebody. That translated into higher overall total pressure loss coefficients for both unscalloped and scalloped lobed mixer. Notably, the scalloped lobed mixer losses are reduced across the board when compared to equivalent conditions for the unscalloped mixer. Further proof that scalloped lobed mixers are superior to unscalloped mixers for MBTF exhaust system performance. However, another interesting discovery was that the unscalloped lobed mixer system produced the lowest losses with 10° core flow swirl. This agrees with previously published findings that inlet swirl up to 10° could be beneficial to the mixing process without producing the same increases in total pressure loss observed with higher degrees of core flow swirl.

7.4 Conclusions

This chapter presented data on the sensitivity of unscalloped and scalloped lobed mixers to increases in core flow swirl. The two lobed mixers were subject to core flow swirl that ranged from 0° up to 30°. Flow field data on vorticity strength, total pressure distribution and velocity streamlines provided insight onto flow structure

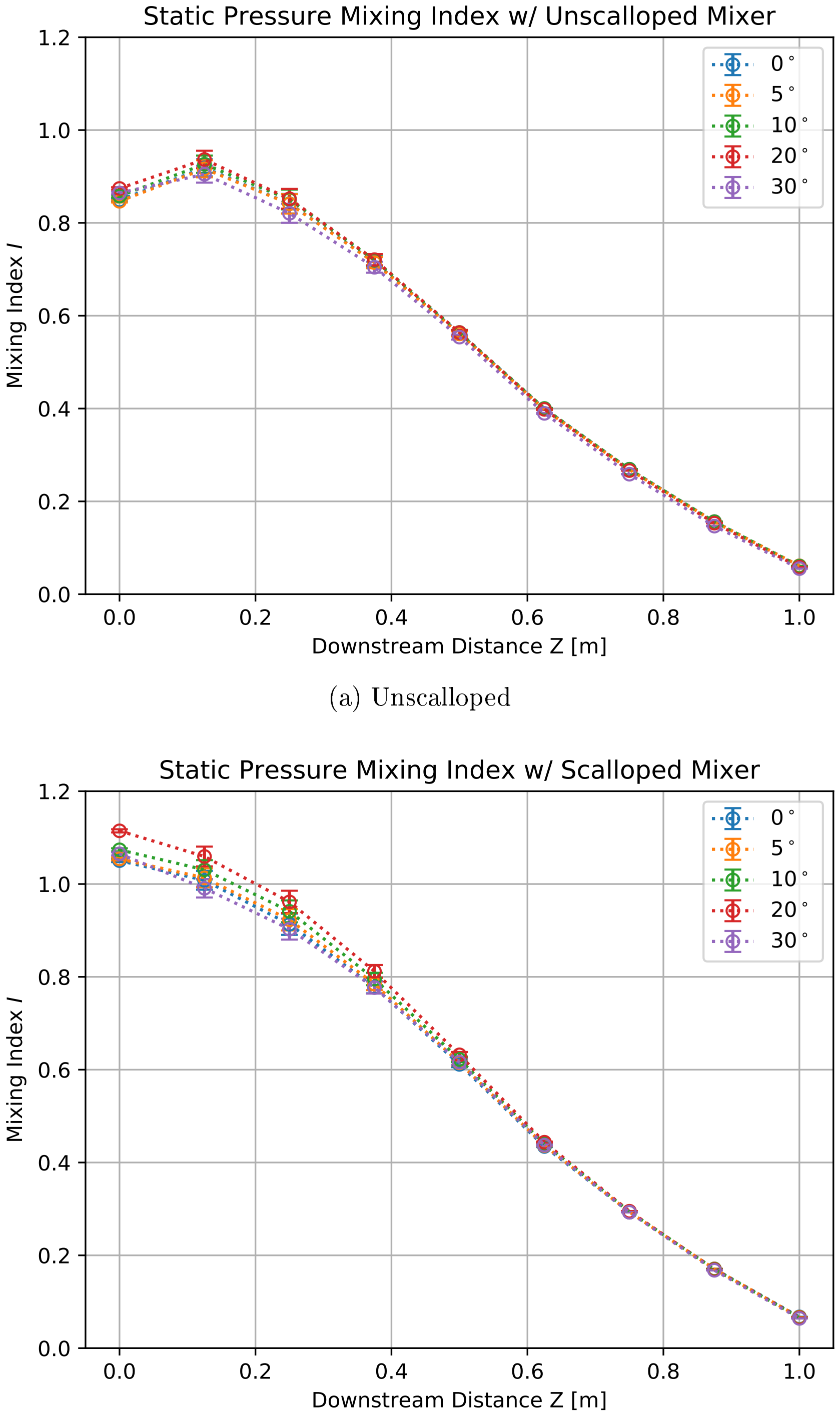

(a) Unscalloped

(b) Scalloped

Figure 7.28: Static pressure mixing index downstream of the mixer with various core flow swirl angles.

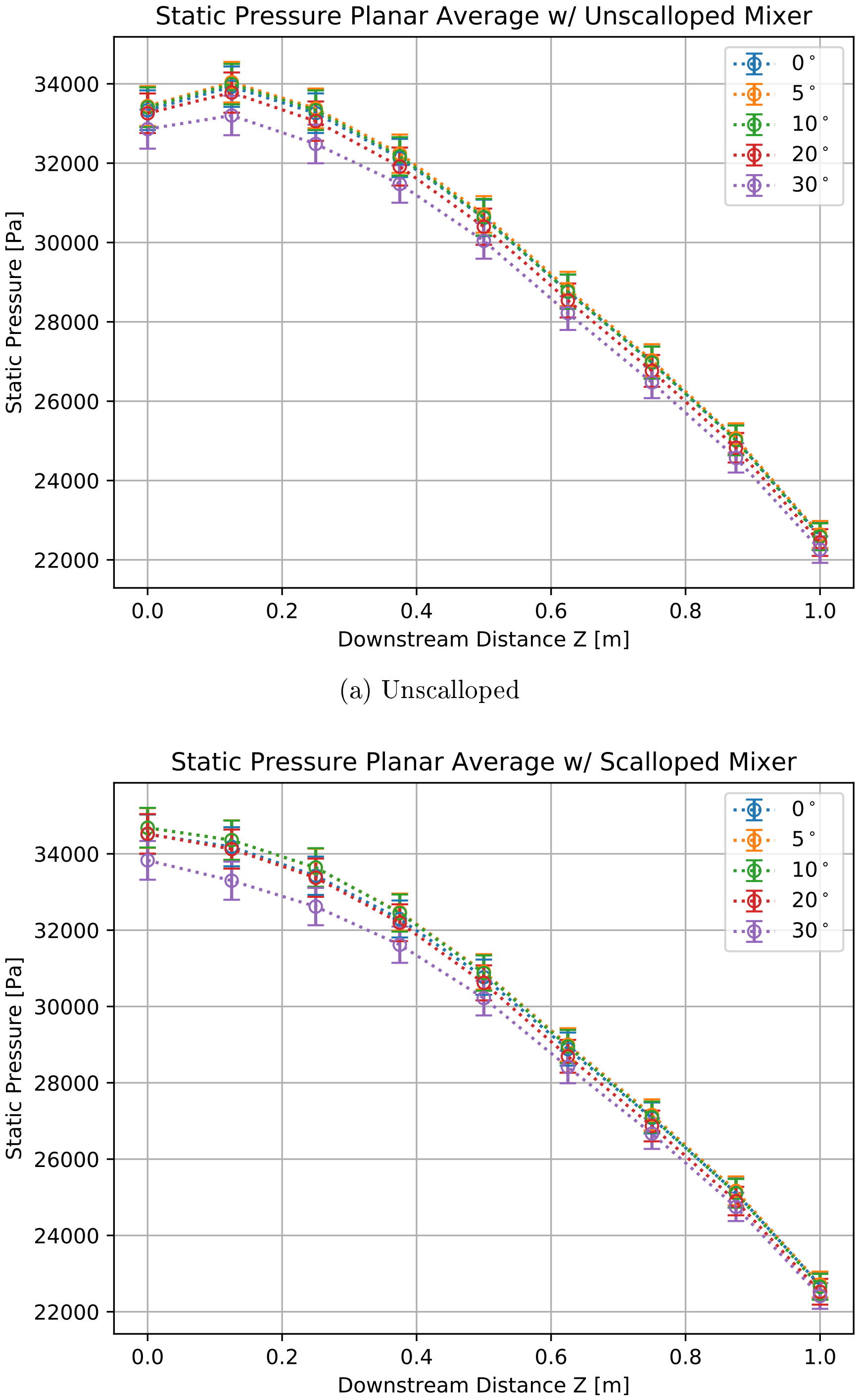

(a) Unscalloped

(b) Scalloped

Figure 7.29: Average static pressure downstream of the mixer with various core flow swirl angles.

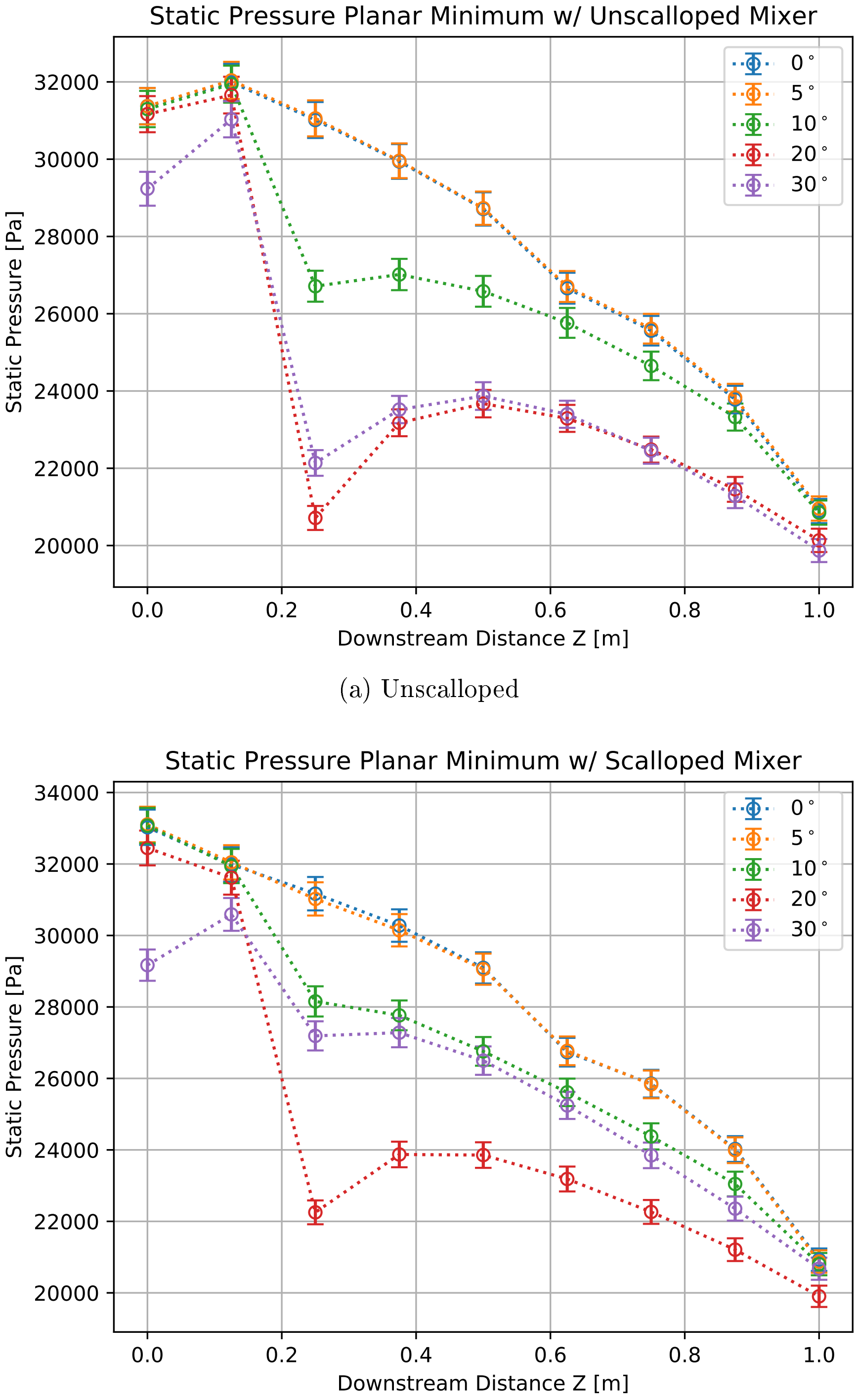

(a) Unscalloped

(b) Scalloped

Figure 7.30: Static pressure minimum downstream of the mixer with various core flow swirl angles.

Table 7.2: Pressure loss, Y and thrust coefficient C_T for various core flow inlet swirl conditions.

(a) Unscalloped lobed mixer

Inlet Swirl	Y	C_T
0°	63.3	62.8
5°	62.1	62.8
10°	61.9	62.9
20°	64.2	62.8
30°	69.7	62.8

(b) Scalloped lobed mixer

Inlet Swirl	Y	C_T
0°	57.5	63.0
5°	57.6	63.0
10°	59.5	63.0
20°	61.8	63.0
30°	67.9	63.0

development and interaction. This information gave context to understand why the performance parameters were affected in the ways they were. For instance, the 20° and 30° core flow swirl cases yielded higher losses than what was observed for lower core flow swirl cases. The flow field data revealed that strong separations ocurred on the 'suction-side' of the lobed mixers and that large amounts of turbulence were generated in the wake of the centrebody in these cases. Core swirl angles less than 10°, however, showed little effect on the performance of the exhaust systems studied. Therefore, it has been concluded that the lobed mixers, both scalloped and unscalloped, can be considered insensitive to core flow swirl angles less than and including 10°, but should not be subject to higher swirl due to potential losses.

A change in the lobed mixer design could improve the high core flow swirl performance. One such option is the integration of the mixing with the deswirling TEC strut.

Chapter 8

Exhaust System Component Integration

The previous chapters have built the foundation for this chapter. Chapter 5 confirmed the simulations used to model the MBTF exhaust system should match the correct flow regime. Chapter 6 confirmed the best mixer design has a moderately scalloped geometry. Chapter 7 confirmed that while a large amount of swirl is detrimental to exhaust system performance, a moderate amount of swirl—less than 10°—can augment system performance. This chapter presents an investigation on the TEC strut and its axial placement relative to the lobed mixer. This MBTF exhaust system is shown to be tolerant of an integrated TEC strut-lobed mixer combination.

8.1 Introduction

The TEC strut has been included in the typical MBTF exhaust system to provide structural support to the aft-duct hardware and also to perform work on the swirling flow coming from the LPT. The TEC strut acts like a diffuser vane, decelerating the flow and turning it from swirling to axial. The TEC strut must have a large chord length in order to achieve this feat without flow separation and incurring even harsher penalties. The general design theories have required this strut to be placed a full chord length upstream of the lobed mixer inlet plane in most production engines to this day. These design requirements have resulted in engines where the aft-end ducting is approximately as long as the power-generating turbomachinery upstream of the exhaust system.

This chapter presents data that challenges the typical design by testing various aft-end ducting designs wherein a similarly profiled TEC strut is moved axially toward—and eventually integrated with—the lobed mixer. This chapter presents a brief analysis of the structures within the flow fields and analysis of the overall performance parameters recorded in each case. The efficacy of the integration strategy is proven by overall performance parameters that are improved or showing negligible alteration as a result of the integration of the TEC strut with the mixer. Data was acquired from four cases, each using the same TEC strut profile placed at varying axial locations ranging from the traditional one chord-length upstream to fully integrated. The geometries involved in each of these cases will be presented in the following section.

8.2 Methodology

This chapter presents the data that solves the problem posed in the Introduction. Medium Bypass Turbofan Engine exhaust systems are large and heavy in comparison to the rest of the engine components. New designs can improve engine performance through reducing their length and therefore mass. The previous three chapters have outlined best practices for simulating the performance of such exhaust systems, identified the best mixer geometry for mixing performance and confirmed that core swirl must be turned axial before it enters the common nozzle.

This investigation compares the flow fields and performance of exhaust systems that feature TEC struts installed in four different axial locations. These test cases are compared to a baseline case with no inlet swirl and a control case with 30° swirl but no TEC struts. The data has been analyzed to determine if any performance differences occur based on TEC strut placement.

8.2.1 Boundary Conditions

Chapter 5 concluded that accurate simulations of MBTF exhaust systems are conducted using compressible boundary conditions. Those boundary conditions are tabulated in Table 8.1. These conditions were chosen because they represent a general cruise condition for the MBTF model.

8.2.2 Test Geometries

There are four new geometries introduced in this chapter. In all instances, the trailing edge of the TEC strut is aligned with the valley of the mixer.

- The first is the traditional design for core flow swirl removal. It consists of a large TEC strut between the final stage LPT and the inlet of the lobed mixer.

Table 8.1: High-speed compressible boundary conditions based on comparable commercial engine cruise conditions.

Boundary	Type	Value
Core	Total Pressure	43.0 kPa
	Total Temperature	728 K
	k	$5\,\mathrm{m}^2\,\mathrm{s}^{-2}$
	ϵ	$30\,000\,\mathrm{m}^2\,\mathrm{s}^{-3}$
Bypass	Total Pressure	45.1 kPa
	Total Temperature	273 K
	k	$5\,\mathrm{m}^2\,\mathrm{s}^{-2}$
	ϵ	$30\,000\,\mathrm{m}^2\,\mathrm{s}^{-3}$
Free Stream	Total Pressure	18.9 kPa
	Total Temperature	223 K
	k	$5\,\mathrm{m}^2\,\mathrm{s}^{-2}$
	ϵ	$30\,000\,\mathrm{m}^2\,\mathrm{s}^{-3}$
Outlet	Average Static Pressure	18.8 kPa

Generally, the strut is one turbine vane chord length downstream of the LPT stage and one TEC strut chord length upstream of the lobed mixer. This represents a large proportion of the overall engine length that exists purely for the purpose of allowing wakes to mix out of the flow before entering the next piece of flow control hardware. There are 12 of these to match the number of lobes. Shown in Figure 8.1a.

- The second is the mid strut which is identical to the traditional design but has been moved a certain distance downstream such that the trailing edge is now in plane with the mixer inlet. This is the first step in an incremental movement of the strut from its traditional location to being fully integrated with the mixer. Shown in Figure 8.1b.

- The third is the partially integrated design. This is similar in design to the traditional strut but is moved downstream such an amount that the strut is now partially integrated with the mixer. The leading edge of the mixer is upstream of the mixer inlet and the trailing edge is within the lobed mixer. Shown in Figure 8.1c.

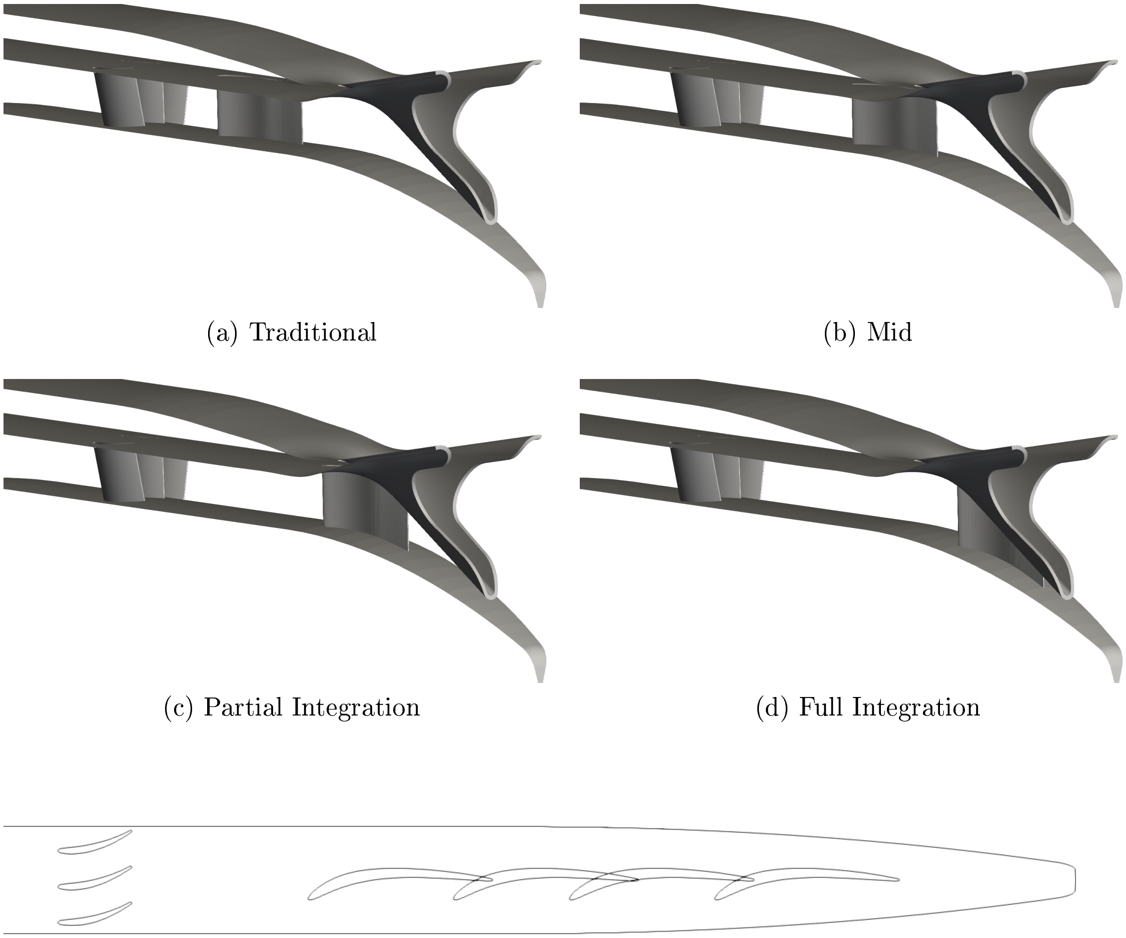

(a) Traditional

(b) Mid

(c) Partial Integration

(d) Full Integration

(e) TEC Strut Locations as Outlined on the Centrebody surface.

Figure 8.1: TEC struts in varying axial locations.

- The last is the fully integrated design wherein the same airfoil from the traditional design is relocated axially downstream and integrated with the lobed mixer valley. Shown in Figure 8.1d. This design shows that aerodynamic performance should not be hindered in any way and that, as a result, the length of the exhaust ducting can be reduced accordingly. This will save weight and fuel.

The relative axial locations of each new case are shown in Figure 8.1e.

The next sections present the analysis of the TEC strut performance as a swirl removal device in conjunction with the scalloped lobed mixer and the resulting effects on flow mixing and exhaust system performance.

8.3 Effects of Swirl Removal

The Control and Test simulations are compared with the Baseline simulation in this section. The primary overall performance parameters of thrust coefficient and total pressure loss are presented, followed by a detailed analysis of the various flow fields to provide further evidence for the efficacy of integrating the TEC struts and scalloped lobed mixer.

8.3.1 Overall Performance

The best quantification of a jet engine exhaust system's performance is the pressure loss through the exhaust system and the thrust generated at the nozzle exit. The total pressure loss was calculated as the change in average total pressure from the reference plane to the nozzle exit plane divided by the average reference plane dynamic pressure. The thrust was calculated as the sum of fluid momentum flux and static pressure over the nozzle area, as outlined in Equation 4.11. The thrust ratio, C_{TR}, was produced by dividing the thrust calculated in the test cases by the thrust calculated in the Baseline case. Lower values are desired for the total pressure loss coefficient and higher values are desired for the thrust coefficient. Table 8.2 summarizes these values for the TEC strut integration cases along with their percent differences from the traditional case. The change was compared to the traditional non-integrated case because that is the status quo for engine design and the goal of this chapter is to make comparisons. The baseline case was included to act as an idealized situation, not a realistic one.

The results of each simulation were very close to each other. The change to the thrust coefficient values in particular were in no case significant enough to be confidently considered changed at all. The pressure loss coefficient differences were large enough to be considered changed and show that engine designers were wise to place the TEC strut in its traditional location rather than any closer to the mixer. However, when the TEC strut was fully integrated, the total pressure loss coefficient returned to a value comparable to the traditional case. This is a positive outcome which suggests future engine designs could and should consider a lobed mixer that has integrated TEC struts for flow turning.

Table 8.2: Pressure loss, Y and thrust coefficient C_T for TEC strut integration cases.

Case	Y	$\|\Delta\%\|$	C_{TR}	$\|\Delta\%\|$
Traditional Non-integrated	62.4	–	98.76	–
Near Non-integrated	66.0	5.7	98.66	0.10
Partial Integration	67.9	8.8	98.60	0.16
Full Integration	62.8	0.64	98.75	0.010

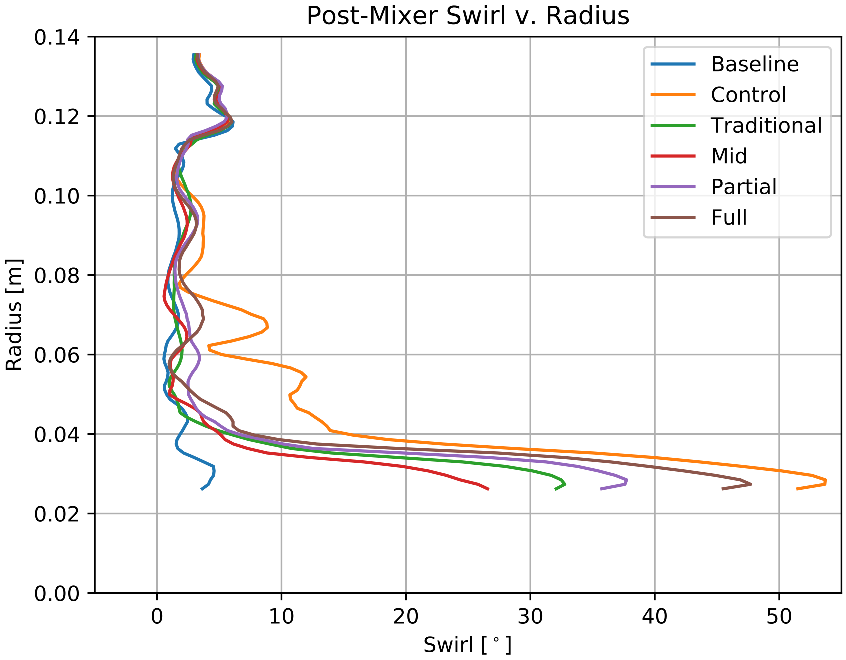

Figure 8.2: Mixer outlet swirl with various TEC strut integrations.

The following section will explain why the performance results were so similar through analysis of the flow fields in each case.

8.3.2 Flow Fields

The analysis presented in previous chapters concluded that it's possible to improve core and bypass flow mixing with thoughtful scalloping of the lobed mixer. It also concluded that while core flow swirl up to angles as high as 10° may improve mixing and flow uniformity, the resulting residual swirl at swirl rates any higher can cause relatively high total pressure losses through the mixing duct. Therefore, it is best to remove core flow swirl prior to the flow exiting the mixer. This section will focus on the flow field difference observed between the Baseline, Traditional Non-integrated and Fully Integrated simulations and the potential causes of those differences.

Figure 8.2 presents the pitchwise average radial swirl distribution at plane $Z = 0.125$. It reveals that there is only a weak relationship between the amount of residual swirl downstream of the mixer and where the TEC struts has been placed axially in relation to the mixer. The main difference is seen near the centrebody, below $r < 0.04$. The residual swirl in the wake of the struts themselves had various residence times in the duct before interacting with the reducing radius at the tail end of the centrebody. That led to the tangential component of velocity accelerating more the closer it occurred to the end of the centrebody. Otherwise, above $r > 0.04$, the swirl is kept in the beneficial zone, $< 10°$.

Figures 8.3 through 8.9 present contour plots of streamwise vorticity coefficient, total pressure coefficient and azimuthal vorticity coefficient from left to right at notable axial planes downstream of the lobed mixer, and one plane upstream. The total pressure coefficient plots in particular show somewhat different results between the Traditional Non-integrated strut-lobed mixer combination and the Fully Integrated strut-lobed mixer combination. Immediately downstream of the lobed mixer at $Z = 0.000$, there appears to be lower total pressure in the region of the core flow, downstream of the Fully Integrated components. However, plane $Z = -0.500$ was included in this section in order to indicate that the low pressure zone was a result of the TEC strut and, in fact, a similar low pressure zone existed downstream of the traditional TEC strut as well. The low pressure zone for the traditional case was mixed out prior to the flow reaching the lobed mixer exit. This goes to show the same overall outcome was possible despite differing flow structures.

The streamwise vorticity coefficient contour plot also reveals an interesting difference between the two simulations. Figure 8.5 shows a large region of clockwise vorticity within the core flow, near the centrebody at the mixer exit plane in the fully integrated case that does not appear in the traditional case. However, referring back to Figure 8.3, reveals a region of clockwise vorticity in the traditional case in the flow downstream of the TEC strut, confirming this clockwise vorticity was a passage vortex generated between TEC struts. That vortex persisted throughout the mixing duct until dissipating somewhere between the $Z = 0.750$ and $Z = 1.000$ plane.

As for the azimuthal vorticity coefficient, very little changed between the cases other than some small changes to the deflection and distortion near the centre of the jet arising from the different streamwise vorticity configurations.

Figure 8.11 shows the static pressure loading on the inner surface of the lobed mixer. These plots indicate that the TEC strut, no matter its axial location, does a good job in redirecting the saddle point that occurs along the valley in the baseline conditions, back to that location and alleviating any potential separation that the core flow swirl would haver otherwise caused at 30°.

The turbulent kinetic energy plots in Figure 8.12 indicate the regions of intense turbulence that formed downstream of the TEC strut.

Finally, three-dimensional velocity streamlines colour by total temperature are presented in Figure 8.13.

8.4 Conclusions

This chapter presented data calculated for four cases of MBTF exhaust systems that featured 30° core flow swirl, TEC struts designed—but not optimized—to return the flow to near 0° core flow swirl and the scalloped lobed mixer in question throughout this thesis. The TEC strut was systematically relocated from the traditional location one chord length upstream of the mixer to a location $0.65D_h$ further downstream where the TEC strut was then integrated with the scalloped lobed mixer. That is to say, the TEC strut and lobed mixer occupied overlapping axial ranges in the exhaust system ducting and the trailing edge of the TEC strut was aligned with the valley of the lobed mixer.

The overall performance parameters calculated in these cases were compared and the differences between traditional non-integrated and fully integrated strut-lobed mixer combinations of 0.64% and 0.01% between the total pressure loss and thrust coefficients, respectively, were found to be within the simulation margin of error of 0.82% for pressure loss calculations and 0.04% for thrust calculations. This was confirmed through analysis of the flow fields which indicated differences in flow structure creation, but ultimately similar flow fields at the end of the nozzle.

Thus, it is concluded that integrating TEC struts with the lobed mixer as used in a MBTF exhaust system is not detrimental to performance. There are potential

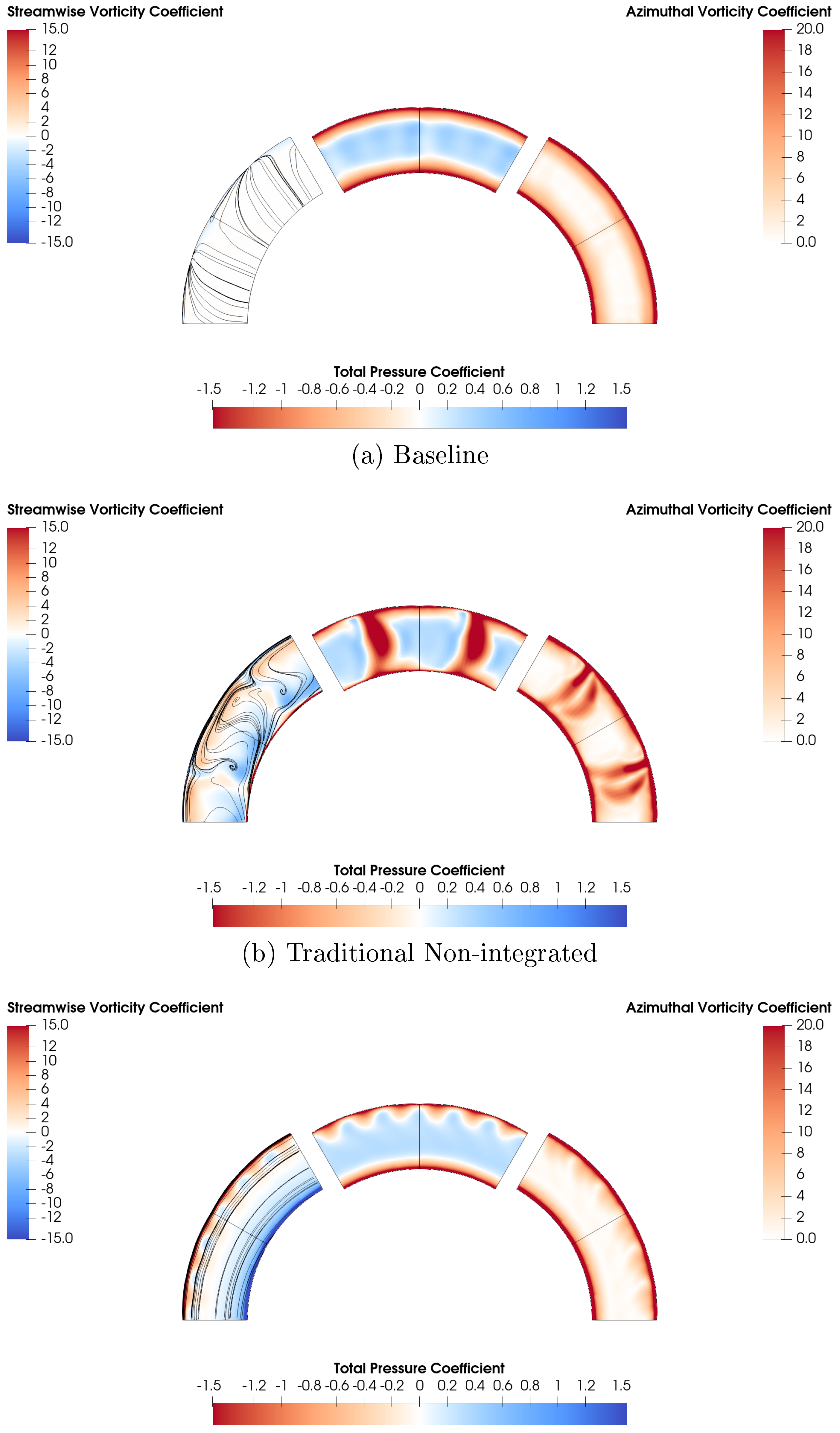

(a) Baseline

(b) Traditional Non-integrated

(c) Fully Integrated

Figure 8.3: Contour plots of streamwise vorticity coefficient, total pressure coefficient and azimuthal vorticity coefficient at $Z = -0.550$ in baseline, non-integrated and integrated exhaust systems.

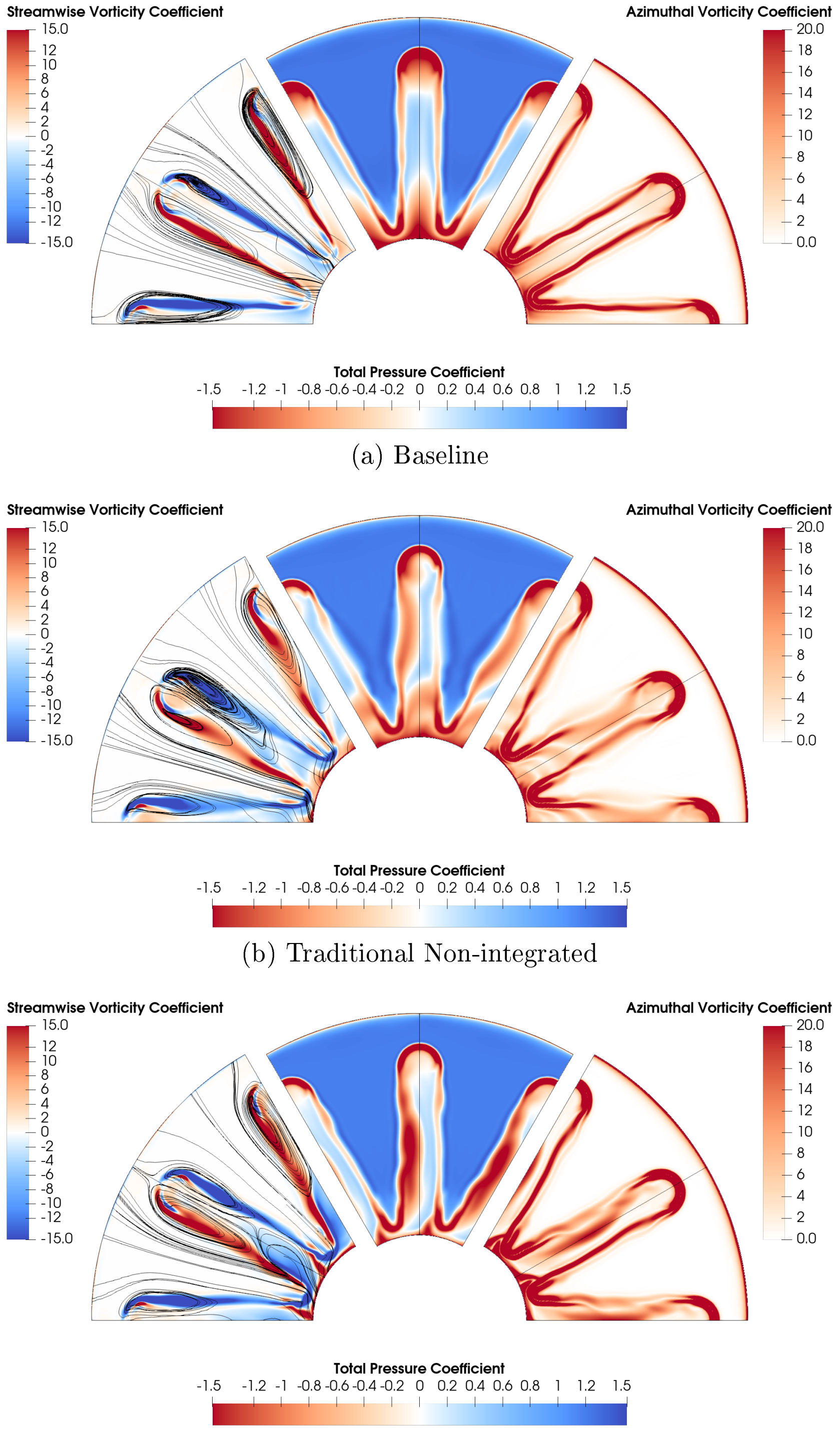

(a) Baseline

(b) Traditional Non-integrated

(c) Fully Integrated

Figure 8.4: Contour plots of streamwise vorticity coefficient, total pressure coefficient and azimuthal vorticity coefficient at $Z = 0.000$ in baseline, non-integrated and integrated exhaust systems.

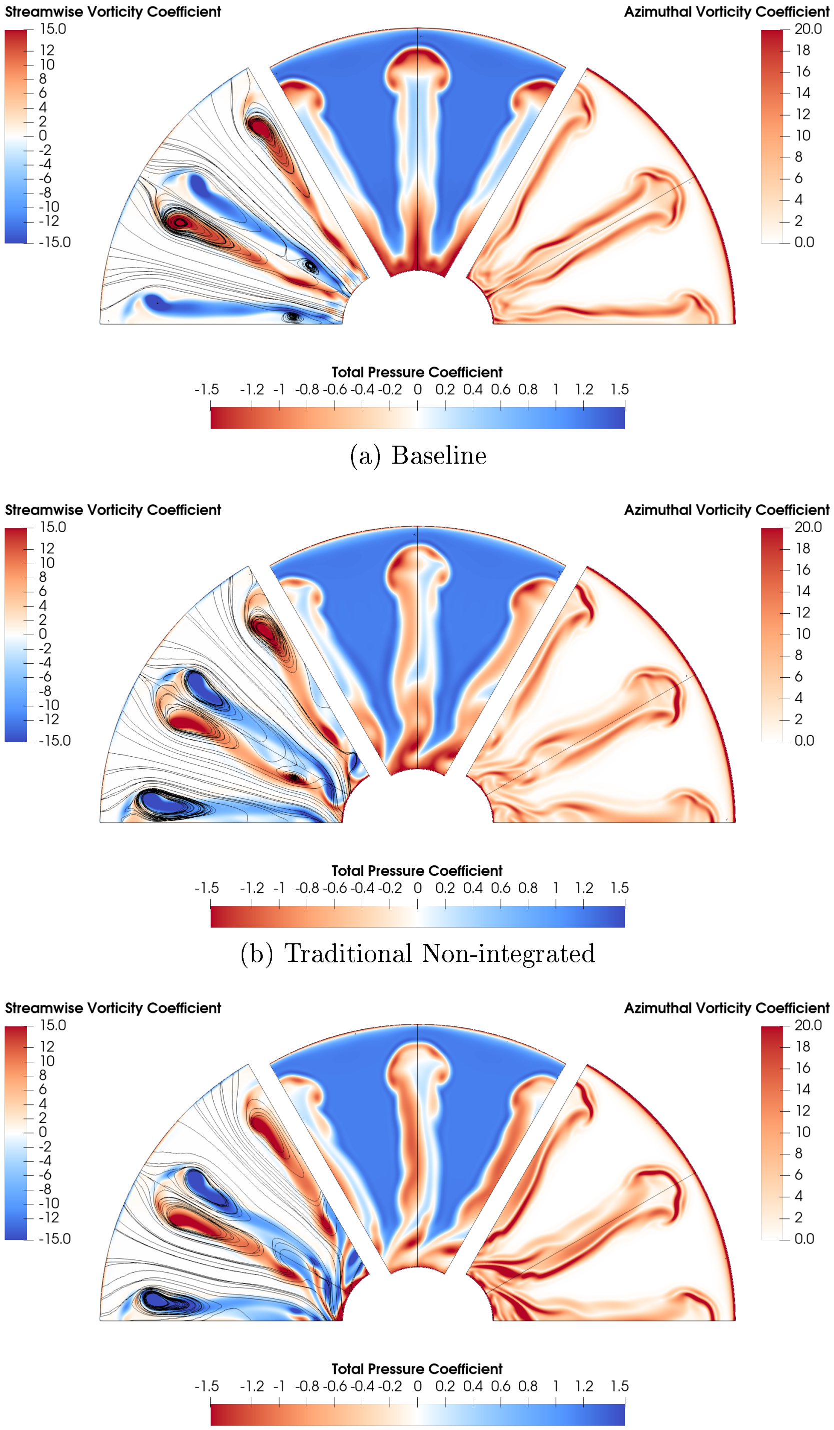

(a) Baseline

(b) Traditional Non-integrated

(c) Fully Integrated

Figure 8.5: Contour plots of streamwise vorticity coefficient, total pressure coefficient and azimuthal vorticity coefficient at $Z = 0.125$ in baseline, non-integrated and integrated exhaust systems.

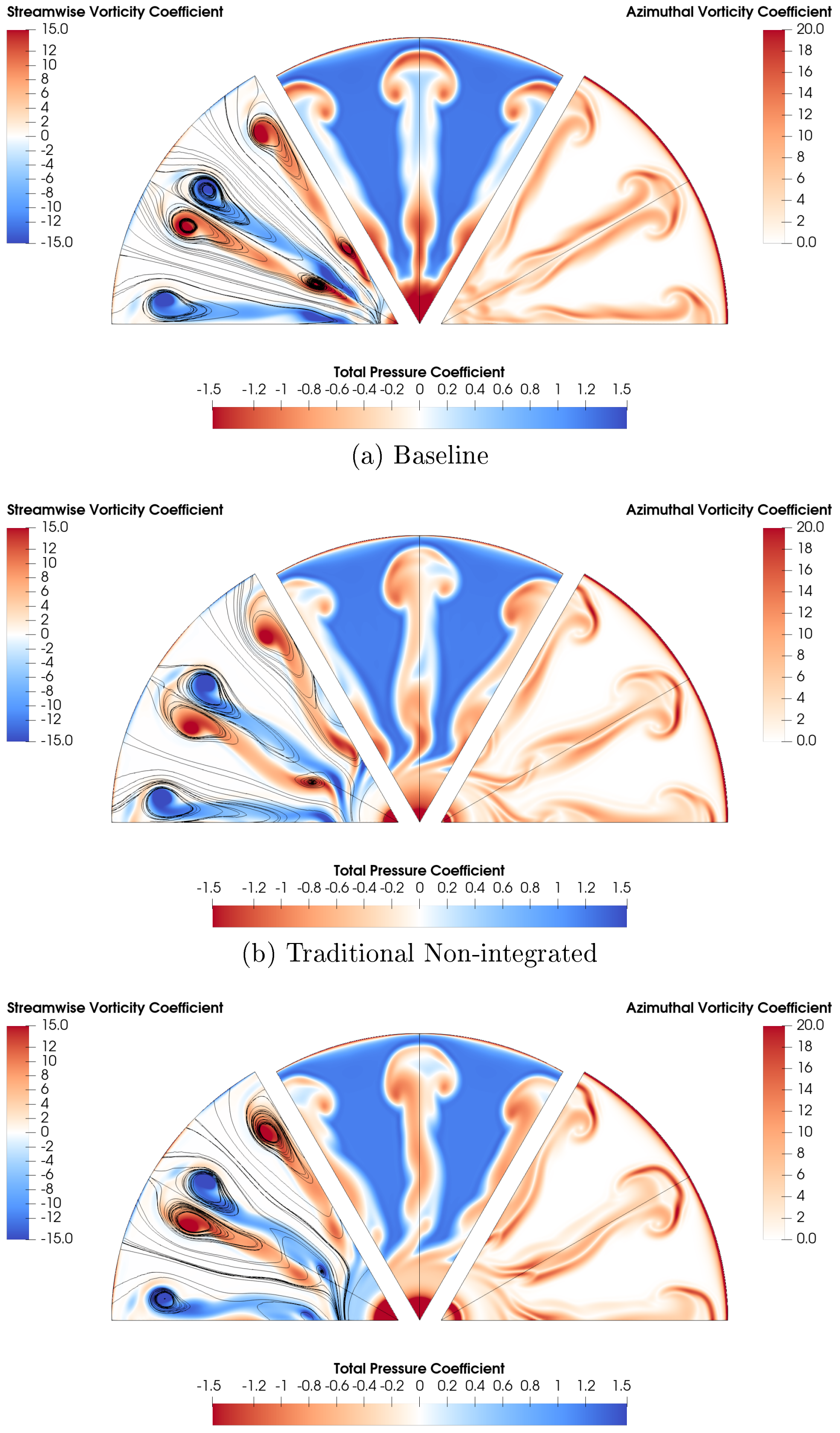

(a) Baseline

(b) Traditional Non-integrated

(c) Fully Integrated

Figure 8.6: Contour plots of streamwise vorticity coefficient, total pressure coefficient and azimuthal vorticity coefficient at $Z = 0.250$ in baseline, non-integrated and integrated exhaust systems.

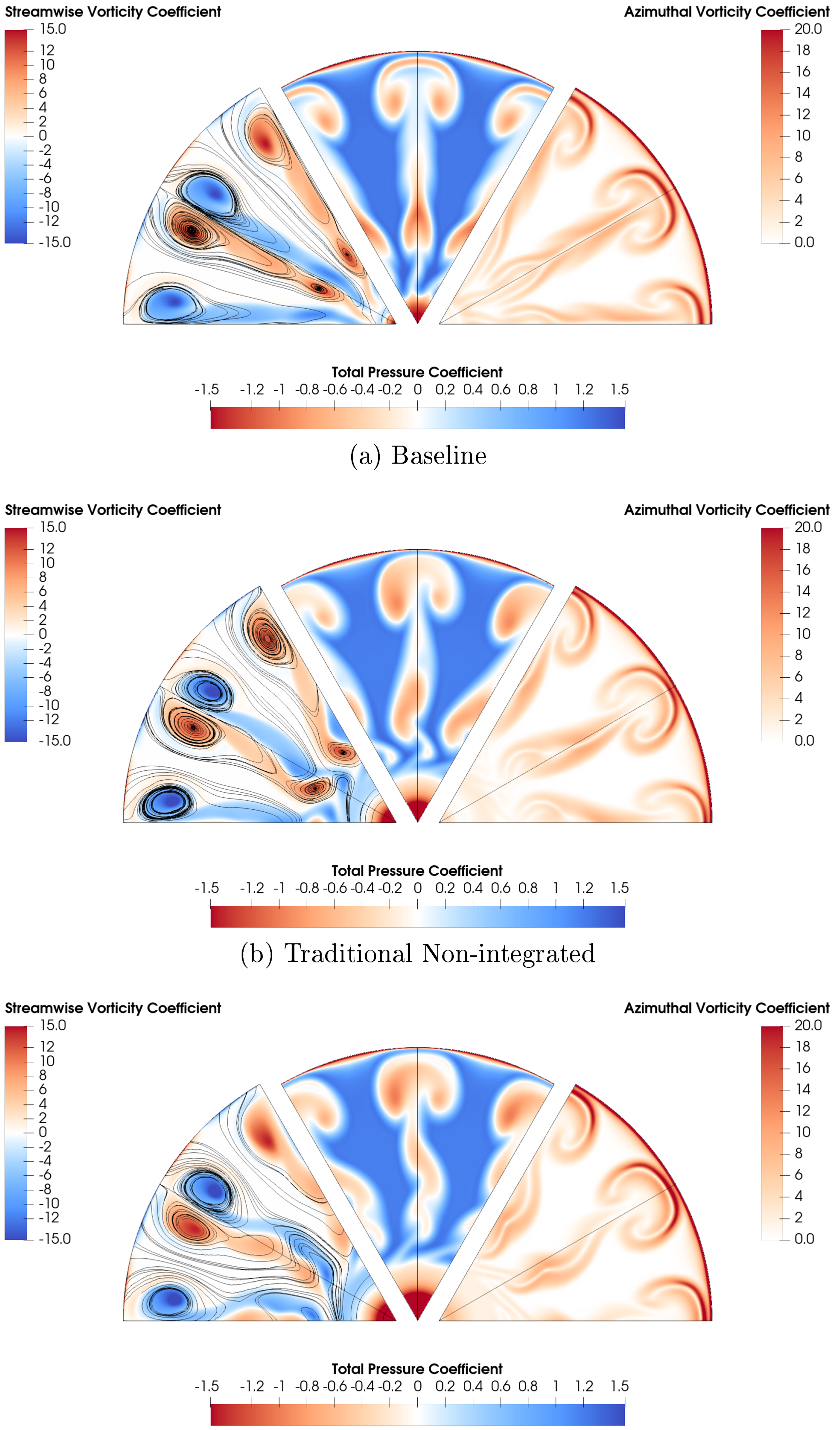

(a) Baseline

(b) Traditional Non-integrated

(c) Fully Integrated

Figure 8.7: Contour plots of streamwise vorticity coefficient, total pressure coefficient and azimuthal vorticity coefficient at $Z = 0.500$ in baseline, non-integrated and integrated exhaust systems.

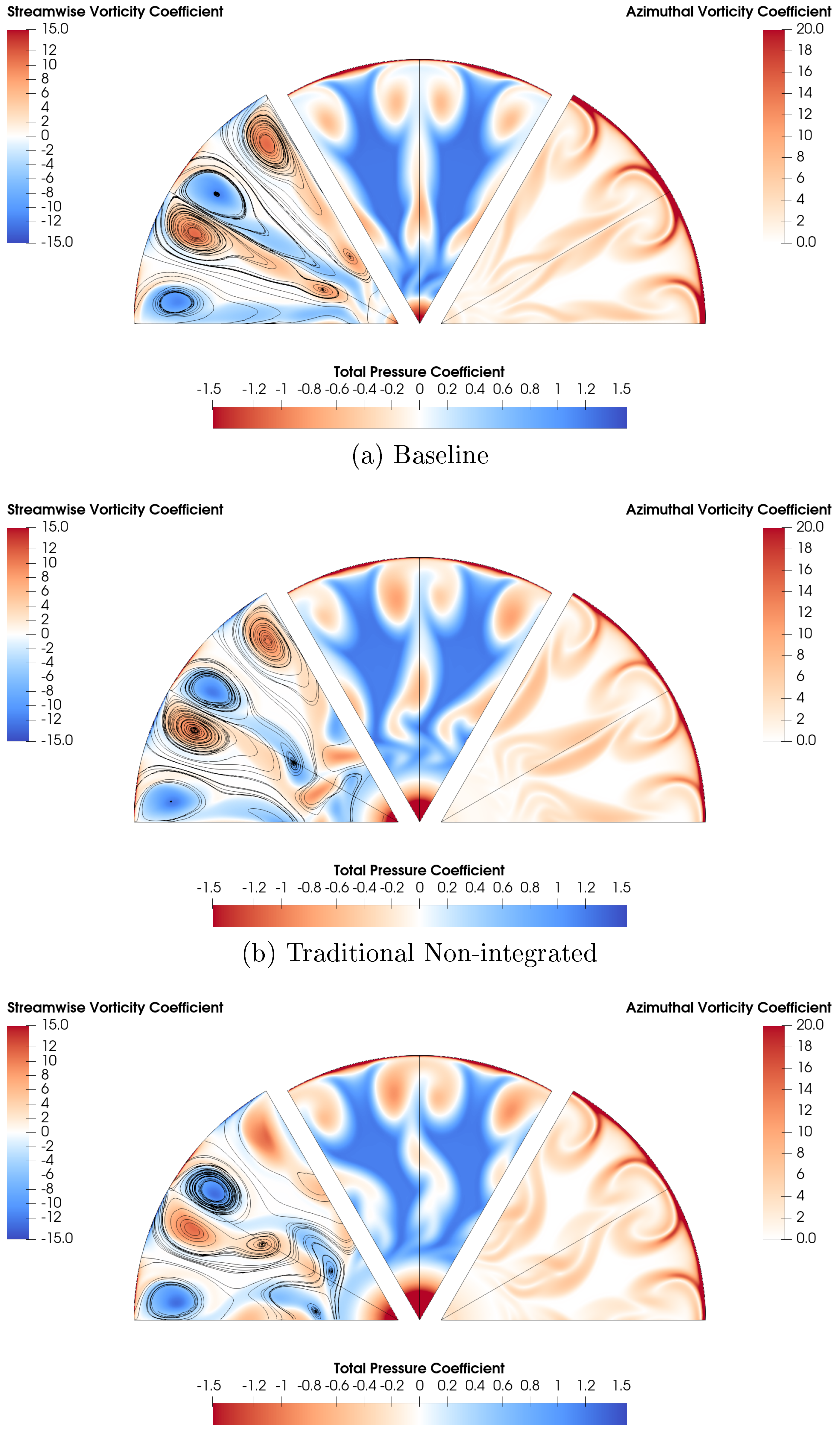

(a) Baseline

(b) Traditional Non-integrated

(c) Fully Integrated

Figure 8.8: Contour plots of streamwise vorticity coefficient, total pressure coefficient and azimuthal vorticity coefficient at $Z = 0.750$ in baseline, non-integrated and integrated exhaust systems.

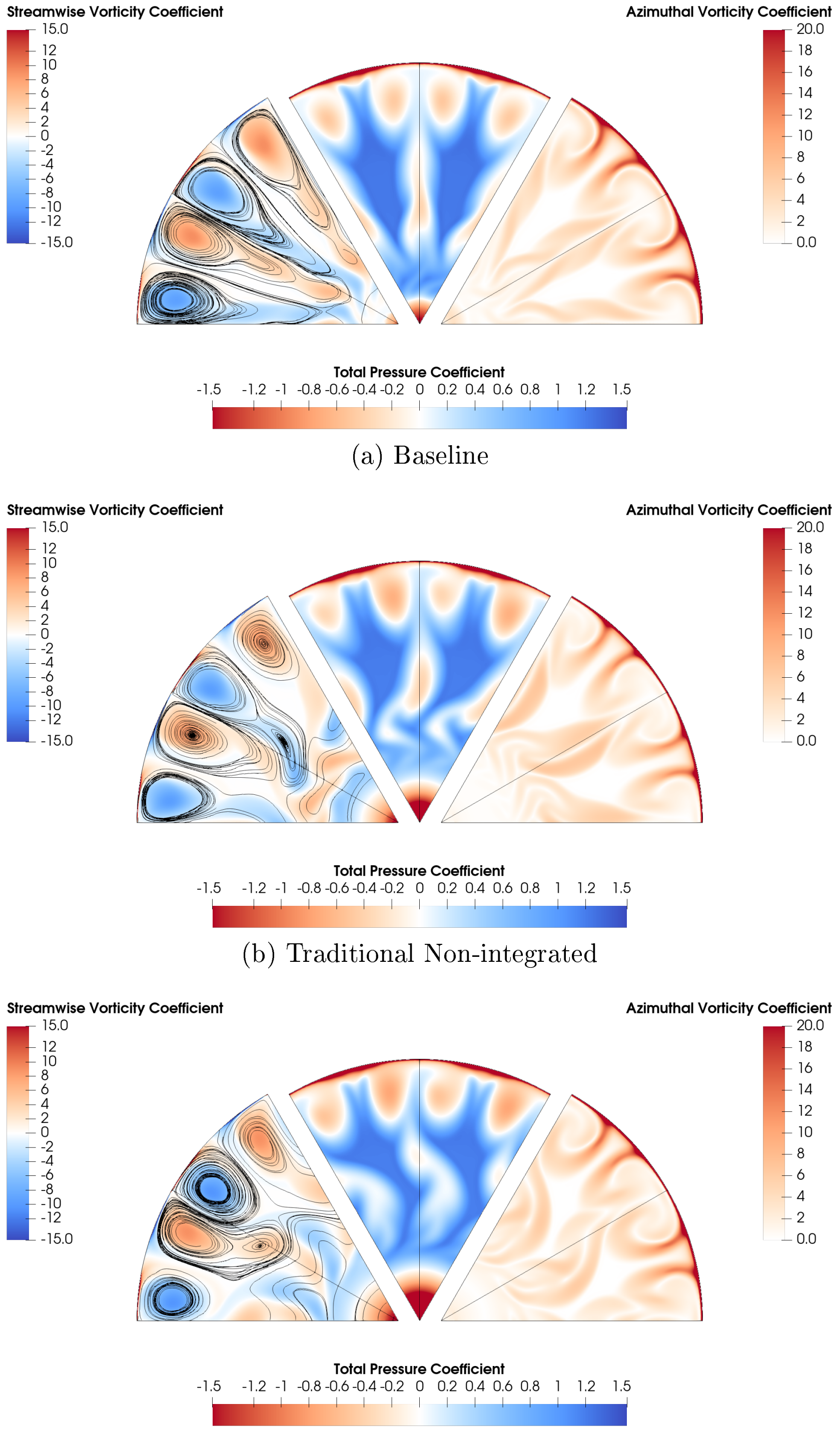

(a) Baseline

(b) Traditional Non-integrated

(c) Fully Integrated

Figure 8.9: Contour plots of streamwise vorticity coefficient, total pressure coefficient and azimuthal vorticity coefficient at $Z = 1.000$ in baseline, non-integrated and integrated exhaust systems.

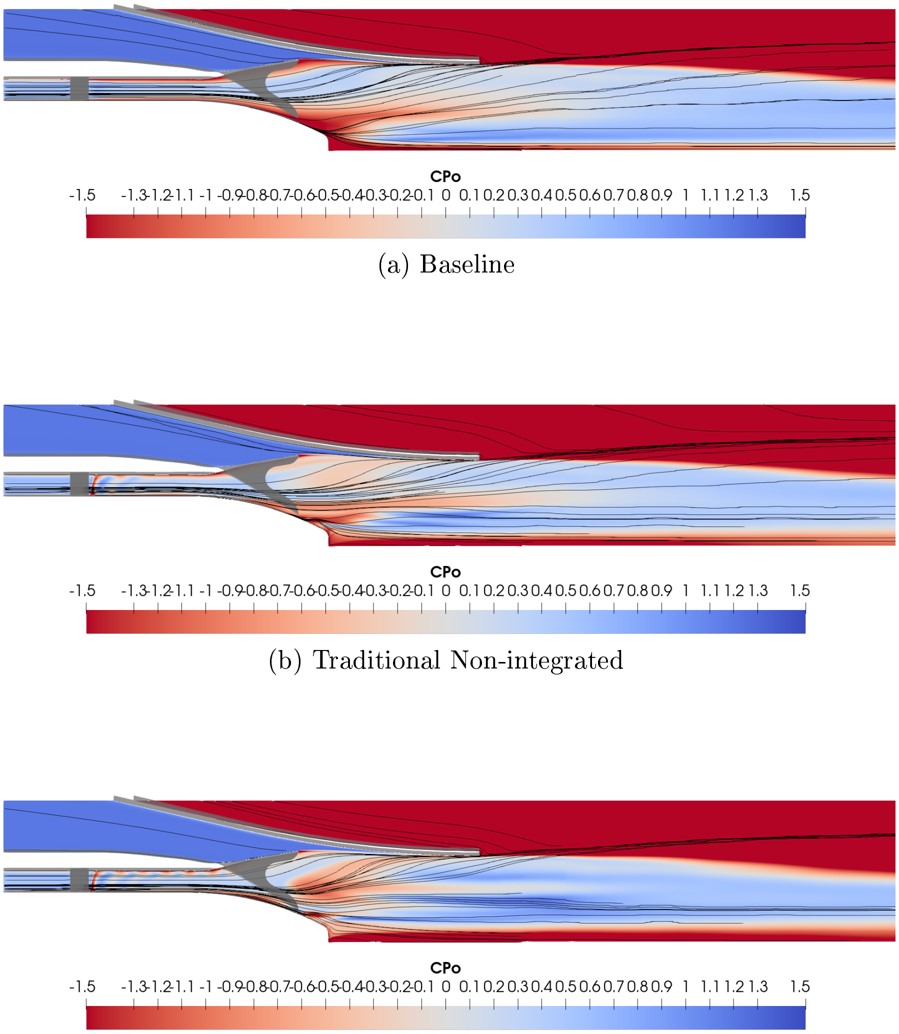

(a) Baseline

(b) Traditional Non-integrated

(c) Fully Integrated

Figure 8.10: Contour plots of streamwise vorticity coefficient, total pressure coefficient and azimuthal vorticity coefficient along the Meridional Crest plane in baseline, non-integrated and integrated exhaust systems.

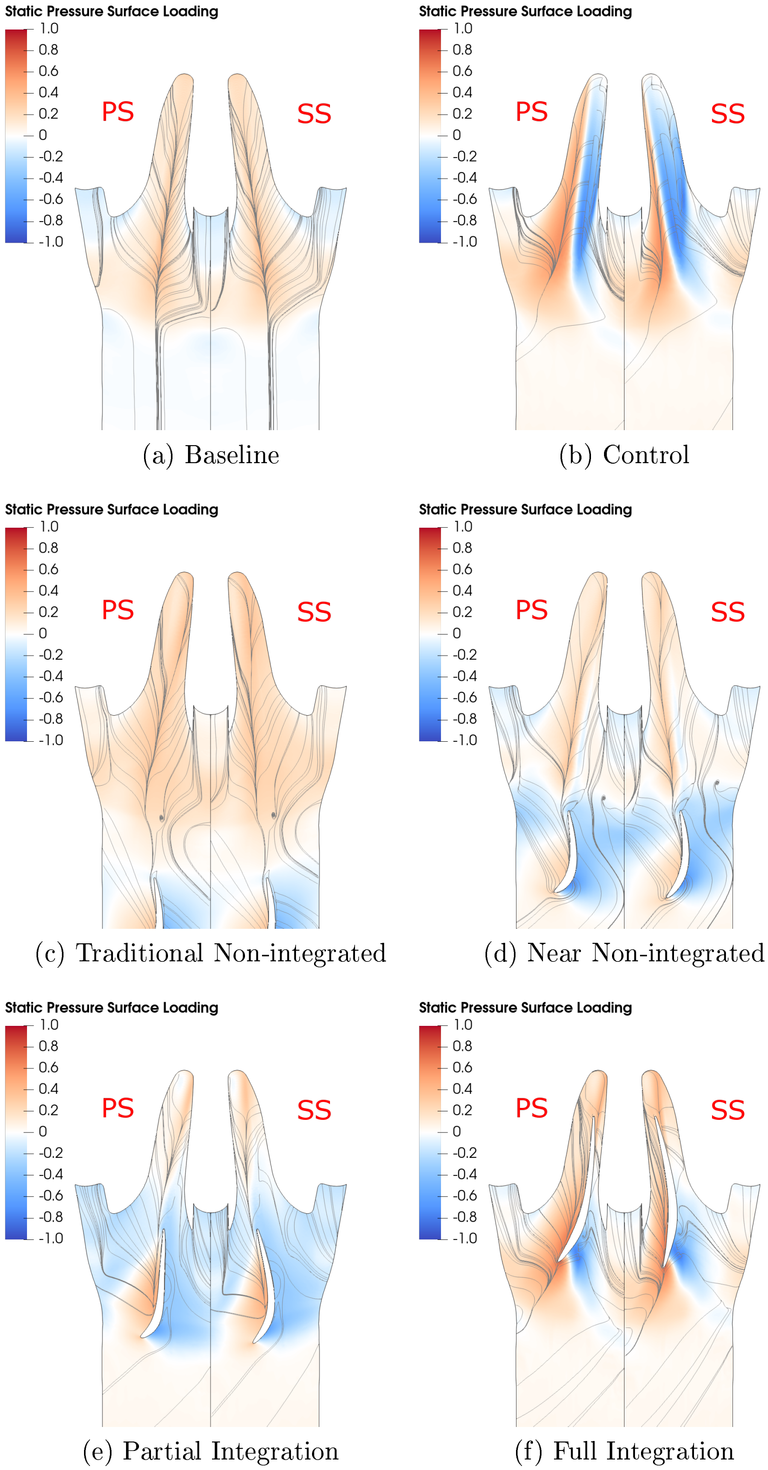

(a) Baseline

(b) Control

(c) Traditional Non-integrated

(d) Near Non-integrated

(e) Partial Integration

(f) Full Integration

Figure 8.11: Surface static pressure loading and limiting streamlines on the core surface of scalloped lobed mixer with various core flow swirl.

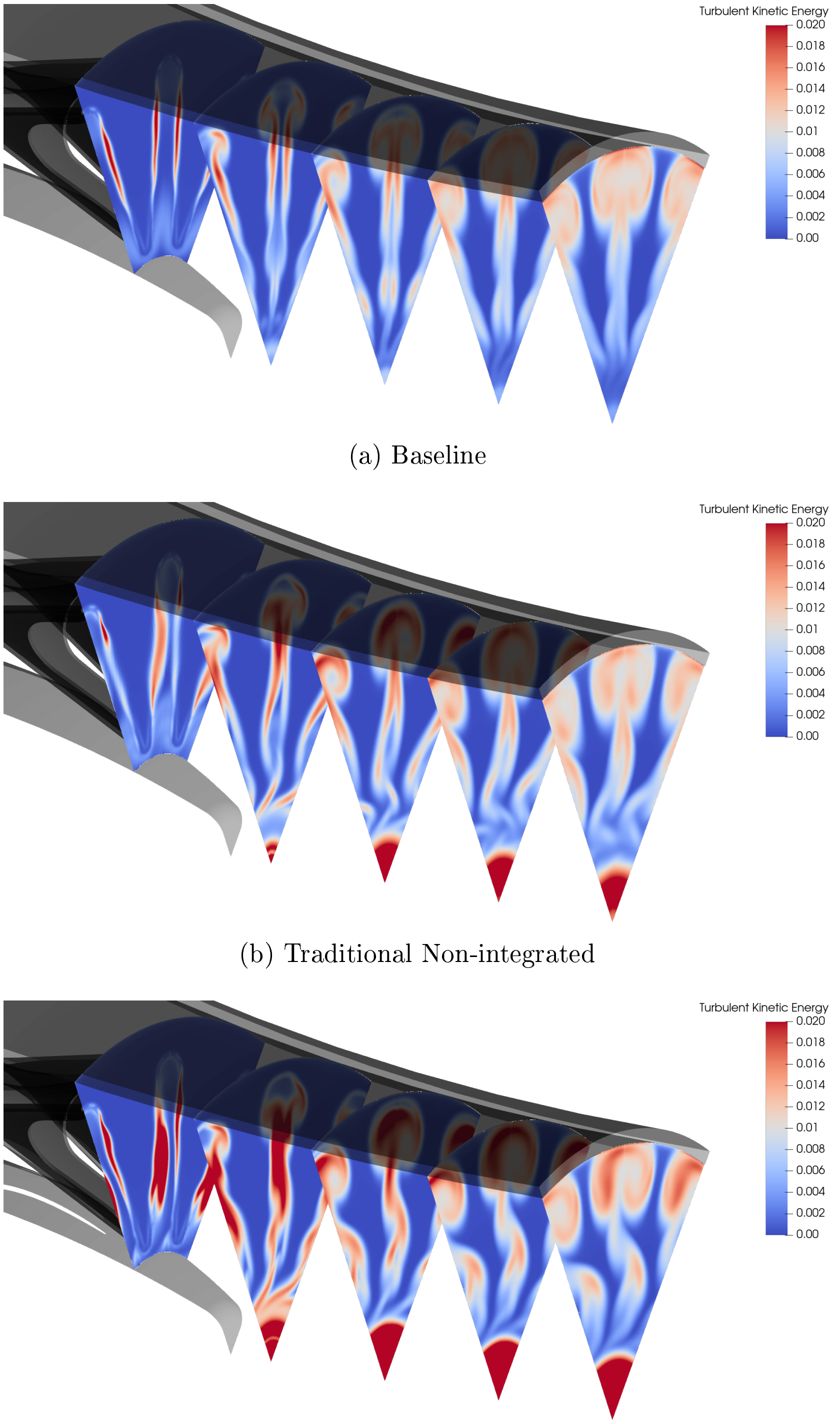

(a) Baseline

(b) Traditional Non-integrated

(c) Fully Integrated

Figure 8.12: Turbulent kinetic energy axial contour plots, downstream of lobed mixers in baseline, non-integrated and integrated exhaust systems.

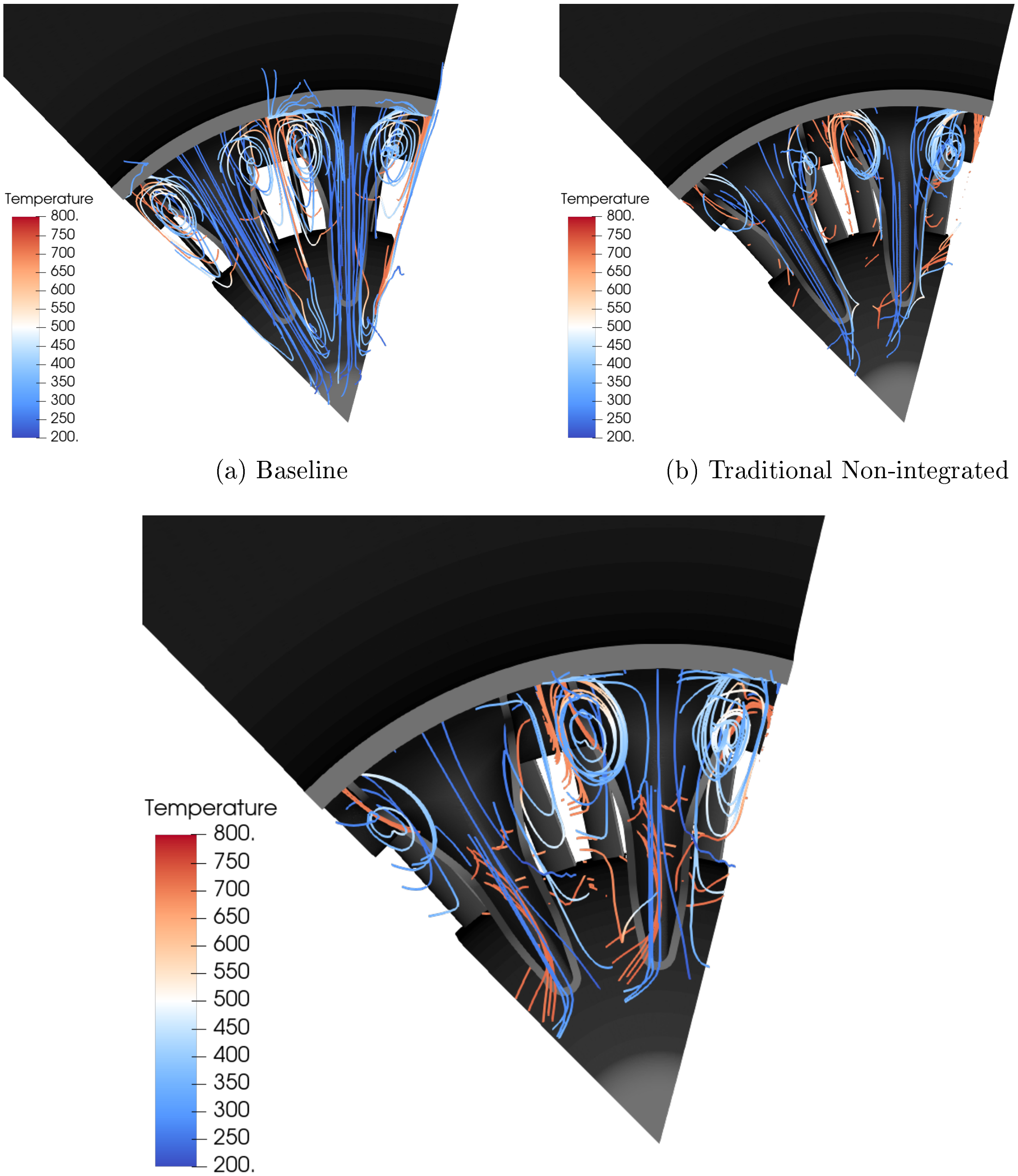

(a) Baseline

(b) Traditional Non-integrated

(c) Fully Integrated

Figure 8.13: Velocity streamlines, coloured by total temperature, downstream of lobed mixers in baseline, non-integrated and integrated exhaust systems.

weight savings through reduction of the overall exhaust ducting length by the $0.65D_h$ distance that the TEC strut was moved.

This information has now answered the problem outlined in the introduction of this thesis. However, the question of mass, momentum and thermal mixing rates downstream of lobed mixers remains unanswered. Chapter 9 presents an investigation of a further set of simulations calculated with the Baseline unscalloped lobed mixer in pursuit of answering that question.

Chapter 9

Mixing Processes with Lobed Mixers

The previous discussion chapters presented a tiered foundational investigation of a lobed mixer used in the exhaust system of a medium bypass turbofan engine and improved design thereof. This chapter will conclude that discussion with data that closes the gap in the literature identified in Chapter 2.

9.1 Introduction

The purpose of the investigation presented in this chapter was to confirm whether the claims in the literature—that the momentum of fluids will always be the last to complete mixing—hold true for lobed mixers as it has for confluent mixers [2, 70]. The streamwise vorticity developed in the wake of lobed mixers introduces a strong and effective method for bulk mixing of fluids. The enhanced mixing may result in the rates of thermal, mass and momentum mixing to change order depending on the initial conditions. The results of this investigation have major economic repercussions on the design of future experimental test rigs for the study of lobed and other streamwise vorticity generating mixer types whose applications involve high velocity and high temperature fluid flow.

Streamwise vorticity enhances mixing through the bulk motion of fluid from one stream into the other. That allows for more rapid flow mixing than observed downstream of confluent or flat planar mixers for which the only mixing mechanism is the azimuthal vorticity generated via the Kelvin-Helmholtz instability within the interfacial shear layer. All published literature about the mixing rates of the three conservative variables found in the literature review was based on flow mixing downstream of confluent, or flat planar mixers. Those studies were robust and well developed. They examined the mixing rates of streams of different species [2, 70] at different temperatures and velocities. Analytical investigations were also presented.

This chapter presents an investigation of many compressible and incompressible boundary conditions applied to the unscalloped mixer used throughout this thesis. The next section shall provide further detail on the methodology.

9.2 Methodology

A major part of this thesis was examining trends in fluid mixing in the exhaust system of medium bypass turbofan engines and developing a framework for future work in the field that is accessible, economical and efficient. The mixing duct of such a system is analogous to constrained concentric jets. This investigation sought to discover the trends in various types of flow mixing with jets of various flow characteristics. Simulations were performed with various boundary conditions of inlet temperature and velocity in order to observe the trends of thermal and momentum mixing.

The question to be answered through this investigation is whether momentum mixing is completed last amongst all other characteristic mixing, whether it is always completed last and whether compressibility matters.

Momentum and thermal energy mixing should occur at different rates through a fluid interface. The two parameters have different mechanisms of transport through the fluids. Thermal mixing can be achieved via convection, conduction or radiation. Momentum mixing can only be achieved through shear transport at fluid interfaces. Mass, or species, mixing can be achieved through convection or random turbulent motion through the interface. Previous reports indicated with near certainty that mass species mixing always leads momentum mixing. This information is helpful as the arrangement used in this investigation made examination of species mixing difficult.

Data has been collected from four compressible and four incompressible simulations. The boundary conditions are expanded on in the next section. The planar averages and coefficients of variance of total temperature, static pressure, density and momentum flux were of particular interest.

The coefficient of variance is a useful statistical measure in this investigation. It is defined as the ratio of the standard deviation, σ, over the local, planar mean of the value. This described a measure of the overall uniformity of the flow at a particular axial location and was more useful than just standard deviation alone due to the acceleration of the flow through the nozzle. As the flow accelerated through the

Table 9.1: High-speed compressible boundary conditions

Case	Boundary	Type	Value
Baseline (H1)	Core	Total Pressure	43.0 kPa
		Total Temperature	728 K
		k	$5\,\mathrm{m^2\,s^{-2}}$
		ϵ	$30\,000\,\mathrm{m^2\,s^{-3}}$
	Bypass	Total Pressure	45.1 kPa
		Total Temperature	273 K
		k	$5\,\mathrm{m^2\,s^{-2}}$
		ϵ	$30\,000\,\mathrm{m^2\,s^{-3}}$
	Free Stream	Total Pressure	18.9 kPa
		Total Temperature	223 K
		k	$5\,\mathrm{m^2\,s^{-2}}$
		ϵ	$30\,000\,\mathrm{m^2\,s^{-3}}$
	Outlet	Average Static Pressure	18.8 kPa
Inverse Temp (H2)	Core	Total Temperature	273 K
	Bypass	Total Temperature	728 K
Temp Ratio 2 (H3)	Core	Total Temperature	546 K
	Bypass	Total Temperature	273 K
Pressure Ratio 2 (H4)	Core	Total Pressure	35.8 kPa
	Bypass	Total Pressure	37.6 kPa

nozzle, it was possible for measures such as the standard deviation to increase purely because the entire population measurement increased in magnitude. The coefficient of variance allows for a locally normalized measurement that makes comparison of all parameters possible.

9.2.1 Boundary Conditions

Compressible Simulations

Four compressible simulations were performed for this study. Their details are outlined in Table 9.1. For brevity, only the conditions modified from the baseline have been included for the other simulations.

Table 9.2: Incompressible boundary conditions

Case	Boundary	Type	Value
Baseline (L1)	Core	Mass Flow	$1.2\,\mathrm{kg\,s^{-1}}$
		Static Temperature	$293\,\mathrm{K}$
		V_x/V	0
		V_x/V	0
		V_x/V	1
		k	$3.75\,\mathrm{m^2\,s^{-2}}$
		ϵ	$4500\,\mathrm{m^2\,s^{-3}}$
	Bypass	Mass Flow	$1.2\,\mathrm{kg\,s^{-1}}$
		Static Temperature	$293\,\mathrm{K}$
		V_x/V	0
		V_x/V	0
		V_x/V	1
		k	$0.8\,\mathrm{m^2\,s^{-2}}$
		ϵ	$4.5\,\mathrm{m^2\,s^{-3}}$
	Free Stream	Total Pressure	$101.325\,\mathrm{kPa}$
		Total Temperature	$293\,\mathrm{K}$
		k	$5\,\mathrm{m^2\,s^{-2}}$
		ϵ	$30\,000\,\mathrm{m^2\,s^{-3}}$
	Outlet	Average Static Pressure	$101.325\,\mathrm{kPa}$
50 K Delta T (L2)	Core	Static Temperature	$343\,\mathrm{K}$
100 K Delta T (L3)	Core	Static Temperature	$393\,\mathrm{K}$
-100K Delta T (L4)	Bypass	Static Temperature	$393\,\mathrm{K}$

Incompressible Simulations

Four incompressible simulations were performed for this study. Their details are outlined in Table 9.2. For brevity, only the conditions modified from the baseline have been included for the other simulations.

9.2.2 Test Geometries

This investigation used the unscalloped mixer, Figure 9.1, and 0° swirl vanes.

The next session presents discussions about the uniformity of flow parameters downstream of the mixer for the conditions described above. This chapter is slightly

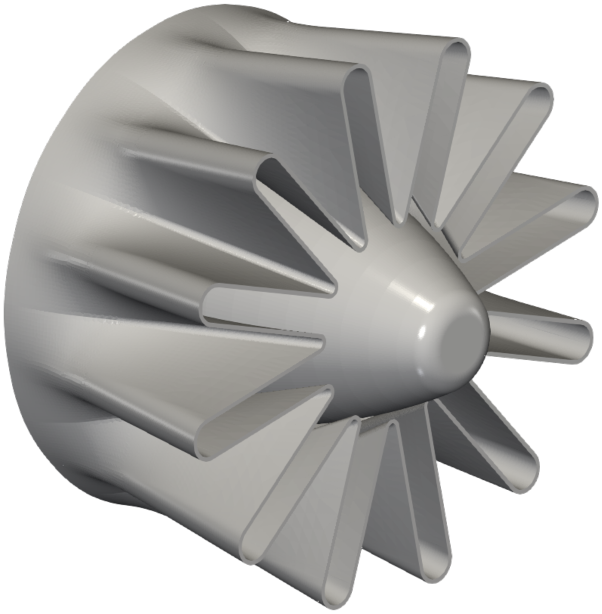

Figure 9.1: The unscalloped lobed mixer.

different in its approach, as each condition is considered first on its own. For example, it does not matter for this study which case produces better mixing, but rather which parameter within individual cases became uniform the fastest.

9.3 Results and Discussion

There are many ways to present the uniformity of fluid characteristic parameters. In this section each case will have data presented on the total temperature, static pressure, density and magnitude of momentum downstream of the mixer. The planar mean of each parameter is presented first to provide the reader with a context of how the overall nature of that parameter changed as the fluids travelled downstream through the nozzle. The mean values have been normalized by the value observed at the lobed mixer exit plane, such that all parameters had a value of 1.0 at $Z = 0.000$. Following that, the coefficient of variation, ‘CoV’, is presented. This value was chosen to represent the uniformity of the flow for several reasons. First, it has a formulation similar to the previously utilized mixing index. Both are based on the standard deviation calculation. Second, it provides a local normalization which accounts for potential bulk growth in a parameter’s magnitude.

The pitchwise radial averages of these parameters are then presented for each case.

These values have not been normalized by the reference plane values because there were no direct comparisons made between cases for these figures. These figures are presented to illustrate the evolution of the pitchwise radial average as the fluid travels downstream. The reader, like the author, can then infer information on the relative uniformity of the parameter from the centre of the jet outward toward the nozzle. The discussion begins with the compressible simulations.

9.3.1 Compressible Simulations

The four compressible simulations presented are:

- Baseline, the standard boundary condition used to model medium bypass turbofan engine exhaust system conditions.

- Inverted Temperature Ratio, the same total pressure conditions were prescribed at the inlet boundaries, however the temperature of the core and bypass fluids were reversed. In this case, the bypass fluid had greater temperature than the core fluid.

- Reduced Temperature Ratio, the same total pressure conditions as the baseline, but the core temperature was reduced from 728 K to 546 K.

- Double Pressure Ratio, where the total pressure prescribed at the inlets were modified to model an engine whose operational pressure ratio was equal to two, rather than 2.5 like the Baseline case.

There were common factors among all of the compressible simulations, observed in Figure 9.2 through Figure 9.5. First, the mean momentum was always observed to grow over the length of the nozzle as expected. There were initial dips in momentum around the $Z = 0.125$ plane. This was due to the step change at the end of the centrebody where the flow rapidly expanded to fill the new gap. The mean temperature was relatively unchanged along the length of the nozzle. This was expected as there were no sources of heat transfer into or out of the domain. Finally, the mean density and static pressure values dropped at similar rates as the flow accelerated toward trans-sonic speed at the nozzle exit plane.

The coefficient of variation revealed trends that disagreed with the expectations laid out in the literature for concentric jet mixing downstream of confluent mixers. The baseline case was analyzed to produce the expected result. Even though Figure 9.2b indicates that the Magnitude of Momentum was more uniform at the nozzle exit plane, the Total Temperature uniformity increased more rapidly. However, Figure 9.3b, shows the magnitude of momentum and total temperature beginning at the lobed mixer exit plane with roughly equivalent values for the coefficient of variation and the magnitude of momentum variation dropped more at the end of the nozzle than the total temperature variation. That suggested the momentum was mixing faster than the temperature. Figure 9.4b also shows the magnitude of momentum variation dropping more rapidly than temperature, but Figure 9.5b returns to agreement with the baseline case and the literature where the temperature of the fluids mixed more rapidly than the momentum.

9.3.2 Incompressible Simulations

The data presented in Figures 9.6 through 9.9 are less conclusive about the relative mixing rates of the temperature and momentum at incompressible conditions. The baseline incompressible case was isothermal and as such the temperature was completely uniform from beginning to end. The other cases involved modification to the temperature profile of the core and bypass. They indicate the coefficient of variation was a function of the temperature difference regardless if it was the core or bypass fluid which had the higher temperature.

9.4 Conclusions

This brief chapter has been included to help close the gap previously identified within the published literature. The relative uniformity of axial total temperature and momentum flux fields calculated at specific planes between the lobed mixer exit plane and the nozzle exit plane were presented as mean and coefficient of variation versus axial distance and as radial pitchwise average plots. The data suggested that the expectation of thermal energy, or temperature of the fluid, to be mixed out prior to the momentum in all cases was not applicable when considering lobed mixers. In some cases, the expected outcome was true and the temperature mixing was observed to

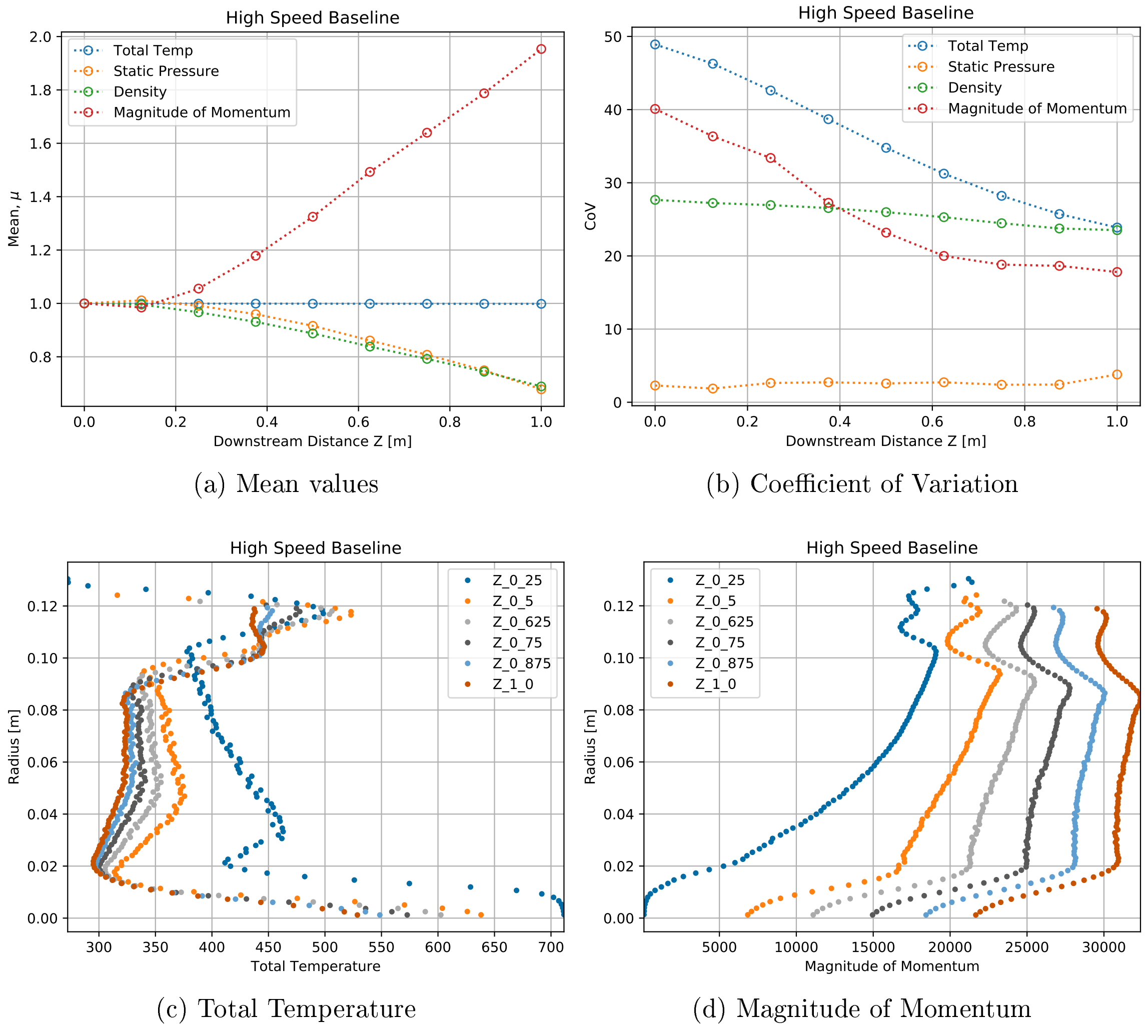

(a) Mean values

(b) Coefficient of Variation

(c) Total Temperature

(d) Magnitude of Momentum

Figure 9.2: Mean and coefficient of variation values for the baseline compressible case.

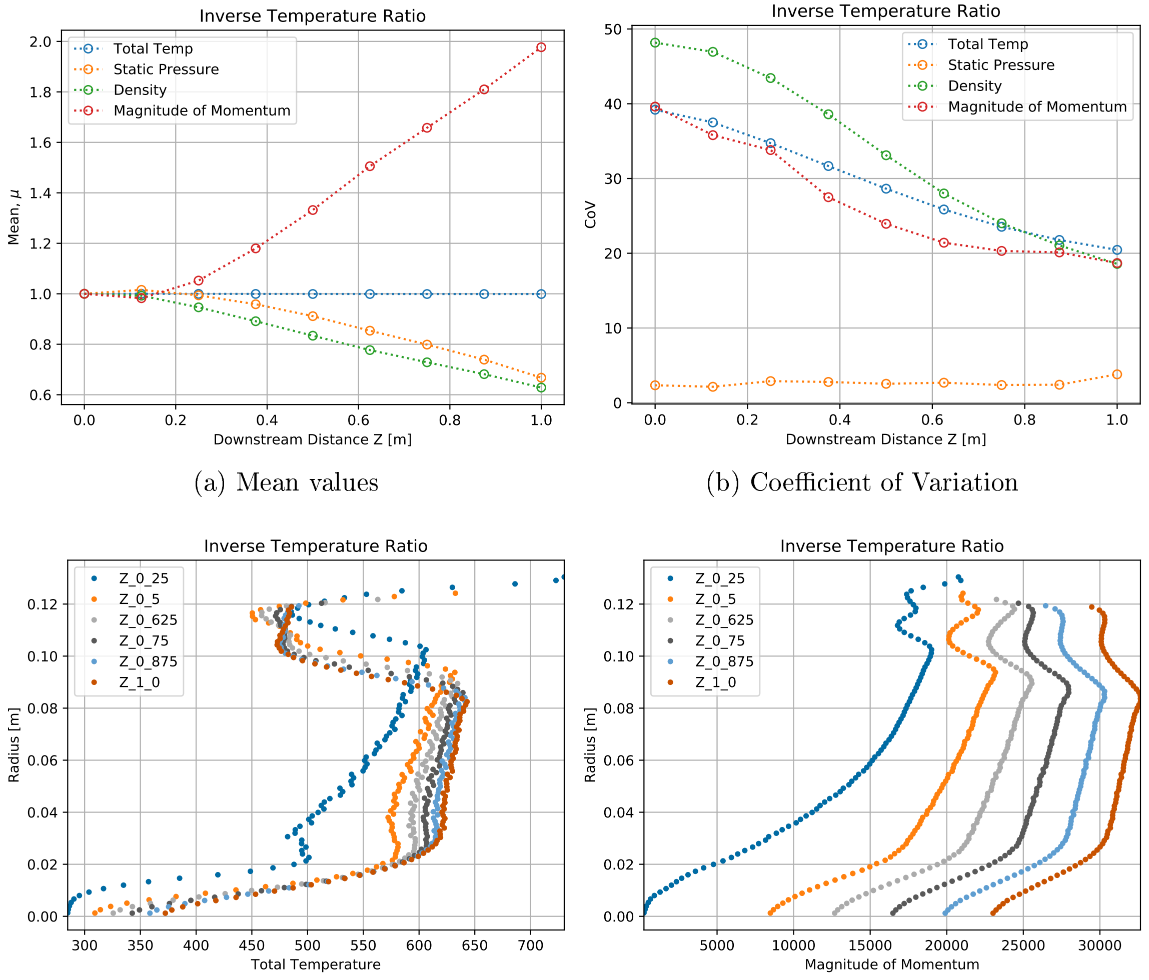

(a) Mean values

(b) Coefficient of Variation

(c) Total Temperature

(d) Magnitude of Momentum

Figure 9.3: Mean and coefficient of variation values for the inverted temperature ratio compressible case.

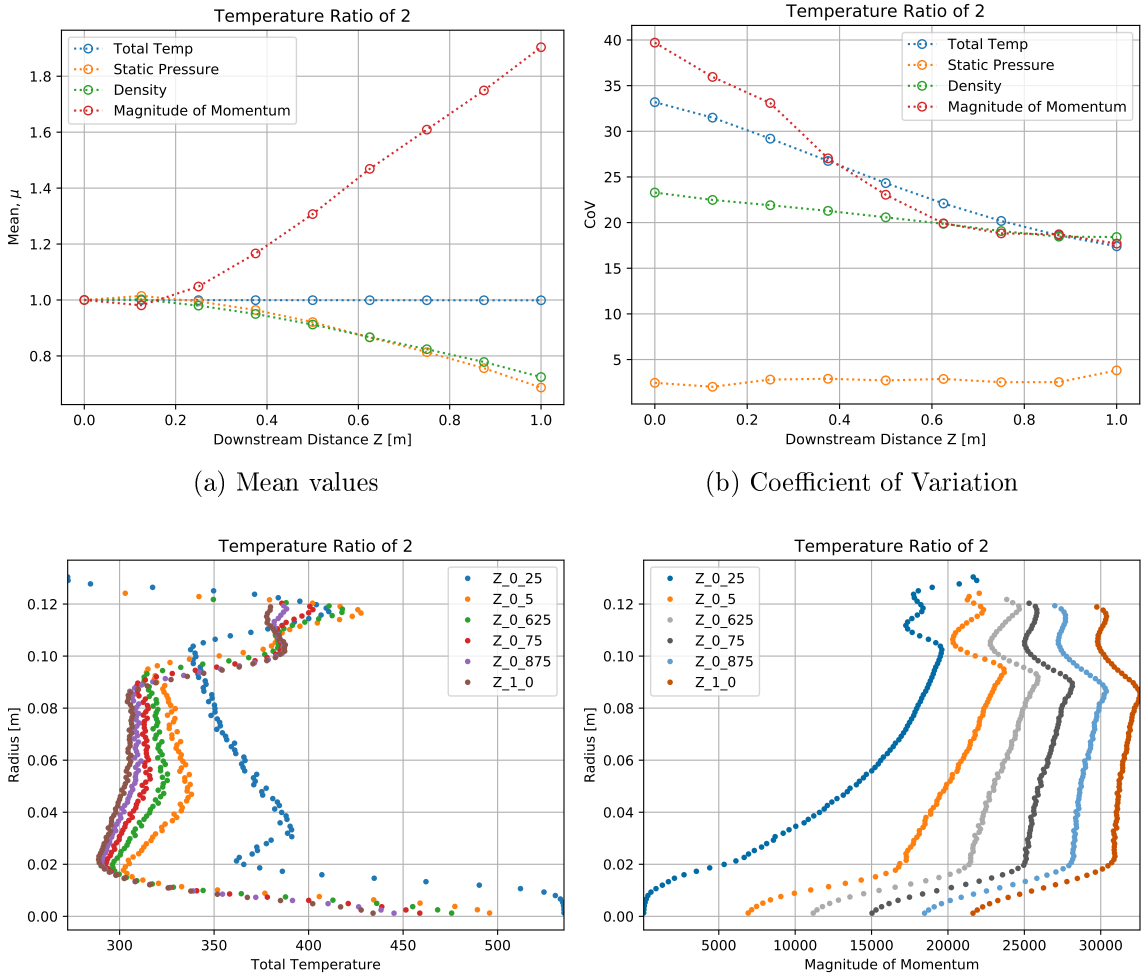

(a) Mean values

(b) Coefficient of Variation

(c) Total Temperature

(d) Magnitude of Momentum

Figure 9.4: Mean and coefficient of variation values for the reduced temperature ratio compressible case.

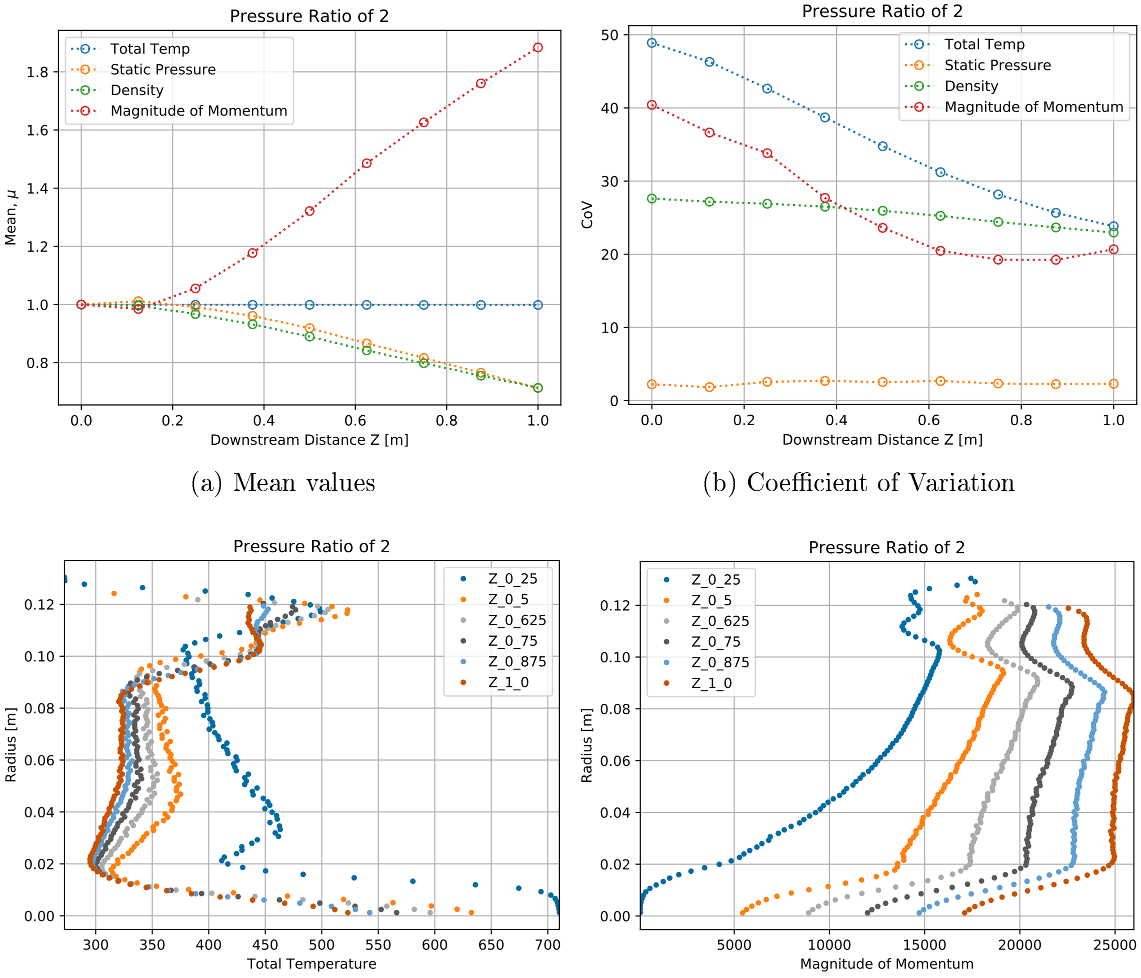

(a) Mean values

(b) Coefficient of Variation

(c) Total Temperature

(d) Magnitude of Momentum

Figure 9.5: Mean and coefficient of variation values for the double pressure ratio compressible case.

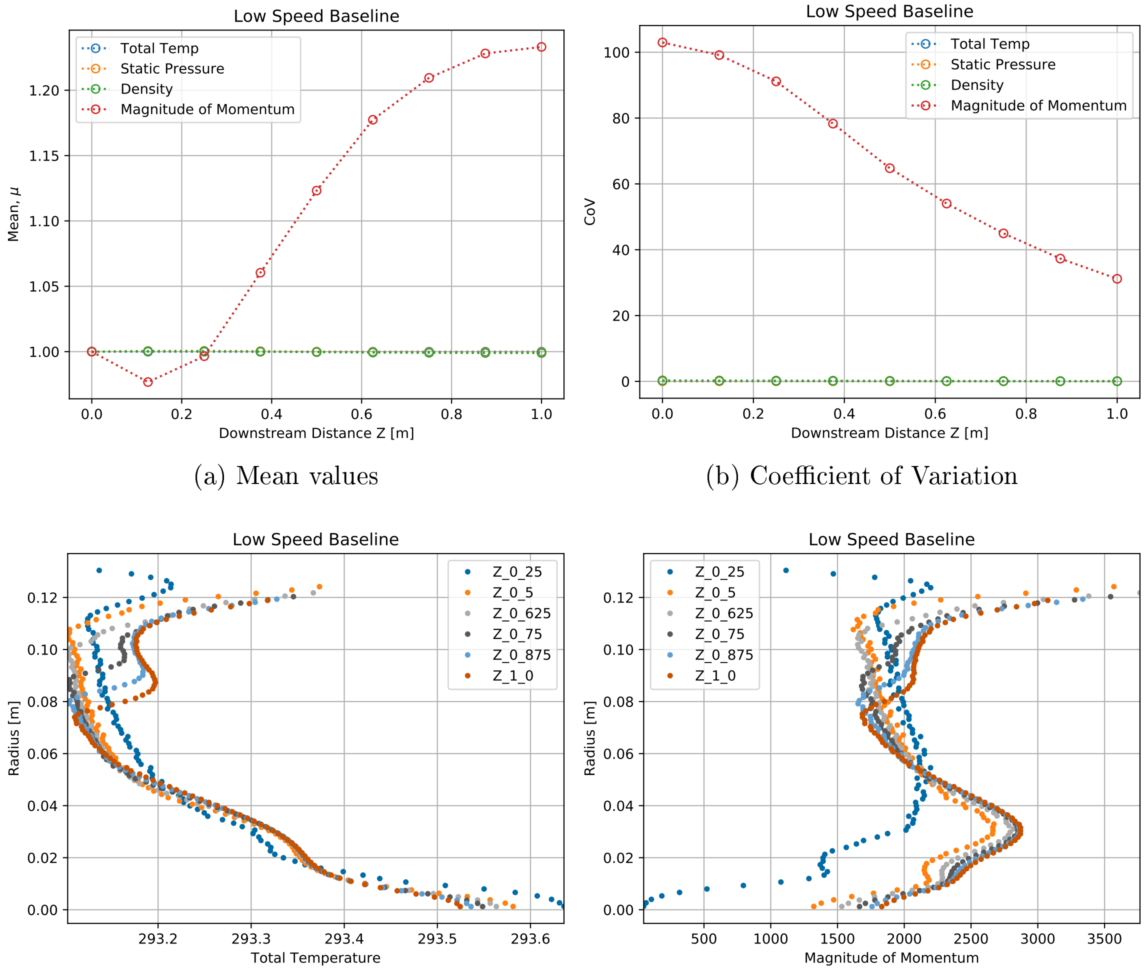

(a) Mean values

(b) Coefficient of Variation

(c) Total Temperature

(d) Magnitude of Momentum

Figure 9.6: Mean and coefficient of variation values for the baseline incompressible case.

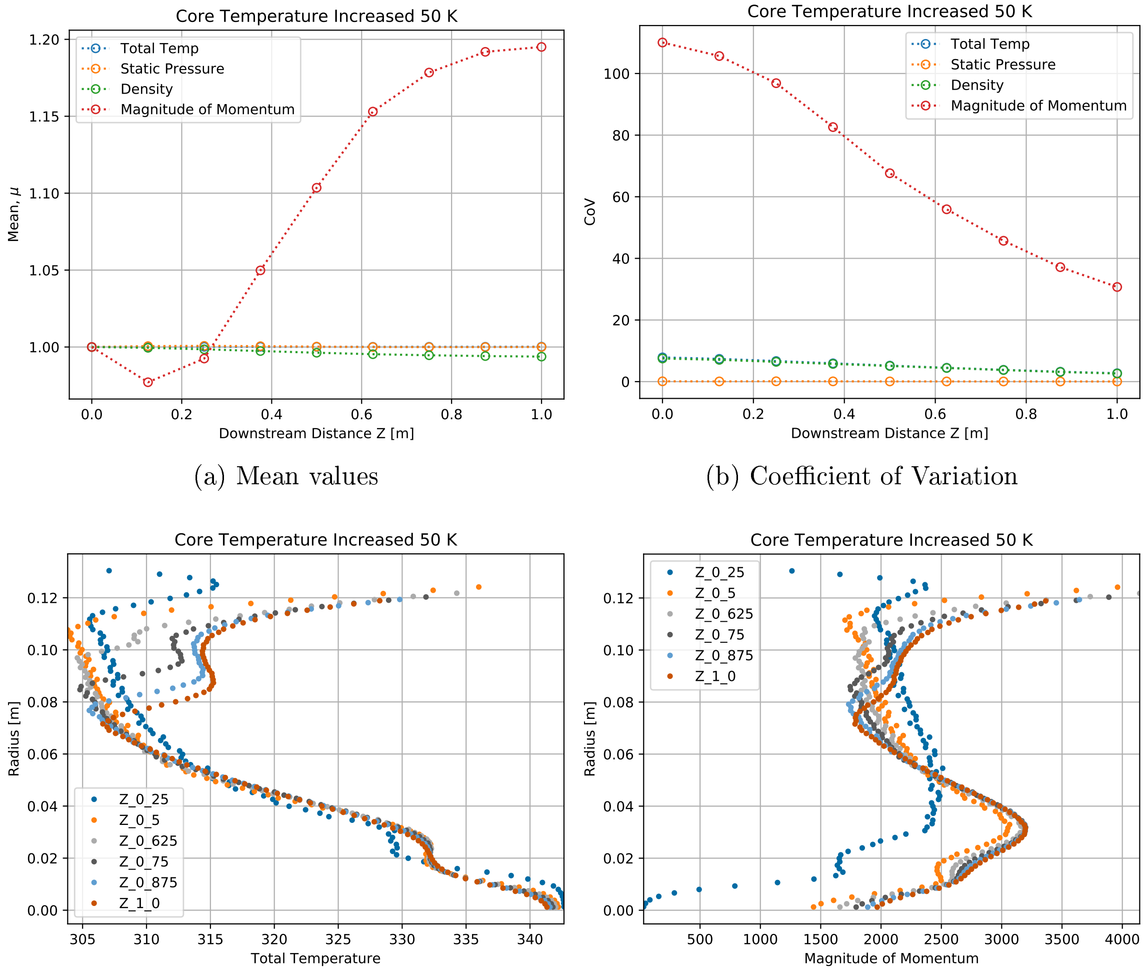

(a) Mean values

(b) Coefficient of Variation

(c) Total Temperature

(d) Magnitude of Momentum

Figure 9.7: Mean and coefficient of variation values for the core temperature increased by 50 K incompressible case.

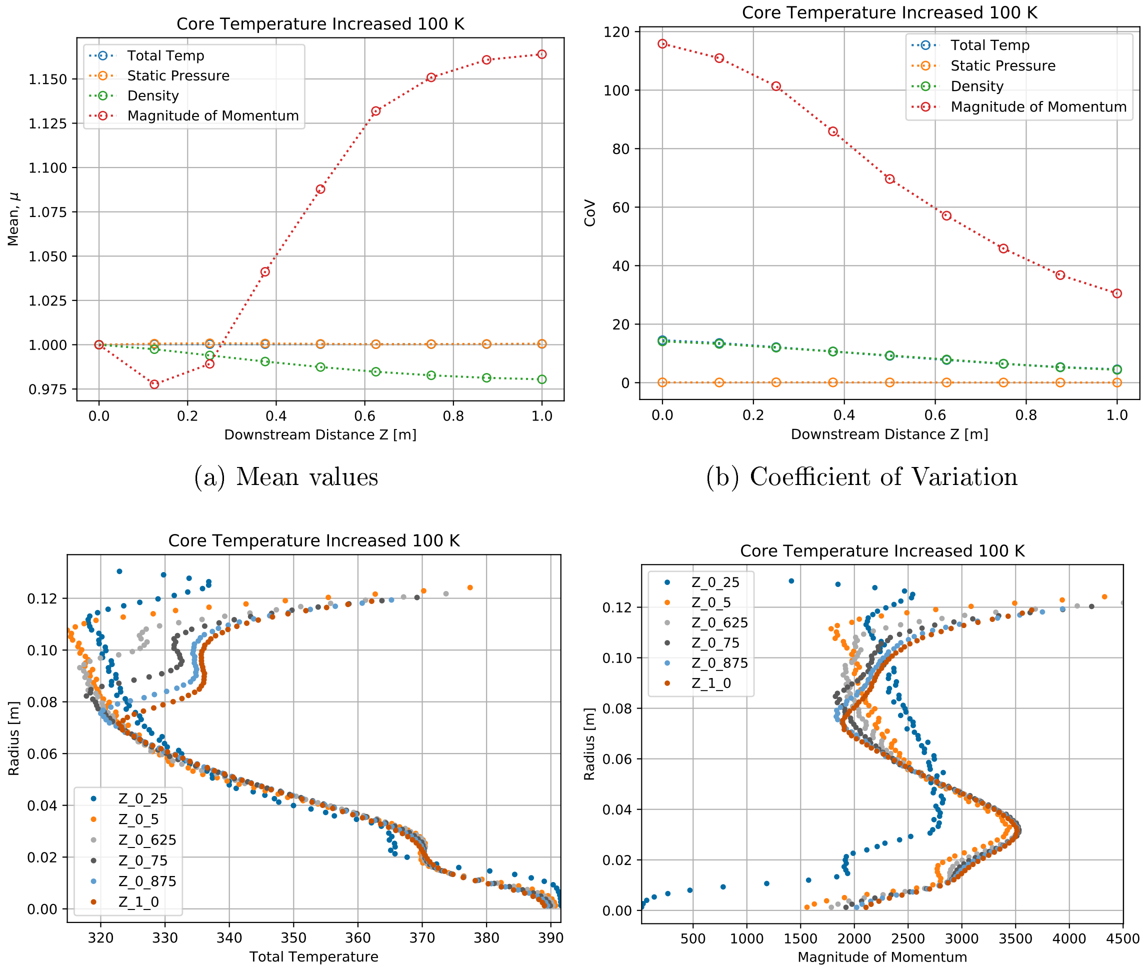

(a) Mean values

(b) Coefficient of Variation

(c) Total Temperature

(d) Magnitude of Momentum

Figure 9.8: Mean and coefficient of variation values for the core temperature increased by 100 K incompressible case.

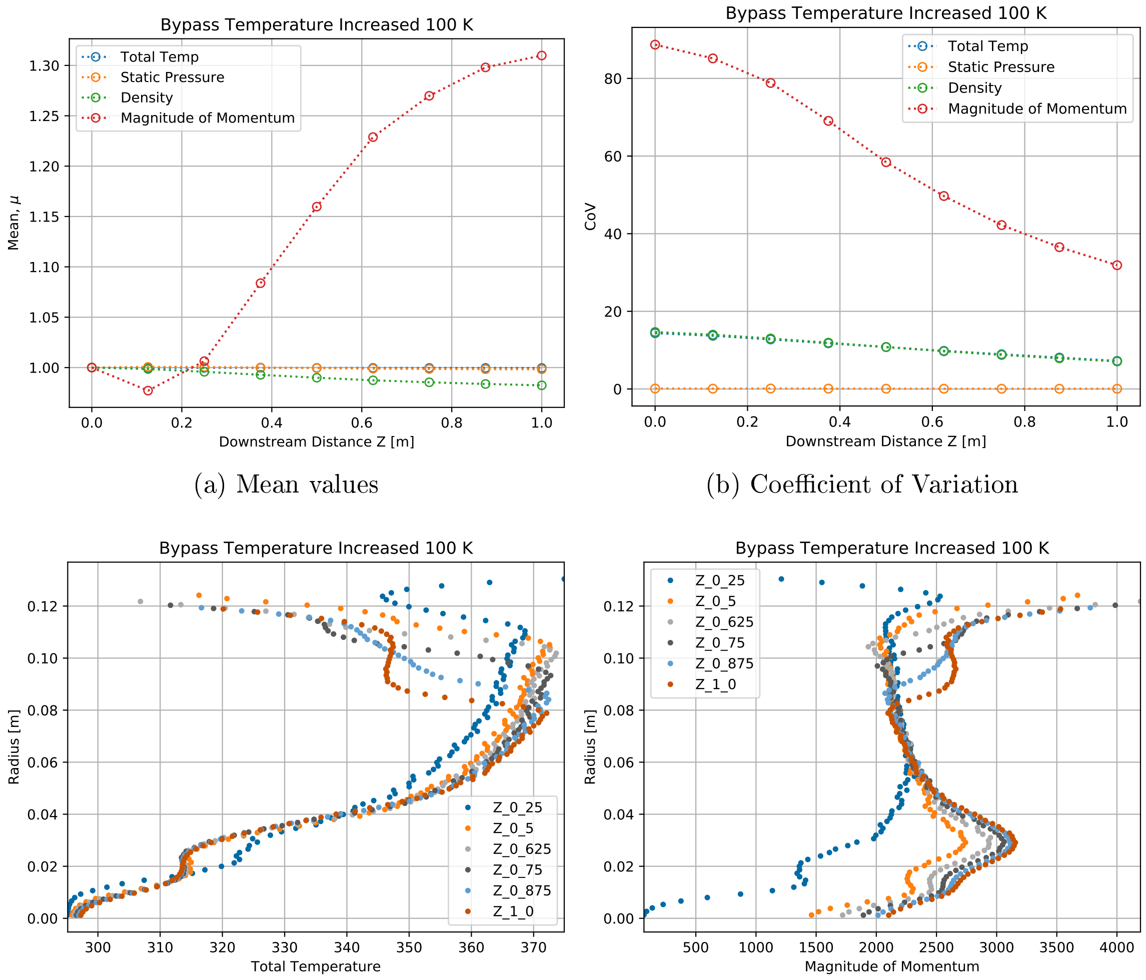

(a) Mean values

(b) Coefficient of Variation

(c) Total Temperature

(d) Magnitude of Momentum

Figure 9.9: Mean and coefficient of variation values for the bypass temperature increased by 100 K incompressible case.

lead the momentum at all points in the flow. However, in certain cases such as when the core and bypass fluid temperatures were inverted for the compressible case, the momentum uniformity led that of the temperature at the nozzle exit plane.

The results of this study, though brief, are significant and require that further work be done to verify the discovery.

Chapter 10

Conclusion

This chapter presents a summary of the investigations, methods and analyses that form this thesis. Conclusions drawn from the analyses are presented and recommendations for future work are suggested.

10.1 Summary

This thesis has been the culmination of a substantial campaign of computational simulations of medium bypass turbofan engine exhaust system performance and co-annular jet mixing within. The ultimate goal was to redesign the aft-end ducting to reduce engine length and save weight. Midway through the process, it came to light that the basis for relying on low-speed experimental and computational simulations was based on assumptions not explicitly covered within the literature.

The body of this thesis begins at that point and began with an examination of whether low-speed compressible simulations that could easily be recreated in the lab were capable of correctly modeling the performance of the exhaust systems which normally operate in high-speed compressible conditions with large thermal gradients. Chapter 5 concluded that low-speed compressible simulations were not adequate and research should be continued with computational simulations at engine representative conditions. Chapters 6 and 7 continued with investigations into the design and performance of lobed mixers. The data from those chapters concluded that lobed mixers work best with moderately deep—approximately 50% lobe depth—scalloping, and can tolerate swirl up to 10° but not beyond—depending on centrebody geometry. The engineering pursuit was put to the test in Chapter 8 where the Turbine Exhaust Casing struts—deswirling hardware normally found between the low pressure turbine and lobed mixer and requiring a great deal of axial length—were systematically integrated with the lobed mixer. The results were that a fully integrated design allowed for performance on-par with the traditional design.

The final task was to begin filling the gap in the literature via computational simulation of various mixing conditions downstream of the lobed mixer. The original approach had been to assume that all thermal uniformity would be achieved faster than momentum uniformity in mixing flows of concentric jets. That assumption was based on research that had only been performed with confluent mixers, not lobed mixers [2, 70, 4]. The relative uniformity of fluid flow temperature and momentum were found to be inconsistent in order of mixing rate depending on the boundary condition imposed, setting up an avenue for future research into the topic.

10.2 Conclusions

The conclusions of this study are:

- Lobed mixer performance should be simulated at the condition of their operation. The boundary conditions, geometry and mixing physics—including streamwise vorticity—are not conducive to scaling.

- The trailing edge of the lobed mixer should be scalloped to a moderate depth and those scalloping edges should be parallel to the penetration angle into the core and bypass flows.

- Swirl within the core flow can be tolerated by lobed mixers up to angles of 10° without swirl removal treatments. If core flow swirl angles are greater than 10°, TEC struts should be used strategically to return the flow to as completely axial as possible.

- The TEC struts can be fully integrated with the lobed mixer without penalty to performance. However, the exhaust system performance is reduced if the TEC strut is not fully integrated and is only moved slightly closer from its traditional location upstream of the lobed mixer.

- The mixing rates of temperature and momentum are not independent of the boundary conditions downstream of lobed mixers. Data show it was possible for momentum to mix more rapidly than temperature in certain cases, which contradicts conventional wisdom based solely on confluent mixer studies.

10.3 Recommendations for Future Work

Suggestions for improvement above and beyond the current work include:

- With proper funding, a physical simulation at engine conditions could be performed to enhance the confidence of the discoveries about the performance of integrated TEC strut and lobed mixer configurations.
- TEC strut design improvements should be performed to further enhance the benefits of TEC strut-lobed mixer integration.
- A more rigorous and systematic investigation should be designed to verify the discoveries outlined in Chapter 9. The results reported provide a justification to develop a physical model to record measurements of mixing rates downstream of a lobed mixer subject to varying temperature and momentum gradients.

Bibliography

[1] Forstall, W. and Shapiro, A. H., 1951, "Momentum and mass transfer in coaxial gas jets," American Society of Mechanical Engineers – Transactions – Journal of Applied Mechanics, **18**(2), pp. 219–220.

[2] Alpinieri, L., 1964, "Turbulent mixing of coaxial jets," AIAA Journal, **2**(9), pp. 1560—-1567.

[3] Brown, G. L. and Roshko, A., 1974, "On density effects and large structure in turbulent mixing layers," Journal of Fluid Mechanics, **64**(4), pp. 775–816.

[4] Schumaker, S. A. and Driscoll, J. F., 2012, "Mixing properties of coaxial jets with large velocity ratios and large inverse density ratios," Physics of Fluids, **24**(5), p. 055101.

[5] Ahmed, S. A., So, R. M. C., and Mongia, H. C., 1985, "Density effects on jet characteristics in confined swirling flow," Experiments in Fluids, **3**(4), pp. 231–238.

[6] Villermaux, E. and Rehab, H., 2000, "Mixing in coaxial jets," Journal of Fluid Mechanics, **425**, pp. 161–185.

[7] Birch, S., Paynter, G., Spalding, D., and Tatchell, D., 1977, "An experimental and numerical study of the 3-D mixing flows of a turbofan engine exhaust system," *15th Aerospace Sciences Meeting*, American Institute of Aeronautics and Astronautics, Los Angeles, CA, USA, http://arc.aiaa.org/doi/10.2514/6.1977-204

[8] Kuchar, A. and Chamberlin, R., 1980, "Scale model performance test investigation of exhaust system mixers for an Energy Efficient Engine /E3/ propulsion system," *18th Aerospace Sciences Meeting*, American Institute of Aeronautics and Astronautics, Pasadena, CA, USA, http://arc.aiaa.org/doi/10.2514/6.1980-229

[9] Smoot, L. D., 1976, "Turbulent mixing coefficients for compressible coaxial submerged andcoflowing jets," AIAA Journal, **14**(12), pp. 1699–1705.

[10] Bernal, L. P. and Roshko, A., 1986, "Streamwise vortex structure in plane mixing layers," Journal of Fluid Mechanics, **170**, pp. 499–525.

[11] Hussain, A. K. M. F., 1986, "Coherent structures and turbulence," Journal of Fluid Mechanics, **173**, pp. 303–356.

[12] Liu, J., 1989, "Coherent Structures In Transitional And Turbulent Free Shear Flows," Annual Review of Fluid Mechanics, **21**(1), pp. 285–315.

[13] Crow, S. C. and Champagne, F. H., 1971, "Orderly structure in jet turbulence," Journal of Fluid Mechanics, **48**(3), pp. 547–591.

[14] Lau, J., 1980, "Laser velocimeter correlation measurements in subsonic and supersonic jets," Journal of Sound and Vibration, **70**(1), pp. 85–101.

[15] Roshko, A., 1976, "Structure of Turbulent Shear Flows: A New Look," AIAA Journal, **14**(10), pp. 1349–1357.

[16] Knowles, K. and Saddington, A. J., 2006, "A review of jet mixing enhancement for aircraft propulsion applications," Proceedings of the Institution of Mechanical Engineers, Part G: Journal of Aerospace Engineering, **220**(2), pp. 103–127.

[17] Gutmark, E. J., Schadow, K. C., and Yu, K. H., 1995, "Mixing Enhancement in Supersonic Free Shear Flows," Annual Review of Fluid Mechanics, **27**(1), pp. 375–417.

[18] Gutmark, E. J. and Grinstein, F. F., 1999, "Flow Control with Noncircular Jets," Annual Review of Fluid Mechanics, **31**(1), pp. 239–272.

[19] Ho, C.-M. and Gutmark, E., 1987, "Vortex induction and mass entrainment in a small-aspect-ratio elliptic jet," Journal of Fluid Mechanics, **179**, pp. 383–405.

[20] Quinn, W. R., 1995, "Turbulent mixing in a free jet issuing from a low aspect ratio contoured rectangular nozzle," The Aeronautical Journal, **99**(988), pp. 337–342.

[21] Quinn, W., 1992, "Turbulent free jet flows issuing from sharp-edged rectangular slots: The influence of slot aspect ratio," Experimental Thermal and Fluid Science, **5**(2), pp. 203–215.

[22] Washington, D., Alvi, F. S., and Krothapalli, A., 1997, "Flowfield characteristics of a mach 2 diamond jet," *The First National Student Conference: NASA University Research Centers at Minority Institutions* (Vol. 214), pp. 386–390.

[23] Lee, S.-J. and Baek, S.-J., 1994, "The effect of aspect ratio on the near-field turbulent structure of elliptic jets," Flow Measurement and Instrumentation, **5**(3), pp. 170–180.

[24] Schadow, K. C., Gutmark, E., Parr, D. M., and Wilson, K. J., 2004, "Selective control of flow coherence in triangular jets," Experiments in Fluids, **6**(2), pp. 129–135.

[25] Su, M. D. and Friedrich, R., 1994, "Investigation of Fully Developed Turbulent Flow in a Straight Duct With Large Eddy Simulation," Journal of Fluids Engineering, **116**(4), pp. 677–684.

[26] Ponton, A. and Smith, A., 1994, "The Effect of Aspect Ratio upon Engine Exhaust Temperature Decay for Rectangular and 2D Coanda Nozzles – Study Using a Small Scale Turbojet Engine," Tech. rep., S and C Thermofluids Ltd., Bath, UK.

[27] Husain, H. S. and Hussain, F., 1999, "The elliptic whistler jet," Journal of Fluid Mechanics, **397**, pp. 23–44.

[28] New, T. H., Lim, K. M. K., and Tsai, H. M., 2005, "Vortical structures in a laminar V-notched indeterminate-origin jet," Physics of Fluids, **17**(5), p. 054108.

[29] Longmire, E. K., Eaton, J. K., and Elkins, C. J., 1992, "Control of jet structure by crown-shaped nozzles," AIAA Journal, **30**(2), pp. 505–512.

[30] Kaushik, M., Thakur, P. S., and Rathakrishnan, E., 2006, "Studies on the Effect of Notches on Circular Sonic Jet Mixing," Journal of Propulsion and Power, **22**(1), pp. 211–214.

[31] Krothapalli, A., King, C., and Strykowski, P., 1993, "The role of streamwise vortices on the sound generation of supersonic jets," *15th Aeroacoustics Conference*, American Institute of Aeronautics and Astronautics, Long Beach, CA, USA, `http://arc.aiaa.org/doi/10.2514/6.1993-4320`

[32] Reeder, M. F. and Samimy, M., 1996, "The evolution of a jet with vortex-generating tabs: real-time visualization and quantitative measurements," Journal of Fluid Mechanics, **311**, p. 73.

[33] Wlezien, R. W. and Kibens, V., 1988, "Influence of nozzle asymmetry on supersonic jets," AIAA Journal, **26**(1), pp. 27–33.

[34] Mengle, V. G. and Dalton, W. N., 2002, "Lobed Mixer Design for Noise Suppression Acoustic and Aerodynamic Test Data Analysis," Tech. rep., Rolls-Royce Allison, Indianapolis, IN, USA.

[35] Frost, T. H., 1966, "Practical Bypass Mixing Systems for Fan Jet Aero Engines," Aeronautical Quarterly, **17**(2), pp. 141–160.

[36] Presz, W. M., 1991, "Mixer/ejector noise suppressors," *27th Joint Propulsion Conference*, American Institute of Aeronautics and Astronautics, Sacramento, CA, USA, `http://arc.aiaa.org/doi/10.2514/6.1991-2243`

[37] Power, G., McClure, M., and Vinh, D., 1994, "Advanced IR suppressor design using a combined CFD/test approach," *30th Joint Propulsion Conference and Exhibit*, American Institute of Aeronautics and Astronautics, Indianapolis, IN, USA, `http://arc.aiaa.org/doi/10.2514/6.1994-3215`

[38] Werle, M. J., Presz, W. M., and Paterson, R. W., 1987, "Flow structure in a periodic axial vortex array," *25th AIAA Aerospace Sciences Meeting*, American Institute of Aeronautics and Astronautics, Reno, NV, USA, p. 10, `http://arc.aiaa.org/doi/10.2514/6.1987-610`

[39] Kozlowski, H. and Kraft, G., 1980, "Experimental evaluation of exhaust mixers for an Energy Efficient Engine," *16th Joint Propulsion Conference*, American Institute of Aeronautics and Astronautics, Hartford, CT, USA, `http://arc.aiaa.org/doi/10.2514/6.1980-1088`

[40] Belovich, V. M. and Samimy, M., 1997, "Mixing processes in a coaxial geometry with a central lobed mixer-nozzle," AIAA Journal, **35**(5), pp. 838–841.

[41] Eckerle, W. A., Sheibani, H., and Awad, J., 1992, "Experimental Measurement of the Vortex Development Downstream of a Lobed Forced Mixer," Journal of Engineering for Gas Turbines and Power, **114**(1), pp. 63–71.

[42] Elliot, J., Manning, T., Qiu, Y., GReitzer, E., Tan, C., and Tillman, T., 1992, "Computational and experimental studies of flow in multi-lobed forcedmixers," *28th Joint Propulsion Conference and Exhibit*, American Institute of Aeronautics and Astronautics, Nashville, TN, USA, `http://arc.aiaa.org/doi/10.2514/6.1992-3568`

[43] McCormick, D. C. and Bennett, J. C., 1994, "Vortical and turbulent structure of a lobed mixer free shear layer," AIAA Journal, **32**(9), pp. 1852–1859.

[44] Yu, S., 1994, "Some aspects of the flows behind lobed forced mixers," International Communications in Heat and Mass Transfer, **21**(6), pp. 849–858.

[45] Yu, S. C. M., Yeo, J. H., and Teh, J. K. L., 1995, "Velocity measurements downstream of a lobed-forced mixer with different trailing-edge configurations," Journal of Propulsion and Power, **11**(1), pp. 87–97.

[46] Hu, H., Kobayashi, T., Saga, T., Segawa, S., and Taniguchi, N., 2000, "Particle image velocimetry and planar laser-induced fluorescence measurements on lobed jet mixing flows," Experiments in Fluids, **29**(7), pp. S141–S157.

[47] Paterson, R. W., 1984, "Turbofan Mixer Nozzle Flow Field—A Benchmark Experimental Study," Journal of Engineering for Gas Turbines and Power, **106**(3), pp. 692–698.

[48] O'Sullivan, M. N., Krasnodebski, J. K., Waitz, I. a., Greitzer, E. M., Tan, C. S., and Dawes, W. N., 1996, "Computational study of viscous effects on lobed mixer flow features and performance," Journal of Propulsion and Power, **12**(3), pp. 449–456.

[49] Yu, S. C. M., Xu, X. G., and Yip, T. H., 1996, "Effects of initial boundary layers to the lobed mixed trailing streamwise vorticity," Journal of Propulsion and Power, **12**(2), pp. 440–442.

[50] Waitz, I., Qiu, Y., Manning, T., Fung, A., Elliot, J., Kerwin, J., Krasnodebski, J., O'Sullivan, M., Tew, D., Greitzer, E., Marble, F., Tan, C., and Tillman, T., 1997, "Enhanced mixing with streamwise vorticity," Progress in Aerospace Sciences, **33**(5-6), pp. 323–351.

[51] Presz, Jr., W., Reynolds, G., and McCormick, D., 1994, "Thrust augmentation using mixer-ejector-diffuser systems," *32nd Aerospace Sciences Meeting and Exhibit*, American Institute of Aeronautics and Astronautics, Reno, NV, USA, http://arc.aiaa.org/doi/10.2514/6.1994-20

[52] Yu, S. and Yip, T., 1997, "Experimental investigation of two-stream mixing flows with streamwise and normal vorticity," International Journal of Heat and Fluid Flow, **18**(2), pp. 253–261.

[53] Yu, S. C. M., Hou, Y., and Chan, W. K., 2000, "Scarfing and Scalloping Effects on Lobed Forced Mixer at Low-Speed Conditions," Journal of Propulsion and Power, **16**(3), pp. 440–448.

[54] Wright, A., Lei, Z., Mahallati, A., Cunningham, M., and Militzer, J., 2013, "Effects of Scalloping on the Mixing Mechanisms of Forced Mixers With Highly Swirling Core Flow," Journal of Engineering for Gas Turbines and Power, **135**(7), pp. 437–448.

[55] Mao, R., Yu, S. C. M., Zhou, T., and Chua, L. P., 2009, "On the vorticity characteristics of lobe-forced mixer at different configurations," Experiments in Fluids, **46**(6), pp. 1049–1066.

[56] Lee, S. S. and Bridges, J., 2006, "Phased-Array Study of Dual-Flow Jet Noise: Effect of Nozzles and Mixers," *12th AIAA/CEAS Aeroacoustics Conference (27th AIAA Aeroacoustics Conference)*, American Institute of Aeronautics and Astronautics, Reston, Virigina, http://arc.aiaa.org/doi/10.2514/6.2006-2647

[57] Skebe, S., Paterson, R., and Barber, T., 1988, "Experimental investigation of three-dimensional forced mixer lobe flow fields," *1st National Fluid Dynamics Conference*, American Institute of Aeronautics and Astronautics, Cincinatti, OH, USA, http://arc.aiaa.org/doi/10.2514/6.1988-3785

[58] Salman, H., McGuirk, J. J., and Page, G. J., 2006, "Prediction of a non-isothermal three-dimensional mixing layer created by a scarfed lobed mixer," Proceedings of the Institution of Mechanical Engineers, Part G: Journal of Aerospace Engineering, **220**(5), pp. 399–419.

[59] Lei, Z., Mahallati, A., Cunningham, M., and Germain, P., 2012, "Effects of Core Flow Swirl on the Flow Characteristics of a Scalloped Forced Mixer," Journal of Engineering for Gas Turbines and Power, **134**(11), p. 111201.

[60] Tew, D. E., Hermanson, J. C., and Waitz, I. a., 2004, "Impact of Compressibility on Mixing Downstream of Lobed Mixers," AIAA Journal, **42**(11), pp. 2393–2396.

[61] Presz, W. M. and Greitzer, E. M., 1988, "A useful similarity principle for jet engine exhaust system performance," *24th Joint Propulsion Conference*, American Institute of Aeronautics and Astronautics, Boston, MA, USA, http://arc.aiaa.org/doi/10.2514/6.1988-3001

[62] Head, V. L., Povinelli, L. A., and Gerstenmaier, W. H., 1984, "Hot-Flow Tests of a Series of 10-Percent-Scale Turbofan Forced Mixing Nozzles," Tech. rep., NASA Lewis Research Center, Cleveland, OH, USA.

[63] Long, D., 2004, "Turbofan Exhaust Noise Using Helium/Air Mixture to Simulate Core Temperature," *10th AIAA/CEAS Aeroacoustics Conference*, American Institute of Aeronautics and Astronautics, Manchester, GB, pp. 1–11, http://arc.aiaa.org/doi/10.2514/6.2004-3018

[64] Wright, A., Mahallati, A., and Militzer, J., 2013, "Establishing a Turbulence Model for Flowfield Predictions of Lobed Mixers with Stiffening Members," *International Symposium on Air Breathing Engines*, Busan, South Korea, pp. 1–9.

[65] Numeca International, 2018, "Theory Guide FINE/Open with OpenLabs 7.2," .

[66] Roache, P. J., 1997, "Quantification of Uncertainty in Computational Fluid Dynamics," Annual Review of Fluid Mechanics, **29**(1), pp. 123–160.

[67] Roache, P. J., 1994, "Perspective: A Method for Uniform Reporting of Grid Refinement Studies," Journal of Fluids Engineering, **116**(3), pp. 405–413.

[68] Kozlowski, H. and Larkin, M., 1981, "Energy Efficient Engine Exhaust Mixer Model Technology," Tech. rep., Pratt and Whitney Aircraft Group; Commercial Products, East Hartford, CT, USA, http://hdl.handle.net/2060/19820014390

[69] Lei, Z., Mahallati, A., Cunningham, M., and Germain, P., 2010, "Influence of Inlet Swirl on the Aerodynamics of a Model Turbofan Lobed Mixer," *Volume 7: Fluid Flow, Heat Transfer and Thermal Systems, Parts A and B*, ASME, Vancouver, BC, Canada, pp. 807–819, https://asmedigitalcollection.asme.org/IMECE/proceedings/IMECE2010/44441/807/339643

[70] Alexander, L. G., Kivnick, A., Comings, E. W., and Henze, E. D., 1955, "Transport of momentum and energy in a ducted jet: I. Experimental study of a non-isothermal jet of air discharging into a duct," AIChE Journal, **1**(1), pp. 55–61.

Appendix A

Python Code for Data Reduction

A.1 Data Reduction and Extraction from CFView

```
CFViewBackward(1210)
#region Functions
def CheckDirectory(P):
  # Checks that the argument P is a directory. If it doesn't exist, it will create the directory and any folders above.
  import os
  if os.path.isdir(P)==False:
    os.makedirs(P)

def CutPlaneMeridion(row):
  # Creates the meridional cut planes used for data extraction.
  # Accepts a pandas dataframe as its argument.
  CutPlaneSave(0,0,0,row['nX'],row['nY'],0,row['Name']+'.D1')

def CutPlaneAxial(row):
  # Creates the Axial cutting planes used for Contour export and data reduction
  # Accepts a pandas dataframe as its argument.
  LimitedCutPlaneSave(0.02,0.08,row['realZ'],0,0,1,0,row['Name'])

def CutPlaneRef(row):
  # Creates the Core and Bypass reference planes used in certain calculations
  # Accepts a pandas dataframe as its argument.
  LimitedCutPlaneSave(0.02,row['Y'],row['Z'],0,0,1,0,row['Name'])

def ReferenceVals(Quantity):
  # Computes reference values used in certain quantity creations
  # Accepts a Quantity String that defines a CFView quantity.
  # Returns a Series with Core, Bypass and Mean (Core+Bypass) average values
  import pandas as pd
  Temp = pd.Series(index=['Core','Bypass','Mean'])
  QntFieldScalar(Quantity)
  SelectFromProject('CoreRef.D1')
  Temp['Core'] = SclAverage() # Extract Average value at core reference plane
  SelectFromProject('BypassRef.D1')
  Temp['Bypass'] = SclAverage() # Extract Average value at bypass reference plane
  SelectFromProject('CoreRef.D1','BypassRef.D1')
  Temp['Mean'] = SclAverage() #Extract Average value at combined core and bypass reference planes (for calculating losses at locations where core and bypass flows mix)
  SelectFromProject('Z_0_0.D1')
  Temp['Mixer'] = SclAverage() #Extract Mass Average value at combined core and bypass reference planes (for calculating losses at locations where core and bypass flows mix)
  return Temp

def ReferenceValsWeighted(Quantity):
  # Computes reference values used in certain quantity creations
  # Accepts a Quantity String that defines a CFView quantity.
  # Returns a Series with Core, Bypass and Mean (Core+Bypass) mass average values
  import pandas as pd
  Temp = pd.Series(index=['Core','Bypass','Mean'])
  QntFieldScalar(Quantity)
  SelectFromProject('CoreRef.D1')
  Temp['Core'] = WeightedIntegral() # Extract Mass Average value at core reference plane
  SelectFromProject('BypassRef.D1')
  Temp['Bypass'] = WeightedIntegral() # Extract Mass Average value at bypass reference plane
  SelectFromProject('CoreRef.D1','BypassRef.D1')
  Temp['Mean'] = WeightedIntegral() #Extract Mass Average value at combined core and bypass reference planes (for calculating losses at locations where core and bypass flows mix)
  SelectFromProject('Z_0_0.D1')
  Temp['Mixer'] = WeightedIntegral() #Extract Mass Average value at combined core and bypass reference planes (for calculating losses at locations where core and bypass flows mix)
  return Temp

def SetRange(Quantity):
  # Sets the CFView range for the quantity so that contour exports are descriptive and have good contrast between high and low values.
  # Accepts a Quantity String that defines a CFView quantity.
  # Returns None
  if Quantity == 'CPo':
    RprRangeIn(-1.5,1.5)
  elif Quantity == 'CPs':
    RprRangeIn(-6,0)
  elif Quantity == 'Cw_s':
    RprRangeIn(-15,15)
  elif Quantity == 'Cw_a':
    RprRangeIn(0,30)
  elif Quantity == 'Mach Number':
    RprRangeIn(0,1)
  elif Quantity == 'Swirl':
    RprRangeIn(0,40)
  elif Quantity == 'CV':
    RprRangeIn(0,3.5)
  elif Quantity == 'CM':
    RprRangeIn(0,2.5)
  elif Quantity == 'CTo':
    RprRangeIn(0.45,1.05)
  elif Quantity == 'CD':
    RprRangeIn(0.8,2.1)
  elif Quantity == 'CTKE':
    RprRangeIn(0,0.02)
  else:
    RprRangeAll()

def ContourExport(row,Quantity,P,Camera):
  # Creates the contour plots for image export.
  # Accepts a pandas dataframe as row, a Quantity String to define a CFView quantity to plot, P is a path string to define where the image is saved, Camera is a string defining which preset to set for the framing of the image.
  # Saves contour plot image to directory P
  DeleteAll()
  SelectFromProject(row['Name']+'.D1') # Select the plane to draw the contour on
  GmtBoundaryVisibility(1) # Turn on the boundary
  SclContourSmooth() # Apply the contour
  UpdateColormapHot() # Change the color map to a divergent map for black and white accessibility
  if Quantity == 'Cw_a':
    ColormapReverseColors() # Reversing the colormap improves contrast for azimuthal vorticity
  if Camera == 'Axial':
    SetCamera(0.000686501,0.0712162,6.69103,0.000686501,0.0712162,...
    1.225,0,1,0,0.085735,0.165602) #Sets the camera to view upstream
    Print(8,0,1,1,100,960,1080,1 ,P+row['Name']+'.png' ,'DRAFT',1,0,2) #Saves a draft image
  elif Camera == 'Meridional':
    SetCamera(-1.47466,0.0904002,0.814555,2.98023e-008,0.0904002,...
    0.814555,0,1,0,0.589864,0.296856) #Sets the camera to view a side profile of the flow
    Print(8,0,1,1,100,1920,1080,1 ,P+row['Name']+'.png' ,'DRAFT',1,0,2) #Saves a draft image
  elif Camera == 'Zoom':
    SetCamera(0.000686501,0.0712162,6.69103,0.000686501,0.0712162,...
    1.225,0,1,0,0.085735,0.165602) #Sets the camera to view upstream and zooms in on the full plane, does not preserve scale between images.
    ViewZoomAll(1)
    Print(8,0,1,1,100,960,1080,1 ,P+row['Name']+'.png' ,'DRAFT',1,0,2)
  GmtBoundaryVisibility(0) #Turn off the boundary line

def PlaneTextOut(row,P):
  # Exports the planar data to a text file for future plotting in a more publications quality manner.
  # Accepts dataframe row and Path P.
  # Returns None
  SelectFromProject(row['Name']+'.D1')
  SaveActiveSurfaces(P+row['Name']+'.dat')
```

```

def Stats(row,Quantity):
  # Computes Min, Max, Mean and Standard Deviation statistics for a quantity on a given plane
  # Accepts dataframe row and Quantity String
  # Returns a pandas series that results in a dataframe when the loop completes.
  import pandas as pd
  QntFieldScalar(Quantity)
  SelectFromProject(row['Name']+'.D1')
  Temp = pd.Series(index=['Z','Min','Max','Mean','StD'])
  Temp['Z']=row['Z']
  (Temp['Min'],Temp['Max']) = QuantityRangeActiveSurfaces()
  Temp['Mean'] = SclAverage()
  Temp['StD'] = QuantityStdDevActiveSurfaces()
  return Temp

def StatsWeighted(row,Quantity):
  # Computes Min, Max, Mass Average Mean and Mass Average Standard Deviation statistics for a quantity on a given plane
  # Accepts dataframe row and Quantity String
  # Returns a pandas series that results in a dataframe when the loop completes.
  import pandas as pd
  import math
  QntFieldScalar(Quantity) #Select the Quantity passed to the function
  SelectFromProject(row['Name']+'.D1') #Select the plane of interest
  Temp = pd.Series(index=['Z','Min','Max','Mean','StD']) #Initialize the pandas series to record the data
  Temp['Z']=row['Z']  #Set the first column to be the normalized axial location of the plane
  (Temp['Min'],Temp['Max']) = QuantityRangeActiveSurfaces() #Extract the Minimum and Maximum values of the quantity on the plane.
  Temp['Mean'] = WeightedIntegral() #Record the Mass Average of the Quantity on the Plane
  Mean = Temp['Mean'] #Save to a temporary variable
```

```
    QntFieldDerived(0, 'Variance', 'pow(('+Quantity+' - '+`Mean`+'),2)','','0') #Compute the variance of the quantity with the mass average
    QntFieldScalar('Variance') #Ensure that the Variance calculated is the Active Quantity
    Temp['StD'] = math.sqrt(math.fabs(WeightedIntegral())) #Compute the Square Root of the Mass Average of the Variance to complete the calculation of the weighted standard deviation
    QntFieldRemove('Variance') #Remove the Quantity so that the Variance can be recalculated for the next plane.
    return Temp

def CirculationCal(row,VCore,Dh):
    # Computes the clockwise and counterclockwise circulation at a given plane.
    # Accepts dataframe row, float VCore the average velocity at the core reference, float Dh the equivalent diameter used as characteristic length.
    # Returns pandas series that creates a dataframe through the loop.
    import pandas as pd
    C = pd.Series(index=['Z','Clockwise','Counterclockwise']) # Initialize the series.
    C['Z']=row['Z'] #Set the first value to be the normalized axial location of the Plane
    QntFieldScalar('Streamwise Vorticity') #Activate the Streamwise Vorticity quantity
    SelectFromProject(row['Name']+'.D1') #Activate the plane of interst
    CutSurfaceSave(0.5,0,0,1,0,0,0,0,0,0,-1,0,0,0,'CirculationClockwise') #Create a cut surface to split the plane into a right hand and left hand side.
    C['Clockwise'] = SclIntegral()/(VCore*Dh) #Calculated the circulation coefficient on the clockwise side of the plane.
    DeleteFromProject('CirculationClockwise.D0') #Delete the plane created previously

    QntFieldScalar('Streamwise Vorticity') #Activate the Streamwise Vorticity quantity
```

```
  SelectFromProject(row['Name']+'.D1') #Activate the plane of interst
  CutSurfaceSave(-0.5,0,0,-1,0,0,0,0,0,0,1,0,0,0,'CirculationCounterclockwise') #Create a cut surface to split the plane into a right hand and left hand side.
  C['Counterclockwise'] = SclIntegral()/(VCore*Dh) #Calculated the circulation coefficient on the counterclockwise side of the plane.
  DeleteFromProject('CirculationCounterclockwise.D0') #Delete the plane created previously
  return C

def ThrustCalc(Plane,Pressure,Lobes):
  # Computes Momentum plus Pressure thrust of a given plane using pressure difference and momentum flux through the plane.
  # Accepts string Plane, float Pressure which is the Ambient Pressure, integer Lobes which is the number of lobed the full mixer would have.
  # Returns float T giving the Thrust in Newtons.
  SelectFromProject(Plane) # Activate the desired plane
  QntFieldScalar('Momentum_Z') #Activate the axial momentum flux quantity
  Momentum = WeightedIntegral() #Calculate the mass average value of axial momentum flux
  QntFieldScalar('Static Pressure') #Activate the static pressure quantity
  StaticPressure = SclAverage() #Calculate the average value of static pressure at the plane
  Area = Lobes*GmtArea() #Extract the area of the plane and multiply by the number of lobes to reveal the total of a full annulus.
  T = (Momentum+StaticPressure-Pressure)*Area #Compute thrust as the sum of the momentum and pressure thrusts
  return T

def RadiusMinMax(row):
  # Computes the minimum and maximum radius of an axial plane
  # Accepts dataframe row
  # Sets two columns of the dataframe as minimum and maximum radius.
  QntFieldScalar('Radius') #Activate the radius quantity
  SelectFromProject(row['Name']+'.D1') #Activate the plane of interest
  (row['r1'],row['r2']) = QuantityRangeActiveSurfaces() #Save the min and max as r1 and r2 in the dataframe.

def PitchwisePlot(row,N,P,Q):
  # Extracts data on circumferential lines for computing the pitchwise average in another python script
  # Accepts dataframe row, integer N as index, Path string P.
  # Outputs data files with profile data at each radius between r1 and r2 as defined by N.
  P=P+'/'+Q+'/'+row['Name']+'/'
  CheckDirectory(P)
  ViewOpenRTZ(-1,1,-1,1) #Open a cylindrical coordinate view of the project
  QntFieldScalar(Q) #Activate the Quantity so we can calculate the pitchwise average Quantity at these planes
  SelectFromProject(row['Name']+'.D1') #Activate plane of interest
  r = row['r1'] #Set the initial radius for extraction
  step = (row['r2']-row['r1'])/(N) #Calculate the step size to allow N steps from r1 to r2
  for i in range(1,N):
    RprSection(r,1,0.4,r,2,0.4,0,0,-1 ,'',1 ,'',0) #Produce a plot of the Quantity in cyclindrical coordinates
    PlotFctOfTheta() #Adjust the plot to have an independent axis of theta
    PlotCurveOutput(P+`i`+'.dat') #Output the plot to a data file
    DeletePlot() #Remove the plot to save memory
    r=r+step #Index the radius to the next value and continue until reaching the outer edge
  ViewClose() #Close the cylindrical coordinate view
  ViewActivate(PName+'.run:1')

def Reynolds(Plane,l):
  SelectFromProject(Plane)
  QntFieldScalar('Dynamic viscosity')
  mu = SclAverage()
  QntFieldScalar('Magnitude of V')
  v = WeightedIntegral()
  QntFieldScalar('Density')
  rho = SclAverage()
  Re = rho*v*l/mu
  return Re
#endregion

import pandas as pd
import numpy as np
#region DEFINE CONSTANTS

Speed = 'High' #Flag as high speed or low speed (A second script has the low speed version. For setting ambient conditions.)
PName = GetProjectName() #Sets a string variable as the current CFView project name. Good for  creating specific directories.

Path = pd.Series() #initialize the series that contains the various path strings for directories
Path['Root'] = 'D:/Alex/OneDrive/PhD/Working/Wright_Thesis/' #A root path which can be used to direct to a separate drive or folder while maintaining overall architecture
Path['Script'] = Path['Root']+'Scripts' #Where the cfview macros are saved (deprecated)
Path['Analysis'] = Path['Root']+'Data/Analysis/' #The general analysis data directory
Path['Quant'] = Path['Root']+'Data/Analysis/'+PName +'/QuantitativeData/' #Project specific directory for quantitative data output
Path['ContourText'] = Path['Root'] + 'Data/Analysis/'+PName +'/Contours/TextFiles/' #Project specific directory for planar data
Path['ContourImage'] = Path['Root'] + 'Data/Analysis/'+PName +'/Contours/Images/' #Project specific directory for contour plots
Path['CGNS'] = Path['Root'] + 'Data/Analysis/'+PName +'/CGNS/' #Project specific directory for CGNS files
Path['Supp'] = Path['Root'] + 'Data/Analysis/'+PName +'/Supplemental/Images/' #Project specific directory for supplemental images (mesh examples, geometry, boundary conditions)
Path['Pitchwise'] = Path['Root'] + 'Data/Analysis/'+PName +'/PitchwiseData/' #Project specific directory for pitchwise data files.
```

```

Path.apply(CheckDirectory) #Run the function to make sure these directories exist

#True Constants
Lobes = 12 #Number of lobes in the mixer
Dh = 0.1624 #m Equivalent Diameter of Mixer
PlaneMixer = 0.651 #Set axial value for Mixer Outlet Plane as measured on Unscalloped Mixer
PlaneNozzle = 0.895 #Set axial value for Nozzle Outlet Plane.

PlanesZ = pd.DataFrame() #Initialize the Axial Planes Dataframe
PlanesZ['Z']=[-0.55, -0.50, -0.45, -0.40, -0.30, -0.20, -0.10, 0.0,...
0.125, 0.25, 0.375, 0.5, 0.625, 0.75, 0.875, 1.0, 1.25, 1.5, 2.0, 2.5, 3.0, 4.0, 5.0, 6.0, 7.0] #Normalized Z values based on the mixer exit plane being 0 and the nozzle exit plane being 1.0
PlanesZ['realZ'] = PlaneMixer + PlanesZ['Z']*(PlaneNozzle-PlaneMixer) #Compute the actual Z values for plane creation
PlanesZ['Name']=['Z_-0_55', 'Z_-0_50', 'Z_-0_45', 'Z_-0_40', 'Z_-0_30', 'Z_-0_20', 'Z_-0_10', 'Z_0_0', 'Z_0_125', 'Z_0_25', 'Z_0_375', 'Z_0_5', 'Z_0_625', 'Z_0_75', 'Z_0_875', 'Z_1_0', 'Z_1_25', 'Z_1_5', 'Z_2_0', 'Z_2_5', 'Z_3_0', 'Z_4_0', 'Z_5_0', 'Z_6_0', 'Z_7_0'] #Strings for naming the planes when they're created.

PlanesRef = pd.DataFrame() #Initialize the reference plane dataframe
PlanesRef['Name'] = ['CoreRef','BypassRef','CoreMixerInlet','BypassMixerInlet','CoreSwirlerInlet','CoreSwirlerOutlet'] #Strings for naming the planes when they're created
PlanesRef['Z'] = [0.4, 0.4, 0.52, 0.52, 0.32, 0.395] #Axial locations for the planes
PlanesRef['Y'] = [0.08, 0.15, 0.08, 0.15, 0.08, 0.08] #Y values so that the planes are cut and saved in the correct region of the domain, Core vs Bypass

PlanesMeridional = pd.DataFrame() #Initialize the meridional plane dataframe
```

```
PlanesMeridional[’Name’] = [’MeridionalCrest’,’MeridionalValley’,’MeridionalScallop1’,’MeridionalScallop2’] #Strings for naming the planes when they’re created
PlanesMeridional[’nX’] = [-3.732052,1.0,7.59575411,-7.59575411] #Plane normals to set the right angle of the meridional plane
PlanesMeridional[’nY’] = [1.0,0.0,1.0,1.0] #Plane normals to set the right angle of the meridional plane

Contours = [’CPo’, ’CPs’, ’Cw_s’, ’Cw_a’, ’Mach Number’, ’Swirl’, ’CV’, ’CM’, ’CTo’, ’CTo_2’, ’CD’, ’CTKE’, ’Static Pressure Mixing Index’, ’Total Pressure Mixing Index’, ’Thermal Mixing Index’, ’Density Mixing Index’] #A list that identifies what contours will be exported for further analysis, both contour plots and statistical data.
Vectors = [’Vxyz’,’Momentum’,’Vorticity vector’] #Vectors to be exported as text data on each plane of interest.

AmbientValues = pd.DataFrame(index = [’Low’, ’High’], columns = [’Pressure’,’Temperature’,’Density’]) #Initialize tha ambient condition values dataframe
AmbientValues.loc[’Low’] = [101325,293,1.2] #Set the low speed conditions with atmospheric pressure, temperature and density
AmbientValues.loc[’High’] = [18800,223,0.294] #Set the high speed conditions with atmospheric pressure, temperature and density at cruise altitude
#endregion

Ambient = pd.Series() #Initialize Ambient Conditions Series

if Speed == ’Low’:
  Ambient = AmbientValues.loc[’Low’] #For Low Speed, set to the Low Row of AmbientValues
elif Speed == ’High’:
  Ambient = AmbientValues.loc[’High’] #For High Speed set to the High Row of AmbientValues

#region CREATE CUTTING PLANES
```

```
PlanesMeridional.apply(CutPlaneMeridion,axis=1) #Apply the CutPlaneMeridion function to each row of the Meridional dataframe.
PlanesZ.apply(CutPlaneAxial,axis=1) #Apply the CutPlaneAxial function to each row of the Axial dataframe.
PlanesRef.apply(CutPlaneRef,axis=1) #Apply the CutPlaneRef function to each row of the Ref dataframe.

SelectFromProjectRegExp(’’) #Select Every plane in the project
GmtBoundaryVisibility(0) #Turn off boundaries to prepare for the contour plot exports
DeleteAll() #Just to be sure everything is cleared from the project view.
#endregion

#region CALCULATE NEW QUANTITIES FOR REDUCTION
Ref = pd.DataFrame(index = [’Total Pressure’,’Static Pressure’,’Velocity’,’Density’,’Total Temperature’, ’Momentum’], columns=[’Core’,’Bypass’,’Mean’]) #Initialize the reference values dataframe.

Ref.loc[’Total Pressure’]  = ReferenceValsWeighted(’Total Pressure’)  #Calculate the mass flow weighted reference values and populate the Total Pressure Row
Ref.loc[’Static Pressure’] = ReferenceVals(’Static Pressure’) #Calculate the basic reference values and populate the Static Pressure Row

# Assign Total Pressure and Static Pressure Reference Values to variables for simpler syntax
TPMean = Ref.loc[’Total Pressure’,’Mean’]
TPCore = Ref.loc[’Total Pressure’,’Core’]
TPBypass = Ref.loc[’Total Pressure’,’Bypass’]
SPMean = Ref.loc[’Static Pressure’,’Mean’]
SPCore = Ref.loc[’Static Pressure’,’Core’]
SPBypass = Ref.loc[’Static Pressure’,’Bypass’]

#Mass Averaged Total Pressure Loss Coefficient CoreReference Plane
```

```
QntFieldDerived(0 ,’Y’ ,’(’+‘TPMean‘ +’-Total Pressure)/(’ + ‘TPMean
    ‘ + ’-’ + ‘SPMean‘ + ’)’ ,’’ ,’0’)

#Mass Averaged Total Pressure Coefficient CoreReference Plane
QntFieldDerived(0 ,’CPo’ ,’(Total Pressure - ’+‘SPMean‘ +’)/(’ + ‘
    TPMean‘ + ’-’ + ‘SPMean‘ + ’)’ ,’’ ,’0’)

#Mass Averaged Total Pressure Coefficient BypassReference Plane
QntFieldDerived(0 ,’CPs’ ,’(Static Pressure - ’+‘SPMean‘ +’)/(’ + ‘
    TPMean‘ + ’-’ + ‘SPMean‘ + ’)’ ,’’ ,’0’)

#Mass Averaged Static Pressure Coefficient CoreReference Plane
QntFieldDerived(0 ,’CPo Bypass’ ,’(Total Pressure - ’+‘SPBypass‘ +’)
    /(’ + ‘TPBypass‘ + ’-’ + ‘SPBypass‘ + ’)’ ,’’ ,’0’)

#Mass Averaged Static Pressure Coefficient BypassReference Plane
QntFieldDerived(0 ,’CPs Bypass’ ,’(Static Pressure - ’+‘SPBypass‘ +’
    )/(’ + ‘TPBypass‘ + ’-’ + ‘SPBypass‘ + ’)’ ,’’ ,’0’)

#Mass Averaged Static Pressure Coefficient CoreReference Plane
QntFieldDerived(0 ,’CPo Core’ ,’(Total Pressure - ’+‘SPCore‘ +’)/(’
    + ‘TPCore‘ + ’-’ + ‘SPCore‘ + ’)’ ,’’ ,’0’)

#Mass Averaged Static Pressure Coefficient BypassReference Plane
QntFieldDerived(0 ,’CPs Core’ ,’(Static Pressure - ’+‘SPCore‘ +’)/(’
     + ‘TPCore‘ + ’-’ + ‘SPCore‘ + ’)’ ,’’ ,’0’)

#Calculate Swirl Angle
QntFieldDerived(0 ,’Vt’ ,’(x*Vxyz_Y - y*Vxyz_X)/sqrt(x*x+y*y)’ ,’’ ,
    ’’ ,’m/s’)
QntFieldDerived(0 ,’Vr’ ,’(x*Vxyz_X + y*Vxyz_Y)/sqrt(x*x+y*y)’ ,’’ ,
    ’’ ,’m/s’)

QntFieldDerived(0 ,’Vxyz_Z’ ,’Vxyz_Z’ ,’’ ,’’ ,’m/s’)
QntFieldDerived(0 ,’Swirl’ ,’abs(-180*atan2(Vt,Vxyz_Z)/pi)’ ,’’ ,’0’
    )

#Calculate Axial Velocity Percentage of Overall Velocity Magnitude
```

```
QntFieldDerived(0 ,'Axial Velocity' ,'abs(Vxyz_Z/Magnitude of V)*100' ,'' ,'m/s')

# Calculate the Turbulent Viscosity
QntFieldDerived(0 ,'Turbulent Viscosity' ,'Dynamic viscosity * Turbulent Viscosity (Mut/Mu)' ,'','','')

#Calculate Vorticty and Vorticity Coefficients
#Initialize radial and tangential vorticity.
QntFieldDerived(0 ,'Vorticity vector_R' ,'(x*Vorticity vector_X + y*Vorticity vector_Y)/sqrt(x*x+y*y)' ,'' ,'' ,'1/s')
QntFieldDerived(0 ,'Vorticity vector_T' ,'(x*Vorticity vector_Y - y*Vorticity vector_X)/sqrt(x*x+y*y)' ,'' ,'' ,'1/s')
QntFieldDerived(0 ,'Streamwise Vorticity' ,'Vorticity vector_Z' ,'' ,'1/s')
QntFieldDerived(0 ,'Azimuthal Vorticity' ,'sqrt(Vorticity vector_R*Vorticity vector_R+Vorticity vector_T*Vorticity vector_T)' ,'' ,'1/s')

#Momentum Flux Vector
QntFieldDerived(2 ,'Momentum' ,'Density*Vxyz_Z*Vxyz_X' ,'Density*Vxyz_Z*Vxyz_Y' ,'Density*Vxyz_Z*Vxyz_Z')
QntFieldDerived(0 ,'Momentum_Z' ,'Momentum_Z' ,'' ,'' ,'')
QntFieldDerived(0 ,'Magnitude of Momentum' ,'sqrt(Momentum_X*Momentum_X +Momentum_Y*Momentum_Y +Momentum_Z*Momentum_Z)' ,'' ,'' ,'')

# Assign reference values for other coefficient calculations
Ref.loc['Velocity'] = ReferenceValsWeighted('Vxyz_Z')
Ref.loc['Density'] = ReferenceValsWeighted('Density')
Ref.loc['Total Temperature'] = ReferenceValsWeighted('Total Temperature')
Ref.loc['Static Temperature'] = ReferenceValsWeighted('Static Temperature')
Ref.loc['Momentum'] = ReferenceValsWeighted('Magnitude of Momentum')
Ref.loc['Viscosity'] = ReferenceValsWeighted('Dynamic viscosity')

VCore = Ref.loc['Velocity','Core']
TTCore = Ref.loc['Total Temperature','Core']
```

```
TTMean = Ref.loc['Total Temperature','Mean']
TSCore = Ref.loc['Static Temperature','Core']
DCore = Ref.loc['Density','Core']
MCore = Ref.loc['Momentum','Core']
MuCore = Ref.loc['Viscosity','Core']
VBypass = Ref.loc['Velocity','Bypass']
TTBypass = Ref.loc['Total Temperature','Bypass']
DBypass = Ref.loc['Density','Bypass']
MBypass = Ref.loc['Momentum','Bypass']
MuBypass = Ref.loc['Viscosity','Bypass']
#Calculate Normalized Axial Velocity
QntFieldDerived(0 ,'CV' ,'Vxyz_Z/'+`VCore` ,'' ,'0')

#Calculate Vorticity Coefficients
QntFieldDerived(0 ,'Cw_s' ,'(Streamwise Vorticity*' +`Dh` + ')/(' + `VCore` +')' ,'' ,'0')
QntFieldDerived(0 ,'Cw_a' ,'(Azimuthal Vorticity*' +`Dh` + ')/(' + `VCore` +')' ,'' ,'0')

#Calculate Nondimensionalized Coefficients for other Quantities
QntFieldDerived(0 ,'CTo' ,'(Total Temperature - '+ `Ambient.Temperature` +') / ('+`TTCore`+' - '+`Ambient.Temperature`+')' ,'' ,'0') #Total Temperature
QntFieldDerived(0 ,'CTo_2' ,'(Total Temperature - '+ `TSCore` +') / ('+`TTCore`+' - '+`TSCore`+')' ,'' ,'0') #Total Temperature

QntFieldDerived(0 ,'CM' ,'Magnitude of Momentum / '+`MCore` ,'' ,'0') #Momentum Flux
QntFieldDerived(0 ,'CD' ,'Density / '+`DCore` ,'' ,'0') #Density
QntFieldDerived(0 ,'CTKE' ,'k / pow('+`VCore`+',2)' ,'' ,'0') #Turbulent Kinetic Energy

#Calculate Radius
QntFieldDerived(0, 'Radius', 'sqrt(pow(x,2)+pow(y,2))','','0')

## Mixing Index of Static Pressure
QntFieldDerived(0 ,'Phi_s' ,'(Static Pressure - '+`Ambient.Pressure` +')/(' + `SPCore` + '-' + `Ambient.Pressure` + ')' ,'' ,'0')
QntFieldDerived(0 ,’Static Pressure Mixing Index’ ,’(Phi_s*Phi_s)’ ,’’ ,’0’)

## Mixing Index of Total Pressure
QntFieldDerived(0 ,’Phi_o’ ,’(Total Pressure - ’+‘Ambient.Pressure‘ +’)/(’ + ‘TPCore‘ + ’-’ + ‘Ambient.Pressure‘ + ’)’ ,’’ ,’0’)
QntFieldDerived(0 ,’Total Pressure Mixing Index’ ,’(Phi_o*Phi_o)’ ,’’ ,’0’)

## Mixing Index of Temperature
QntFieldDerived(0 ,’Phi_t’ ,’(Total Temperature - ’+‘Ambient.Temperature‘ +’)/(’ + ‘TTMean‘ + ’-’ + ‘Ambient.Temperature‘ + ’)’ ,’’ ,’0’)
QntFieldDerived(0 ,’Thermal Mixing Index’ ,’(Phi_t*Phi_t)’ ,’’ ,’0’)

## Mixing Index of Density
QntFieldDerived(0 ,’Phi_rho’ ,’(Density - ’+‘Ambient.Density‘ +’)/(’ + ‘DCore‘ + ’-’ + ‘Ambient.Density‘ + ’)’ ,’’ ,’0’)
QntFieldDerived(0 ,’Density Mixing Index’ ,’(Phi_rho*Phi_rho)’ ,’’ ,’0’)
#endregion

#region EXPORT CONTOUR DATA
for Q in Contours:
  QntFieldScalar(Q) #Activate Quantity from list
  SetRange(Q) #Pass Quantity to Function to set the range for contour plotting
  CheckDirectory(Path[’ContourText’]+Q) #Create the directory for the specific quantity to hold each plane text data
  CheckDirectory(Path[’ContourImage’]+Q) #Create the directory for the specific quantity to hold each plane image

  PlanesZ.apply(ContourExport, axis=1, Quantity=Q, P=Path[’ContourImage’]+Q+’/’, Camera=’Axial’) #Export contour plots on axial Z planes
  PlanesRef.apply(ContourExport, axis=1, Quantity=Q, P=Path[’ContourImage’]+Q+’/’, Camera=’Zoom’) #Export contour plots on reference planes
  PlanesMeridional.apply(ContourExport, axis=1, Quantity=Q, P=Path['ContourImage']+Q+'/', Camera='Meridional') #Export contour plots on Meridional planes
  PlanesZ.apply(PlaneTextOut, axis=1, P=Path['ContourText']+Q+'/') #Export plane data as text file
  PlanesRef.apply(PlaneTextOut, axis=1, P=Path['ContourText']+Q+'/')
  PlanesMeridional.apply(PlaneTextOut, axis=1, P=Path['ContourText']+Q+'/')

for V in Vectors:
  CheckDirectory(Path['ContourText']+V) #Creat the directory for the specific vector quantity to hold each plane data as text files
  QntFieldVector(V) #Activate the vectory quantity
  PlanesZ.apply(PlaneTextOut, axis=1, P=Path['ContourText']+V+'/') #Export the vector data of axial planes in text files
  PlanesMeridional.apply(PlaneTextOut, axis=1, P=Path['ContourText']+V+'/') #Export the vector data of meridional planes in text files

Export Contour on Mixer Inner Lobe
DeleteAll() #Clear anything left over from contour plotting
SetCamera(4.79575e-005,0.40665,0.590132,4.79575e-005,0.0140887,...
0.590132,0.0668182,0,-2.98023e-008,0.157025,0.0159084) #Adjust camera to capture the core side of the mixer
SelectFromProject('solidMixerID Solid') #Activate the inner surface of the mixer
GmtBoundaryVisibility(1) #Turn on the boundary lines
QntFieldScalar('CPs Core') #Activate the Static Pressure Coefficient
RprRangeIn(-1,1) #Set the range
SclContourSmooth() #Activate the contour plot
UpdateColormapHot() #Change to divergent colormap
Print(8,0,1,1,100,1920,1080,1 ,Path['ContourImage']+'MixerLoading.png' ,'DRAFT',1,0,2) #Save to image file
GmtBoundaryVisibility(0) #Turn off Mixer boundary lines

# Save Contour Data to CGNS Format for Paraview plotting.
SelectFromProjectRegExp('')
```

```
CGNSSaveSurfaces(Path['CGNS']+PName+'.cgns' ,'Surfaces' ,'Static Temperature' ,'Total Temperature' ,'Static Pressure' ,'Total Pressure' ,'Static enthalpy' ,'Density' ,'Magnitude of V' ,'Mach Number' ,'k' ,'Production' ,'Radius' ,'Y' ,'CPo' ,'CPs' ,'CPo Bypass' ,'CPs Bypass' ,'CPo Core' ,'CPs Core' ,'Vt' ,'Vxyz_Z' ,'Swirl' ,'Axial Velocity' ,'Vorticity vector_R' ,'Vorticity vector_T' ,'Streamwise Vorticity' ,'Azimuthal Vorticity' ,'Momentum_Z' ,'Magnitude of Momentum' ,'CV' ,'Cw_s' ,'Cw_a' ,'CTo' ,'CM' ,'CD' ,'CTKE' ,'Phi_s' ,'Pressure Mixing Index' ,'Phi_t' ,'Thermal Mixing Index' ,'Phi_rho' ,'Density Mixing Index' ,'Vorticity vector' ,'Vxyz' ,'Momentum')
endregion

region EXPORT SUPPLEMENTAL IMAGES
RprColormap(0) #Remove the colormap range key from the screen
SelectFromProject() #Deselect Everyplane
DeleteAll() #Remove anything in the view that is left from contour export
SetCamera(-6.26953,1.49312,5.95972,-0.155842,0.538826,1.02257,0.107232,...
0.992479,-0.0590492,3.16641,1.33089) #Set the camera for isometric viewing angle

# Set Solid Boundaries
SelectFromProjectRegExp('solid') #Select all surfaces with 'solid' in the name
RenderGouraud() #Render the surface
UpdateMaterial(0,0,0.6,0,0,1,4,0,0,0,1,1 ,'metal - polished',0.85) #Change the colour
SelectFromProject() #Unselect all surfaces

# Set Inlet Boundary
SelectFromProject('Inlets') #Select the Inlets group
RenderGouraud()
UpdateMaterial(120,1,1,0,0,1,4,0,0,0,1,0 ,'metal - polished',0.85)
SelectFromProject()

# Set Periodic Boundary
```

```
SelectFromProject('MeridionalCrest.D1') #Select the crest line meridional plane to represent the periodic boundary
RenderGouraud()
UpdateMaterial(300,1,1,0,0,1,4,0,0,0,1,0 ,'metal - polished',0.85)
SelectFromProject()

# Set Outlet Boundary
SelectFromProject('outlet Outlet') #Select the outlet
RenderGouraud()
UpdateMaterial(0,1,1,0,0,1,4,0,0,0,1,0 ,'metal - polished',0.85)
SelectFromProject()

# Set External Boundary
SelectFromProjectRegExp('External') #Select the External boundary
UpdateMaterial(0,0,0,0,0,1,4,0,0,0,1,0 ,'metal - polished',0.85)
SelectFromProject()

Print(8,0,1,1,100,1920,1080,1 ,Path['Supp']+'BoundaryCondition.png','DRAFT',1,0,2) #Save the boundary condition image

SelectFromProject('Inlets','MeridionalCrest','outlet Outlet','solidExternal Solid') #Select all but the solid surfaces of the actual test section
RenderGouraud() #Undo the render
ViewZoomAll(1) #Zoom in on remaining surfaces
Print(8,0,1,1,100,1920,1080,1 ,Path['Supp']+'Geometry.png' ,'DRAFT',1,0,2) #Save the geometry image

#Remove Nozzle
SelectFromProject()
SelectFromProjectRegExp('Nozzle')
RenderGouraud()
# Set Camera for Mixer Capture
SetCamera(-0.674267,0.184512,1.13953,-0.341691,0.1326,0.870951,0.107232,...
0.992479,-0.0590492,0.172248,0.142007)
Print(8,0,1,1,100,1920,1080,1 ,Path['Supp']+'Mixer.png' ,'DRAFT',1,0,2)
```

```

#Remove Mixer
SelectFromProject()
SelectFromProjectRegExp('Mixer')
RenderGouraud()
# Set Camera for Swirler Capture
SetCamera(-0.624603,0.179663,0.859408,-0.457031,0.153506,0.724084,...
0.107232,0.992479,-0.0590492,0.0867888,0.0642025)
Print(8,0,1,1,100,1920,1080,1 ,Path['Supp']+'Swirler.png' ,'DRAFT',1,0,2)

# Capture Mixer Only
SelectFromProject()
GmtRepetitionNumber(Lobes-1) #Set the number of repeitions to render
GmtRepetitionSet(1) #Activate geomertry repeptition
DeleteAll() #Delete all other rendering
SelectFromProjectRegExp('Centrebody')
SelectFromProjectRegExp('Deswirl')
SelectFromProjectRegExp('solidMixer') #Select mixer related surfaces
RenderGouraud() #Render the mixer, centrebody and deswirler
UpdateMaterial(0,0,0.6,0,0,1,4,0,0,0,1,1 ,'metal - polished',0.85) #Change color
SetCamera(-0.351747,0.184402,1.62019,-0.136275,0.0677655,0.954162,...
0.119986,0.983764,-0.133462,0.283864,0.307213)
RprColormap(0) #Remove the range key
Print(8,0,1,1,100,1920,1080,1 ,Path['Supp']+'Mixer_12.png' ,'DRAFT',1,0,2) #Save the image of the full mixer render
GmtRepetitionSet(0) #Turn off repetition

DeleteAll() #Remove all rendering
SelectFromProject() #Unselect all surfaces

# Printing Mesh Examples
SelectFromProjectRegExp('solid') #Select all solid surfaces
RenderGouraud() #Render them
UpdateMaterial(0,0,0.6,0,0,1,4,0,0,0,1,1 ,'metal - polished',0.85) #Change the color
```

```
SelectFromProject('solidExternal Solid') #Select the external boundary surface
RenderGouraud() #Turn off its rendering
SetCamera(-1.92119,0.423687,1.99922,-0.408494,0.187568,0.777606,...
0.107232,0.992479,-0.0590492,0.783465,0.312371)
SelectFromProject('MeridionalValley.D1') #Activate the valley meridional plane
GmtGridVisibility(1) #Turn on the mesh grid visibility
Print(8,0,1,1,100,1920,1080,1 ,Path['Supp']+'Valley_Mesh_1.png' ,'DRAFT',1,0,2) #Save the image
SetCamera(-0.674267,0.184512,1.13953,-0.341691,0.1326,0.870951,...
0.107232,0.992479,-0.0590492,0.172248,0.142007) #Zoom in
Print(8,0,1,1,100,1920,1080,1 ,Path['Supp']+'Valley_Mesh_2.png' ,'DRAFT',1,0,2) #Save another image
SetCamera(-0.603463,0.14777,1.09332,-0.338799,0.106458,0.879586,...
0.107232,0.992479,-0.0590492,0.137076,0.108836) #Zoom in again
Print(8,0,1,1,100,1920,1080,1 ,Path['Supp']+'Valley_Mesh_3.png' ,'DRAFT',1,0,2) #Save another image
GmtGridVisibility(0) #Turn off the mesh grid visibility

# Do the same for the crest and scallop meridional planes
SetCamera(-1.92119,0.423687,1.99922,-0.408494,0.187568,0.777606,...
0.107232,0.992479,-0.0590492,0.783465,0.312371)
SelectFromProject('MeridionalCrest.D1')
GmtGridVisibility(1)
Print(8,0,1,1,100,1920,1080,1 ,Path['Supp']+'Crest_Mesh_1.png' ,'DRAFT',1,0,2)
SetCamera(-0.674267,0.184512,1.13953,-0.341691,0.1326,0.870951,...
0.107232,0.992479,-0.0590492,0.172248,0.142007)
Print(8,0,1,1,100,1920,1080,1 ,Path['Supp']+'Crest_Mesh_2.png' ,'DRAFT',1,0,2)
SetCamera(-0.603463,0.14777,1.09332,-0.338799,0.106458,0.879586,...
0.107232,0.992479,-0.0590492,0.137076,0.108836)
Print(8,0,1,1,100,1920,1080,1 ,Path['Supp']+'Crest_Mesh_3.png' ,'DRAFT',1,0,2)
GmtGridVisibility(0)

SetCamera(-1.92119,0.423687,1.99922,-0.408494,0.187568,0.777606,...
0.107232,0.992479,-0.0590492,0.783465,0.312371)
```

```
SelectFromProject(’MeridionalScallop1.D1’)
GmtGridVisibility(1)
Print(8,0,1,1,100,1920,1080,1 ,Path[’Supp’]+’Scallop_Mesh_1.png’ ,’DRAFT’,1,0,2)

SetCamera(-0.674267,0.184512,1.13953,-0.341691,0.1326,0.870951,...
0.107232,0.992479,-0.0590492,0.172248,0.142007)
Print(8,0,1,1,100,1920,1080,1 ,Path[’Supp’]+’Scallop_Mesh_2.png’ ,’DRAFT’,1,0,2)

SetCamera(-0.603463,0.14777,1.09332,-0.338799,0.106458,0.879586,...
0.107232,0.992479,-0.0590492,0.137076,0.108836)
Print(8,0,1,1,100,1920,1080,1 ,Path[’Supp’]+’Scallop_Mesh_3.png’ ,’DRAFT’,1,0,2)
GmtGridVisibility(0)
#endregion

#region DATA REDUCTION AND CSV WRITING
Outputs = list(Contours) #Copy the list of contours from above
# Outputs.append(’Y’) #Add Total Pressure Loss Coefficient to the list.
for x in Outputs:
  WeightedOutput = PlanesZ.apply(StatsWeighted, axis=1, Quantity=x) #Apply the StatsWeighted function to each Z Plane and save them into a dataframe called WeightedOutput
  # WeightedOutput[’Mean’] = np.sqrt((WeightedOutput[’Mean’])) # Apply Square Root to the Weighted Average to complete the Mixing Index calculation.
  WeightedOutput.set_index(’Z’).to_csv(Path.Quant+x+’_Weighted.csv’) #Adjust the index of the dataframe to be the normalized Z values and save to a csv file.

  StatsOutput = PlanesZ.apply(Stats, axis=1, Quantity=x)  #Apply the Stats function to each Z Plane and save them into a dataframe called StatsOutput
  StatsOutput.set_index(’Z’).to_csv(Path.Quant+x+’.csv’)  #Adjust the index of the dataframe to be the normalized Z values and save to a csv file.

```

```
Circulation = PlanesZ.apply(CirculationCal, axis=1, VCore=VCore, Dh=Dh) #Apply the CirculationCal function to each Z plane and save in a dataframe called Circulation
Circulation.set_index('Z').to_csv(Path.Quant+'Circulation.csv') #Adjust the index of the dataframe to be the normalized Z values and save to a csv file

Performance = pd.DataFrame(columns=['Core Thrust','Bypass Thrust','Nozzle Thrust','Thrust Coefficient','Nozzle Loss']) #Initialize the dataframe for the bulk performance quantities of the simulation
Performance.at[PName,'Core Thrust']= ThrustCalc('CoreRef.D1',Ambient.Pressure,Lobes) #Calculate the Core Thrust at the Core Reference Plane
Performance['Bypass Thrust'] = ThrustCalc('BypassRef.D1',Ambient.Pressure,Lobes) #Calculate the Bypass Thrust at the Bypass Reference Plane
Performance['Nozzle Thrust'] = ThrustCalc('Z_1_0.D1',Ambient.Pressure,Lobes) #Calculate the Actual Engine thrust at the Nozzle Exit Plane
Performance['Thrust Coefficient'] = 100*(Performance['Nozzle Thrust']/(Performance['Core Thrust']+Performance['Bypass Thrust'])) #Calculate the Thrust Coefficient by dividing the actual thrust by the sum of the thrusts at the reference plane

#Calculate the Total Pressure Loss Through the Nozzle
QntFieldScalar('Total Pressure') #Activate the Total Pressure quantity
SelectFromProject('Z_1_0.D1') #Activate the nozzle exit plane
TPNozzle = WeightedIntegral() #Calculate the mass average total pressure at the nozzle exit plane
Performance['Nozzle Loss'] = 100*((TPMean-TPNozzle)/(TPMean-SPMean)) #Calculation the Loss Coefficient at this location

QntFieldScalar('CV') #Activate the Normalized Axial Velocity Quantity
SelectFromProject('Z_1_0.D1') #Activate the Nozzle Exit Plane

```

```
Performance['Nozzle Velocity'] = WeightedIntegral() #Extract the mass averaged value of the normalized axial velocity

#Save the Performance dataframe to a csv. Don't rewrite the headings if the file already exists.
f = Path.Analysis+'Performance.csv'
if not os.path.isfile(f):
  Performance.to_csv(f, mode='a', header=True)
else:
  Performance.to_csv(f, mode='a', header=False)
endregion

region PITCHWISE AVERAGE EXTRACTION
PitchwiseQuantity = ['Swirl','CM','CV','CD','CTo']
Pitchwise = pd.DataFrame(columns = ['Name','r1','r2']) #Initialize the dataframe for the Planes that we want to extract pitchwise information for.
Pitchwise['Name'] = ['CoreSwirlerInlet', 'CoreSwirlerOutlet', 'CoreMixerInlet', 'Z_0_0', 'Z_0_125', 'Z_0_25', 'Z_0_375', 'Z_0_5', 'Z_0_625', 'Z_0_75', 'Z_0_875', 'Z_1_0'] #Indicate the planes of interest
n=101 #Set the number of pitchwise planes to extract from the data
Pitchwise.apply(RadiusMinMax, axis=1) #Apply this function to calculate the minimum and maximum radii for each plane in the list.
Pitchwise.to_csv(Path['Pitchwise']+'Radius.csv',index=False)
#endregion

#region CHAPTER 9 DATA EXTRACTION
Ch9 = ['Mach Number', 'CV', 'CTo', 'Turbulent Viscosity', 'CD', 'CM', 'CPo', 'CPs']
SelectFromProject('CoreRef.D1')
Chapter9Core = pd.DataFrame(columns = Ch9)
for Q in Ch9:
  QntFieldScalar(Q)
  Chapter9Core.at[PName,Q] = WeightedIntegral()
Chapter9Core.at[PName,'CPs'] = SclAverage()
Chapter9Core.at[PName,'Reynolds Number'] = DCore*VCore*Dh/MuCore

```

```
SelectFromProject('BypassRef.D1')
Chapter9Bypass = pd.DataFrame(columns = Ch9)
for Q in Ch9:
  QntFieldScalar(Q)
  Chapter9Bypass.at[PName,Q] = WeightedIntegral()
Chapter9Bypass.at[PName,'CPs'] = SclAverage()
Chapter9Bypass.at[PName,'Reynolds Number'] = DBypass*VBypass*Dh/MuBypass

SelectFromProject('Z_0_0.D1')
QntFieldScalar('Vr')
[Vrmin,Vrmax] = QuantityRangeActiveSurfaces()

Chapter9Ratio = pd.DataFrame()
Chapter9Ratio = Chapter9Bypass.div(Chapter9Core)

Chapter9 = pd.DataFrame()
Chapter9 = Chapter9Core.join(Chapter9Bypass, lsuffix = '_Core', rsuffix='_Bypass')
Chapter9.at[PName,'Vrmin'] = Vrmin
Chapter9.at[PName,'Vrmax'] = Vrmax
Chapter9 = Chapter9.join(Chapter9Ratio, lsuffix = '', rsuffix='_Ratio')
# Save the CH 9 dataframe to a csv. Don't rewrite the headings if the file already exists.
f = Path.Analysis+'Chapter9.csv'
if not os.path.isfile(f):
  Chapter9.to_csv(f, mode='a', header=True)
else:
  Chapter9.to_csv(f, mode='a', header=False)

#endregion

# Quit() #Close CFView entirely to free memory
```

A.2 Figure Creation in Paraview

Axial Contours

```
def CheckDirectory(P):
    # Checks that the argument P is a directory. If it doesn’t exist, it will create the directory and any folders above.
    import os
    if os.path.isdir(P)==False:
        os.makedirs(P)

def BaseTransform(Name,In,Translate,Rotate):
    Name = Transform(Input=In)
    Name.Transform.Translate = Translate
    Name.Transform.Rotate = Rotate


#### import the simple module from the paraview
from paraview.simple import *
import numpy as np
from datetime import date
import os
today = date.today().strftime("%Y-%m-%d")

ReadPath = ’T:/PhD_CGNS/CGNS/’
F=[]
for file in os.listdir(ReadPath):
    if file.endswith("Scalloped_LowSpeed.cgns"):
        file = file[:-5]
        F.append(file)


Resolution = [1940, 1000]
FontSize = 25
ColorBarWidth = 40

```

```
Names = ['Z_-0_55', 'Z_-0_50', 'Z_-0_45', 'Z_-0_40', 'Z_-0_30', 'Z_-0_20', 'Z_-0_10', 'Z_0_0', 'Z_0_125', 'Z_0_25', 'Z_0_375', 'Z_0_5', 'Z_0_625', 'Z_0_75', 'Z_0_875', 'Z_1_0', 'Z_1_25', 'Z_1_5', 'Z_2_0', 'Z_2_5', 'Z_3_0', 'Z_4_0', 'Z_5_0', 'Z_6_0', 'Z_7_0']

# S=F[1]
for S in F:
    SavePath = 'T:/PhD_CGNS/Figures/'+today+'/'+S
    CheckDirectory(SavePath)

    # print(ReadPath+S)

    # set active view
    # SetActiveView(None)
    # Create a new 'Render View'
    renderView1 = CreateView('RenderView')
    renderView1.CameraParallelProjection = 1
    # Hide orientation axes
    renderView1.OrientationAxesVisibility = 0
    # uncomment following to set a specific view size
    renderView1.ViewSize = Resolution
    renderView1.UseLight = 0

    # create a new 'CGNS Series Reader'
    Data_CGNS = CGNSSeriesReader(FileNames=[ReadPath+S+'.cgns'])

    # Properties modified on Data_CGNS
    Data_CGNS.PointArrayStatus = ['CV','Cw_a', 'Cw_s', 'Vxyz']

    # get active source.
    clip1 = Clip(Input=Data_CGNS)

    # Properties modified on clip1
    clip1.ClipType = 'Cylinder'
    clip1.ClipType.Center = [0.0, 0.0, 0.0]
    clip1.ClipType.Axis = [0.0, 0.0, 1.0]
    clip1.ClipType.Radius = 0.2

    # create a new 'Extract Block'
    extractBlock1 = ExtractBlock(Input=clip1)
    # Properties modified on extractBlock1
    extractBlock1.BlockIndices = [17]
    # create a new 'Transform'
    transform1 = Transform(Input=extractBlock1)
    transform1.Transform.Translate = [-0.01, 0.0, 0.0]
    transform1.Transform.Rotate = [0.0, 0.0, 45.0]
    transform1Display = Show(transform1, renderView1)
    # create a new 'Angular Periodic Filter'
    angularPeriodicFilter1 = AngularPeriodicFilter(Input=transform1)
    angularPeriodicFilter1.IterationMode = 'Manual'
    angularPeriodicFilter1.NumberOfPeriods = 2
    angularPeriodicFilter1.RotationAngle = 30.0
    angularPeriodicFilter1.Axis = 'Axis Z'
    angularPeriodicFilter1.Center = [-0.01, 0.0, 0.0]
    angularPeriodicFilter1Display = Show(angularPeriodicFilter1, renderView1)
    ColorBy(angularPeriodicFilter1Display, ('POINTS', 'Cw_s'))

    Outline1 = AngularPeriodicFilter(Input=transform1)
    Outline1.IterationMode = 'Manual'
    Outline1.NumberOfPeriods = 2
    Outline1.RotationAngle = 30.0
    Outline1.Axis = 'Axis Z'
    Outline1.Center = [-0.01, 0.0, 0.0]
    Outline1Display = Show(Outline1, renderView1)
    Outline1Display.SetRepresentationType('Feature Edges')
    Outline1Display.AmbientColor = [0.0, 0.0, 0.0]
    Outline1Display.DiffuseColor = [0.0, 0.0, 0.0]

    # create a new 'Mask Points'
    maskPoints1 = MaskPoints(Input=angularPeriodicFilter1)
    maskPoints1.MaximumNumberofPoints = 20
    maskPoints1.RandomSampling = 1
    maskPoints1.OnRatio = 50
    # create a new 'Stream Tracer With Custom Source'
    streamTracerWithCustomSource1 = StreamTracerWithCustomSource(Input=angularPeriodicFilter1,
        SeedSource=maskPoints1)
```

```
 streamTracerWithCustomSource1.Vectors = ['POINTS', 'Vxyz']
 streamTracerWithCustomSource1.MaximumStreamlineLength = 0.2
 streamTracerWithCustomSource1.SurfaceStreamlines = 1
 streamTracerWithCustomSource1.ComputeVorticity = 0

 streamTracerWithCustomSource1Display = Show(streamTracerWithCustomSource1, renderView1)
 streamTracerWithCustomSource1Display.Representation = 'Surface'
 ColorBy(streamTracerWithCustomSource1Display, None)
 streamTracerWithCustomSource1Display.AmbientColor = [0.0, 0.0, 0.0]
 streamTracerWithCustomSource1Display.DiffuseColor = [0.0, 0.0, 0.0]

 # Render()
 # create a new 'Transform'
 transform2 = Transform(Input=extractBlock1)
 transform2.Transform.Translate = [0.0, 0.0, 0.0]
 transform2.Transform.Rotate = [0.0, 0.0, -15.0]
 transform2Display = Show(transform2, renderView1)
 # create a new 'Angular Periodic Filter'
 angularPeriodicFilter2 = AngularPeriodicFilter(Input=transform2)
 angularPeriodicFilter2.IterationMode = 'Manual'
 angularPeriodicFilter2.NumberOfPeriods = 2
 angularPeriodicFilter2.RotationAngle = 30.0
 angularPeriodicFilter2.Axis = 'Axis Z'
 angularPeriodicFilter2.Center = [0.0, 0.0, 0.0]
 angularPeriodicFilter2Display = Show(angularPeriodicFilter2, renderView1)
 ColorBy(angularPeriodicFilter2Display, ('POINTS', 'CV'))

 Outline2 = AngularPeriodicFilter(Input=transform2)
 Outline2.IterationMode = 'Manual'
 Outline2.NumberOfPeriods = 2
 Outline2.RotationAngle = 30.0
 Outline2.Axis = 'Axis Z'
 Outline2.Center = [0.0, 0.0, 0.0]
 Outline2Display = Show(Outline2, renderView1)
 Outline2Display.SetRepresentationType('Feature Edges')
```

```
    Outline2Display.AmbientColor = [0.0, 0.0, 0.0]
    Outline2Display.DiffuseColor = [0.0, 0.0, 0.0]
    # Render()


    # create a new 'Transform'
    transform3 = Transform(Input=extractBlock1)
    transform3.Transform = 'Transform'
    transform3.Transform.Translate = [0.01, 0.0, 0.0]
    transform3.Transform.Rotate = [0.0, 0.0, -75.0]
    transform3Display = Show(transform3, renderView1)
    # create a new 'Angular Periodic Filter'
    angularPeriodicFilter3 = AngularPeriodicFilter(Input=transform3)
    angularPeriodicFilter3.IterationMode = 'Manual'
    angularPeriodicFilter3.NumberOfPeriods = 2
    angularPeriodicFilter3.RotationAngle = 30.0
    angularPeriodicFilter3.Axis = 'Axis Z'
    angularPeriodicFilter3.Center = [0.01, 0.0, 0.0]
    angularPeriodicFilter3Display = Show(angularPeriodicFilter3,
   renderView1)
    ColorBy(angularPeriodicFilter3Display, ('POINTS', 'Cw_a'))

    Outline3 = AngularPeriodicFilter(Input=transform3)
    Outline3.IterationMode = 'Manual'
    Outline3.NumberOfPeriods = 2
    Outline3.RotationAngle = 30.0
    Outline3.Axis = 'Axis Z'
    Outline3.Center = [0.01, 0.0, 0.0]
    Outline3Display = Show(Outline3, renderView1)
    Outline3Display.SetRepresentationType('Feature Edges')
    Outline3Display.AmbientColor = [0.0, 0.0, 0.0]
    Outline3Display.DiffuseColor = [0.0, 0.0, 0.0]
    # Render()

    # get color transfer function/color map for 'Cw_'
    Cw_sLUT = GetColorTransferFunction('Cw_s')
    Cw_sPWF = GetOpacityTransferFunction('Cw_s')
    Cw_sPWF.RescaleTransferFunction(-15.0, 15.0)
    Cw_sLUT.RescaleTransferFunction(-15.0, 15.0)
    Cw_sLUT.AutomaticRescaleRangeMode = 'Never'
    Cw_sLUT.RGBPoints = [-15.0, 0.231373, 0.298039, 0.752941, 0.0, 1, 1, 1, 15.0, 0.705882, 0.0156863, 0.14902]
    Cw_sLUT.ScalarRangeInitialized = 1.0

    # get color legend/bar for Cw_sLUT in view renderView1
    Cw_sLUTColorBar = GetScalarBar(Cw_sLUT, renderView1)
    Cw_sLUTColorBar.WindowLocation = 'UpperLeftCorner'
    Cw_sLUTColorBar.Title = 'Streamwise Vorticity Coefficient'
    Cw_sLUTColorBar.ComponentTitle = ''
    Cw_sLUTColorBar.TitleJustification = 'Left'
    Cw_sLUTColorBar.HorizontalTitle = 1
    Cw_sLUTColorBar.TitleColor = [0.0, 0.0, 0.0]
    Cw_sLUTColorBar.TitleBold = 1
    Cw_sLUTColorBar.TitleFontSize = FontSize
    Cw_sLUTColorBar.LabelColor = [0.0, 0.0, 0.0]
    Cw_sLUTColorBar.LabelFontSize = FontSize
    Cw_sLUTColorBar.ScalarBarThickness = ColorBarWidth
    Cw_sLUTColorBar.ScalarBarLength = 0.5
    Cw_sLUTColorBar.RangeLabelFormat = '%-#6.1f'
    # get color transfer function/color map for 'CV'
    CVLUT = GetColorTransferFunction('CV')
    CVPWF = GetOpacityTransferFunction('CV')
    CVPWF.RescaleTransferFunction(0, 1.5)
    CVLUT.RescaleTransferFunction(0, 1.5)
    CVLUT.AutomaticRescaleRangeMode = 'Never'
    CVLUT.RGBPoints = [0, 0.231373, 0.298039, 0.752941, 0.75, 1, 1, 1, 1.5, 0.705882, 0.0156863, 0.14902]
    CVLUT.ScalarRangeInitialized = 1.0
#       CVLUT.InvertTransferFunction()


    # get color legend/bar for CVLUT in view renderView1
    CVLUTColorBar = GetScalarBar(CVLUT, renderView1)
    CVLUTColorBar.Orientation = 'Horizontal'
    CVLUTColorBar.WindowLocation = 'LowerCenter'
    CVLUTColorBar.Title = 'Velocity Coefficient'
    CVLUTColorBar.ComponentTitle = ''
    CVLUTColorBar.TitleJustification = 'Centered'
    CVLUTColorBar.HorizontalTitle = 1
    CVLUTColorBar.TitleColor = [0.0, 0.0, 0.0]
    CVLUTColorBar.TitleBold = 1
    CVLUTColorBar.TitleFontSize = FontSize
    CVLUTColorBar.LabelColor = [0.0, 0.0, 0.0]
    CVLUTColorBar.LabelFontSize = FontSize
    CVLUTColorBar.ScalarBarThickness = ColorBarWidth
    CVLUTColorBar.ScalarBarLength = 0.5
    CVLUTColorBar.RangeLabelFormat = ’%-#6.1f’

    # get color transfer function/color map for ’Cw_a’
    cw_aLUT = GetColorTransferFunction(’Cw_a’)
    cw_aPWF = GetOpacityTransferFunction(’Cw_a’)
    cw_aPWF.RescaleTransferFunction(0.0, 20)
    cw_aLUT.RescaleTransferFunction(0.0, 20)
    cw_aLUT.AutomaticRescaleRangeMode = ’Never’
    cw_aLUT.RGBPoints = [0.0, 1, 1, 1, 20.0, 0.705882, 0.0156863, 0.14902]
    cw_aLUT.ScalarRangeInitialized = 1.0

    # get color legend/bar for cw_aLUT in view renderView1
    cw_aLUTColorBar = GetScalarBar(cw_aLUT, renderView1)
    cw_aLUTColorBar.WindowLocation = ’UpperRightCorner’
    cw_aLUTColorBar.Title = ’Azimuthal Vorticity Coefficient’
    cw_aLUTColorBar.ComponentTitle = ’’
    cw_aLUTColorBar.TitleJustification = ’Right’
    cw_aLUTColorBar.HorizontalTitle = 1
    cw_aLUTColorBar.TitleColor = [0.0, 0.0, 0.0]
    cw_aLUTColorBar.TitleBold = 1
    cw_aLUTColorBar.TitleFontSize = FontSize
    cw_aLUTColorBar.LabelColor = [0.0, 0.0, 0.0]
    cw_aLUTColorBar.LabelFontSize = FontSize
    cw_aLUTColorBar.ScalarBarThickness = ColorBarWidth
    cw_aLUTColorBar.ScalarBarLength = 0.5
    cw_aLUTColorBar.RangeLabelFormat = ’%-#6.1f’

    ResetCamera()
    camera=GetActiveCamera()
    camera.SetFocalPoint(0,0.05,1)
    camera.SetPosition(0,0.05,2.5)
    camera.SetParallelProjection(True)
    camera.SetParallelScale(0.1)

    for i in range(2,26):
        index = str(i)
        # Properties modified on extractBlock1
        extractBlock1.BlockIndices = [i]

        # update the view to ensure updated data information
        UpdatePipeline()
        # ResetCamera()

        # save screenshot
        SaveScreenshot(SavePath+’/’+Names[i-2]+’.png’, renderView1,
        ImageResolution=Resolution,
        OverrideColorPalette=’WhiteBackground’,
        TransparentBackground=1,
        # PNG options
        CompressionLevel=’5’)
    # Quit()
    Disconnect()
    Connect()
```

Meridional Contours

```
def CheckDirectory(P):
# Checks that the argument P is a directory. If it doesn’t exist, it will create the directory and any folders above.
    import os
    if os.path.isdir(P)==False:
        os.makedirs(P)

def BaseTransform(Name,In,Translate,Rotate):
    Name = Transform(Input=In)
    Name.Transform.Translate = Translate
    Name.Transform.Rotate = Rotate

```

```

#### import the simple module from the paraview
from paraview.simple import *
import numpy as np
from datetime import date
import os
today = date.today().strftime("%Y-%m-%d")

ReadPath = ’T:/PhD_CGNS/CGNS/’
F=[]
for file in os.listdir(ReadPath):
    if file.endswith("Scalloped_LowSpeed.cgns"):
        file = file[:-5]
        F.append(file)

Resolution = [1940, 700]
FontSize = 25
ColorBarWidth = 40
Parameters = [’CD’, ’CM’, ’CPo’, ’CPs’, ’CTKE’, ’CTo’, ’CV’, ’Cw_a’, ’Cw_s’, ’Mach Number’, ’Vxyz’, ’Y’]
P = ’CV’
Planes = [27,28,29,30]
Min = 0
Max = 1.5
Mid = (Min+Max)/2

Names = [’MeridionalScallop2’,’MeridionalScallop1’,’MeridionalValley’,’MeridionalCrest’]

# for S in F[21:25]:
for S in F:
    SavePath = ’T:/PhD_CGNS/Figures/’+today+’/’+S
    CheckDirectory(SavePath)

    # print(ReadPath+S)

    # set active view
    # SetActiveView(None)
    # Create a new ’Render View’
    renderView1 = CreateView('RenderView')
    renderView1.CameraParallelProjection = 1
    # Hide orientation axes
    renderView1.OrientationAxesVisibility = 0
    # uncomment following to set a specific view size
    renderView1.ViewSize = Resolution
    renderView1.UseLight = 0

    # create a new 'CGNS Series Reader'
    Data_CGNS = CGNSSeriesReader(FileNames=[ReadPath+S+'.cgns'])

    # Properties modified on Data_CGNS
    Data_CGNS.PointArrayStatus = Parameters

    clip1 = Clip(Input=Data_CGNS)
    clip1.ClipType = 'Cylinder'

    # Properties modified on clip1.ClipType
    clip1.ClipType.Center = [0.0, 0.0, 0.0]
    clip1.ClipType.Axis = [0.0, 0.0, 1.0]
    clip1.ClipType.Radius = 0.2

    # show data in view
    # clip1Display = Show(clip1, renderView1)

    # create a new 'Clip'
    clip2 = Clip(Input=clip1)
    clip2.ClipType = 'Plane'
    clip2.Scalars = ['POINTS', 'CD']
    clip2.Value = 0.6998854950070381

    # Properties modified on clip2.ClipType
    clip2.ClipType.Origin = [0.0, 0.0, 1.5]
    clip2.ClipType.Normal = [0.0, 0.0, 1.0]

    # show data in view
    # clip2Display = Show(clip2, renderView1)

    # create a new 'Clip'
```

```
clip3 = Clip(Input=clip2)
clip3.ClipType = ’Plane’
clip3.Scalars = [’POINTS’, ’CD’]
clip3.Value = 0.6998854950070381

# Properties modified on clip3.ClipType
clip3.ClipType.Origin = [0.0, 0.0, 0.25]
clip3.ClipType.Normal = [0.0, 0.0, -1.0]

# show data in view
# clip3Display = Show(clip3, renderView1)

# create a new ’Extract Block’
extractBlock1 = ExtractBlock(Input=clip3)
# show data in view
extractBlock1Display = Show(extractBlock1, renderView1)
Mixer = ExtractBlock(Input=clip3)
Mixer.BlockIndices = [31, 40, 34, 35, 32, 33, 38, 39, 36, 37] # Without Deswirler
MixerDisplay = Show(Mixer, renderView1)
MixerDisplay.AmbientColor = [0.45,0.45,0.45]
MixerDisplay.DiffuseColor = [0.45,0.45,0.45]
MixerDisplay.Opacity = 0.5

# create a new ’Mask Points’
maskPoints1 = MaskPoints(Input=extractBlock1)

# set active source
SetActiveSource(extractBlock1)

# create a new ’Stream Tracer With Custom Source’
streamTracerWithCustomSource1 = StreamTracerWithCustomSource(Input=extractBlock1,
    SeedSource=maskPoints1)
streamTracerWithCustomSource1.Vectors = [’POINTS’, ’Vxyz’]
streamTracerWithCustomSource1.MaximumStreamlineLength = 1.25
streamTracerWithCustomSource1.SurfaceStreamlines = 1
# Properties modified on maskPoints1
maskPoints1.OnRatio = 50
```

```
 maskPoints1.MaximumNumberofPoints = 40
 maskPoints1.RandomSampling = 1

 # show data in view
 streamTracerWithCustomSource1Display = Show(streamTracerWithCustomSource1, renderView1)

 # change solid color
 streamTracerWithCustomSource1Display.AmbientColor = [0.0, 0.0, 0.0]
 streamTracerWithCustomSource1Display.DiffuseColor = [0.0, 0.0, 0.0]


 ResetCamera()
 camera=GetActiveCamera()
 camera.SetFocalPoint(0,0.1,0.85)
 camera.SetPosition(-1,0.1,0.85)
 camera.SetParallelProjection(True)
 camera.SetParallelScale(0.22)
 # camera.Roll(180)
 # set scalar coloring
 ColorBy(extractBlock1Display, (’POINTS’, P))

 # show color bar/color legend
 extractBlock1Display.SetScalarBarVisibility(renderView1, True)

 # get color transfer function/color map for P
 ColorMap = GetColorTransferFunction(P)

 # get opacity transfer function/opacity map for P
 OpacityMap = GetOpacityTransferFunction(P)


 ColorMap = GetColorTransferFunction(P)
 ColorMap.RescaleTransferFunction(Min, Max)
 RGBPoints = [Min, 0.231373, 0.298039, 0.752941, Mid, 1.0, 1.0, 1.0, Max, 0.705882, 0.0156863, 0.14902]
 ColorMap.AutomaticRescaleRangeMode = ’Never’
```

```
    ColorMap.ScalarRangeInitialized = 1.0
    # ColorMap.InvertTransferFunction()
    # get color legend/bar for ColorMap in view renderView1
    ColorMapColorBar = GetScalarBar(ColorMap, renderView1)
    ColorMapColorBar.Orientation = 'Horizontal'
    ColorMapColorBar.WindowLocation = 'LowerCenter'
    ColorMapColorBar.Title = P
    ColorMapColorBar.ComponentTitle = ''
    ColorMapColorBar.TitleJustification = 'Centered'
    ColorMapColorBar.HorizontalTitle = 1
    ColorMapColorBar.TitleColor = [0.0, 0.0, 0.0]
    ColorMapColorBar.TitleBold = 1
    ColorMapColorBar.TitleFontSize = FontSize
    ColorMapColorBar.LabelColor = [0.0, 0.0, 0.0]
    ColorMapColorBar.LabelFontSize = FontSize
    ColorMapColorBar.ScalarBarThickness = ColorBarWidth
    ColorMapColorBar.ScalarBarLength = 0.8
    ColorMapColorBar.RangeLabelFormat = '%-#6.1f'
    j=0
    for i in Planes:

        index = str(i)
        # Properties modified on extractBlock1
        extractBlock1.BlockIndices = [i]

        # update the view to ensure updated data information
        UpdatePipeline()
        renderView1.Update()
        # ResetCamera()

        # save screenshot
        SaveScreenshot(SavePath+'/'+P+'_'+Names[j]+'.png',
    renderView1,
        ImageResolution=Resolution,
        OverrideColorPalette='WhiteBackground',
        TransparentBackground=1,
        # PNG options
        CompressionLevel='5')
        j+=1
    # Quit()
    Disconnect()
    Connect()
```

3D Streamlines

```
def CheckDirectory(P):
    # Checks that the argument P is a directory. If it doesn’t exist, it will create the directory and any folders above.
    import os
    if os.path.isdir(P)==False:
        os.makedirs(P)

def BaseTransform(Name,In,Translate,Rotate):
    Name = Transform(Input=In)
    Name.Transform.Translate = Translate
    Name.Transform.Rotate = Rotate


#### import the simple module from the paraview
from paraview.simple import *
import numpy as np
from datetime import date
import os
today = date.today().strftime("%Y-%m-%d")

PathCGNS = ’T:/PhD_CGNS/CGNS/’
PathLarge = ’T:/PhD_CGNS/Large/’
F=[]
for file in os.listdir(PathCGNS):
    if file.endswith("hiSpeed.cgns"):
        file = file[:-5]
        F.append(file)


Resolution = [1032, 820]

for S in F:
    print(S)
    SavePath = 'T:/PhD_CGNS/Figures/'+today+'/'+S
    CheckDirectory(SavePath)
    # load state
    LoadState('D:\Alex\OneDrive\Desktop\Wright Style Guide\Thesis\Chapters\Current\Scalloping\Figures\Streamlines.pvsm', LoadStateDataFileOptions='Choose File Names',
        DataDirectory='T:/PhD_CGNS/',
        PlanesFileNames=[PathCGNS+S+'.cgns'],
        StreamlinesFileNames=[PathLarge+S+'.cgns'])


    # find view
    renderView1 = FindViewOrCreate('RenderView1', viewtype='RenderView')
    # uncomment following to set a specific view size
#    renderView1.ViewSize = Resolution

    # set active view
    SetActiveView(renderView1)
    # save screenshot
    # SaveScreenshot(SavePath+'/MixerLoading_Deswirl.png', renderView1,
    SaveScreenshot(SavePath+'/Streamlines.png', renderView1,
    ImageResolution=Resolution,
    TransparentBackground=1,
    # PNG options
    CompressionLevel='5')
    # Quit()
    Disconnect()
    Connect()
```

Static Pressure Loading

```
def CheckDirectory(P):
    # Checks that the argument P is a directory. If it doesn't exist, it will create the directory and any folders above.
    import os
    if os.path.isdir(P)==False:
        os.makedirs(P)

def BaseTransform(Name,In,Translate,Rotate):
    Name = Transform(Input=In)
    Name.Transform.Translate = Translate
    Name.Transform.Rotate = Rotate

#### import the simple module from the paraview
from paraview.simple import *
import numpy as np
from datetime import date
import os

#### disable automatic camera reset on ’Show’
paraview.simple._DisableFirstRenderCameraReset()

today = date.today().strftime("%Y-%m-%d")

ReadPath = ’T:/PhD_CGNS/CGNS/’
F=[]
for file in os.listdir(ReadPath):
    if file.endswith(".cgns"):
        file = file[:-5]
        F.append(file)

i=36
Resolution = [970, 1000]
FontSize = 25
ColorBarWidth = 40
Min = -1
Max = 1
Mid = (Min+Max)/2

# S=F[1]
for S in F:
    SavePath = ’T:/PhD_CGNS/Figures/’+today+’/’+S
    CheckDirectory(SavePath)


    # create a new ’CGNS Series Reader’
    Data_CGNS = CGNSSeriesReader(FileNames=[ReadPath+S+’.cgns’])
    # Properties modified on Data_CGNS
    Data_CGNS.PointArrayStatus = [’CPs Core’, ’Vxyz’,
         ’Viscous stress (wall to fluid)’]

    # get active view
    renderView1 = GetActiveViewOrCreate(’RenderView’)
    # Hide orientation axes
    renderView1.OrientationAxesVisibility = 0

    renderView1.ViewSize = Resolution
    renderView1.UseLight = 0

    # create a new ’Extract Block’
    extractBlock1 = ExtractBlock(Input=Data_CGNS)
    # Properties modified on extractBlock1
    extractBlock1.BlockIndices = [i]
    # create a new ’Transform’
    transform1 = Transform(Input=extractBlock1)
    transform1.Transform.Rotate = [0.0, 0.0, -15.0]
    # transform1Display = Show(transform1, renderView1)
    # ColorBy(transform1Display,(’POINTS’, ’CPs Core’))

    # create a new ’Mask Points’
    maskPoints1 = MaskPoints(Input=transform1)

    # create a new ’Angular Periodic Filter’
    angularPeriodicFilter1 = AngularPeriodicFilter(Input=transform1)
    angularPeriodicFilter1.IterationMode = ’Manual’
    angularPeriodicFilter1.NumberOfPeriods = 2
    angularPeriodicFilter1.RotationAngle = 30.0
    angularPeriodicFilter1.Axis = ’Axis Z’
    angularPeriodicFilter1Display = Show(angularPeriodicFilter1,
   renderView1)
    angularPeriodicFilter1.BlockIndices = [1]
    ColorBy(angularPeriodicFilter1Display, (’POINTS’, ’CPs Core’))

```

```
# create a new 'Transform'
transform2 = Transform(Input=extractBlock1)
transform2.Transform.Rotate = [0.0, 0.0, -15.0]


Outline1 = AngularPeriodicFilter(Input=transform2)
Outline1.IterationMode = 'Manual'
Outline1.NumberOfPeriods = 2
Outline1.RotationAngle = 30.0
Outline1.Axis = 'Axis Z'
Outline1Display = Show(Outline1, renderView1)
Outline1.BlockIndices = [1]
Outline1Display.SetRepresentationType('Feature Edges')
Outline1Display.AmbientColor = [0.0, 0.0, 0.0]
Outline1Display.DiffuseColor = [0.0, 0.0, 0.0]


# create a new 'Stream Tracer With Custom Source'
streamTracerWithCustomSource1 = StreamTracerWithCustomSource(Input=transform1,
    SeedSource=maskPoints1)
streamTracerWithCustomSource1.Vectors = ['POINTS',
     'Viscous stress (wall to fluid)']
streamTracerWithCustomSource1.MaximumStreamlineLength = 1.25
streamTracerWithCustomSource1.SurfaceStreamlines = 1
# Properties modified on maskPoints1
maskPoints1.OnRatio = 50
maskPoints1.MaximumNumberofPoints = 100
maskPoints1.RandomSampling = 1

# show data in view
streamTracerWithCustomSource1Display = Show(streamTracerWithCustomSource1, renderView1)

Streamline = AngularPeriodicFilter(Input=streamTracerWithCustomSource1)
Streamline.IterationMode = 'Manual'
Streamline.NumberOfPeriods = 2
Streamline.RotationAngle = 30.0
```

```
    Streamline.Axis = 'Axis Z'
    StreamlineDisplay = Show(Streamline, renderView1)
    Streamline.BlockIndices = [1]
    StreamlineDisplay.AmbientColor = [0.5, 0.5, 0.5]
    StreamlineDisplay.DiffuseColor = [0.5, 0.5, 0.5]


    # # change solid color
    # streamTracerWithCustomSource1Display.AmbientColor = [0.0, 0.0, 0.0]
    # streamTracerWithCustomSource1Display.DiffuseColor = [0.0, 0.0, 0.0]

    # get color transfer function/color map for 'CP'
    CPsCoreLUT = GetColorTransferFunction('CPs Core')
    CPsCorePWF = GetOpacityTransferFunction('CPs Core')
    CPsCorePWF.RescaleTransferFunction(Min, Max)
    CPsCoreLUT.RescaleTransferFunction(Min, Max)
    CPsCoreLUT.AutomaticRescaleRangeMode = 'Never'
    CPsCoreLUT.RGBPoints = [Min, 0.231373, 0.298039, 0.752941, Mid, 1, 1, 1, Max, 0.705882, 0.0156863, 0.14902]
    CPsCoreLUT.ScalarRangeInitialized = 1.0

    # get color legend/bar for CPsCoreLUT in view renderView1
    CPsCoreLUTColorBar = GetScalarBar(CPsCoreLUT, renderView1)
    CPsCoreLUTColorBar.WindowLocation = 'UpperLeftCorner'
    CPsCoreLUTColorBar.Title = 'Static Pressure Surface Loading'
    CPsCoreLUTColorBar.ComponentTitle = ''
    CPsCoreLUTColorBar.TitleJustification = 'Left'
    CPsCoreLUTColorBar.HorizontalTitle = 1
    CPsCoreLUTColorBar.TitleColor = [0.0, 0.0, 0.0]
    CPsCoreLUTColorBar.TitleBold = 1
    CPsCoreLUTColorBar.TitleFontSize = FontSize
    CPsCoreLUTColorBar.LabelColor = [0.0, 0.0, 0.0]
    CPsCoreLUTColorBar.LabelFontSize = FontSize
    CPsCoreLUTColorBar.ScalarBarThickness = ColorBarWidth
    CPsCoreLUTColorBar.ScalarBarLength = 0.5
    CPsCoreLUTColorBar.RangeLabelFormat = '%-#6.1f'



    ResetCamera()
    camera=GetActiveCamera()
    camera.SetPosition(-1e-6, -0.7, -0.4)
    camera.SetFocalPoint(1e-6, -0.03, 0.45)
    camera.SetParallelProjection(True)
    camera.SetParallelScale(0.1)
    camera.Roll(180)

    # update the view to ensure updated data information
    UpdatePipeline()
    RenderAllViews()

    # ResetCamera()

    # save screenshot
    # SaveScreenshot(SavePath+'/MixerLoading_Deswirl.png', renderView1,
    SaveScreenshot(SavePath+'/MixerLoading.png', renderView1,
    ImageResolution=Resolution,
    OverrideColorPalette='WhiteBackground',
    TransparentBackground=1,
    # PNG options
    CompressionLevel='5')
    # Quit()
    Disconnect()
    Connect()
```